Title

Computational Modeling of Electrochemical Systems for Energy Conversion Using Density Functional Theory and Many-Body Perturbation Theory

Author

Wei, Ziyang

Publication Date

2022

Peer reviewed|Thesis/dissertation

UNIVERSITY OF CALIFORNIA

Los Angeles

Computational Modeling of Electrochemical Systems for Energy Conversion Using Density Functional Theory and Many-Body Perturbation Theory

A dissertation submitted in partial satisfaction
of the requirements for the degree
Doctor of Philosophy in Chemistry

by

Ziyang Wei

2022

ABSTRACT OF THE DISSERTATION

Computational Modeling of Electrochemical Systems for Energy Conversion Using Density Functional Theory and Many-Body Perturbation Theory

by

Ziyang Wei
Doctor of Philosophy in Chemistry
University of California, Los Angeles, 2022
Professor Philippe Sautet, Chair

Electrocatalysis plays a key role in sustainable energy conversion and storage. Although tremendous efforts from the experimental side have been devoted to elucidating the reaction mechanism, the detailed reaction pathways are still controversial due to intrinsic difficulty of *in situ* spectroscopy under electrochemical conditions. Therefore, computational studies based on density functional theory (DFT) energetics serve as an important tool to clarify the reaction mechanism. However, several aspects such as solvation effects and the electrochemical potential effects are important for the electrochemical systems while such effects are often absent in the simulations. Moreover, current DFT exchange correlation functionals present certain qualitative and quantitative errors, while the combination of solvation treatments and the more advanced computational methods are not established. To address these concerns, this thesis work on two different levels, stressing on incorporating the necessary effects to model the electrochemical processes. At the DFT level, we model the complicated sulfur reduction reaction process on heteroatom doped holey graphene framework. Specifically, we elucidate the electrocatalytic origin of the improved battery performance with these catalysts and decipher the complex 16-electron process. At the more advanced many-body perturbation theory (MBPT) level, we focus on the random phase approximation (RPA), as a promising approach to address certain DFT errors such as the carbon monoxide (CO)

adsorption puzzle: the commonly used functionals give incorrect prediction of the CO adsorption site and energy on transition metal catalysts, which is key for several catalytic processes including the industrial catalysis for methanol synthesis from synthesis gas, the water-gas shift reaction, and the electrochemical carbon dioxide reduction reaction. Nevertheless, the cost of RPA for surface systems is often unaffordable, and the combination of RPA with implicit solvation and further the grand canonical treatment of electrons to describe the electrochemical potential, is generally not established. In this thesis, to pave the way to further electrochemical applications using RPA, we exploit a k-space extrapolation scheme to reduce the cost for surface calculations. Then we further combine the RPA framework for electrified interfaces, including implicit solvation described using the linearized Poisson-Boltzmann equation and the grand canonical treatment of electrons. We show that the RPA results are qualitatively and quantitatively different from commonly used functionals and match better with the experimental results.

The dissertation of Ziyang Wei is approved.

Anastassia N. Alexandrova

Daniel Neuhauser

Benjamin Joel Schwartz

Philippe Sautet, Committee Chair

University of California, Los Angeles

2022

To my parents . . .

who now know

Jacob's ladder.

Table of Contents

List of Figures

List of Tables

Acknowledgments

First, I would like to express my deepest appreciation to my amazing advisor Philippe Sautet, who made this long journey enjoyable. I still recall the moment when he encouraged me in one of my darkest hours: *Ziyang, we are computational chemists, if we don't believe our results, who will?* He sets the example of a great scientist and an even greater educator.

I would like to express my gratitude to my committee members, Anastassia Alexandrova, Daniel Neuhauser, and Benjamin Schwartz, for their constructive suggestions for the candidacy exam, the exit seminar and the dissertation. Additionally, I would like to thank Anastassia for her computational chemistry course, Danny for his quantum chemistry notes and Ben for his marvelous statistical mechanics course. I would also like to give special thanks to Kainning Duanmu, Geng Sun, Stephan Steinmann, and Florian Göltl. This work cannot be finished without their help. I'd like to acknowledge my group members, especially George Yan, for their help and discussions. Thanks should also go to all my collaborators.

Finally, I would be remiss in not mentioning my friends and parents. I cannot describe how surprised I was when my father asked me whether the RPA I mentioned is the one on Jacob's ladder.

Several chapters and sections of chapters in this dissertation are a collection of the previous publications listed below: Chapter 2 contains part adapted with permission from publication "A fundamental look at electrocatalytic sulfur reduction reaction" Peng, L.; Wei, Z.; Wan, C.; Li, J.; Chen, Z.; Zhu, D.; Baumann, D.; Liu, H.; Allen, C. S.; Xu, X., et al. *Nature Catalysis* **2020**, *3*, 762–770. Copyright (2020) Springer Nature Limited. This work is supported by the Center for Synthetic Control Across Length-scales for Advancing Rechargeables, an Energy Frontier Research Center funded by the US Department of Energy, Office of Science Basic Energy Sciences programme under award DE-SC0019381. The calculations were performed on the Hoffman2 cluster at UCLA Institute for Digital Research and Education (IDRE), The National Energy Research Scientific Computing Center (NERSC), and the Extreme Science and Engineering Discovery Environment (XSEDE),

which is supported by National Science Foundation grant number ACI-1548562, through allocation TG-CHE170060.

Chapter 3 is adapted with permission from publication "Atomic Environments in N-doped Graphene Probed by First-principle Calculations and Nuclear Magnetic Resonance" Wei, Z.; Becwar, S. M.; Chmelka, B. F.; Sautet, P.; *the Journal of Physical Chemistry C* **2021**, *125*, 8779- 8787. Copyright (2021) American Chemical Society. This work is supported by the Center for Synthetic Control Across Length-scales for Advancing Rechargeables, an Energy Frontier Research Center funded by the US Department of Energy, Office of Science Basic Energy Sciences programme under award DE-SC0019381. The calculations were performed on the Hoffman2 cluster at UCLA Institute for Digital Research and Education (IDRE) and the Extreme Science and Engineering Discovery Environment (XSEDE), which is supported by the National Science Foundation grant number ACI-1548562, through allocation TG-CHE170060.

Chapter 4 is adapted with permission from publication "Diffusion Barriers for Carbon Monoxide on the Cu (001) Surface Using Many-Body Perturbation Theory and Various Density Functionals" Wei, Z.; Göltl, F.; Sautet, P. *Journal of Chemical Theory and Computation* **2021**, *17*, 7862–7872. Copyright (2022) American Chemical Society. The calculations were performed on the Hoffman2 cluster at UCLA Institute for Digital Research and Education (IDRE) and the Extreme Science and Engineering Discovery Environment (XSEDE), which is supported by National Science Foundation grant number ACI-1548562, through allocation TG-CHE170060.

Curriculum Vitae

2012 – 2017 B.S. (Chemistry), Fudan University, Shanghai, China.

Awards

1. 2020-2021 UCLA Graduate Division Dissertation Year Fellowship

Publications

1. Steinmann, S. N.; Wei, Z.-Y.; Sautet, P. Theory and experiments join forces to characterize the electrocatalytic interface. *Proceedings of the National Academy of Sciences* **2019**, *116*, 7611–7613.

2. Peng, L.; Wei, Z.; Wan, C.; Li, J.; Chen, Z.; Zhu, D.; Baumann, D.; Liu, H.; Allen, C. S.; Xu, X., et al. A fundamental look at electrocatalytic sulfur reduction reaction. *Nature Catalysis* **2020**, *3*, 762–770.

3. Yan, Q.; Whang, G.; Wei, Z.; Ko, S.-T.; Sautet, P.; Tolbert, S. H.; Dunn, B. S.; Luo, J. A Perspective on interfacial engineering of lithium metal anodes and beyond. *Applied Physics Letters* **2020**, *117*, 080504.

4. Whang, G.; Yan, Q.; Li, D.; Wei, Z.; Butts, D.; Sautet, P.; Luo, J.; Dunn, B. Avoiding dendrite formation by confining lithium deposition underneath Li–Sn coatings. *Journal of Materials Research* **2021**, *36*, 797-811.

5. Wei, Z.; Becwar, S. M.; Chmelka, B. F.; Sautet, P.; Atomic Environments in N-doped Graphene Probed by First-principle Calculations and Nuclear Magnetic Resonance. *the Journal of Physical Chemistry C* **2021**, *125*, 8779- 8787

6. Wei, Z.; Göltl, F.; Sautet, P. Diffusion Barriers for Carbon Monoxide on the Cu (001) Surface Using Many-Body Perturbation Theory and Various Density Functionals. *Journal of Chemical Theory and Computation* **2021**, *17*, 7862–7872

7. Wei, Z.; Sautet, P. Revisiting the Link between Magnetic Properties and Chemisorption at Graphene Nanoribbon Zigzag Edge. *Journal of Chemical Physics* **2022**, *156*, 044706

8. Wei, Z.; Sautet, P. Towards More Accurate Modelling of CO_2 Electroreduction Mechanism with Many-body Perturbation Theory. *Submitted*

9. Wei, Z.; Göltl, F.; Steinmann S.; Sautet, P. Modeling Electrochemical Processes with Grand Canonical Treatment of Many-body Perturbation Theory. *Submitted*

Presentations

1. Wei, Z.; Göltl, F.; Sautet, P. Applications of Many Body Perturbation Theory: From Vacuum to Electrochemical Systems. *ACS Spring 2022* San Diego, USA, 2022.

CHAPTER 1

Motivation and Challenges in Computational Modeling of Electrochemical Systems

1.1 Climate Change and Electrocatalysis

The contemporary climate change has raised serious concerns as the environmental impacts are broad and far-reaching[1, 2]. Related phenomena include but are not limited to global warming, global sea level rising, and a higher frequency of extreme weather. These phenomena further lead to ecological collapse such as the widespread coral bleaching of the Great Barrier Reef and direct economic damages originating from the more frequent droughts.

To mitigate these problems, in 2016, the Paris Climate Accords[3] was signed under the leadership of the United Nations Framework Convention on Climate Change. Three aims were proposed[3]: (a) Holding the increase in the global average temperature to well below 2 °C above pre-industrial levels and to pursue efforts to limit the temperature increase to 1.5 °C above pre-industrial levels, recognizing that this would significantly reduce the risks and impacts of climate change; (b) Increasing the ability to adapt to the adverse impacts of climate change and foster climate resilience and low greenhouse gas emissions development, in a manner that does not threaten food production; (c) Making finance flows consistent with a pathway towards low greenhouse gas emissions and climate-resilient development. It is clear from the accords that the greenhouse gas emission control[4] is at the heart of holding the global warming and it is generally agreed that the carbon-dioxide (CO_2) is important among the greenhouse gases[5]. Therefore, these targets pose a pressing need of lower CO_2 emission.

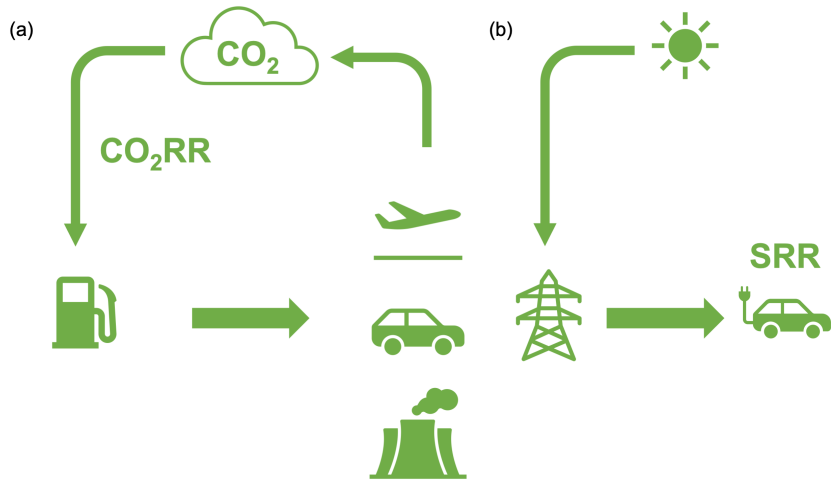

Figure 1.1: Schematic representation of different strategies proposed to control the greenhouse gas emission. (a) Green cycle where the CO_2 can be recycled instead of accumulating in the atmosphere. (b) The electrification strategy where the fossil fuel is not involved and hence CO_2 emission can be reduced.

Different strategies have been proposed to serve the purpose of low greenhouse gas emissions development. One is to establish a green cycle where the CO_2 can be recycled instead of accumulating in the atmosphere[5], as shown in Fig. 1.1 (a). The electrification strategy[6] as shown in Fig. 1.1 (b), which has now deeply transformed the portable electronics and transport, is another important strategy since the CO_2 emission is avoided in the process. Electrocatalysis is at the heart of various sustainable energy conversion and storage technologies needed for both the aforementioned strategies[7]. To fulfill the green cycle, The electrochemical CO_2 reduction reaction (CO_2RR) is a promising approach to convert the CO_2 into useful products[5]. To fulfill the electrification strategy, the highest energy storage possible for current commercial Li-ion batteries is insufficient and going beyond the horizon of Li-ion batteries is necessary.

To understand the electrocatalytic processes and design better catalysts, tremendous efforts have been devoted from the experimental side. Nevertheless, the detailed reaction mechanism is often unclear from the experimental side due to limited *in situ* spectroscopy[8].

In this context, first principles modeling[9, 10] plays a key role, since it is a method that can assign reaction energies and barriers to all possible reaction steps. When combining this information with microkinetic modeling[11, 12] or kinetic Monte Carlo simulations[13], it is then possible to predict reaction rates and selectivities for a specific catalytic system. This enables the screening of possible catalyst candidates or eventually the rational design of desired catalysts. However, several aspects such as solvation effects and the electrochemical potential effects are important for the electrochemical systems while such effects are often absent in the simulation[14].

To address these concerns, this thesis work on two different levels. At the more commonly used density functional theory (DFT) level, we model the complicated SRR process on heteroatom doped holey graphene framework (HGF). The lithium-sulfur (Li-S) battery[6] is a promising candidate for the next generation battery and it has been shown that electrocatalysis[15] is a successful strategy to accelerate the sulfur reduction reaction (SRR) and improve the battery performance. In combination with experiment, we show that electrocatalysis is a successful strategy and elucidate the origin of the improved battery performance with these catalysts and decipher the complex 16-electron process. To elucidate the structure of this complicated heteroatom doped HGF system, we perform DFT calculations to predict and explain the chemical shifts of N, C, H atoms in N-doped graphene system. The major difference between the chemical shifts of graphitic/pyridinic/pyrrolic N-moieties is understood by comparing the electronegativities of the various environments. At the more advanced many-body perturbation theory (MBPT) level, the calculations for surface systems are often unaffordable and the electrochemical treatments are generally not established. We focus on one specific form of the MBPT, the random phase approximation (RPA). We exploit a k-space extrapolation scheme to reduce the cost for surface calculations and then combine the RPA framework with electrochemical treatments, including implicit solvation described using the linearized Poisson-Boltzmann equation and the grand canonical treatment of electrons. We show that the RPA results are qualitatively and quantitatively different from commonly used functionals and match better with the experimental results.

1.2 Modeling of Electrochemical Systems with Density Functional Theory

The surging demand for energy storage has made it more important than any time in the past[16, 6]. After its commercialization in the 1990s[17], Li-ion batteries have reshaped portable electronics and electric vehicles in the last ten years. Nevertheless, the continuously increasing demand for energy storage calls for even higher energy storage density, i.e., to go beyond the theoretical specific energy (energy per unit weight) and energy density (energy per unit volume) of Li-ion batteries[18]. This field has attracted intense interest with Li-S batteries[19]: the theoretical specific energy of 2567 Wh/kg and energy density of 2199 Wh/L are respectively approximately six and two times that of the values of Li-ion batteries, 387 Wh/kg and 1015 Wh/L[6]. However, despite the extensive efforts made in Li-S battery systems since 1940s, fundamental issues remain to be addressed after seventy years[20, 21]. One major problem is the limited rate due to slow reaction processes[20, 21]. Additionally, this problem also leads to loss of capacity, due to shuttling and eventually loss of active materials during the reaction processes[22].

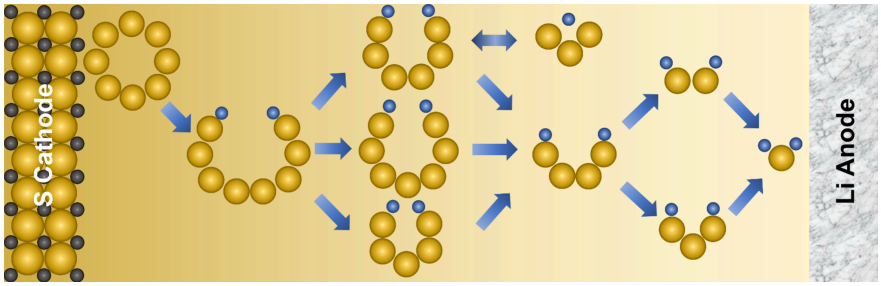

Figure 1.2: A schematic illustration of the SRR reaction network involved in the Li-S battery.

As catalysts have been utilized in other systems to accelerate the reaction process for hundreds of years, an electrocatalytic approach[23, 24, 25, 15] to accelerate the conversion seems to be a natural strategy to prevent the accumulation and shuttling of lithium polysulfides (LiPSs). Heteroatom doped holey graphene frameworks (HGF) exhibit tunable electrocatalytic properties[26, 15] and hence serve as a promising candidate for the electrocat-

alyst. However, the various sites exhibited in the HGF, together with the complex reaction network, as shown in Fig. 1.2, hinders the understanding of the system. Nevertheless, determining the nature of active sites, deciphering such reaction network, and understanding the relevant mechanism are essential for the rational design of the electrocatalysts. Therefore, we perform a systematic density functional theory (DFT) investigation of electrocatalytic SRR mechanism. We firstly show that the defect engineering and heteroatom doping are two strategies to tune the p-band center and hence the adsorption strength of intermediates. We then combine the DFT calculations with experimental spectroscopies to understand the complicated 16-electron process and also the catalytic effects in the overall reaction. We show that the larger output potential in the lower potential region also accelerates the conversion in the higher potential region and avoids unnecessary disproportionation, via the reaction equilibria existing in the reaction network. Our results rationalize and highlight the electrocatalytic approach as a promising strategy to tackle the fundamental challenges in Li-S batteries.

To elucidate the structure of this complicated heteroatom doped HGF system, we perform DFT calculations to predict and explain the chemical shifts of N, C, H atoms in N-doped graphene system. Comparisons of predicted chemical shifts with experimental 2D ^{13}C-^{15}N spectra show good agreement. The major difference between the chemical shifts of graphitic/pyridinic/pyrrolic N-moieties is understood by comparing the electronegativities of the various environments. Furthermore, for each type of environment, the general concept of signal broadening is decomposed into four different factors, the influences of which are discussed in detail. The first factor is the standalone N/C geometry, where a larger curvature of the graphene edge is found to give a more positive chemical shift. The second factor is the effect of a second N atom nearby: a graphitic N atom close to a pyridinic N decreases the chemical shift, while a pyridinic N close to a graphitic N increases the chemical shift. The third factor is that for each specific structure, the second neighbor C atom experiences a lower chemical shift. The fourth factor is the influence of residual water, which is important to understand the aqueous environment in oxygen reduction reaction or hydrogen evolution

reaction. Introduction of this factor matches with the experimental 2D ^{15}N-^{1}H spectrum and provides better agreement with the experimental ^{13}C-^{15}N spectrum. With the free energy taken into account, water adsorption on pyrrolic and pyridinic N sites is found to be more stable and to induce a positive or negative deviation in the chemical shift, respectively. An intuitive correlation between the charge of the probed atom and the chemical shift is confirmed: the smaller the charge, i.e., the higher the electron density, the more shielded the nucleus is, and hence the smaller the chemical shift. The relationship between charge and chemical shifts is discussed, enabling a more detailed understanding of the electronic influence of N doping.

1.3 Modeling of Electrochemical Systems with Many-Body Perturbation Theory

Although exchange correlation functionals[27, 28] at the generalized gradient approximation[29, 30, 31] (GGA) level are the most commonly used method to understand the reaction mechanisms, these functionals present qualitative and quantitative errors in the description of molecular adsorption. One important example of this shortcoming is the CO adsorption puzzle[32, 33, 34, 35]: predict the preference for adsorption in the face center cubic (FCC) site on the (111) facets and the hollow site on the (100) facets instead of the experimentally determined adsorption in the on top position and overestimate the adsorption energy. The CO adsorption description is important for several different catalytic processes, including the industrial catalyst for methanol synthesis from synthesis gas[36, 37, 38, 39], the water-gas shift reaction[40, 41], and the aforementioned electrochemical CO_2RR[42, 43, 44, 45]. While the incorrect prediction of the relative stability of CO adsorption to different high-symmetry surface sites is already concerning in its own right, it further poses the question, to what degree the description of the adsorption of other CO related intermediates involved in these reactions, is influenced by this shortcoming. Therefore, to better understand the mechanism of these important reactions including CO_2RR and eventually design better catalysts, a com-

putational method, which is intrinsically free of the aforementioned CO adsorption puzzle, is needed.

One way to solve these problems is to move to more accurate methods[46]. In particular, the RPA[47, 48], a post-Hartree-Fock (post-HF) method that is based on MBPT[49, 50], is a promising approach to address surface catalysis problems, since an implementation for plane waves in periodic boundary conditions exists[51, 52]. On top of that, RPA is the on method that correctly predicts the surface energy of Cu(111) and adsorption of CO in the top position on Cu(111) and multiple other late transition metal surfaces[53].

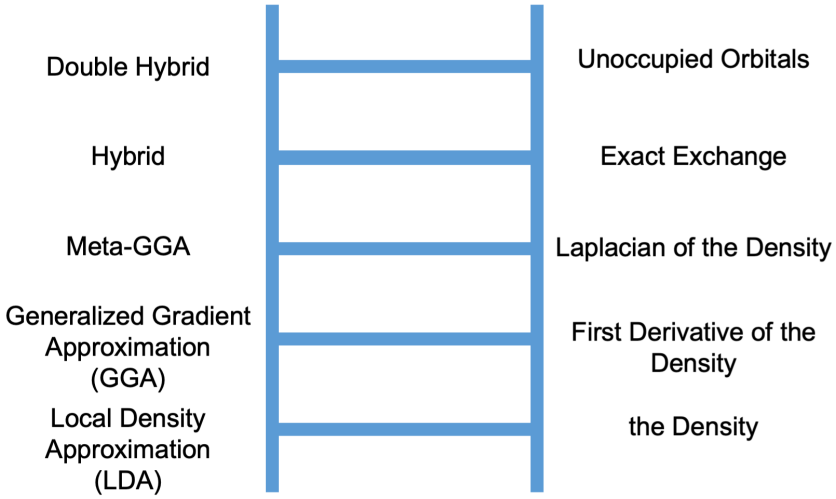

Figure 1.3: Jacob's ladder of density functional approximations. The rungs are labeled on the left, and the added ingredients are shown on the right. The RPA is on the fifth rung.

Nevertheless, as a method on the fifth rung of the Jacob's ladder, as shown in Fig. 1.3, the correlation component of the RPA energy relies on both the occupied and unoccupied orbitals[54, 49, 50, 55, 56]:

$$E_c = \int_0^1 d\lambda \int_0^\infty \frac{d\omega}{2\pi} Tr\{\nu[\chi^\lambda(i\omega) - \chi^0(i\omega)]\} \tag{1.1}$$

$$\chi^0_{\boldsymbol{G}\boldsymbol{G}'}(\boldsymbol{q}, i\omega) = \frac{1}{V} \sum_{n,n',\boldsymbol{k}} 2g_{\boldsymbol{k}}(f_{n'\boldsymbol{k}+\boldsymbol{q}} - f_{n\boldsymbol{k}}) \times \frac{\langle \psi_{n'\boldsymbol{k}+\boldsymbol{q}} | e^{i(\boldsymbol{q}+\boldsymbol{G})r} | \psi_{n\boldsymbol{k}} \rangle \langle \psi_{n\boldsymbol{k}} | e^{-i(\boldsymbol{q}+\boldsymbol{G}')r} | \psi_{n'\boldsymbol{k}+\boldsymbol{q}} \rangle}{\epsilon_{n'\boldsymbol{k}+\boldsymbol{q}} - \epsilon_{n\boldsymbol{k}} - i\omega} \tag{1.2}$$

$$\chi^{\lambda}(\boldsymbol{q}) = \chi^{0}(\boldsymbol{q}) + \chi^{0}(\boldsymbol{q})[\lambda\nu(\boldsymbol{q}) + f_{xc}^{\lambda}(\boldsymbol{q}, i\omega)]\chi^{\lambda}(\boldsymbol{q}) \tag{1.3}$$

As a result, RPA is significantly more expensive compared to GGA and hybrid functionals. Moreover, the reliance on unoccupied orbitals, as shown in Eq. 1.2, also introduces extra cost for surface systems: the number of unoccupied orbitals increases proportionally to the unit cell size. Therefore, the surface systems, with the presence of vacuum separation and hence significantly larger volumes, requires a significantly larger amount of unoccupied bands compared to the bulk systems, as shown in Fig. 1.4. Consequently, the practical yet critical problem of applying the RPA method to surface systems is the cost, and an approach to efficiently reduce the cost of RPA calculations is needed.

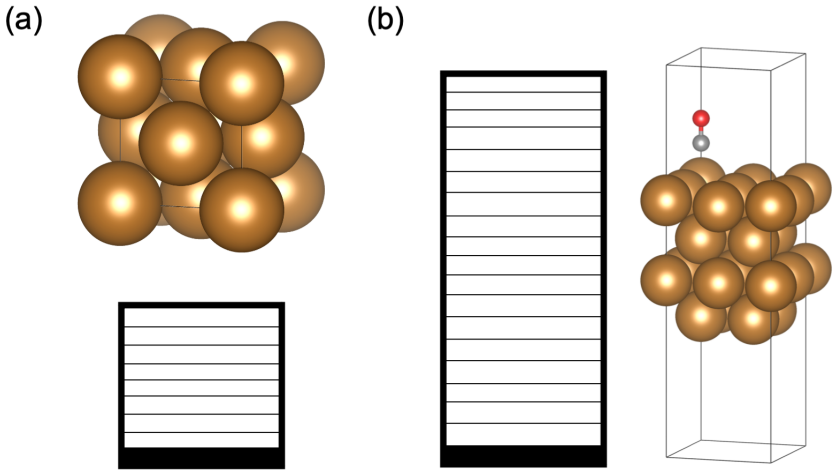

Figure 1.4: Schematic representation of the significantly larger amount of unoccupied bands in the surface system, (b), compared to the bulk system, (a). The shaded part corresponds to the occupied bands and the striped part corresponds to the unoccupied bands. The number of occupied bands does not change significantly between the bulk and surface systems as it is determined by the number of atoms. The number of unoccupied bands increases significantly in the surface system as it is proportional to the volume of the cell.

Therefore, we exploit a k-space extrapolation scheme to reduce the cost for surface calculations. We validate the proposed scheme and apply it to the CO diffusion on Cu(100) facet. We show that among the GGA, metaGGA, and hybrid functionals we considered,

RPA is the only method to give simultaneously correct description of the surface energy, CO adsorption and CO diffusion.

Besides, the modeling of electrochemical systems also requires the description of solvation and potential effects. Nonetheless, explicit solvation treatment, i.e., modeling the solvation effect with explicit water molecules, further increases the cost of the RPA calculations and the computational cost often becomes in practice not affordable; the more affordable implicit solvation treatment, i.e., modeling the solvation effect using polarizable continuum models, is not established for RPA calculations. Therefore, the combination of the RPA framework and implicit solvation is a promising and affordable approach to describe the solvation effects at the RPA level.

We explore the combination of the RPA framework and the implicit solvation described by the lPB equation. We the apply this methods to the electrochemical CO_2RR and found that RPA results, being compatible with experimental observations, are qualitatively different from the results of commonly used GGA functionals.

Moreover, the electrochemical systems are exposed to external applied potentials and thence in reduced or oxidized states. Different strategies have been proposed to model this effect. The simpler linear free energy relationship for electrode potentials was proposed first:

$$G(adsorption, U) = G(adsorbate*) - G(*) - \mu(adsorbate, U) \tag{1.4}$$

where $G(adsorption)$ stands for the adsorption free energy, $G(adsorbate*)$ stands for the free energy of the surface with adsorbates, $G(*)$ stands for the free energy of the bare surface, and $\mu(adsorbate, U)$ is the chemical potential of the adsorbate. The U notation indicates the potential dependence of the free energy. This treatment assumes only the free energy of the cation-electron pair is dependent on the electrochemical potential. For example, the computational hydrogen electrode is the case for proton-electron pair:

$$\mu(H^+) + \mu e^- = \frac{1}{2}\mu(H_2) - eU - ln10k_bTpH \tag{1.5}$$

However, it is clearly unphysical to assume the energies of bare surface and the surface with the adsorbate are unaffected when the potential is changed. In a nutshell, this can be viewed

as a *a posteriori* correction to the neutral system. To model the effects of potential on the surface systems, the more advanced constant potential model (CPM) was proposed later:

$$G(adsorption, U) = G(adsorbate*, U) - G(*, U) - \mu(adsorbate, U) \tag{1.6}$$

This requires, however, grand canonical treatment of the electrons, i.e., explicitly changing the number of electrons in the system to adjust the potential of the system, to model the potential dependent free energy of the surface systems, $G(adsorbate*, U)$ and $G(*, U)$. One key difficulty to combine the RPA framework with the CPM is the lack of self-consistent electronic structure: the Fermi level of the non-self-consistent RPA calculation is not simply available despite it being essential to determine the potential of the system. These concerns call for an approach to circumvent this difficulty is necessary to combine the RPA calculations with the CPM.

Therefore, we develop an alternative approach, which is purely based on the system's energy and can be used to determine the Fermi level via a partial derivative of the energy with respect to the number of electrons. We show that at the DFT level, this approach is equivalent to using the Fermi level value obtained from self-consistent electronic structure calculations. We furthermore demonstrate how this energy based approach can be used to perform grand canonical RPA (GC-RPA) calculations. We then apply this method to the potential dependent adsorption of carbon monoxide (CO) on Cu(100), and show that GC-RPA calculations lead to a qualitatively different description of this process compared to results obtained at the GGA level of theory.

1.4 Thesis Objectives

The objective of this thesis is to understand the electrochemical systems with DFT or RPA. In particular, I will explore the combination of the RPA framework with implicit solvation and grand canonical treatment of electrons to pave the way to further electrochemical applications of RPA. Chapter 2 describes the modeling of the SRR performed on different heteroatom doped graphene with DFT. This chapter aims to understand the origin of the

improved performance of the heteroatom doped graphene in SRR and the main branch of the complex reaction network. Chapter 3 describes the modeling of the structure and nuclear magnetic resonance (NMR) spectroscopy of the N-doped carbon material with DFT. This chapter aims to elucidate the structure-spectroscopy relationship and cast light on the detailed structure. Chapter 4 describes the modeling of the CO diffusion on Cu(100) facet with RPA and different functionals. This chapter aims to establish the k-space extrapolation scheme to reduce the cost of RPA calculation of surface systems and explore the difference in surface energy, adsorption description, and diffusion process. Chapter 5 describes the modeling of the CO_2 reduction reaction on Cu(100) facet with RPA and different functionals. This chapter aims to explore the combination of the RPA framework and implicit solvation described by the linearized Poisson-Boltzmann equation. Chapter 6 describes the effort of combining the RPA framework with the grand canonical treatment of electrons. One key aspect is to explore an alternative approach to obtain the Fermi level of the non-self-consistent RPA implementation.

CHAPTER 2

Deciphering the Reaction Networks for the Sixteen-Electron Sulfur Reduction Reaction

2.1 Introduction

The sulfur reduction reaction (SRR) in lithium-sulfur chemistry undergoes a complex 16-electron conversion process, transforming S_8 ring molecules into a series of soluble lithium polysulfides (LiPSs) with variable chain lengths before fully converting them into insoluble Li_2S_2/Li_2S products. This 16-electron SRR process is of considerable interest for high-density energy storage with a theoretical capacity of 1,672 mAh $\cdot$ g^{-1}, but the chemistry is plagued by sluggish sulfur reduction kinetics and the polysulfide (PS) shuttling effect. In practical Li-S cells, these effects limit the rate capability and cycle life[20, 21]. These limitations are fundamentally associated with the slow and complex reduction reaction involving S_8 ring molecules. In general, the insulating nature of elemental sulfur and its reduced products, and the sluggish charge transfer kinetics lead to incomplete conversion of S_8 molecules into soluble LiPSs. These polysulfides may shuttle across the separator to react with and deposit on the lithium anode, resulting in rapid capacity fading[22]. Considerable efforts have been devoted to combating the PS shuttling effect, typically by employing a passive strategy that uses various sulfur host materials to physically or electrostatically trap the LiPSs in the cathode structure[57, 58, 59, 60, 61, 62, 63, 64, 65, 66]. These passive confinement/entrapping strategies have partly mitigated the PS shuttling effect and led to improved performance, but are fundamentally incapable of completely preventing the dissolution of LiPSs into the electrolyte.

The PS shuttling effect originates from the formation, dissolution and accumulation of LiPS intermediates in the electrolyte. In this regard, the slow conversion kinetics of the soluble LiPSs into the insoluble final products leads to continued accumulation of LiPSs in electrolyte that exacerbates the PS shuttling effect[6, 67]. An electrocatalytic approach to accelerate the conversion of soluble LiPS intermediates into insoluble Li_2S_2/Li_2S seems to be a natural strategy to prevent the accumulation and shuttling of LiPSs. The use of electrocatalysis would address the PS shuttling effect while simultaneously improving the rate capability. Although the concept of an electrocatalytic approach has been suggested in a few recent studies[23, 24, 25], the fundamental electrocatalytic kinetics of the SRR are largely unexplored and the underlying basis for using such an electrocatalytic effect to address the PS shuttling issues has not been clearly addressed. Heteroatom doped holey graphene frameworks (HGF) exhibit tunable electrocatalytic properties in SRR and hence serve as a promising candidate for the electrocatalyst.

Moreover, deciphering such reaction network and understanding the relevant mechanism is essential for the rational design of the electrocatalysts. Despite extensive efforts devoted to improving the practical performance of Li-S batteries, the fundamental reaction mechanism remains unsettled. The 16-electron conversion process involves a complex reaction with numerous possible interwoven branches among different LiPSs. The main branch in this potential reaction network for SRR remains a topic of considerable debate[68, 69, 70, 71, 72, 73, 74]. Electrocatalysis is proposed here to be an efficient approach to reduce the accumulation of the soluble LiPS species and eventually mitigate the shuttling problem[23, 24, 25]. The aforementioned heteroatom doped HGF, with tunable electrocatalytic properties in SRR[15, 75], serve as a good model system for investigating the fundamental reaction mechanism and also the catalytic effects.

Here we perform a systematic density functional theory (DFT) investigation of electrocatalytic SRR mechanism. We firstly investigate the catalytic activity origin of the nitrogen, sulfur dual-doped HGF (N,S-HGF) electrocatalysts, which is experimentally found to be an effective catalyst. We show that the defect engineering and heteroatom doping are two

strategies to tune the p-band center and hence the adsorption strength of intermediates. The optimal adsorption strength, neither too strong nor too weak, leads to a smaller overpotential and further the improved battery performance. These results validate and rationalize the catalytic approach to accelerate the LiPS conversion and mitigate the PS shuttling effect.

Moreover, we exploit the N,S-HGF and non-doped HGF as model systems to explore the full 16-electron reaction network and the impact of different catalysts. Combining DFT calculations with experimental spectroscopies including cyclic voltammetry (CV) and *in situ* Raman spectroscopy, we elucidate the dominant reaction pathway before and after the central Li_2S_4 intermediate, identify the key species as S_8, Li_2S_8, Li_2S_6, $LiS_3\cdot$, Li_2S_4, and Li_2S, and determine that a non-electrochemical disproportionation reaction between Li_2S_8 and Li_2S_4 is the main path forming or removing Li_2S_6. Comparison between HGF and N,S-HGF confirms the same key species in the reaction network, whilst the N,S-HGF catalyst accelerates LiPS conversion, leading to a faster depletion of LiPS at higher potential to mitigate polysulfide shuttling effect and produce a larger output potential. Our results stresses the importance of the catalyst: the larger output potential in the lower potential region, via the simultaneous reaction equilibria, also accelerates the conversion in the higher potential region and avoids unnecessary disproportionation. The far-reaching catalytic effects highlight the electrocatalytic approach as a promising strategy to tackle the fundamental challenges in Li-S batteries.

2.2 Methods

2.2.1 Computational Setup

Calculations were performed with DFT using the Vienna ab initio simulation package[76]. For the section focusing on the final two electron steps, The Perdew–Burke-Ernzerhof[31] (PBE) exchange correlation functional at the generalized gradient approximation[29, 30, 31] (GGA) level and the density-dependent dispersion correction (dDsC)[77, 78] Van der Waals correction were used. For latter sections considering the comprehensive 16-electron process,

a detailed benchmark and comparison between different functionals were considered. The strongly constrained and appropriately normed[79] (SCAN) functional at the meta-GGA level was chosen as the energetics and geometries are found to match well with experimental values.

The solvation effects are described using a hybrid model, as shown in Fig. 2.1 (a), which is noted as microsolvation, to take care of the strong cation nature of Li^+ like species: the first solvation shell is described using explicit solvation molecules and the rest is described by an implicit solvation model. DOL molecule is chosen to describe the first solvation shell since the dielectric constant, 7.13, is close to the one of the mixtures, 7.0, and the compact structure of the DOL molecule (compared to the DME molecule) reduces the difficulty of force convergence. The implicit solvation is described using the VASPSol add on package[80, 81] which implements linearized Poisson-Boltzmann (lPB) model in the periodic boundary condition. The dielectric constant is set as 7.0. We use a cutoff charge as 0.0002 to avoid unphysical invasion of the implicit solvent invasion into the first solvation shell. The accuracy is set to be accurate as recommend by VASPSol. The cavitation energy contribution is neglected for numeric stability. The Debye screening length is set to give an electrolyte concentration as 1M, which is the experimental value.

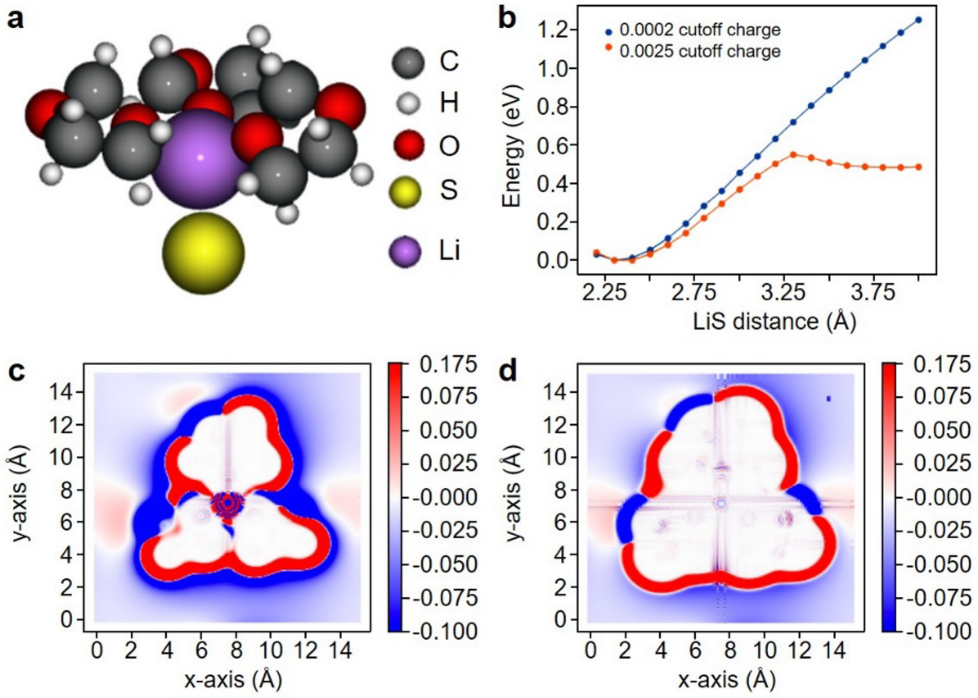

Figure 2.1: (a) Atomic structure of a microsolvated 3DOL-LiS complex. Color scheme: grey: C, white: H, red: O, yellow: S, purple: Li. (b) Energy of the complex as function of Li-S distance using 0.0002/0.0025 cutoff charge, respectively. (c) Bound charge density on xy plane cutting through Li atom of 3DOL-LiS complex using the default cutoff charge value, 0.0025. (d) Bound charge density xy plane cutting through Li atom of 3DOL-LiS complex using the smaller cutoff charge value, 0.0002.

To achieve reasonable description of Li^+ like species, tuning the cutoff charge, which controls the boundary of the lPB equations, is essential. As shown in Fig. 2.1 (b), the default cutoff charge gives an unphysical second minimum and this disappears with a smaller cutoff charge. Moreover, with a default cutoff charge, as shown in Fig. 2.1 (c), there is unphysical invasion of the bound charge into the first solvation shell, whereas in the smaller cutoff charge case, as shown in Fig. 2.1 (d), the unphysical invasion disappears. It can be seen that with a treatment combining both smaller cutoff charge and microsolvation provides a decent description outside the first solvation shell. We have also tested the

For the section focusing on the final two electron steps, the Li_sv pseudopotential, as recommended by the VASPsol package, was used. For latter section considering the comprehensive 16-electron process, the SCAN functional is a metaGGA functional and requires the kinetic energy density of the core-electrons. The kinetic energy density, however, is not provided in the Li_sv pseudopotential while VASPSol generally recommends Li_sv pseudopotential for solvation calculations. We have tested at the PBE level and find that the energetic difference between using Li and Li_sv pseudopotential in the micro-solvation treatment to be smaller than 5 meV. This is not surprising as the direct solvation effects are described by the explicit first solvation shell. Hence for the SCAN calculations we use the Li pseudopotential.

All the calculations were developed on a basis set of plane waves. A Gaussian smearing with sigma value of 0.1 eV was used through all calculations. All calculations for molecules, surface, and surface with adsorbates were spin-polarized with a cutoff energy as 500 eV. For models without adsorbates, forces are optimized to 0.02 eV/Å; for surface models with adsorbates and micro-solvated lithium polysulfides, forces were optimized to 0.05 eV/Å. 3×3×1, 1×3×1, and 3×1×1 k-point meshes are used for terrace, armchair, and zigzag models, respectively. a Γ point only k-point mesh is used for molecules. The force criteria, cutoff energy, and k-point mesh settings used for solid calculations for benchmarking purpose are reported separately in appendix A.1.

Catalytic sites are considered based on three different sets of models: armchair edge model, zigzag edge model, and inner defect edge model, as shown in Fig. 2.2. The armchair edge model consists of 84 C atoms and 12 H atoms; the zigzag edge model consists of 80 C atoms and 10 H atoms; The inner defect edge model is created by removing 10 C atoms from a 6×6 terrace model, which consists of 72 C atoms before creating the defect and saturation of the dangling bonds with H atoms. The vacuum in the z-axis was set to 20 Å. For the armchair/zigzag ribbon model, the in plane vacuum between the ribbons was at least 15 Å.

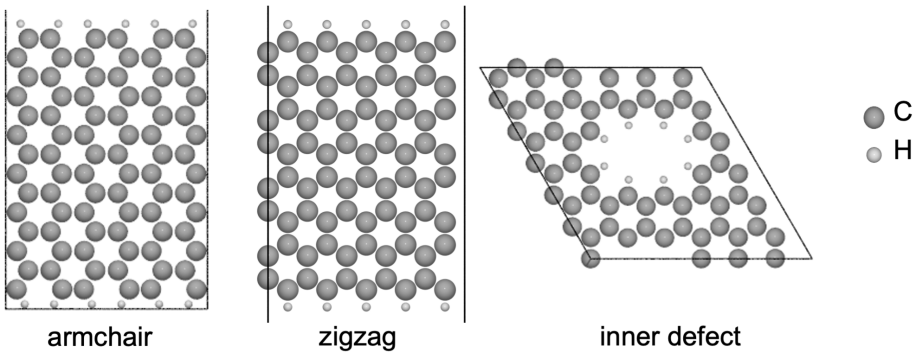

Figure 2.2: Atomic structures of nondoped graphene models used in this study. Color scheme: grey: C, white: H, pink: C chosen to be the interacting site, blue: N, yellow: S.

The effects of doping are considered by adding different combination of N and S heteroatoms into these models. Single N doped, single S doped, and N,S-codoped are considered. The N,S-codoped structures considered are shown below.

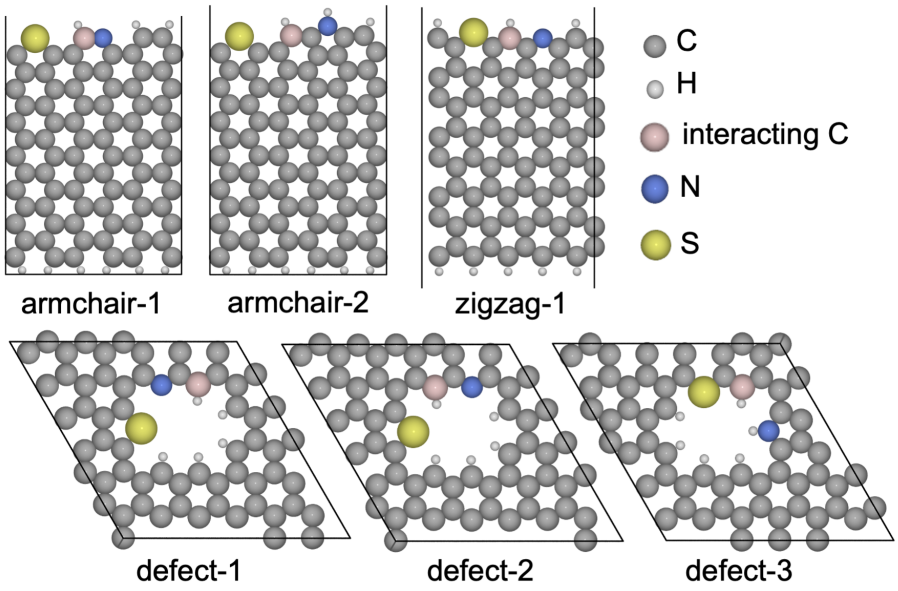

Figure 2.3: Atomic structures of N,S-codoped graphene models used in this study. Upper column: armchair-1, armchair-2, zigzag-1. Lower column: defect-1, defect-2, defect-3. Color scheme: grey: C, white: H, pink: C chosen to be the interacting site, blue: N, yellow: S.

Structures of the catalytic sites with adsorbates are shown for the site with largest output potential: N,S-codoped defect-1 model.

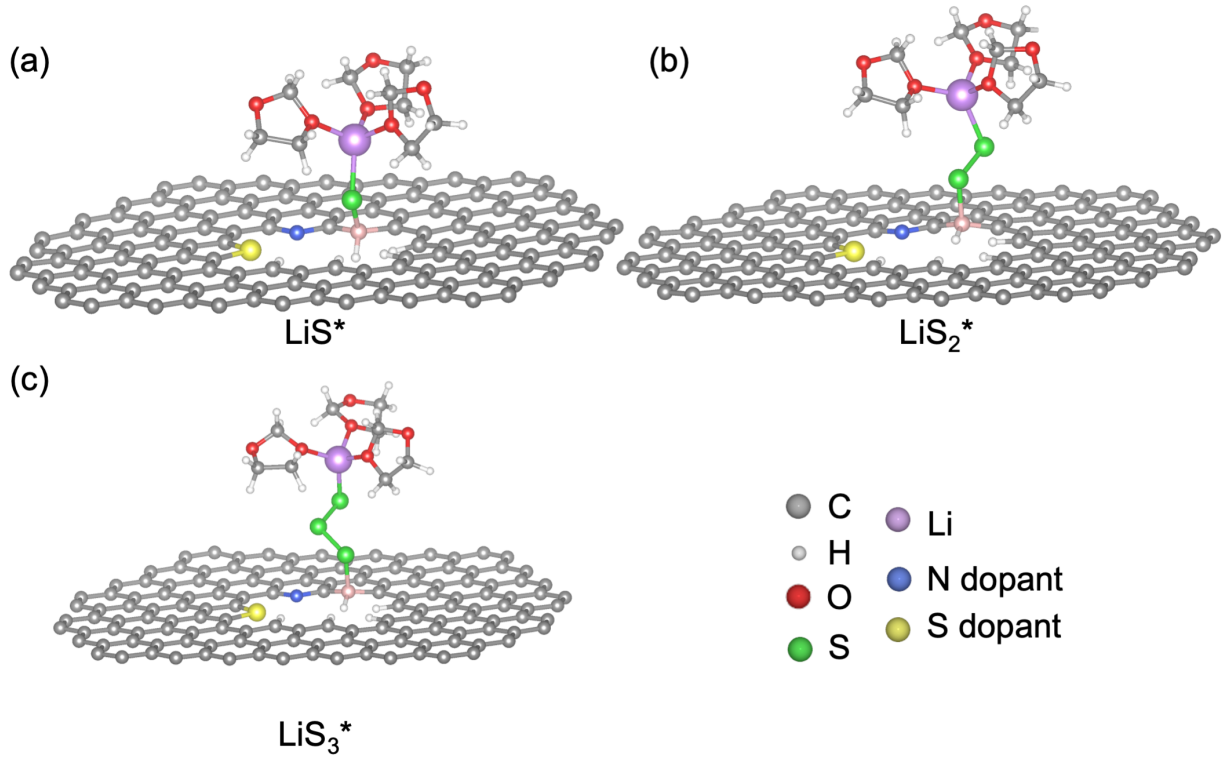

Figure 2.4: Atomic structures of N,S-codoped defect-1 model with adsorbate as (a) LiS, (b) LiS_2, and (c) LiS_3. Color scheme: grey: C, white: H, pink: C chosen to be the interacting site, blue: N, yellow: dopant S, green: reactant S.

2.2.2 Multistep Volcano Plot

The reduction process starting from Li_2S_4 involves multiple probable branches: the reaction $Li_2S_4 + 6Li^+ + 6e^- \rightleftharpoons 4Li_2S$, which involves 6 electrons, can be decomposed into different combinations of 2 electrons ($2e^-$) steps, 4 electron ($4e^-$) steps, and 6 electron ($6e^-$) steps. There are 14 different $2e^-$, $4e^-$, and $6e^-$ steps considering LiS, LiS_2, LiS_3, S, and S_2 as adsorbates. $2e^-$ steps correspond to the steps where close shell species can be formed and desorbed from the catalytic sites after 2 electrons of reduction. Similarly, $4e^-$ or $6e^-$ steps indicate that at least one species maintains as adsorbate during the 4 or 6 electrons reduction process,

respectively.

For each specific pathway, the overall thermodynamic output potential is calculated as the minimum output potential of the consisting single electron steps. More specifically, regardless of the combination, 6 electrons, hence 6 single electron steps are involved, and we denote the reaction Gibbs free energies of each single electron process as ΔG_i where i=1-6. The overall output potential of a specific combination is calculated as:

$$\Delta U_{overall} = min(\Delta U_i) = -max(\frac{\Delta G_i}{e}) \tag{2.1}$$

This gives the output potential at 0 V vs Li/Li+ electrode. The combination of the reactions can only happen at voltage lower than this value, as the reaction Gibbs free energy of the least exergonic step becomes 0 at $\Delta U_{overall}$ vs Li/Li+ electrode, and the reaction stops. This is the Li analogy with the CHE.

The 14 different $2e^-$, $4e^-$, and $6e^-$ steps, 12 different probable combinations, and the volcano plots of these combinations are provided in the appendix A.4.

2.2.3 Potential Dependent Concentration

To construct the potential dependent concentrations of the different species, we consider the simultaneous equilibrium of the following reactions:

$$S_8 + 2Li^+ + 2e^- \rightleftharpoons Li_2S_8 \tag{2.2}$$

$$Li_2S_8 + 2Li^+ + 2e^- \rightleftharpoons 2Li_2S_4 \tag{2.3}$$

$$Li_2S_4 + 6Li^+ + 6e^- \rightleftharpoons 4Li_2S \ \Delta G_{Li_2S_4} \tag{2.4}$$

$$Li_2S_8 + Li_2S_4 \rightleftharpoons 2Li_2S_6 \tag{2.5}$$

$$Li_2S_6 \rightleftharpoons 2LiS_3 \tag{2.6}$$

The first three reactions are electrochemical reactions and the last two are chemical reactions. Electrochemical equilibria are affected by both the potential and the concentrations while the chemical equilibria are affected by concentrations. The DFT calculated energetics are

ΔG° of reactions and the ΔG which considers the potential and concentration can be linked as (taking the second equilibrium of Li_2S_8 to Li_2S_4 as example):

$$\Delta G = \Delta G^\circ + 2eU_{Li/Li^+} + k_bT\frac{[Li_2S_4]^2}{[Li_2S_8]} \tag{2.7}$$

At each specific U, we have 6 unknown concentrations: the ones of S_8, Li_2S_8, Li_2S_6, Li_2S_4, Li_2S_2 and LiS_3. The aforementioned 5 chemical equilibria provide 5 constraints and the last constraint comes from the conservation of amount of S:

$$[S_8] + [Li_2S_8] + \frac{3}{4}[Li_2S_6] + \frac{1}{2}[Li_2S_4] + \frac{1}{8}[Li_2S] + \frac{3}{8}[LiS_3] = [S_8]_{initial} \tag{2.8}$$

We use the experimental concentration of $[S_8]_{initial}$ as 0.054 M and this set of equilibria is solved numerically using the fsolve function of the scipy package.

It is worth mentioning we use a $\Delta G^\circ_{Li_2S_4,effective}$ which contains the thermodynamic part and kinetic activation barrier: $\Delta G^\circ_{Li_2S_4,effective} = \Delta G_{Li_2S_4} + E_a$, as the work of Peng et al. shows that the barriers become larger and hence more important in the later stage in the SRR process.

For the N,S-HGF system, the ΔG° of the reactions are: -2.34 eV, -2.16 eV, -2.03 eV, -0.16 eV and 0.21 eV, respectively. $\Delta G^\circ_{Li_2S_4,effective}$ is the best calculated output potential of the N,S-codoped sites for the multistep reactions: U_{output}=2.18 V, corresponding to $\Delta G^\circ_{Li_2S_4,effective}$=-2.18 eV. For E_a, the experimental barrier of the N,S-codoped HGF system, 0.15 eV, is taken from the work of Peng et al.

For the HGF system, the only difference is $\Delta G^\circ_{Li_2S_4,effective} = -1.86eV$ as the thermodynamic part is the best calculated output potential of the nondoped sites for the multistep reactions: U_{output}=2.11 V, corresponding to $\Delta G^\circ_{Li_2S_4,effective}$=-2.11 eV. For E_a, the experimental barrier of the nondoped HGF system, 0.25 eV, is taken from the work of Peng et al.

2.2.4 Raman Spectra Simulation

The Raman cross section was calculated within the double harmonic approximation based on the micro-solvated structures. For lithium polysulfides (Li_2S_8, Li_2S_6, Li_2S_4, and LiS_3.),

we consider the freedom on the Li_xS_y part, i.e., we calculate the vibrational modes by a direct diagonalization of the dynamical matrix considering the perturbation on the Li_xS_y atoms. Two different displacements are performed on each of the x, y, and z coordinates. Then the derivative of the polarizability with respect to the normal mode is calculated to get the Raman cross section:

$$I^{Raman} = 45\alpha'^2 + 7\beta'^2 \tag{2.9}$$

where

$$\alpha' = \frac{1}{3}(\tilde{\alpha}_{xx} + \tilde{\alpha}_{yy} + \tilde{\alpha}_{zz}) \tag{2.10}$$

$$\beta' = \frac{1}{2}((\tilde{\alpha}_{xx} - tilde\alpha_{yy})^2 + (\tilde{\alpha}_{yy} - tilde\alpha_{zz})^2 + (\tilde{\alpha}_{zz} - tilde\alpha_{xx})^2 + 6(\tilde{\alpha}_{xy} + \tilde{\alpha}_{yz} + \tilde{\alpha}_{zx})^2) \tag{2.11}$$

and the $\tilde{\alpha}$ is the polarizability tensor.

2.3 Results and Discussion

2.3.1 Catalytic Activity Origin

To better understand the fundamental origins of the SRR catalytic activity of the heteroatom-doped HGFs, we first look at how heteroatom doping affects the catalytic activity, using the the PBE functional with the dDsC Van der Waals correction. Most of the state-of-the-art theoretical understanding are focusing on how strong the adsorption of the LiPS intermediates is on the sulfur hosts brought by the conventional trapping strategy, but It is generally believed that moderate adsorption (not too strong or too weak) of the adsorbate on the catalytic sites is the key prerequisite for an efficient electrocatalyst. Therefore, an excessively strong adsorption energy in the conventional trapping strategy does not explain the origin of the improved activity.

The fundamental SRR process for the catalysts involves a series of reduction reactions that progress from S_8 ring molecules to the final product of Li_2S: $S_8 \rightarrow Li_2S_8 \rightarrow Li_2S_6 \rightarrow Li_2S_4 \rightarrow Li_2S_2 \rightarrow Li_2S$. As inspired by the research on heteroatom-doped carbon materials for the oxygen reduction reaction, the carbon atoms adjacent to the heteroatoms are the preferential

binding sites for the sulfur intermediates rather than the heteroatoms themselves due to the charge redistribution induced by the heteroatom doping. The carbon atoms adjacent to the heteroatoms therefore provide the optimal adsorption sites and are the most probable active sites for the catalytic SRR process.

As the final two-electron step of the reaction ($Li_2S_2 + 2Li^+2e^- \rightarrow 2Li_2S$) represents the rate-determining step, we focus our calculations on the modeling of this part. We assumed that the conversion of Li_2S_2 to Li_2S involves the formation of a LiS radical intermediate, which is solvated by the 1,3-dioxolane (DOL) solvent and interacts with the catalytic active site. The microsolvated LiS intermediate interacting with the active site (*) is denoted as 3DOL-LiS*, as expressed in the following equations:

$$3DOL + Li_2S_2 + Li^+ + e^- + * \rightarrow 3DOL - LiS* + Li_2S \tag{2.12}$$

$$3DOL - LiS* + Li^+ + e^- + * \rightarrow Li_2S + * + 3DOL \tag{2.13}$$

According to Eq. 2.12 and 2.13 , the adsorption Gibbs free energy of LiS*, $\Delta G(LiS*)$, on the active sites can be expressed in Eq. 2.14 and the Gibbs free energy (ΔG) of the final two steps can be written as a function of $\Delta G(LiS*)$:

$$\Delta G(LiS*) = G(3DOL - LiS*) + G(Li_2S) - G(*) - 3G(DOL) - G(Li_2S_2) - G(Li^+ + e^-) \tag{2.14}$$

$$\Delta G_1 = \Delta G(LiS*) \tag{2.15}$$

$$\Delta G_2 = -\Delta G(LiS*) + 2G(Li_2S)_2G(Li^+ + e^-) - G(Li_2S_2) \tag{2.16}$$

The catalytic activity is closely related to the thermodynamic overpotential for the Li_2S_2 to Li_2S conversion reaction, which appears in a volcano plot as a function of $\Delta G(LiS*)$ when catalyzed at different catalytic sites, with special sites reaching the optimal value. $\Delta G(LiS*)$ for carbon atoms on the basal plane of graphene are in the region of weak adsorption, which is because the distortion of C-C bonds induced by the carbon hybridization change from sp^2 to

sp^3 requires too much energy that cannot be compensated by C-S bond formation during the catalytic SRR process. The edge carbon atoms, however, provide the opportunity to show reasonable adsorption energy as the distortion is much easier. In this regard, the carbon atoms located at the armchair edge, zigzag edge and inner defect edge were considered as various active sites to analyze the adsorption energy and the catalytic activity, as shown in Fig. 2.5. We have performed test calculations on carbon atoms of the basal plane and found the adsorption energy to be too weak.

Governed by the Sabatier principle, the relationship between the overpotential and the adsorption energy displays a volcano shape, as shown in Fig. 2.5, where several edge carbon sites on the N,S-HGF catalyst and on the N-HGF, S-HGF and HGF catalyst models are compared. For the structures on the left leg of the volcano plot, step 2 is the potential limiting step, whereas on the right side of the volcano, the potential is limited by reaction step 1. Perfect non-doped graphene presents sites that bind LiS either too strongly (such as on the zigzag edge, ∼3.00 eV) or too weakly (such as on the armchair edge, ∼1.73 eV) and they are therefore intrinsically bad catalytic sites. As for the inner defective non-doped HGF, the edge carbon atoms show a hybrid geometry between armchair and zigzag edges. This structure results in a favorable adsorption energy of ∼2.14 eV, presenting a good compromise of LiS binding and consequently a low overpotential. Moreover, N,S dual-doping further provides finer tuning, pushing the N,S-HGF system almost at the top of the volcano plot and further decreasing the overpotential to a negligible value.

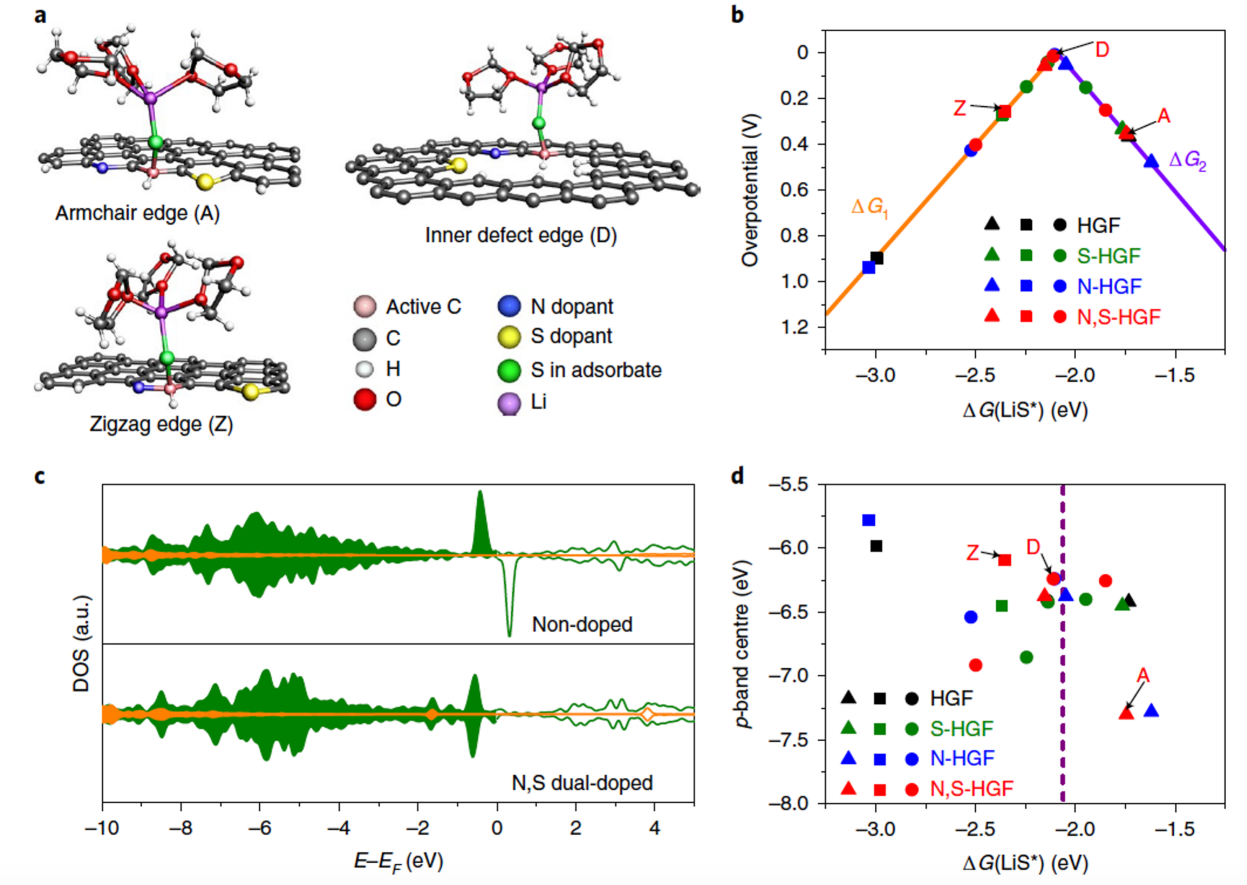

Figure 2.5: The activity origin of the heteroatom-doped HGFs on SRR. (a) Atomic structures showing the interaction between three representative active sites in N,S-HGF with the microsolvated LiS radical adsorbates. (b) A volcano plot linking the overpotential for the final step to the adsorption energies of the LiS radical intermediate on different active sites (triangles, squares and circles represent the active sites at different armchair, zigzag and inner defect edges, respectively). (c) p-band center shift and modification of the pDOS of the catalytic carbon atoms induced by nitrogen and sulfur dual-doping: non-doped HGF (top) and N,S-HGF (bottom). E_F denotes the Fermi level. (d) The relation between the p-band center and LiS adsorption energy at different active carbons. The purple dashed line represents the adsorption energy associated with the top of the volcano in (b). The data points labelled A, D, Z in (b) and (d) correspond to the representative structures shown in (a).

To unravel the origin of the high catalytic SRR activity, we considered the doping process as an approach to engineering the p-orbital of the catalytic sites and thereby the catalytic performance, as shown in Fig. 2.5 (c). Inspired by d-band center theory for metallic catalysts, we used the p-band center for the density of states projected on the active carbon as a descriptor of the electronic structure of the heteroatom-doped catalysts and found a relationship with the adsorption energy of LiS. Before adsorption, the valence p-band in the projected density of states (pDOS) of the sulfur atom in the LiS radical shows an isolated feature. After adsorption on the catalysts, a considerable change to the pDOS shape of the valence p-band arises from the bonding with the p-orbital of the catalytic carbon atoms. The bonding strength, according to classical bonding theory, is related to the energy gap between these bonding orbitals: as the p-orbital of sulfur atom in LiS radical can be considered at constant position, tuning the position of the p-orbital of catalytic carbon atoms to manipulate the adsorption can be achieved by heteroatom doping.

2.3.2 Reaction Network in SRR

The previous results show that heteroatom doping is an effective strategy to improve the catalyst performance by tuning the p-band center and hence the adsorption energy of the material. We then move to the modeling of the complete 16-electron process. The overall energetic description becomes more important here, and the SCAN functional is used as the benchmark calculations show that the SCAN functional provides a better overall energetic and geometry description, as shown in appendix A.1. The SRR reaction network starts with the conversion from the S_8 molecule to the Li_2S_8 molecule, giving the highest calculated output potential among all the steps, 2.34 V (Fig. 2.6 (d)). The further conversion of the Li_2S_8 molecule involves multiple possible branches: in a 2 e- process, it can be converted into (1) one Li_2S molecule paired with one Li_2S_7 molecule, (2) one Li_2S_2 molecule paired with one Li_2S_6 molecule, (3) one Li_2S_3 molecule paired with one Li_2S_5 molecule, or (4) two Li_2S_4 molecules. The calculated energetics shows that the Li_2S_4 pathway is the most exergonic and hence favored one, yielding an output potential of 2.16 V.

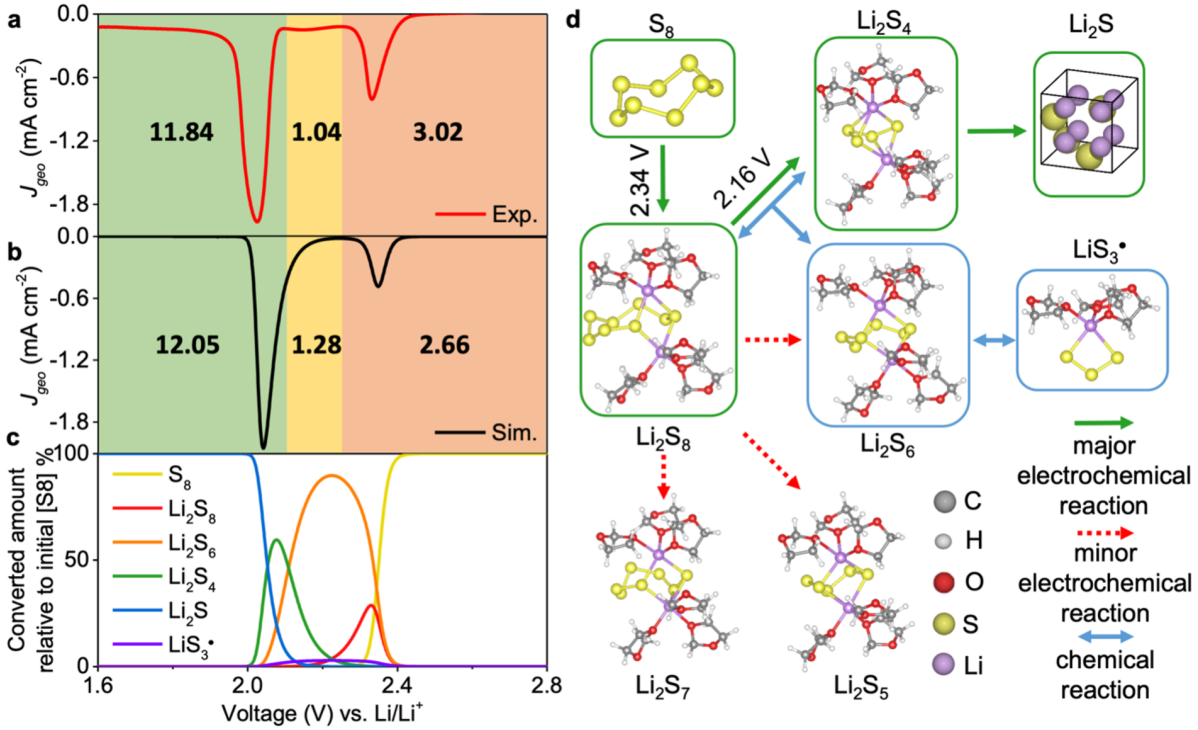

Figure 2.6: Charge analysis and reaction network for the sulfur reduction reaction. (a) Experimental CV curve with the charge integration results, separated into three regions with a ratio as 3.02:1.04:11.84 from high potential to low potential. (b) Simulated CV curve with the charge integration results, separated into three regions with a ratio as 2.66:1.28:12.05. (c) Simulated voltage dependent concentrations of the major species considered: S_8, Li_2S_8, Li_2S_6, Li_2S_4, Li_2S and $LiS_3\cdot$. The concentrations are normalized according to the sulfur amount. (d) The dominant reaction mechanism suggested by DFT energetics: $S_8 \rightarrow Li_2S_8 \rightarrow 2Li_2S_4 \rightarrow 8Li_2S$ ($Li_2S_8 + Li_2S_4 \leftrightarrow 2Li_2S_6 \leftrightarrow 4LiS_3\cdot$) where the chemical part is in parentheses. Solid green and dotted red lines indicate major and minor electrochemical reactions, respectively. Blue lines indicate chemical reactions. Major products are labelled with green and blue boxes, corresponding to electrochemical and chemical origin. Thermodynamic output potentials are denoted for major electrochemical reactions. The catalytic site dependent output potentials for Li_2S_4 to Li_2S are detailed in Fig. 2.9.

As the experimentally observed plateau might be originated from the delayed electro-

chemical conversion of disproportionation or back-disproportionation products, we checked the possibilities starting with one Li_2S_8 molecule and one Li_2S_4 molecule, or two Li_2S_4 molecules, and found that the reaction Li_2S_8+Li_2S_4→2Li_2S_6 is the only exergonic one, with a reaction Gibbs free energy of -0.16 eV. We further checked the disproportionation reaction with either Li_2S_8 and Li_2S_6 molecules, or Li_2S_4 and Li_2S_6 molecules, but in both cases the reactions were found to be endergonic. These results suggest that Li_2S_6 formation by disproportionation of Li_2S_4 and Li_2S_8 is the only chemical elementary step that competes with the network of electrochemical reaction, and that further disproportionation is not significant.

We also considered the equilibrium between $LiS_3\cdot$ and Li_2S_6, as $LiS_3\cdot$ has been observed previously and widely suggested as an important intermediate species in SRR13,17,39,40. This reaction was found to be endergonic, 0.21 eV, in the direction forming $LiS_3\cdot$, indicating that the concentration of $LiS_3\cdot$ will be relatively small during the reaction process. Combining the aforementioned balances (Fig. 2.6 (d)), with the effects of voltages as described in section 2.2.3, the potential dependent concentrations of different polysulfides were simulated, giving a sequence of dominant LiPS species as S_8, Li_2S_8, Li_2S_6(↔$LiS_3\cdot$), Li_2S_4, Li_2S with reducing potential (Fig. 2.6 (c)). The simulated CV curve was further derived from the simulated concentrations, giving the charge ratio as 12.05:1.28:2.66, in the green, yellow and orange zones of Fig. 2.6 (b), respectively, which matches well with the experimental ratio in Fig. 2.6 (a), 3.02:1.04:11.84. Although Li_2S_6 appears right after Li_2S_8, it is not formed by electrochemical reduction of Li_2S_8. Instead, a fraction of Li_2S_8 (∼1/3) is electrochemically transformed into Li_2S_4, providing a fractional amount of charge in the orange region of Fig. 2.6 (a) and (b) (∼2/3 e), while the rest is involved in the disproportionation with the produced Li_2S_4 to yield a large concentration of Li_2S_6 at ∼2.25 V. Note that the exergonic nature of the Li_2S_8+Li_2S_4→2Li_2S_6 disproportionation provides additional driving force to initiate the electrochemical reduction of Li_2S_8 to Li_2S_4 at a potential higher (∼2.35 V) than its equilibrium (2.16 V). At lower potential, in the yellow zone, where electrochemical reduction of Li_2S_8 to Li_2S_4 becomes exergonic, the disproportionation reaction operates backwards to produce Li_2S_4 and Li_2S_8 (2Li_2S_6→Li_2S_8+Li_2S_4), in which Li_2S_8 is electrochemically reduced

to Li_2S_4 to result in the charge plateau seen in the yellow region. We have considered the direct reduction of Li_2S_6 to Li_2S_4, Li_2S_3 or other lower order polysulfides, and found these reactions cannot occur at a potential higher than 1.89 V, and therefore the back disproportionation reaction is the only viable path. At even lower potential in the green zone, Li_2S_4 is eventually reduced in Li_2S, involving the extra 12 electrons of the electrochemical reduction reaction. This multi-electron step will be further discussed below.

To validate the proposed mechanism, we further compare the voltage dependent concentrations to the ones derived from *in situ* Raman spectroscopy. The *in situ* Raman spectra were taken along with a discharge CV scan. The real-time CV curve, along with the voltage dependent *in situ* Raman spectra are shown in Fig. 2.7 (a) and (b), respectively. In the beginning of the SRR process, the existence of elemental sulfur is confirmed by the typical S_8 peaks at 150 cm^{-1}, 218 cm^{-1} and 470 cm^{-1}. With reducing potential, S8 signals gradually decrease and completely disappear at ∼2.40 V, accompanied by the emergence of the Li_2S_8 signal at 441 cm^{-1}. This 441 cm^{-1} peak then starts shifting to 452 cm^{-1} at 2.38 V, indicating the appearance of Li_2S_6. As we discussed in the computation section, this occurs by electrochemical transformation of Li_2S_8 to Li_2S_4 and the rapid disproportionation between the formed Li_2S_4 and the remaining Li_2S_8 to form Li_2S_6. Soon after the emergence of Li_2S_6, the Li_2S_4 peak at 200 cm^{-1} appears at 2.36 V. The Li_2S_8 peak at 441 cm^{-1} largely disappear at 2.24 V, while the Li_2S_6 peak at 452 cm^{-1} reaches its maximum, marking the depletion of Li_2S_8 while Li_2S_6 reaches its highest intensity. Subsequently, the Li_2S_6 peak at 452 cm^{-1} starts to decrease and disappears at 2.01 V. The disappearance of Li_2S_4 happens at a similar voltage, ca 2.01 V, indicating the conversion from Li_2S_4 to Li_2S_x(x=1,2,3) (see Fig. 2.9 for more details). The peak of $LiS_3\cdot$ radical at 533 cm^{-1} coexists within the voltage range of 2.42 V to 2.01 V, originating from the chain split of Li_2S_6. The DFT calculated frequencies match well with the experimental observations (S_8: 150 cm^{-1}, 230 cm^{-1}, and 490 cm^{-1}; Li_2S_8: 440 cm^{-1}; Li_2S_6: 471 cm^{-1}; Li_2S_4: 198 cm^{-1}; $LiS_3\cdot$: 541 cm^{-1}). The detailed intensity of simulated Raman spectroscopy can be found in the appendix A.5.

The voltage dependent concentration of each LiPS was derived from the peak intensity

and the results are shown in Fig. 2.7 (c) (left panel), with a comparison to the computational results shown in Fig. 2.7 (c) (right panel). The concentration is normalized with respect to the highest concentration of each species. The experimental and computational results give the same apparent polysulfide concentration evolution sequence Li_2S_8, $Li_2S_6(\leftrightarrow LiS_3\cdot)$, Li_2S_4 with decreasing potential with comparable peak positions. It is interesting to note that $Li_2S_6(\leftrightarrow LiS_3\cdot)$ and Li_2S_4 are roughly depleted at a rather similar potential, suggesting the dynamic balance between these two species through the back-and-forth disproportionation reactions discussed above.

We also note that experimental peak for Li_2S_4 appeared at a slightly higher potential value (by 0.12 V) than the theory prediction. Two factors may contribute to such difference between experiments and theory: (1) Only thermodynamics was considered in the simulated voltage dependent equilibrium concentration, while the formation of Li_2S_6 could be slow due to kinetics and diffusion barriers, and thus Li_2S_4 accumulation may start at a slightly higher voltage. The earlier accumulation of Li_2S_4 compared to purely thermodynamically predicted value further validates the Li_2S_6 is originated from the disproportionation reaction; (2) due to limited solubility in the DOL/DME solvent, Li_2S_4 may get saturated during the SRR process in the high concentration limit (as also indicated by the concentration plateau at ∼2.15-2.25 V). Such a saturation behavior at high concentration limit could boost the apparent signal at low concentration limit and lead to an earlier onset. As shown in appendix A.3, a plateau beginning at ∼2.20 V is achieved for simulated concentration after applying the solubility constraint, matching well with the experimental peak. In summary, *in situ* Raman spectroscopy provides a semi quantitative polysulfide tracking, with the excellent agreement between spectroscopic feature evolution and computed values validating the SRR molecular pathway obtained by theory: $S_8 \rightarrow Li_2S_8 \rightarrow 2Li_2S_4$ ($Li_2S_8 + Li_2S_4 \leftrightarrow 2Li_2S_6 \leftrightarrow 4LiS_3\cdot$) $\rightarrow 8Li_2S$.

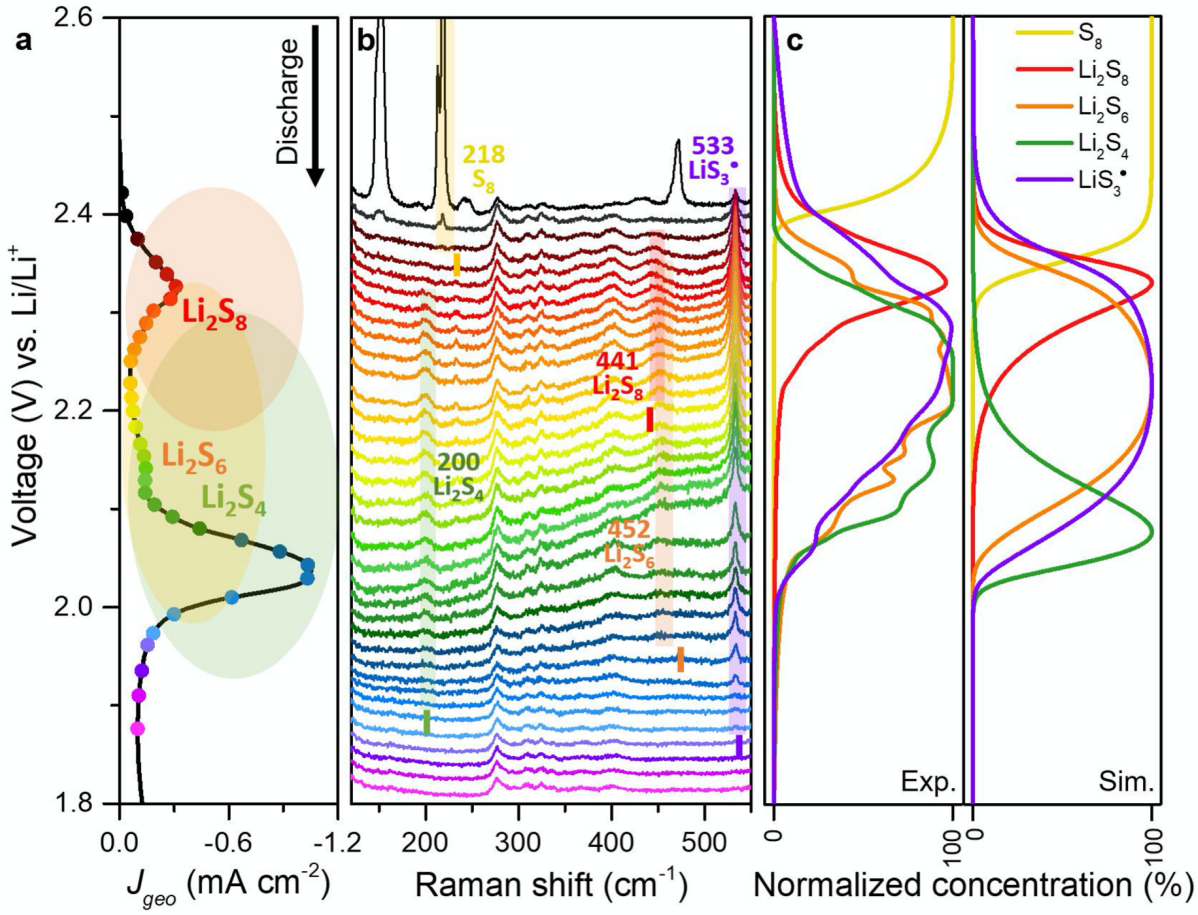

Figure 2.7: *In situ* Raman results during discharge with the N,S-HGF catalytic electrode. (a) (b) The CV profile (a) and the corresponding experimental *in situ* Raman spectra (b), where the same color indicates the same voltage. Characteristic peaks used to quantify the intermediates are marked with correspondingly colored shades. Small labels with darker color indicate the computed frequency values. (c) The comparison between potential dependent experimental concentrations (left panel) derived from *In situ* Raman spectra (b) and simulated concentrations from DFT (right panel). Each species is normalized with respective to its highest concentration.

2.3.3 Role of Catalysis in SRR

To better understand the influence of electrocatalysts on the complex reaction network, we also investigated the non-doped HGF, as a less active catalytic system compared to the N,S-HGF. Similar to the N,S-HGF system, a systematic analysis of the peak intensity of the *in situ* Raman spectra at different discharge potentials give the voltage dependent concentrations for each polysulfide in HGF electrode. Overall, the HGF electrode shows a similar polysulfide evolution sequence $Li_2S_8 \rightarrow Li_2S_6 \rightarrow Li_2S_4$, but with different voltage range for each species (Fig. 2.8).

In particular, the first step of discharge at high potential are only weakly affected by two different catalysts, the peak center for Li_2S_8 being almost unchanged between HGF (2.35 V) and N,S-HGF (2.33 V). Transformation of Li_2S_6 is delayed, with an average peak value at 2.17 V with HGF (compared to 2.23 V in N,S-HGF) and with a disappearance at 1.80 V with HGF (compared to 2.01 V in N,S-HGF). A similar delay is seen for Li_2S_8, from higher overpotential in the later steps, with an average peak value at 2.18 V with HGF (compared to 2.21 V in N,S-HGF) and with a disappearance at 1.94 V with HGF (compared to 2.01 V in N,S-HGF). The delayed disappearance of Li_2S_8 and Li_2S_6 until a much lower potential with non-doped HGF electrodes implies a more sluggish conversion kinetics to lower-order polysulfide, which could also lead to a more severe shuttling problem in the Li-S battery. The exothermic chemical disproportionation (Li_2S_8+$Li_2S_4 \leftrightarrow 2Li_2S_6$) favors the accumulation of Li_2S_6 rather than Li_2S_8 or Li_2S_8 in the electrolyte, explaining why the depletion of Li_2S_8 occurs earlier than that of Li_2S_6.

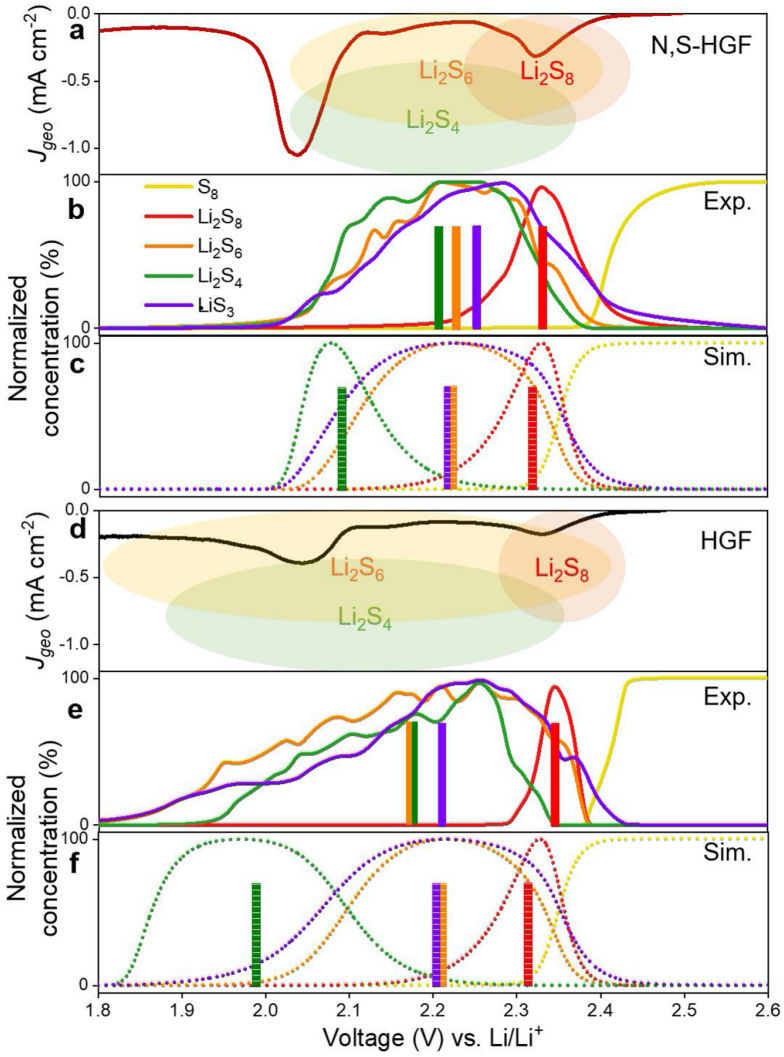

Figure 2.8: Comparison of different catalysts in SRR reactions. (a) (d) Experimental CV curves taken during *in situ* Raman spectroscopy for N,S-HGF (a) and HGF (d). (b) (e) Voltage dependent concentration for each polysulfide species in N,S-HGF (b) and HGF (e) derived from experimental *in situ* Raman spectra. (c) (f) Simulated voltage dependent concentration for each polysulfide species in N,S-HGF (c) and HGF (f). Each species is normalized with respect to its highest concentration.

Our calculations described above indicate that there is no favorable path for direct electrochemical reduction of Li_2S_6 to lower order LiPSs in the potential regime above 1.89 V.

Instead, it relies on the back disproportionation reaction to convert back to Li_2S_8 and Li_2S_4 for further reduction. However, the back disproportionation reaction ($2Li_2S_6 \leftrightarrow Li_2S_8 + Li_2S_4$) is thermodynamically unfavorable and relies on the rapid depletion of Li_2S_4 to drive this reaction forward. In this case, a slower conversion kinetics of Li_2S_4 could seriously delay the conversion and reduction of Li_2S_6 until a much lower potential regime (<1.89 V), where a direct electrochemical reduction of Li_2S_6 may also start to occur. Overall, such slower conversion kinetics results in an accumulation of Li_2S_6 in a wider potential range and leads to a more severe PS shuttling problem.

To understand the distinct potential range of these two systems, we further investigated the reaction pathways of the second stage, i.e., the conversion from Li_2S_4 to Li_2S. The reaction network is complicated when considering all the possible $2e^-$, $4e^-$, and $6e^-$ steps starting from Li_2S_2 (Fig. 2.9) and we examined a total of 12 different reaction pathways in the second stage, in the presence of various catalyst models: armchair edge of graphene, zigzag edge and inner defects in graphene plane with various doping situation (non-doped, S-doped, N-doped, and N,S-doped). Two pathways were found to give the largest output potential among the different catalytic sites: (1) one $4e^-$ step: $Li_2S_4 + 4Li^+ + 4e^- \rightarrow Li_2S_2 + 2Li_2S$, followed by one $2e^-$ step: $Li_2S_2 + 2Li^+ + 2e^- \rightarrow 2Li_2S$ (Fig. 2.9 (c)); (2) a pathway consisting of one $6e^-$ step, i.e., at least one radical species is adsorbed on the surface during the reduction process: $Li_2S_4 + 6Li^+ + 6e^- \rightarrow 4Li_2S$ (Fig. 2.9 (d)). We included the N and S single doped sites as these are present in the N,S-HGF as well. The results clearly show that in both pathways, the largest output potential obtained by N,S-codoped sites, 2.18V, is larger than the largest output potential given by non-doped sites: 2.10 V, in line with the experimental results showing superior performance of N,S-HGF catalyst.

Interestingly, among the models we considered, the inner defected models, shown as filled circles in Fig. 2.9 (c) and Fig. 2.9 (d), appear closest to the top of the volcano plot. These results confirm hetereoatom doping and defect engineering in holey graphene as two effective approaches to improve the electrocatalysts. It is worth mentioning that conversion from LiS to Li_2S solid is the potential limiting step for most of the sites with relatively

large output potentials (¿2.1 V), while one site has the adsorption of LiS as the potential limiting step. This indicates that the potential limiting step is the final conversion from Li_2S_2 to Li_2S, in line with the experimental observation where the finals steps were found to give the largest overpotential. As a result, the LiS adsorption energy can be used as a descriptor to classify the output potentials of all the various sites. Moreover, a smaller output potential in the second stage has far-reaching effects: the sluggish conversion of Li_2S_4 to lower order polysulfides could considerably retard the already thermodynamically unfavorable back disproportionation reaction ($2Li_2S_6 \leftrightarrow Li_2S_8 + Li_2S_4$) that is necessary for further reduction of Li_2S_6, thus leading to an undesirable accumulation of high order LiPS species that can worsen the PS shuttling problem.

In line with the experimental results, the simulated potential dependent concentrations for the HGF electrode show more sluggish conversion, i.e., lower disappearing potentials, for Li_2S_4 and Li_2S_6 species, 1.85 V and 2.0 V as shown in HGF compared to 2.0 V and 2.05 V for the N,S-HGF system (Fig. 2.8). The simulation of HGF and N,S-HGF effective output potential only differs significantly in the second stage, largely comparable to the experimental results. Such a close correlation between the experiments and theory further validates the electrocatalytic strategy to tackle the PS shuttling in Li-S batteries. A better electrocatalyst that can accelerate the polysulfide cannot not only produce a larger output potential, but also significantly reduce the potential range that the LiPSs could appear and effectively mitigate the PS shuttling effect.

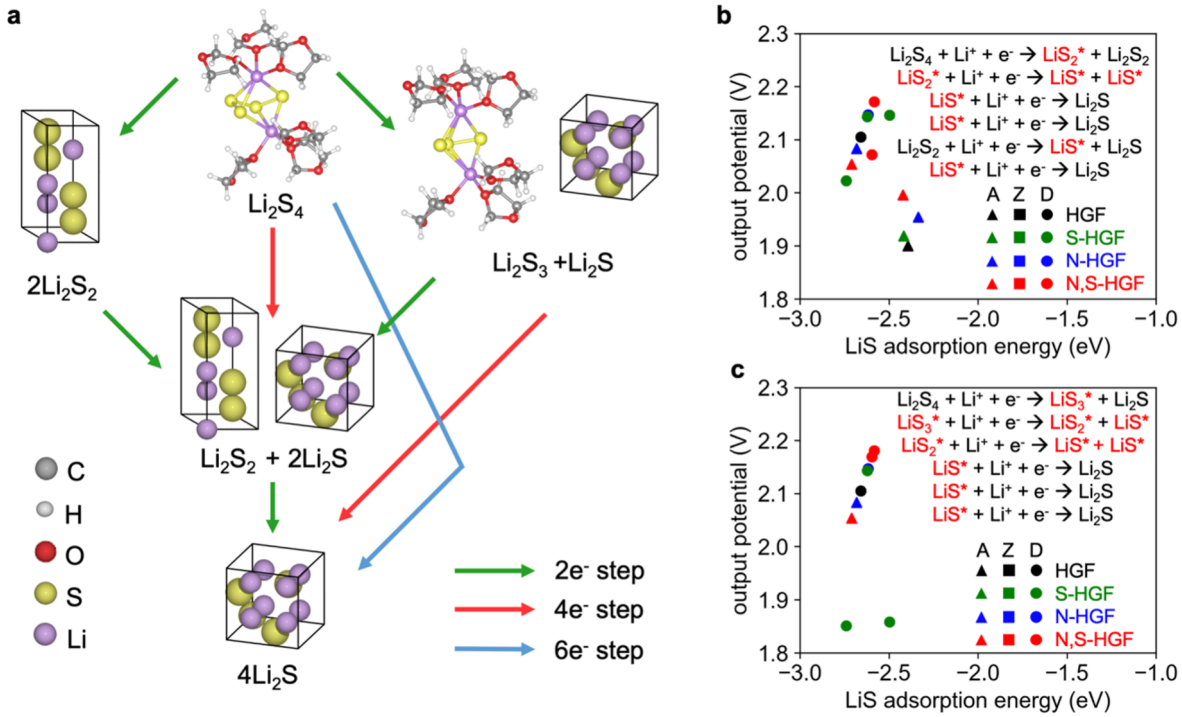

Figure 2.9: Simulated site-specific output potential of the Li_2S_4 to Li_2S conversion. (a) Different possible combinations of $2e^-$, $4e^-$, and $6e^-$ steps considered for second stage of SRR, the conversion of Li_2S_4 to Li_2S. Green, red, and blue lines indicate $2e^-$, $4e^-$, and $6e^-$ steps, respectively. (b) (c) Simulated multistep output potential from Li_2S_4 to Li_2S for the two pathways with largest output potentials considering different catalytic electrode models: armchair edge (A, triangles), zigzag edge models (Z, squares), and inner defect models (D, filled circles). Four types of dopants are considered: non-doped (black), S (green), N (blue) and N,S (red).

2.4 Conclusion

In summary, we have conducted a systematic investigation of the SRR mechanism. We show that the defect engineering and the heteroatom doping are two strategies to tune the p-band center of the adsorption sites, which are the edge C atoms, and hence the adsorption energy of the intermediates. Consequently, the optimal intermediate adsorption energy of the

heteroatom doped HGF leads to the decrease of the overpotential and the improved battery performance. DFT calculations were further used to explore the complex reaction network for 16-electron SRR process, revealing two stages separated by the central Li_2S_4 intermediate, in line with experimental CV observations. Moreover, Combining the DFT calculations with *in situ* Raman spectroscopy, we demonstrate that Li_2S_4 and Li_2S_6 represents the dominant intermediates, in which Li_2S_6 is generated by the disproportionation reaction between Li_2S_8 and Li_2S_4 and doesn't directly participate in electrochemical reactions, but contributes to the shuttling problem due to its high solubility and energy favoring its accumulation in the electrolyte. It is found that the optimized N,S-HGF catalytic electrode, benefitting from smaller overpotential, considerably accelerates the conversion of high order LiPSs, leading to faster depletion of soluble LiPSs at higher potential regime, hence mitigating the PS shuttling effect and boosting the output potential. Insights achieved here can be applied to other systems beyond the heteroatom-doped HGF model system described in current study, including other potential SRR electrocatalysts, including single transition metal atom catalysts, metal oxides or metal sulfides. A central strategy is to search for the electrocatalyst that reduces the overpotential, especially in the second stage.

CHAPTER 3

Atomic Environments in N-containing Graphitic Carbon Probed by First-principle Calculations and Solid-State Nuclear Magnetic Resonance

3.1 Introduction

Nitrogen-doped graphenes have emerged as an important class of materials due to their attractive electronic properties with applications as electrodes[82, 83], electrocatalysts[84, 85] and catalyst supports[86]. Typical N doping of graphene, however, provides a mix of different local N structures where the simplest species[87] are pyrrolic, pyridinic, and graphitic nitrogen. Materials with high extents of doping are desired, and present a large range of lateral assembly and interactions among these three basic types of N centers. In order to establish tentative perfomance-structure relations, numerous efforts have been made to detect the local environments of N-doped graphene via tools including Raman spectroscopy[88], X-ray photoelectron spectroscopy[82, 89] (XPS), scanning tunneling microscopy[88, 90] (STM), and nuclear magnetic resonance[91] (NMR) spectroscopy. However, Raman spectroscopy can provide only limited insights into the detailed local structure of N atoms since distributions of various local moieties are present, which limit the resolution. XPS, in principle, is sensitive to the local bonding near surfaces, but the slight differences in binding energies are hard to accurately simulate and interpret, especially since the resolution is low.[82, 89]. STM provides high resolution images of local structures, but the sampling of the various sites is challenging. Two-dimensional (2D) solid-state NMR (ssNMR), benefitting from advances in sensitivity and resolution in the recent years[92], is a promising tool to cast light onto the

atomic-scale structure of these materials and is particularly amenable to combined analyses with first-principles calculations.

Although solid-state NMR has been utilized to determine the local structures of different periodic carbon materials[93, 91], theoretical predictions of NMR spectral features from ab initio calculations are generally scarce, limiting the accuracy in the interpretation of the spectra in terms of local structures. Such predictions had been limited to finite systems until Mauri et al. extended the theory to periodic systems[94]. Mauri et al. later made improvements to account for the translational invariance when the projector augmented wave (PAW) method is used; this is known as the gauge including projector augmented wave (GIPAW) approach[95, 96]. The GIPAW method has been utilized in various systems to represent the influences of structural variations on NMR signals[97, 98, 99, 100].

Periodic models are important to representing the variations in NMR chemical shifts, especially for systems with delocalized wavefunctions. Thonhauser et al. investigated both finite and periodic carbon systems and showed that a relatively large finite system, coronene, is still different from a periodic model[101]. Results of Özcan et al.[102] also showed in the case of graphene that for cluster models, five to six concentric hexagonal shells, i.e., 150 to 216 C atoms in the model, are needed to achieve a converged ^{13}C chemical shifts on center C atoms at the level of 5 ppm, in line with the results of Vähäkangas et al.[103] The results of Skachkov et al.[104] and de Souza et al. [105] are achieved using periodic graphene models, although the reported ^{13}C chemical shifts are different from the value reported by Thonhasuer (roughly by 10 ppm). Instead, results of Skachkov et al.[104] and de Souza et al. [105] match better with the value obtained by Casabianca[106] using a cluster model. Moreover, none of these studies investigated the effect of N-heteroatoms. For the N-doped graphene system, to the best of our knowledge, the only relevant work has been done by Zhang et al. using cluster models[107] and there is no study done using periodic models.

In this work, density functional theory (DFT)-based first-principles calculations are performed on periodic N-doped graphene models to simulate a 2D ^{13}C-^{15}N heteronuclear multiple quantum coherence (HMQC) spectrum, in order to understand the relation between

local structure and ^{13}C or ^{15}N chemical shifts. Results are compared to a experimental 2D NMR spectra and allow a more detailed interpretation of it. Various local structures with a mix of multiple basic N species are modeled to provide insights into the structure-related broadening, which can be further decomposed into (1) standalone geometry effects, and (2) influences of additional proximate N atoms. The influence of a small amount of adsorbed water is modeled by adding explicitly water molecules to reflect the experimental measurement condition. In order to better understand the link between local structure and chemical shift, the relationships between local structure, atomic charge and chemical shifts are discussed, enabling a more detailed understanding of the influence of N doping motifs on the electronic structure. These results open the rational design of N-doped carbon materials with desired electronic properties to improve electrochemical performance.

3.2 Methods

3.2.1 Computational Setup

The Vienna Ab initio Simulation Package[76] (VASP) was used for calculations. The Perdew–Burke-Ernzerhof[31] (PBE) exchange correlation functional at the generalized gradient approximation (GGA) level is used. The density-dependent dispersion correction (dDsC)[77, 78] Van der Waals correction was applied for all structures. Three different sets of graphene structures were used: a hexagonal terrace model which consists of 72 C atoms (6×6 supercell), an armchair edge model which consists of 66 C atoms and 12 H atoms (before substitution with N), and a zigzag edge model consisting of 40 C atoms and 8 H atoms. The vacuum in the z-axis was set to 20 Å. For the armchair/zigzag ribbon model, the in plane vacuum between the ribbons was at least 15 Å. For geometry optimizations, a Monkhorst-Pack 3×3×1 k-point mesh was used for terrace model, 1×3×1 for armchair and 3×1×1 for zigzag. For NMR calculation, a 5×5×1 k-point mesh was used for terrace model, 1×7×1 for armchair and 7×1×1 for zigzag. The test for the convergence of the chemical shifts in non-doped models with respect to the k-points mesh is shown in appendix B Table

B.1, and convergence to the level of 1-2 ppm was achieved.

All the calculations were developed on a basis set of plane waves. A Gaussian smearing with sigma value of 0.1 eV was used through all calculations. For energy calculations, a cutoff energy for the plane wave basis set at 500 eV and an electronic step convergence criterion of 10^{-6} eV were used. For geometry optimizations, forces were optimized to 0.02 eV/Å. For NMR calculations, a cutoff energy for the plane wave basis set at 600 eV and an electronic step convergence criterion of 10^{-10} eV were set for most cases due to the requirement of such calculations. For some models (a full list can be found in appendix B.2) that do not converge under this criterion, electronic step convergence criterion may be loosened to at most 10^{-7} eV and it has been tested on the graphitic N system that the influence on the calculated NMR chemical shifts is only up to 0.01 ppm, as shown in appendix B Fig. B.1. The variation of the chemical shifts of non-doped models with respect to the cutoff energy is shown in appendix B Table B.2, and convergence to the level of 1 ppm was achieved for a value of 600 eV. The accurate precision setting was always used. Default values are used for the order of the stencils used to calculate the magnetic susceptibility and the step size for the finite difference k-space derivative, corresponding to equations 38, 40, and 47 in the work of Yates et al.[96].

VASP outputs the chemical shift tensor following the convention $\delta_{11} > \delta_{22} > \delta_{33}$ and the isotropic shift is calculated as[108]:

$$\delta_{iso} = \frac{\delta_{11} + \delta_{22} + \delta_{33}}{3} \tag{3.1}$$

The output values without core contribution were used as this will only lead to negligible difference of smaller than 0.001 ppm, as shown in appendix B Table B.3. We used the values without the **G=0** contribution since the **G=0** contribution is not a bulk property and is affected by the surface currents that appear on the surface of the sample[95]. VASP assumes a spherical shape for the **G=0** contribution[95], which may not be the case for the N-doped graphene sample. More details can be found in appendix B.5. The conversion to a value that is amenable to experimental measurement and comparison was done via[104, 105, 101]:

$$\delta = \delta_{system,calc} - \delta_{ref,calc} + \delta_{ref,exp} \tag{3.2}$$

The reference system here is chosen as α glycine for ^{13}C, ^{15}N and ^{1}H. The experimental values used are 33.4 ppm for $\delta_{ref,exp,N}$, 172.7 ppm for $\delta_{ref,exp,C}$ and 3.54 ppm for $\delta_{ref,exp,H}$. It is worth mentioning that the $\delta_{ref,exp,H}$ is an average chemical shift value of three H atoms in the NH_3 group of glycine[100]. Note that the reference values for the ^{13}C, ^{15}N, and ^{1}H isotropic chemical shifts are consistent relative to commonly used standards: tetramethylsilane (TMS) as 0 ppm for ^{13}C and ^{1}H and liquid ammonia as 0 ppm[109] for ^{15}N. The CHARGEMOL package is used to calculate the Density Derived Electrostatic and Chemical (DDEC6) charge[110, 111] based on VASP charge density.

For the construction of 2D ^{13}C-^{15}N spectra, we consider the first neighbor C-N pairs since the experimental dipole-mediated 2D NMR spectrum depicts signal intensity that is proportional to r^{-3}, where r is the distance between the two nuclei[112, 113]. For pristine graphene, the second neighbor distance in the network is 1.73 times the first neighbor distance. This ratio is maintained after geometry optimizations in graphitic N and pyridinic N models, whereas in pyrrolic N models, the ratio is found to be 1.54. As the result, the 2D NMR signal intensity from a second neighbor will be only roughly one fifth compared to the signal strength arising from a first neighbor in graphitic or pyridinic N models, and one fourth in pyrrolic N models.

3.2.2 Experimental Setup

Experimentally, a mesoporous N-carbon material containing 16 atom% N was synthesized from a 1:3 molar ratio of cyclohexanehexone octahydrate and uniformly ^{13}C,^{15}N-enriched urea, with the synthesis reported by Fechler et al.[114] Nuclear enrichment made solid-state NMR characterization of the N-carbons possible. ^{13}C and ^{15}N chemical shifts were referenced to their respective values in uniformly ^{13}C,^{15}N-enriched glycine powder, using the same values as mentioned in the computational settings. The carbon materials were diluted with KBr at a sample:KBr ratio of 1:3 w/w before being loaded into the MAS rotor. The KBr served as both an internal temperature probe[115] and to reduce undesirable sample heating that may arise from rapid rotation of conductive samples in the high magnetic field required for

the NMR measurements[116].

Solid-state two-dimensional (2D) ^{13}C-^{15}N heteronuclear multiple quantum coherence (HMQC) experiments were used to correlate ^{13}C and ^{15}N isotropic chemical shifts of ^{13}C and ^{15}N nuclei that are dipole-dipole-coupled through space. A schematic diagram of the 2D NMR pulse sequence is provided as appendix B Fig. B.2 (a). Briefly, the solid-state dipolar-mediated ^{13}C-^{15}N HQMC NMR spectrum was acquired using the $SR4_1{}^2$ sequence to filter polarization transfer from ^{13}C to ^{15}N (for indirect detection) and back to the ^{13}C (for direct detection). These experiments were performed with 100 kHz ^{1}H decoupling, using zirconia rotors, Vespel caps, and under 8 kHz MAS on a Bruker AVANCE II HD 400 DNP-NMR spectrometer with a 9.4 T superconducting magnet operating at 400.20, 100.64, and 40.56 MHz for ^{1}H, ^{13}C, and ^{15}N nuclei, respectively, and equipped with a variable-temperature 3.2 mm HXY MAS probehead. $SR4_1{}^2$ was used as the dipolar recoupling scheme according to Hu et al.[117] Heteronuclear ^{13}C-^{15}N dipole-dipole couplings scale with respect to the cube of the distance separating two nuclear spins[112, 113], making these measurements sensitive principally to ^{13}C and ^{15}N nuclei that are covalently bonded directly, or to a lesser extent, by weak next-nearest neighbor interactions. The latter contribute negligibly to the overall measured signal intensity as consequence of the short ^{13}C-^{15}N recoupling times used here (0.6 ms, sensitive out to 2–3 bond distances),[118] but preferentially detect dipolar-coupled nuclei over shorter (1-2 bond) distances. The 2D dipole-mediated ^{13}C-^{15}N HMQC NMR spectrum[119] was acquired using 1024 transients, with 32 t_1 increments in the indirect dimension in STATES-TPPI acquisition mode. Recycle times of 10 s (corresponding to 1.3 T_1 of ^{15}N nuclei) were used for maximum signal sensitivity. Low-temperature conditions were used to improve NMR signal sensitivity through enhanced polarization from the Boltzmann distribution and to mitigate the influences of rapid nuclear spin relaxation effects. The temperature measured in the MAS gas stream nearest to the stator was 95 K, and the actual sample temperature was estimated from ^{79}Br T_1 relaxation measurements to be *ca.* 99 K.

Similarly, 2D ^{15}N-^{1}H heteronuclear correlation (HETCOR)-MAS experiments were used to correlate ^{1}H and ^{15}N isotropic chemical shifts of ^{1}H and ^{15}N nuclear spin pairs that

are dipole-dipole-coupled through space over sub-nanometer distances and corroborate the assignment of pyrrolic N. A schematic diagram of the 2D NMR pulse sequence is provided as appendix B Fig. B.2 (b). Specifically, following a 90 degree pulse, ^{1}H polarization was allowed to evolve for incremented durations (for indirect detection), after which a shaped pulse was used to transfer ^{1}H polarization to dipole-dipole-coupled ^{15}N nuclei for direct detection. The N-doped material was exposed to atmospheric conditions for one week, and surface adsorbed water accounted for 0.5 mass% of the sample. These experiments were performed using zirconia rotors, Vespel caps, and under 10 kHz MAS on a 500 MHz Bruker AVANCE NMR spectrometer with a 11.7 T superconducting magnet operating at 500.24 and 50.69 MHz for ^{1}H and ^{15}N nuclei, respectively, and equipped with a 4 mm HXY MAS probehead. The spectrum was acquired at room temperature, with a contact time of 3000 μs, and 4000 scans.

3.3 Results and Discussion

DFT calculations are first performed on non-doped graphene systems to investigate ^{13}C chemical shifts and validate the computational parameters. The structures of the three basic models without N doping are shown in Fig. 3.1, and some characteristic structures with N doping are shown in Fig. 2. The numbers on the C atoms correspond to those of Table 3.1.

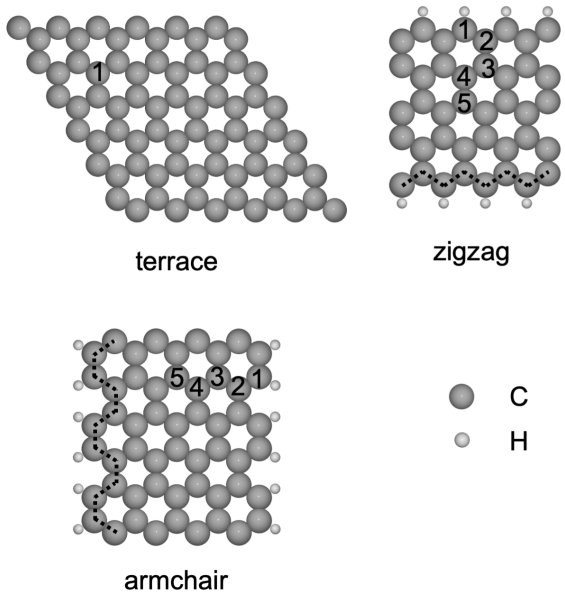

Figure 3.1: Atomic structures of the three basic unit cell models used in this study. The terrace model is 2D, while the armchair and the zigzag ribbons are 1D. One or two long repeat vectors are added to generate a 3D structure for the plane wave calculation. Atom numbers correspond to the values shown in Table 3.1, with atoms depicted as follows: grey: C, white: H. Dotted lines indicate the armchair and zigzag edges.

The graphene terrace atom is calculated to have a ^{13}C isotropic chemical shift of 119.2 ppm, which matches the experimental range between 117 and 123 ppm in the literature[120, 121, 122, 123]. Also, compared with other computational results, our result generally matches the 118.0 ppm value reported by Thonhauser et al.[101], but is roughly 7 ppm lower than the values reported by Skachkov et al.[104], 127.1 ppm, and de Souza et al. [105], 127.6 ppm. Thonhauser used Quantum Espresso with benzene as the reference molecule and Skachkov used ADF-BAND with TMS as the reference molecule. The reference difference may lead to this 7 ppm difference. However, the difference between Thonhauser and de Souza is unexplained as they both use Quantum Espresso with benzene as the reference molecule. The center C atoms in our zigzag and armchair models are calculated to have a ^{13}C chemical shift value of 108.6 ppm and 111.3 ppm, which is slightly smaller than the ^{13}C chemical

shift in the terrace model by 10 and 8 ppm, respectively. Further increasing the thickness of the both models cannot improve the match, as shown in appendix B Table B.4, and the thicknesses of both models are used through this work: 9 for armchair model and 5 for zigzag model. We have checked the influence of multilayer stacking by comparing graphene and graphite: ^{13}C isotropic chemical shift values change from 119.2 ppm to 120.3 ppm and 123.7 ppm for inequivalent sites in graphite. The values match well with experimental results[124, 125] around 119 ppm and the trend matches the results of de Souza[105]. We focus on single layer models in this study since the effects will be smaller than 5 ppm.

Model	Atom	^{13}C Chemical Shift (ppm)
Terrace	1	119.2
Zigzag	1	117.0
	2	124.4
	3	111.6
	4	110.8
	5	108.6
Armchair	1	110.0
	2	116.6
	3	112.5
	4	110.2
	5	111.3

Table 3.1: ^{13}C isotropic chemical shifts of different C atoms in terrace, zigzag and armchair models. Labelled atoms are shown in Fig 3.1.

Agreement of theoretically predicted chemical shifts with experimental data for the non-doped systems validates the general modeling approach. Thus, N-doped systems are calculated with the abovementioned settings. We first investigate different structure models with one N atom: a graphitic N atom in a graphene terrace model (Fig. 3.2 structure 1), a pyrrolic N atom at an armchair edge (Fig. 3.2 structure 4) and a pyridinic N atom at a

zigzag edge (Fig. 3.2 structure 2) and other inner defect edges (Fig. 3.3 structure 1, 2, 3, and 4). Subsequently, the influence of introducing a second N atom is taken into account by considering various models with graphitic-graphitic, pyridinic-graphitic, pyrrolic-graphitic, and pyridinic-pyridinic N pairs. Pyrrolic-pyrrolic and pyrrolic-pyridinic N pairs are not taken into account since these pairs are separated by larger distances than the 2-3 bond distances that are possible to probe via HMQC solid-state NMR[118]. The simulated 2D ^{13}C-^{15}N results are shown in Fig. 3.2. For each inequivalent C atom as a first neighbor of N atoms, a C-N data point is added using the simulated ^{13}C and ^{15}N chemical shift. Because both the number of equivalent C atoms, and the ratio of different modeling structures are not taken into account, the point density in a certain region cannot be quantitatively linked with the experimental signal intensity. The symbol type indicates the presence and distance (in the term of bonds) of other nearby N atoms. Circles stand for N atoms without other N atoms within three bond distances. Triangles represent N atoms with a nearby N as second neighbor and squares represent N atoms with a third neighbor N. The color indicates the type of the local N structure: blue represents graphitic N atoms, which are bonded to three C atoms. Orange represents pyridinic N atoms, which are bonded to 2 C atoms. White represents pyrrolic N atoms, which are bonded to 2 C atoms and 1 H atom. For triangles and squares, the left half indicates the type of the probed N atom and the right half indicates the type of neighbor N atom. The match between the calculated and experimental chemical shifts will be investigated in the next step.

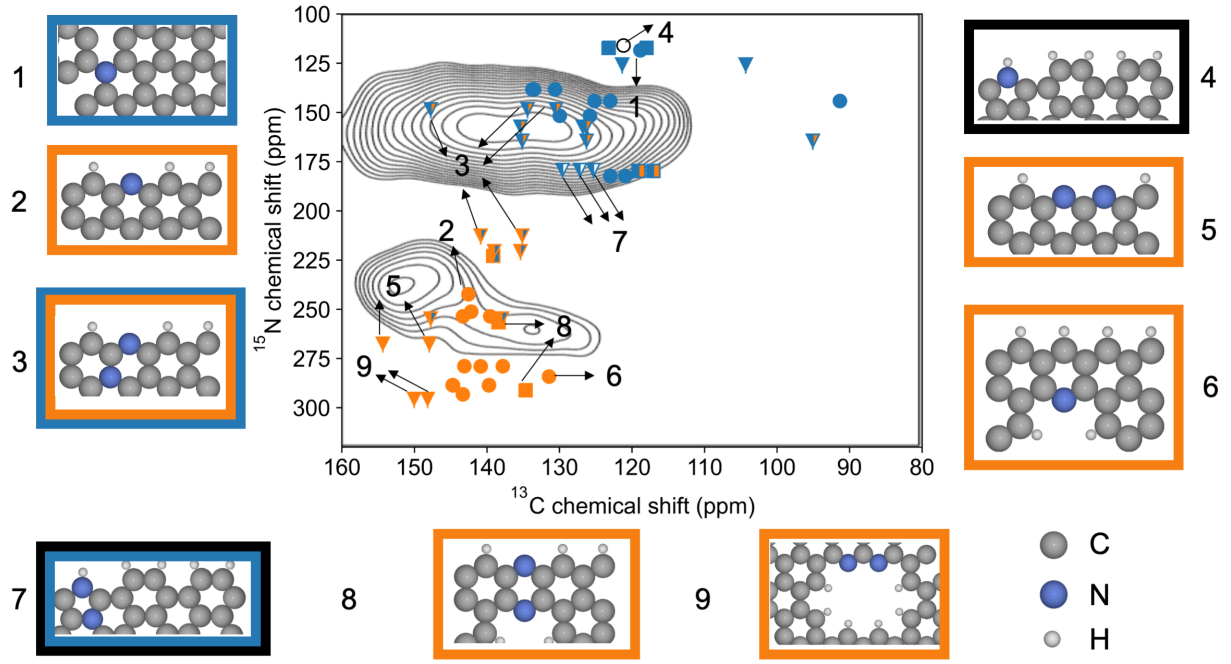

Figure 3.2: Simulated ^{13}C-^{15}N correlation NMR chemical shifts, together with the experimental 2D ^{13}C-^{15}N intensity. Experimentally, a mesoporous N-carbon material containing 16 atom% N was synthesized from a 1:3 molar ratio of cyclohexanehexone octahydrate and uniformly ^{13}C, ^{15}N-enriched urea, as described by Fechler et al.[114] Scatter points are simulated results and contour lines indicates experimental signal. The scatter styles indicate other nearby N atoms. Filled circles: atoms without other N atoms nearby, triangles:atoms with another N atom as second neighbor, squares: atoms with another N atom as third neighbor. The color indicates the type of the local N structure: blue for graphitic N atoms, orange for pyridinic N atoms and white for pyrrolic N atoms (with black outline when necessary). For triangles and squares, the left half indicates the type for the probed N atom and right half indicates the type for the neighbor N atom.

In general, the calculated ^{13}C and ^{15}N isotropic chemical shifts match well with the experimental data (as shown in Fig. 3.2) and explain the observed signal broadening. A perfect match is not necessary, since some local structures probed in the calculations might not be present in large enough quantities in the experimental sample to provide a detectable

signal. The spectrum can be separated into two general regions. The upper region containing both pyrrolic N and graphitic N shows ^{15}N and ^{13}C chemical shifts in the ranges of 120-200 ppm and 110-160 ppm, respectively. The lower region containing various pyridinic structures shows intensity spanning the ranges of 220-280 ppm and 120-160 ppm for ^{15}N and ^{13}C isotropic chemical shifts, respectively. Comparison with previous ^{13}C and ^{15}N NMR chemical shift assignments of the various N-moieties in carbonaceous materials and graphitic carbon nitrides shows agreement with our assignments[126, 127, 128, 129, 130]. ^{15}N chemical shifts exhibit clear trends with respect to local N environments: pyrrolic N atoms have the lowest ^{15}N isotropic chemical shifts, followed by graphitic, and pyridinic N with the highest ^{15}N isotropic chemical shifts. This trend also holds for ^{13}C isotropic chemical shifts, although there are overlaps between different types of N environments. This can be understood by incorporating the the influence of the bonding environment: the pyrrolic and graphitic N atoms have 3 neighbors whereas pyridinic N has 2 neighbors, which leads to a decrease in the electron density on pyridinic N atoms and the adjacent C atoms. The relatively smaller difference between pyrrolic and graphitic N atoms stems from the electronegativity difference between C (2.55) and H (2.20): pyrrolic N and C atoms have a slightly larger electron density and hence smaller chemical shift.

A more detailed understanding can be achieved by decomposing the structure-related broadening into two aspects: the geometric effect for the N atom itself, and the neighbor effect influenced by the proximity of other N atoms. The neighboring effect follows a general trend: a graphitic N neighbor decreases the ^{15}N isotropic chemical shifts of pyridinic N environments, and a pyridinic N neighbor increases the ^{15}N isotropic chemical shifts of graphitic and pyridinic N environments. This is consistent with the fact that the electron-rich graphitic N atom transfers some electronic density to its less rich pyridinic neighbor. Although graphitic N has a larger ^{15}N chemical shift than pyrrolic N (118.4 ppm >115.3 ppm), a graphitic N neighbor decreases the ^{15}N isotropic chemical shift of a pyrrolic N nuclei, and a pyrrolic N neighbor increases the ^{15}N isotropic chemical shift of a graphitic N nuclei. The influence of a graphitic N neighbor on an adjacent graphitic moiety is small: with a second

or third graphitic N neighbor, the ^{15}N chemical shift changes from 118.4 ppm to 125.6 or 117.2 ppm, respectively. The influence of a pyridinic N neighbor on a pyridinic N center is complicated and no simple trend is found. The effect of pyridinic or pyrrolic N neighbors on a pyrrolic moiety are not investigated since they cannot act as close neighbors within a distance of three bonds. All the possible combinations of N moieties are explored and the calculated ^{15}N and ^{13}C chemical shifts explain a large part of the observed broadening of the spectrum in both dimensions.

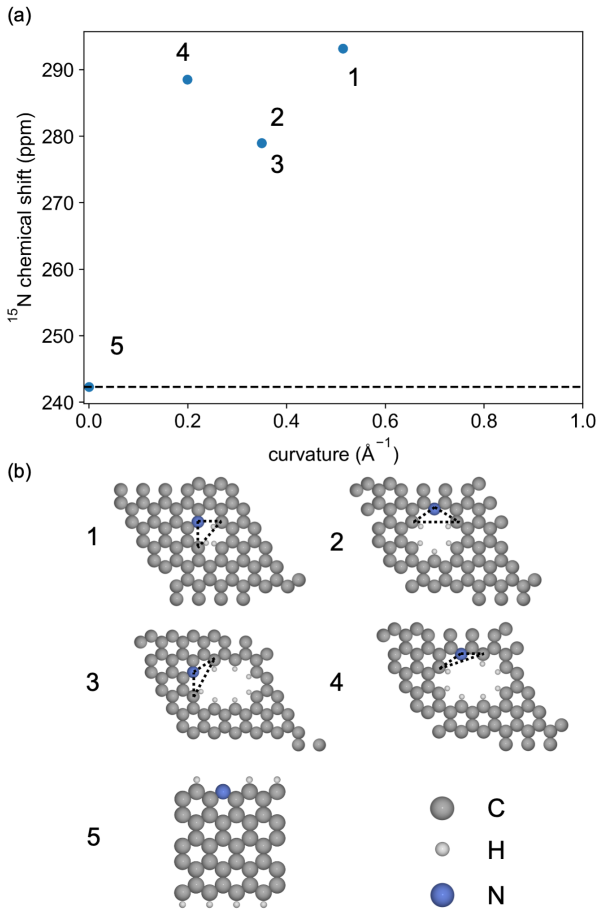

Figure 3.3: (a) Relationship between curvature and ^{15}N isotropic chemical shift. The dotted line indicates the ^{15}N isotropic chemical shift at the limit of zero curvature, i.e., simple edge pyridinic N at zigzag edge, structure 5 in (b). This is also structure 2 in Fig. 3.2. (b) Underlying structures of the data points appearing in (a). The models are listed in an order of decreasing curvature with atoms depicted as follows: grey: C, white: H, blue: N. Dotted lines indicate the N atom and the two most adjacent edge C atoms used to calculate the Menger curvature.

The influence of the morphology on the ^{13}C and ^{15}N isotropic chemical shifts of the graphene edges, straight or curved at vacancy islands can be quantified by the the Menger curvature c, which is the reciprocal of the radius of the circle that passes through three points[131]. This descriptor captures the local curvatures of the signaling C/N atoms. The

center N atom and two most adjacent edge C atoms give 3 2D positions, x_1, x_2, and x_3. The Menger curvature is defined by:

$$c(x_1, x_2, x_3) = \frac{4A}{\|x_1 - x_2\|\|x_2 - x_3\|\|x_3 - x_1\|} \tag{3.3}$$

where A denotes the area of the triangle spanned by x_1, x_2, and x_3. The symbol $\|\|$ denotes the L^2 norm in the 2D space.

Thus, the ^{15}N isotropic chemical shifts can be correlated with the curvatures, which are a descriptor of the local geometry. This relationship in different N-doped graphene systems is shown in Fig. 3.3. The idea of local curvature is validated via the data point of N-doped 6C defected terrace model: Fig. 3.3 (b), structure 2, and the data point of N-doped 10C defected terrace model: Fig. 3.3 (b), structure 3. Although globally these two structures are very different, the local curvatures of these two N atoms are rather similar and the ^{15}N chemical shifts are very close. The 6C and 10C defected terrace model are created by removing 6 and 10 C atoms from the pristine terrace model, saturating dangling bonds with H atoms and substituting one edge C-H pair with a N atom. The local geometry effect correlates the extent of defect curvature with ^{15}N chemical shifts. Specifically, environments with increased local curvature are found to have increasing chemical shifts (Fig. 3.3). This is similar to the relationship between surface curvature and ^{13}C chemical shifts in carbon nanotube systems[106].

NMR detects differences in electronic shielding which is manifested as differences in isotropic chemical shifts and which can intuitively be connected to atomic charge[132]. In Fig. 3.4, the relationship between the DDEC6 charge of the signal atom and the curvatures is shown. The data points generally follow a trend: the smaller the charge, i.e., the higher the electron density, the more shielded the nucleus and hence the smaller the chemical shift. For N-doped systems, the larger the curvature, the more positive the charge, meaning the curvature hinders N atoms taking electrons from neighbor C atoms.

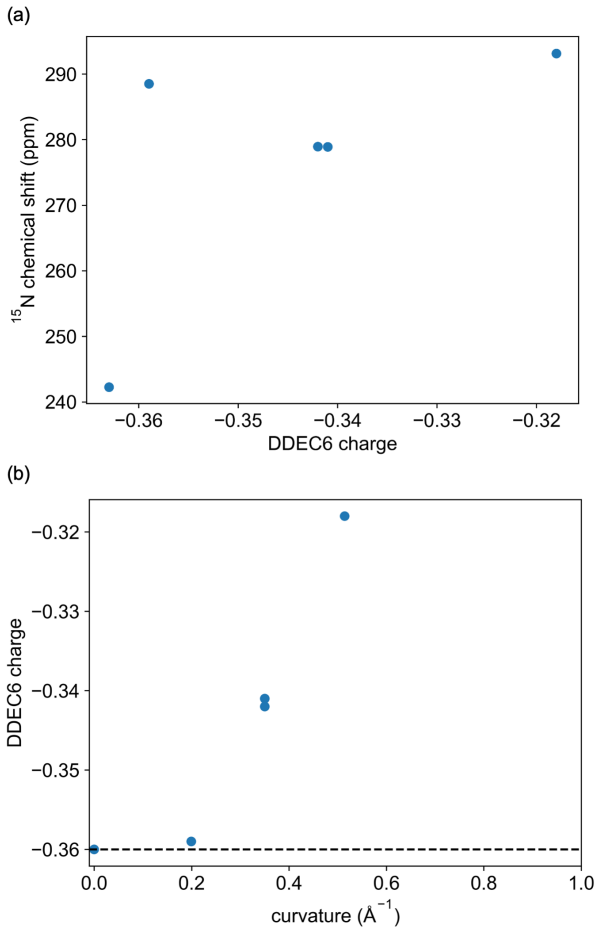

Figure 3.4: The relationship between (a) atomic charge and chemical shift and (b) charge and curvature of the models shown in Fig. 3.3 (b). Negative values denote an accumulation of electron density (negative charge), positive values indicate electron density depletion (positive charge).

Now that the atomic charge descriptor has been established, both the ^{15}N and ^{13}C chemical shifts of the 2D NMR spectrum (Fig. 3.2) can be analyzed and correlated using this descriptor. Fig. 3.5 shows the relationship between atomic charges and chemical shifts for N and C atoms, in panels (a) and (b), respectively. Once again, both ^{13}C and ^{15}N chemical shifts follow a general trend: within each type, more negative charge (higher electron density) corresponds to more shielding (thus, smaller chemical shifts).

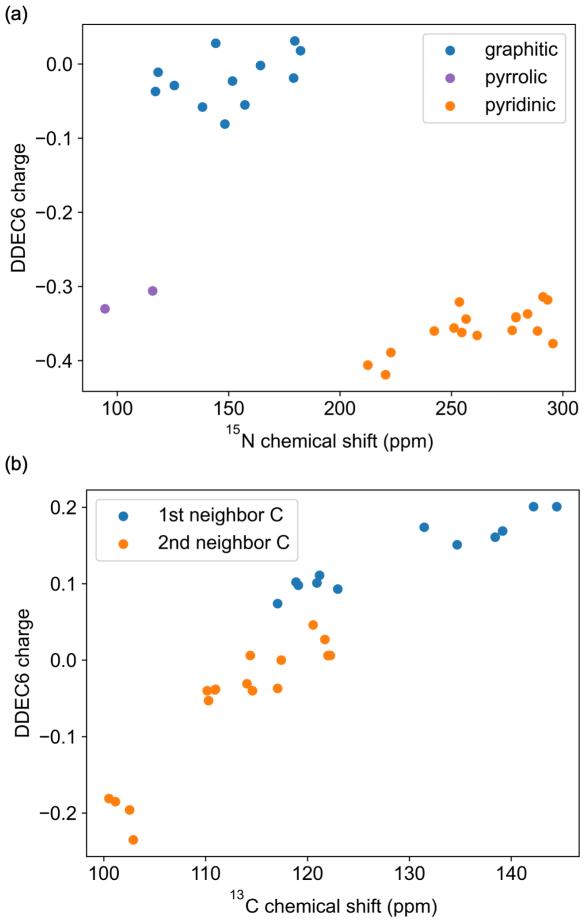

Figure 3.5: The relationship between charge and chemical shift of (a) N atoms and (b) C atoms as first and second neighbor of N atoms from the models utilized in this study. Negative values denote an accumulation of electron density (negative charge), positive values indicate electron density depletion (positive charge).

Interestingly, unlike the ^{13}C chemical shifts in Fig. 3.5(b) following a single scaling relation, different N species give different offsets. Differences in first neighbors of the center N atoms explain the differences in offsets: 2 C atoms for pyridinic N centers, 3 C atoms for graphitic N centers, and 2 C atoms with 1 H atom for pyrrolic N centers. It is also worth mentioning that the second C neighbors, although not shown in Fig. 3.2, show generally negative charge, whereas first neighbor C atoms show generally positive charge. As N has a greater electronegativity (3.04) than C (2.55), electron density is transferred from the first

neighbor to N, creating a depletion zone around the N atom. The second neighbor C atom experiences increased electron density, forming a charge ripple. This also contributes to the broadening of ^{13}C chemical shifts.

Experimentally, water is used to probe the presence of N species on the material surface. Thus, modeling this effect is crucial for understanding experimental results under such operating conditions. The interaction between surface adsorbed water and surface N atoms varies strongly with respect to the type of N atom, see appendix B Fig. B.4 for structures. For a pyrrolic N atom, the O atom from water forms a hydrogen bond with the H atom from the pyrrolic NH group. Since O has a greater electronegativity (3.44) than N (3.04) and H (2.20), the electron density is transferred from NH to O. Thus, the N and H nuclei are both effectively deshielded and accordingly exhibit larger ^{15}N and ^{1}H isotropic chemical shifts, as shown in Fig. 3.6. To test the convergence of this effect with the number of water molecules, up to four water molecules are added to the pyrrolic N model, and the influence after three molecules added is small, see Fig. 3.6.

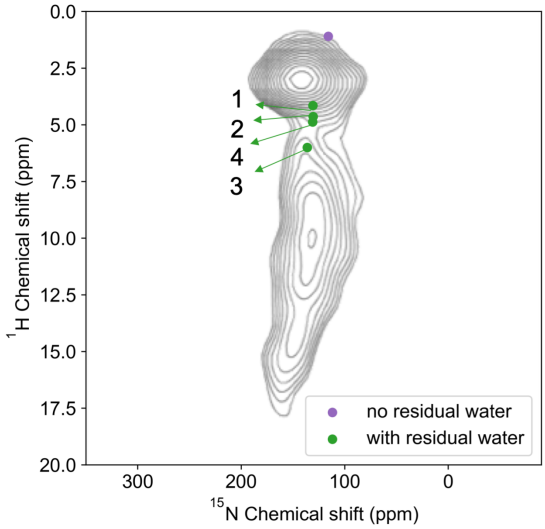

Figure 3.6: Simulated and experimental 2D ^{15}N-^{1}H NMR correlation for a 16 atom% N graphitic N-carbon material. Scatter points are simulated results and contour lines indicate experimental signal intensity. The data points shown are from pyrrolic N model with 0, 1, 2, 3, and 4 water molecules. Numbers next to scatters indicate the numbers of water molecules in the models.

Residual water has an effect on the other two types of N atoms, but this is not directly reflected in the 2D spectrum of Fig. 3.6 since there's no first neighbor H of pyridinic N and graphitic N. For pyridinic N, interactions with adsorbed water results in greater shielding of the pyridinic ^{15}N nucleus and corresponding deshielding of the ^{1}H nucleus in water. It is also found that the O atom, instead of the H atom, will interact with the graphitic N atom. As a result, graphitic N is deshielded, but this is not reflected on the 2D ^{15}N-^{1}H spectrum since the distance from the water H atom to graphitic N atom is large. For the 2D ^{13}C-^{15}N spectra, the overall result of water coordination is that the ^{15}N chemical shift of pyrrolic N will be shifted towards larger values with a magnitude of 15-20 ppm, graphitic N will be shifted towards larger values with a magnitude of about 6 ppm and pyridinic N will be shifted towards smaller values with a magnitude of about 25 ppm. Detailed values are listed in appendix B Table B.5. If we consider the Gibbs free energy change of water on

graphitic/pyrrolic/pyridinic moieties, as shown in appendix B Table B.6, we find that water adsorption is favorable on pyrrolic and pyridinic N sites. This explains why in Fig. 3.2, where water adsorption is not included, the pyrrolic structure (4) appears with an underestimated chemical shift compared to the experimental data, and why some pyridinic group chemical shifts are overestimated. Correction for the influence of water significantly improves the agreement. The influence of residual water on the ^{15}N and ^{1}H isotropic chemical shifts can also be reflected on the atomic charge, see appendix B Fig. B.5. This influence is relevant for applications since it indicates that the electronic properties will be altered when the materials are in electrocatalytic conditions.

3.4 Conclusion

DFT calculations are used in this work to predict and explain the chemical shifts of N, C, H atoms in N-doped graphene systems. A number of different models are investigated: non-doped models (terrace, zigzag edge, and armchair edge), single N-doped models (graphitic, pyridinic, and pyrrolic N), and N pair models (graphitic-graphitic, pyridinic-pyridinic, pyrrolic-graphitic, and pyridinic-pyridinic). Comparisons of predicted chemical shifts with experimental 2D ^{13}C-^{15}N spectra show good agreement, especially when the influence of water adsorption is included. The major difference between the chemical shifts of graphitic/pyridinic/pyrrolic N-moieties is understood by comparing the electronegativities of the various environments.

Furthermore, for each type of environment, the general concept of signal broadening is decomposed into four different factors, the influences of which are discussed in detail. The first factor is the standalone N/C geometry, where a larger curvature of the graphene edge is found to give a more positive chemical shift. The second factor is the effect of a second N atom nearby: a graphitic N atom close to a pyridinic N decreases the chemical shift, while a pyridinic N close to a graphitic N increases the chemical shift. The trends of other types of moiety mixing are more complicated, but the overall signal broadening matches the experimental spectrum well. The third factor is that for each specific structure, the second

neighbor C atom experiences a lower chemical shift. The fourth factor is the influence of residual water, which is important to understand the aqueous environment in oxygen reduction reaction or hydrogen evolution reaction. Introduction of this factor matches with the experimental 2D ^{15}N-^{1}H spectrum and provides better agreement with the experimental ^{13}C-^{15}N spectrum. With the free energy taken into account, water adsorption on pyrrolic and pyridinic N sites is found to be more stable and to induce a positive or negative deviation in the chemical shift, respectively.

An intuitive correlation between the charge of the probed atom and the chemical shift is confirmed: the smaller the charge, i.e., the higher the electron density, the more shielded the nucleus is, and hence the smaller the chemical shift. The relationship between charge and chemical shifts is discussed, enabling a more detailed understanding of the electronic influence of N doping. These results can be used for the rational design of N-containing carbon materials with desirable electronic properties to improve electrochemical performance. They can also lead to a determination of the nature of active sites in these electrocatalysts by comparison of several N-doped carbon materials.

CHAPTER 4

Diffusion Barriers for Carbon Monoxide on the Cu(001) Surface Using Many-Body Perturbation Theory and Various Density Functionals

4.1 Introduction

Transition metal catalysts are among the prime candidates in the conversion of CO to various hydrocarbons, either through thermal catalysis in the conversion of synthesis gas[36, 37, 38, 39] and the water-gas shift reaction[40, 41], or electrocatalysis in the CO and CO_2 reduction reaction[5]. In these processes, multiple reactions take place simultaneously on the surface and only a detailed understanding of this reaction network allows to identify predominant reaction pathways, reaction rate, and product selectivity. In this context, first principles modeling[9, 10] plays a key role, since it is a method that can assign reaction energies and barriers to all possible reaction steps. When combining this information with microkinetic modeling[11, 12] or kinetic Monte Carlo simulations[13], it is then possible to predict reaction rates and selectivities for a specific catalytic system.

Density Functional Theory (DFT)[27, 28] in its Generalized Gradient Approximation[133] has become the most commonly used method to model surface reactions, due to a reasonable accuracy paired with a high computational efficiency. However, it is reported that many DFT-based methods fail in capturing the correct adsorption site preference of CO on several metal surfaces[32, 33, 34, 35], which is often referred to as the CO-adsorption puzzle. While the incorrect prediction of the relative stability of CO adsorption to different high-symmetry surface sites is already concerning in its own right, it also poses the question, to what degree

other aspects of CO interactions with metal surfaces, such as surface reactions or molecular diffusion, are influenced by this shortcoming.

A good example for these problems is the interactions of CO with Cu surfaces. CO interactions with Cu surfaces are of particular interest, since Cu is the main component of the industrial catalyst for methanol synthesis from synthesis gas[36, 37, 38, 39] and the water-gas shift reaction[40, 41], and plays a key role for the electroreduction of CO_2 into C_1[42, 43, 44] or C_2[134, 45] products. A main controversy for Cu is the diffusion of CO on the Cu(001) surface. At an experimental level, Graham and Toennies[135] report a minimum diffusion pathway from the top over the bridge site, while Alexandrowicz et al.[136] identify the diffusion over the fourfold coordinated hollow site as energetically more favorable. Subsequently, this dispute has drawn significant interest from the theory community, who have arrived at different conclusions considering the shape of the potential energy surface for CO diffusion, a debate that has not been settled so far. However, the computational efforts were made based on GGA DFT energetics[137, 138, 139] and suffer from the wrong prediction of CO adsorption site preference.

One way to resolve this dispute is to move to post-Hartree-Fock methods[46]. In particular the Random Phase approximation (RPA)[47, 48], a post-HF method that is based on many-body perturbation theory[49, 50], is a promising approach to address surface catalysis problems, since an implementation for plane waves in periodic boundary conditions exists[51, 52]. On top of that, RPA is the only method that correctly predicts the surface energy of Cu(111) and adsorption of CO in the top position on Cu(111) and multiple other late transition metal surfaces[53].

In this contribution, we use RPA to study the Cu(001) surface energy as well as the adsorption and diffusion of CO on the Cu(001) surface. In a first step, we discuss the challenges for RPA calculations on transition metal surfaces and propose a k-space embedding scheme to reduce computational cost. Subsequently, we apply this methodology to the diffusion of CO along the [110] and [100] directions of the Cu(001) surface. We compare the RPA results with different DFT exchange correlation functionals including the

Perdew-Burke-Ernzerhof (PBE) functional[31], the PBE functional with D2[140] or D3[141] correction, the RPBE functional[142], the Bayesian error estimation functionals (BEEF-vdW)[143], the strongly constrained and appropriately normed (SCAN) functional[79], and the Heyd-Scuseria-Ernzerhof (HSE06) functional[144]. All these results are then compared with experimental measurements in the literature.

4.2 Methods

4.2.1 Theory

In this contribution, we calculate total energies using the Adiabatic Connection Fluctuation Dissipation Theorem (ACFDT)[49, 50] in its RPA, a method originating from many-body perturbation theory that has been reformulated within the framework of density functional theory. The total energy expression within RPA can be written as[51, 52]

$$E^{RPA} = E^{EXX}([\phi_{occ}]) + E_c^{RPA}([\phi_{occ}, \phi_{uocc}]) \tag{4.1}$$

where E^{RPA} denotes the RPA total energy. This energy is composed of E^{EXX} the exact exchange energy, which only depends on the occupied orbitals ϕ_{occ}, and the RPA correlation energy E_c^{RPA}, which depends on all occupied and unoccupied orbitals ϕ_{occ}, ϕ_{uocc}[145, 146].

The focus on occupied and unoccupied orbitals leads to two challenges: First, the true orbitals are unknown, and they are typically approximated by orbitals obtained from semi-local DFT functionals[147, 148, 149, 150, 51]. Second, in principle an infinite number of unoccupied orbitals exists, and all orbitals need to be considered to arrive at an accurate E_c^{RPA}. However, evaluating expressions for an infinite number of orbitals is not possible in a realistic computational setting. In practical implementations, E_c^{RPA} is evaluated at different orbital cut off energies E_{cut}^{χ}, and is extrapolated to an infinite orbital cut-off energy using

$$E_c^{RPA}(E_{cut}^{\chi}) = E_c^{RPA}(\infty) + \frac{A}{{E_{cut}^{\chi}}^{\frac{3}{2}}} \tag{4.2}$$

Even though E_c^{RPA} is extrapolated to infinite orbital cut-off energy, extrapolations based on higher E_{cut}^{χ} values improve the accuracy. At the same time, a higher E_{cut}^{χ} significantly

increases the cost of calculations and in many cases makes the modeling of extended, periodic systems unfeasible. One option to circumvent this problem is to only model a small part of a periodic system at a high level and embed the small part in the fully periodic system modeled at a lower level of theory. At the most basic level, this approach has been introduced as the ONIOM approach[151, 152], where the energy of the total system is corrected by the energy difference between high-level and low level methods for the cluster description[153, 154, 155]. However, the geometry of a small cluster does not correctly capture the symmetry of an extended metallic system leading to delocalized wavefunctions. To address these issues, a density embedding scheme was developed by Carter et al.[156, 157, 158, 159, 160, 161] to address these shortcomings and to more accurately treat metal surfaces. However, this approach still did not address the fundamental symmetry mismatch between the embedded cluster and the metallic surface and required significant effort to account for the delocalized wavefunctions. Hence, an approach that naturally matches the symmetry of the model system would be highly desirable.

In this contribution we choose such an approach: extended metals are best modeled using periodic boundary conditions. Here, a unit cell is used, which directly interacts with its adjacent mirror images. If only one unit cell was present, the delocalized nature of the wave functions, which often extend far further than the dimensions of a single unit cell, could not be correctly captured. This shortcoming is compensated by working in reciprocal space and treating multiple k-points. From a real space perspective, the number of k-points indicates, how many multiples of the unit cell are considered in each direction when solving quantum mechanical equations. At the same time, the number of k-points included in the computational modeling is directly correlated to the computational cost and in particular for high cut-off RPA calculations, using a dense k-point mesh is often not feasible.

To address this problem, we apply an ONIOM like embedding scheme in k-space[162], as shown in Scheme 4.1, named after the ONIOM scheme developed for real space embedding[151, 152]. In this approach we start modeling our system using RPA with a maximum E_{cut}^{χ} value of 150 eV and a 3×3×1 k-point mesh. Subsequently, we embed these calculations in RPA

calculations with a maximum E^{χ}_{cut} value of 100 eV and an 8×8×1 k-point mesh, and finally, we embed these two calculations in PBE model using a 15×15×1 k-point mesh. Using this approach, we express the RPA energy as

$$\begin{aligned} E^{RPA}(150\ eV, 15\times15\times1) = E^{RPA}(150\ eV, 3\times3\times1)+ \\ E^{RPA}(100\ eV, 8\times8\times1) - E^{RPA}(100\ eV, 3\times3\times1)+ \\ E^{PBE}(15\times15\times1) - E^{PBE}(8\times8\times1) \end{aligned} \tag{4.3}$$

In this expression, the first number in brackets refers to the maximum E^{χ}_{cut} value, while the second set of numbers refers to the k-point mesh used. Since we are studying a metallic slab extended in x and y direction, only one k-point is used in z direction.

Throughout this manuscript, we will also report values calculated using the different functionals along with the energetics of each embedding step for all calculations. This approach allows us to better understand the impact of using RPA and of potential compromises in computational setup on the observed diffusion energetics. The convergence test of energetics with respect to E^{χ}_{cut} can be found in appendix C, Table C.1, and numerical validation of k-space ONIOM like like approach is provided in appendix C, Table C.2. Errors from applying the k-space ONIOM like scheme are estimated to be below 15 meV.

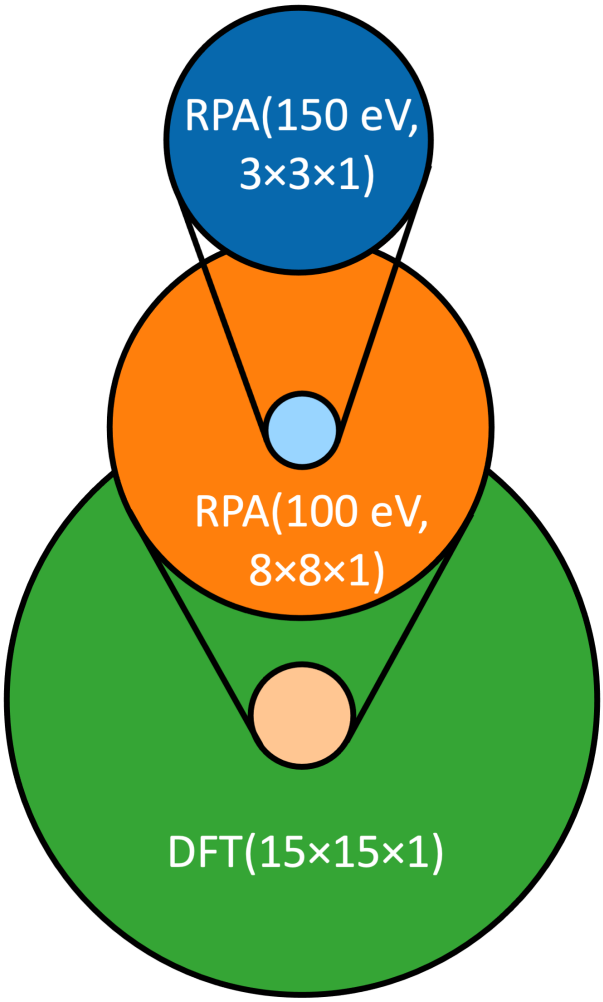

Figure 4.1: Schematic representation of the extrapolations applied for the RPA calculations using different k-point meshes in this work. The applied approach shows large similarities to the ONIOM scheme, with the embedding being performed in k-space. The text indicates the used level of theory, and numbers in brackets indicate k-point meshes for RPA and PBE calculations, and cutoff energy values for RPA calculations.

4.2.2 Computational Models

As mentioned above, we calculate three different properties and compare them to experimental measurements, namely the surface energy of Cu(001), the adsorption strength of CO to Cu(001), and the diffusion barriers along the [100] and [110] directions of the Cu(001)

surface. In this section, we describe the models chosen to calculate these different properties.

4.2.2.1 Surface Energy

The surface energy is calculated as

$$E_\sigma = \frac{E_{slab} - n * E_{bulk}}{\sigma} \tag{4.4}$$

where E_{slab} is the energy of a symmetric slab with two equivalent surfaces, and n is the number of atoms in this slab. E_{bulk} is the bulk energy per atom and σ is the surface area.

Bulk energies were calculated using a face centered cubic primitive unit cell containing one Cu atom with a 14×14×14 k-point mesh. Careful tests reveal that further increasing the k-point density only leads to small changes in energy (<1 meV). For this unit cell, lattice parameters were determined for most functionals. Only for HSE06 and RPA calculations, equilibrium lattice parameters reported in the literatures were used, namely 3.626 Å for HSE06[163] and 3.581Å for RPA[52]. For calculations with other functionals, the equilibrium lattice parameters were determined using a seven-point fit to a Birch-Murnaghan equation of state, where the lattice parameter in the calculations was varied by ±15%. Lattice parameters for all methods are reported in the Supporting Information, Table S3. Our PBE lattice parameter, 3.629 Å matches well with previous literatures, 3.630 Å.[163, 52]

Energies of the slab were calculated for a six layer slab exposing a 1×1 Cu(001) surface. In this slab the two center layers were kept fixed and the outer two layers of the slab were allowed to relax. For most functionals, we first performed the structural optimizations with a 20×20×1 k-point mesh and reported total energies for calculations with a 30×30×1 k-point mesh. HSE06 and RPA energies were single point energies based on PBE optimized structures (using HSE06 and RPA lattice parameters) with a 20×20×1 k-point mesh. For most functionals, we increased the cutoff energy of the plane wave basis to 700 eV. Only for RPA and HSE06 calculations a cutoff energy as 550 eV was used.

4.2.2.2 CO adsorption

We calculate interactions between CO and the Cu(001) in a 2×2 unit cell (see Fig. 4.2 (a)) of a four layer slab. We use the experimental lattice constant of 3.615 Å[163] for all the functionals. This value is a good compromise between the PBE value, 3.629 Åand the RPA value, 3.581 Å[53]. This choice ensures that the RPA and PBE energetics in the embedding scheme are corresponding to comparable structures. Repeated images of the slabs are separated by 13 Å (21 Å) for RPA (and DFT). In DFT calculations, dipole corrections were applied. For RPA, dipole corrections are not available. In the past, Lébegue et al.[164] have shown that the correlation energy uncertainty is ca. 0.2 meV for vacuum separations larger than 13 Å. We performed test for slabs separated by 12/13/14 Å of vacuum using RPA and find convergence of results within 4 meV. Numerical values for convergence tests are provided in appendix C Table C.4. In the optimization process, the bottom two layers of Cu atoms are kept fixed and the top two layers are relaxed. In all calculations one CO molecule was placed in each unit cell, which leads to a coverage of 0.25. For the CO adsorption and diffusion calculations, a cutoff energy for the plane wave basis of 700 eV was used for SCAN calculations as it improves the quality of diffusion profile whereas a cutoff energy of 550 eV was used for other DFT calculations: PBE, PBE+D2, PBE+D3, RPBE, BEEF-vdW, and HSE06.

The adsorption enthalpy is calculated as

$$H_{ads} = E_{slab+CO} - E_{slab} - E_{CO} + \Delta ZPE + E_{correction}, \tag{4.5}$$

where the ΔZPE is the difference of zero-point energy of CO in gas phase and on the surface, which was calculated within the harmonic approximation. We calculated ΔZPE at PBE level of theory and tests using RPBE show changes in ΔZPE of less than than 1 meV. $E_{correction}$ summarizes an extrapolation from 4 layer to 6 layer results and (for RPA and HSE06) corrections for a denser k-point mesh. Numerical values for all components of H_{ads} are reported in the Supporting Information Table S5. All adsorption enthalpies are reported for CO adsorption in the top position. Structures of the slab and CO adsorbed on

the slab for methods other than HSE06 and RPA were firstly optimized using a 10×10×1 k-point mesh. Final energies were reported for an increased k-point mesh of 15×15×1. We assumed structural convergence for forces lower than 0.01 eV/Å. HSE06 and RPA energies were single point energies based on PBE optimized structures using an 8×8×1 k-point mesh.

For all DFT methods, the energy of a CO molecule reference energy was calculated using a 11×12×13 Å^3 supercell to suppress the spurious interactions between periodic images. RPA calculations relied on optimized PBE structures, and the values were extrapolated to the isolated molecule limit based on a series of calculations with different box sizes (7×8×9 Å^3, 8×9×10 Å^3, 9×10×11 Å^3, and 10×11×12 Å^3 for E_{cut}^{χ} =200 eV and 250 eV, and additional 11×12×13 Å^3 for E_{cut}^{χ} =100 eV and 150 eV). Molecular calculations were performed with a $\mathbf{\Gamma}$ point only k-point mesh. Adsorption energies were found to be converged within <1 meV for E_{cut}^{χ}=200 eV. Further details for convergence can be found in appendix C Table C.6.

4.2.2.3 Diffusion Barriers

For the calculation of diffusion barriers, we rely on the computational setup used for adsorption energy calculations (see Fig. 4.2 (a)). We study two different paths for surface diffusion, namely along the [100] direction from the top to the bridge site, Fig. 4.2 (b), and along the [110] direction from the top to the hollow position on this surface, Fig. 4.2 (c). For each path, 15 equally spaced points along the high symmetry pathway from the top to the bridge or hollow site were optimized using the following methods keeping the x and y coordinate of the C atom in CO fixed. For PBE, PBE+D2, PBE+D3, BEEF-vdw and RPBE functionals, optimizations were performed using a 10×10×1 k-point mesh. For SCAN, HSE06, and RPA calculations, PBE optimized structures were used. We checked the influence of using PBE structures by comparing the energetics using BEEF-vdW for BEEF-vdW and PBE optimized structures. The values are reported in appendix C Table C.7. Reported DFT energy profiles correspond to single point calculations based on optimized structures at the respective level of theory with a 8×8×1 k-point mesh for HSE06 and a 15×15×1 k-point mesh for other functionals.

As shown in Fig. 4.2 (d), the following geometry parameters are analyzed for the structures along the pathways: r_{CO}, the distance between the C and O atom, $d_{CCu,\ z}$, the z coordinate difference between the C atom and the Cu(001) surface plane, $d_{CCu,\ x}/d_{CCu,\ xy}$, the distance between the C and Cu atom projected along the [100]/[110] direction, and θ_{OCz}, the angle spanned by the axis of the CO molecule and the $[00\overline{1}]$ direction. It is worth mentioning that the $d_{CCu,\ x}/d_{CCu,\ xy}$ distances are calculated with respected to the fixed Cu atoms in the third layer of the slab, since this approach mitigates the influence of structural relaxation of the top two layers. Additionally, a potential energy surface for moving CO in the z direction perpendicular to the surface was calculated at the RPA level, where all PBE coordinates were kept fixed, except the z coordinate of C and O, which were shifted away from the surface simultaneously by 0.02 Å, 0.04 Å, and 0.06 Å in z-direction. Detailed energetics are provided in appendix C Table C.8.

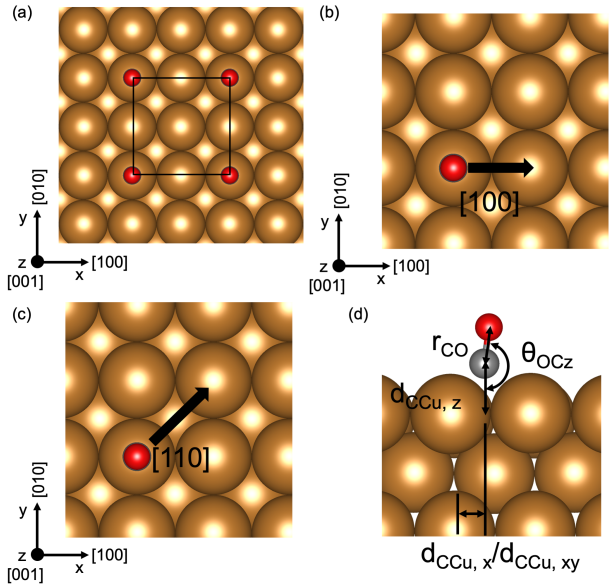

Figure 4.2: (a) The unit cell of the Cu(001) surface used in this work. (b) The top-bridge-top diffusion pathway along the [100] direction of the Cu(001) surface. (c) The top-hollow-top diffusion pathway along the [110] direction of the Cu(001) surface. (d) The metal carbonyl complex motif showing geometry parameters: r_{CO}, the distance between the C and O atom, $d_{CCu,\ z}$, the z coordinate difference between the C atom and the Cu(001) surface plane, $d_{CCu,\ x}/d_{CCu,\ xy}$, the distance between the C and Cu atom projected along the [100]/[110] direction, and θ_{OCz}, the angle spanned by the axis of the CO molecule and the $[00\bar{1}]$ direction. Cu atoms are shown as brown, O atoms red and C atoms grey.

In all our calculations periodic boundary conditions are used, which leads to all CO molecules diffusing simultaneously, results being given for one CO molecule. To better understand the impact of concerted diffusion and coverage effects, we performed calculations for 4-layer slabs using 3×3 and 4×4 unit cells, which used 7×7×1 and 5×5×1 k-point meshes, respectively.

4.2.3 Computational Setup

All calculations in this paper were performed using the Vienna Ab-Initio Simulation Package[76] (VASP), a code using plane wave basis sets, projector augmented wave[165] (PAW) pseudopotentials, and periodic boundary conditions. In this work we rely on VASP implementations of PBE, PBE+D2, PBE+D3, RPBE, BEEF-vdW, HSE06, and RPA.

GW pseudopotentials were used for all calculations, and more details can be found in appendix C Table C.11. First order Methfessel-Paxton smearing with sigma value of 0.2 eV was used for all DFT slab optimizations and DFT single point energies whereas Gaussian smearing with sigma value of 0.05 eV was used for molecular references. For RPA calculations, Gaussian smearing with sigma value of 0.05 eV was used. K-point grids and cut off energies were described in the preceding section.

RPA calculations rely on single-particle orbitals calculated at LDA, GGA, or hybrid functional level of theory. It has been demonstrated that RPA total energies are rather insensitive to the starting orbitals for molecules[147, 148, 149] and solids[150, 51]. In this work, we rely on RPA calculations using PBE orbitals and PBE one-electron energies (RPA@PBE), which is consistent with previous RPA calculations for metals[52] and metal-O[53] systems. We have further tested RPA based on RPBE orbitals and RPBE one-electron energies (RPA@RPBE) and we find differences smaller than 1 meV for barriers and high symmetry site energy differences. Detailed energetics are provided in appendix C Table C.12.

4.3 Results and Discussion

4.3.1 Surface Energy and Adsorption Enthalpy

We start the discussion of results by focusing on surface energies and adsorption enthalpies and results are shown in Fig. 4.3. The adsorption enthalpy measures the adsorption strength while the surface energy gives information about the surface stability. The correct description of surface stability is essential as it overall affects the adsorption strength across different

adsorbates, and ensures the correct description when impurities, defects, and reconstructions are introduced. In the past it has been shown that multiple density functional theory-based methods exist that describe either the surface energy or the CO adsorption strength accurately but have problems in describing both properties well at the same time.

We find that RPBE, HSE06, and BEEF-vdW, which describe the adsorption enthalpy accurately, give significantly lower surface energies compared to experimental value. SCAN, which leads to an accurate surface energy, significantly overestimates the adsorption strength. Only RPA leads to surface energies and adsorption enthalpies in close agreement with experimental data. These results agree well with reports in the literature for close packed (111) surfaces, where it was found that for DFT functionals the sum of adsorption enthalpy and surface energy underestimates the experimentally observed values and only RPA leads to reasonable agreement between theory and experiment.[53].

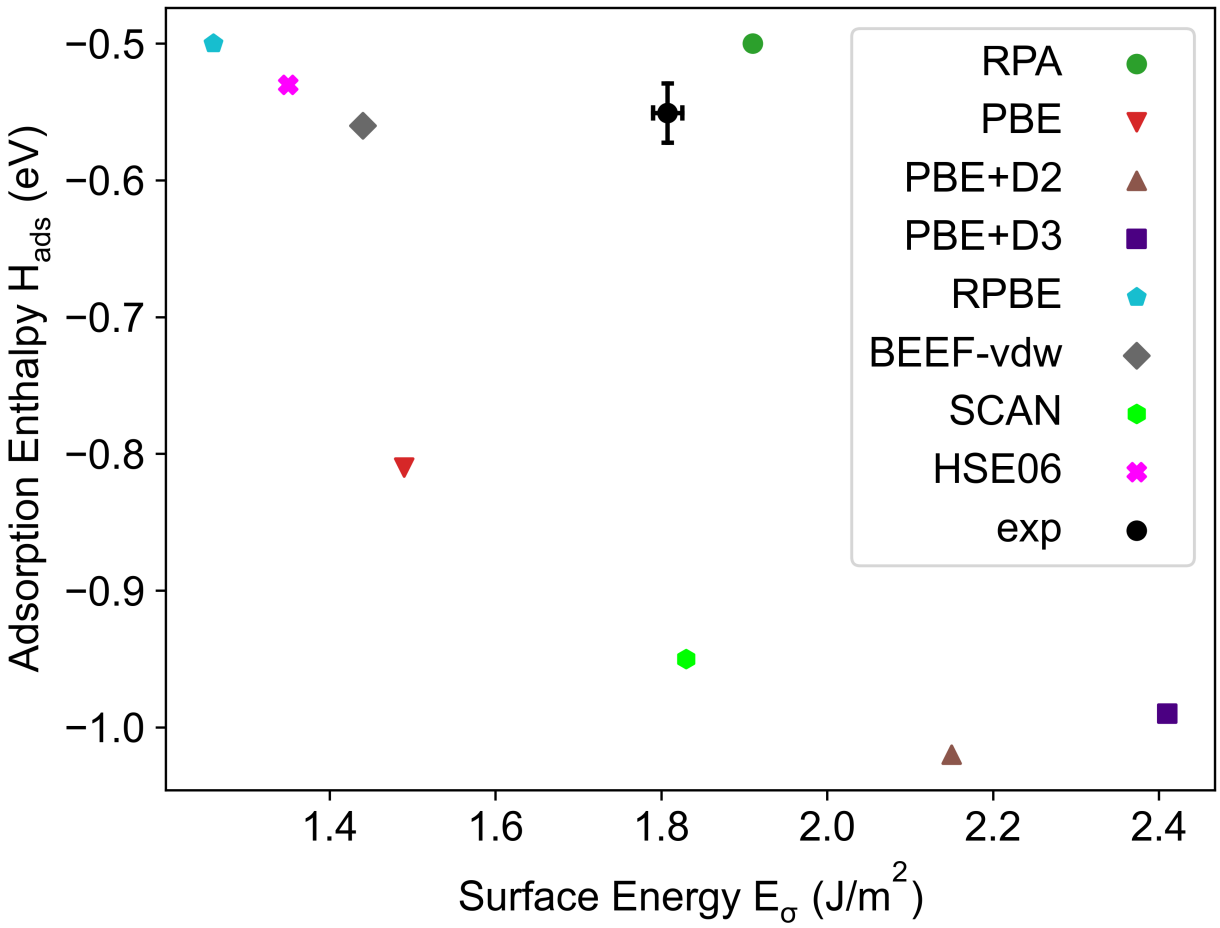

Figure 4.3: Cu(001) surface energy and CO adsorption enthalpy values of the methods used here. Experimental values are shown with error bar. Experimental surface energy is deduced from liquid-metal data as an average for all surfaces. Surface energy values are shown in the unit of J/m^2 and CO adsorption enthalpy values are shown in unit of eV per CO molecule.

4.3.2 Top-Bridge-Top Diffusion

Subsequently, we study CO diffusion along the [100] direction of the Cu(001) surface, as shown in Fig. 4.2 (b). In this pathway, the CO molecule is moved from the top to the bridge position along the $d_{CCu,\ x}$ direction and the corresponding energy profile is shown in Fig. 4.4. In agreement with results for the Cu(111) surface[53], we find that RPA predicts a preference for CO adsorption in the top position over the bridge position by 114 meV, hence providing

the correct site in comparison with experiments. Additionally, the top site preference in RPA slightly increases for a higher k-point sampling (90 meV for 3×3×1 k-point mesh, 113 meV for 8×8×1 k-point mesh). PBE prefers adsorption in the bridge position over the top position by 38 meV. D2 and D3 van der Waals corrections further stabilize the bridge site to a total energy difference of 64 and 42 meV, respectively. SCAN agrees with PBE based functionals on the site preference and predicts the bridge site to be more stable by 21 meV compared to the top site. The RPBE and BEEF-vdW functionals on the other hand give the correct site preference, with bridge-top differences calculated to be 11 and 26 meV. HSE06 leads to results most similar to RPA with a preference for the top site over the bridge site by 108 meV.

In agreement with the significant differences in relative energies between top and bridge positions, diffusion barriers are also vastly different. While the overall barrier for top-bridge diffusion at RPA level is 132 meV (117 meV for 3×3×1 k-point mesh and 130 meV for 8×8×1 k-point mesh, respectively), the lowest barrier for the displacement from top to bridge site is found using PBE-D3 (11 meV). The other values lie between these two extremes with HSE06 leading to a barrier most closely resembling RPA values. BEEF-vdW, even it correctly describes the preferred top site and it adsorption enthalpy, gives a much smaller diffusion barrier (51 meV) linked with a smaller energy difference between top and bridge site. Functionals that prefer the bridge site over the top site (SCAN, PBE and PBE with dispersion correction) lead to the lowest barriers. However, in this case the overall diffusion barrier is obtained when moving from bridge to top site, and not from top to bridge, which increases these barriers to 60 meV (PBE), 53 meV (PBE-D2), 84 meV (PBE-D3), and 49 meV (SCAN).

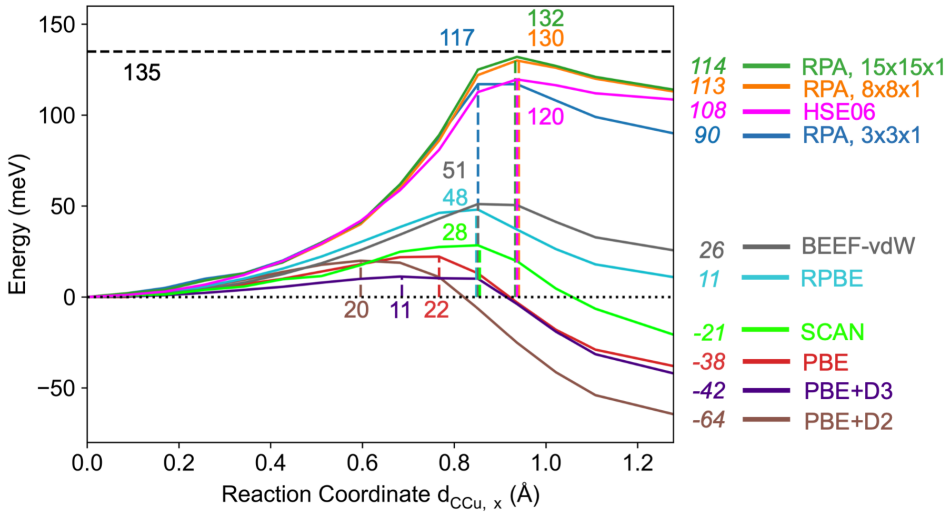

Figure 4.4: Energy profiles for the CO diffusion from the top site to the bridge site along the [100] direction calculated using different functionals and RPA with different k-point meshes. The distance between the C and Cu atom projected along the [100] direction, $d_{CCu,\ x}$, is utilized as the reaction coordinate. The horizontal dashed black line indicates the experimental barrier[136], 135 meV. Vertical dashed lines indicate the position of transition states calculated with different methods. Non-italicized values correspond to the barriers and italicized values correspond to the bridge-top energy differences.

Further analysis of the potential energy surface for diffusion shown in Fig. 4.4 reveals that also the position of the transition state is shifted between different methods. To keep the discussion tractable, we report and discuss structural parameters for PBE, BEEF-vdW, and RPA in the main text. Structural parameters for the other methods are provided in the Supporting Information Table S13. While the PBE and BEEF-vdW transition states lie at $d_{CCu,\ x}$=0.77 Å and 0.85 Å, the RPA transition state lies at $d_{CCu,\ x}$=0.94 Å and therefore later along the reaction coordinate. Given the significant difference in final state energies, a shift in transition state coordinate between the different methods is not unexpected.

We furthermore analyzed the geometries of CO adsorbed in the different positions along the diffusion path and the atomistic structures are shown in Fig. 4.5. In the top adsorption

site CO adsorbs perpendicular to the surface plane with a r_{CO} (the distance between C and O atoms, see Fig. 4.2 (d)) value of 1.15 Å for both PBE and BEEF-vdW. (RPA shares the same r_{CO} with PBE since the RPA geometry is only optimized by simultaneously shifting the z coordinate of C and O atoms). This distance slightly increases to 1.17 and 1.16 Å in the bridge position for PBE and BEEF-vdW, respectively. Using PBE we find a $d_{CCu,\ z}$ (the difference in z coordinate between the C atom and the closest Cu surface atom, see Fig. 4.2 (d)) value of 1.84 Å for the top position and 1.52 Å in the bridge position. Optimizing $d_{CCu,\ z}$ at RPA level leads to an increase of 0.02 Å (top position) and 0.04 Å (bridge position). For the transition state (TS) geometry, it is not surprising to see that RPA gives a TS geometry closer to the bridge site one, since the TS lies later along the pathway, indicated the values for $d_{CCu,\ z}$ of 1.71 Å, 1.70 Å, and 1.60 Å for PBE, BEEF-vdW, and RPA, respectively.

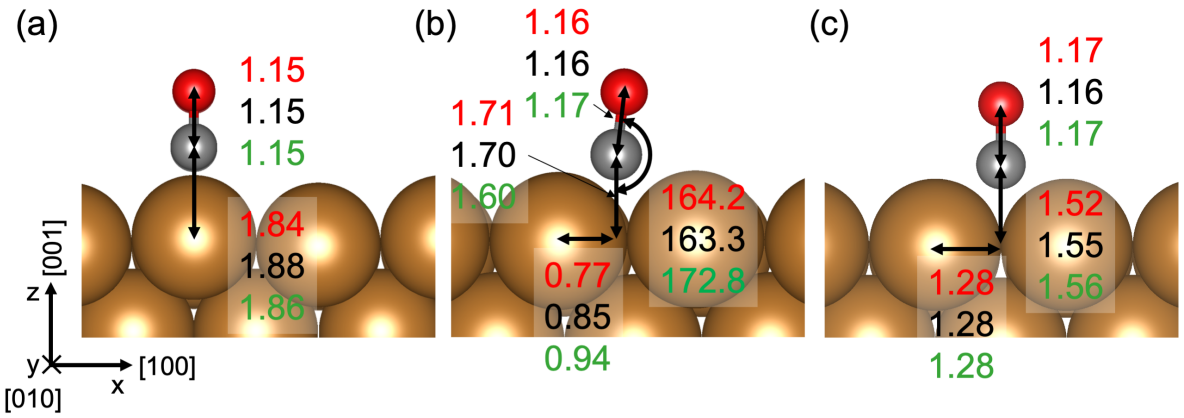

Figure 4.5: Structures along the [100] diffusion pathway. (a) Top site structure. (b) Transition state structure. (c) Bridge site structure. As defined in Fig. 4.2 (d), values are shown for r_{CO}, the distance between the C and O atom, $d_{CCu,\ z}$, the z coordinate difference between the C atom and the Cu(001) surface plane, $d_{CCu,\ x}$, the distance between the C and bulk (fixed) Cu atom projected along the [100] direction, and θ_{OCz}, the angle spanned by the axis of the CO molecule and the $[00\bar{1}]$ direction. Similar to the color scheme used in the energy profile, values shown in red, black, and green correspond to PBE, BEEF-vdW and RPA results. Presented numbers are given in Å for distances and degree for angles. Cu atoms are shown as brown, O atoms red and C atoms grey. Numerical values for transition state geometries of the other functionals are given in appendix C Table C.13.

4.3.3 Top-Hollow-Top Diffusion

As a next step we focus on diffusion from the top site to the hollow site along the [110] direction of the Cu(001) surface, as shown in Fig. 1 (c), and the potential energy surface for this process is shown in Fig. 4.6. Again, a similar picture to top-bridge diffusion emerges, where the top site is the minimum for RPA (245 meV, 234 meV, and 227 meV more stable than the hollow site for 15×15×1, 8×8×1, and 3×3×1 k-point meshes, respectively), while the hollow site is 8 meV more stable using PBE. Similar trends are found for PBE+D2 where the hollow site is stabilized by 31 meV compared to the top site. PBE+D3 and

SCAN give the right site preference but with a rather small difference: the top site is 13 meV more stable than hollow site. RPBE and BEEF-vdW functionals give the right site preference with a larger difference: the top site is 89 and 123 meV more stable than the hollow site, respectively. HSE06 functional once again gives results similar to RPA with a top site preference by 254 meV.

Following this trend, diffusion barriers from the top to the hollow position are increased to 250 meV, 241 meV, and 232 meV for RPA with 15×15×1, 8×8×1, and 3×3×1 k-point meshes and to 55 meV for PBE. However, the effective barrier for PBE, which corresponds to diffusion from the hollow to the top site, is only slightly increased to 63 meV compared to the barrier of 60 meV for the bridge-top diffusion. Applying D2 and D3 van der Waals corrections gives slightly lower barriers: 44 and 49 meV, respectively for diffusion from the top site to the hollow site. SCAN, RPBE, and BEEF-vdW functionals predict higher barriers of 75, 106 and 132 meV, respectively. We do not find a local minimum in the hollow site using the HSE06 functional and the overall barrier of 254 meV is again close to the RPA value 250 meV.

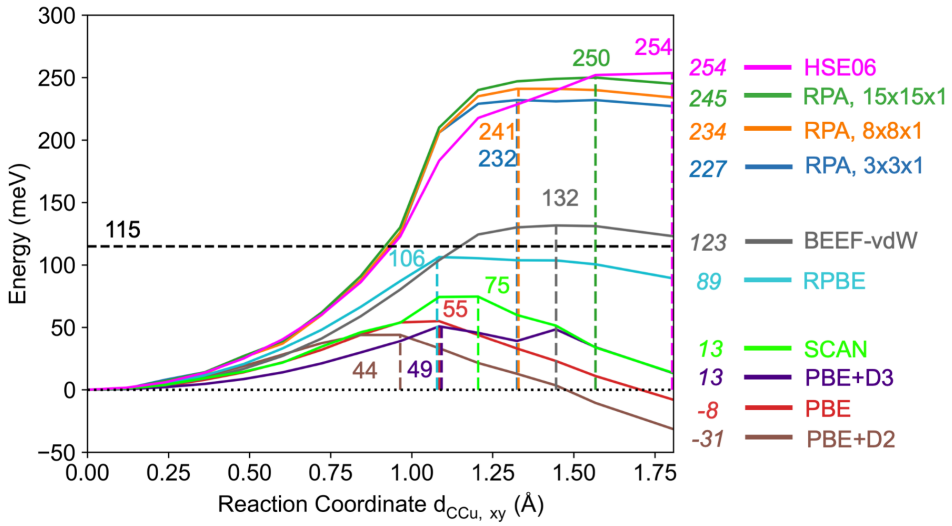

Figure 4.6: Energy profiles for the CO diffusion from the top site to the hollow site along the [110] direction using different functionals and RPA with different k-point meshes. The distance between the C and Cu atom projected along the [110] direction, $d_{CCu,\ xy}$, is utilized as the reaction coordinate. The horizontal dashed black line indicates the experimental barrier[136], 115 meV. Vertical dashed lines indicate the position of transition states calculated with different methods. Non-italicized values correspond to the barriers and italicized values correspond to the hollow-top energy differences. Numerical values for transition state geometries of the other functionals are given in appendix C Table C.13.

Similar to top-bridge diffusion, the RPA transition state lies later along the top-hollow path than the PBE and BEEF-vdW transition state with $d_{CCu,\ xy}$ (the distance along the [110] direction from top to hollow site, see Fig. 4.2(d)) values of 1.08 Å for PBE, 1.44 Å for BEEF-vdW, and 1.57 Å (1.32 Å) for RPA with 15×15×1 k-point mesh (8×8×1 and 3×3×1 k-point meshes). The difference in transition state position, also significantly affects the transition state geometry, as shown in Fig. 4.6 and Fig. 4.7 (b). r_{CO} increases from 1.17 (PBE) and 1.18 Å (BEEF-vdW) to 1.19 Å (RPA), $d_{CCu,\ z}$ decreases from 1.44 and 1.30 Å to 1.20 Å, and θ_{OCz} increases from 163 and 170 ° to 174°. For adsorption in the hollow position, CO binds perpendicular to the Cu surface, and the geometry parameters are shown in Fig.

4.7 (c).

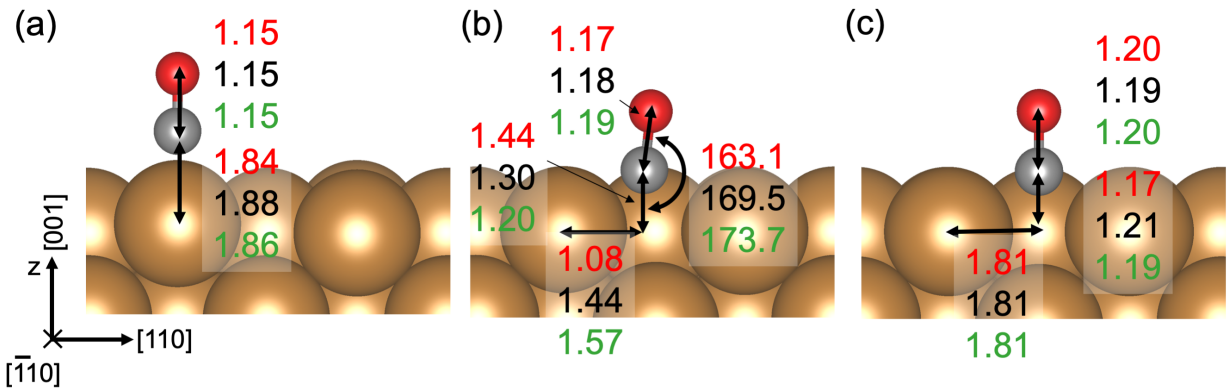

Figure 4.7: Structures along the [110] diffusion pathway. (a) Top site structure. (b) Transition state structure. (c) Hollow site structure. As defined in Fig. 4.2 (d), values are shown for r_{CO}, the distance between the C and O atom, $d_{CCu,\ z}$, the z coordinate difference between the C atom and the Cu(001) surface plane, $d_{CCu,\ xy}$, the distance between the C and bulk (fixed) Cu atom projected along the [110] direction, and θ_{OCz}, the angle spanned by the axis of the CO molecule and the [00$\bar{1}$] direction. Similar to the color scheme used in the energy profile, values shown in red, black, and green correspond to PBE, BEEF-vdW and RPA results. Presented numbers are given in Å for distances and degree for angles. Cu atoms are shown as brown, O atoms red and C atoms grey.

The results presented in this work agree with data in the literature that RPA is able to predict both, adsorption enthalpies and surface energies correctly, which is not achieved by the other functionals studied in this work. Additionally, RPA and HSE06 correctly predict the preference of CO adsorption in the top position of the Cu(001) surface, which is shared with the BEEF-vdW and RPBE functionals, even though the latter two methods show a smaller preference compared to the former methods. PBE based functionals and the SCAN functional, on the other hand predict the stabilization of CO in the bridge and hollow sites. Qualitatively, these results agree with the work of Schimka et al.[53], who showed that RPA correctly predicts CO adsorption on the top site on Cu(111), while for the (111) surface

PBE shows a preference for CO adsorption in the hollow site. In the following, we restrict the discussion of the diffusion barriers on PBE, BEEF-vdW and RPA, since they provide qualitatively different descriptions.

The impact of the difference in site preference on the diffusion behavior is significant and becomes apparent when studying the full energy profiles for diffusion along [100] and [110] directions from top to top position, as displayed in Figure 4.8. At the PBE level, the CO molecule is most of the time at the bridge site and we consider three diffusion pathways: (1) The bridge-top-bridge diffusion pathway in the [100] direction with a barrier of 60 meV. The top site is a local minimum with a barrier of 22 meV to leave it. (2) A bridge-hollow-bridge diffusion pathway in the [100] direction of the surface. (3) A direct bridge-bridge diffusion pathway generally along the [110] direction. We performed climbing image nudged elastic band (CI-NEB)[166] calculations to determine the barrier of pathways (2) and (3). A barrier of 50 meV is found for the bridge-hollow-bridge diffusion pathway and the energy profile is shown in appendix C Fig. C.4. No bridge-bridge diffusion along the [110] direction is found. Considering the barrier values at PBE level, bridge-hollow-bridge diffusion is favored.

At the RPA level, the CO molecule is most of the time at the top site, which agrees with experimental observations[167]. Diffusion along the [100] direction corresponds to a top-bridge-top path with a barrier of 125 meV and the bridge site is metastable, with a barrier of 18 meV to leave it. Diffusion in the [110] direction corresponds to a top-hollow-top path with a barrier of 250 meV, with a very shallow minimum at the hollow site: 5 meV is required to leave it. For both directions, the residence time in the intermediate position is very short, and the diffusion is effectively a single jump from top to top. Considering the barrier values at RPA level, two successive top-bridge-top diffusion processes will be more favored than one top-hollow-top diffusion process, which indicates that the diffusion in the [110] direction may correspond to two combined diffusion processes in perpendicular [100] and [010] directions.

Using the BEEF-vdW functional, the qualitative behavior is similar to the results at RPA level but the barrier values are significantly lower. Diffusion along the [100] direc-

tion corresponds to a top-bridge-top path with a barrier of 51 meV and the bridge site is metastable, with a barrier of 25 meV to leave it. Diffusion in the [110] direction corresponds to a top-hollow-top path with a barrier of 132 meV, with a very shallow minimum at the hollow site, where only 9 meV are required to leave it. However, at BEEF-vdW level, the THT barrier is still higher than the TBT barrier.

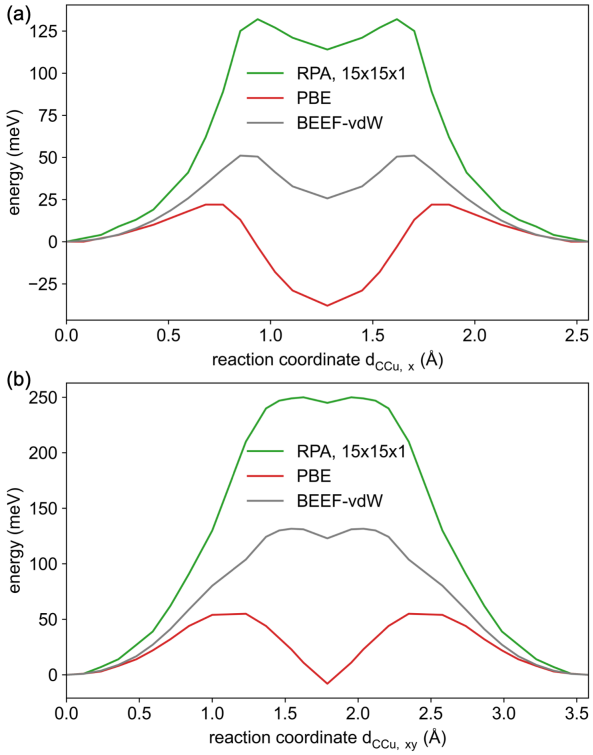

Figure 4.8: Full energy profile for PBE, BEEF-vdW and RPA for diffusion from top to top site along the [100] (a) and [110] (b) direction. PBE profile is shown as red, BEEF-vdW is shown as grey and RPA is shown as green.

Comparing our results to work in the literature is not entirely straightforward. Initial DFT calculations by Ge and King[137] show a very similar energy profile to our PBE calculations, while Fouquet et al.[138] found a significantly different behavior using localized basis sets, with a maximum at the bridge position, but a significantly lower diffusion barrier compared to this study. Marquardt et al.[139] used potential energy surface achieved by fitting DFT energies and observed a significantly narrower barrier compared to other works and to

this study, which lead them to the assumption that tunneling is a significant contributor to the diffusion processes. The shape of the barriers calculated using RPA in this work exclude significant contributions of tunneling to diffusion. The CO molecule would have to tunnel almost the entire distance between top sites along either direction, which is highly unlikely, due to the high mass of the molecule.

Experimental results for the diffusion barriers for CO on the Cu(001) surface are quite ambiguous. Initial measurements performed by Graham and Toennies[135] suggest a total diffusion barrier of 31±10 meV. However, more refined measurements in combination with molecular dynamic modeling by Alexandrowicz et al.[136] suggest two diffusion pathways with barriers of 135±20 meV along the [100] direction and 115±20 meV along the [110] direction. For the diffusion along the [100] direction RPA leads to quantitative agreement with experiment. At the same time, barriers for diffusion along the [110] direction calculated at BEEF-vdW level of theory show excellent agreement with experimental data. However, both methods agree on a roughly 1:2 ratio in diffusion barriers between the [100] and [110] directions. This disagrees with the observations of Alexandrowicz et al.,[136] which indicate a roughly 1:1 ratio between those two barriers.

To investigate this correlation more closely and understand whether a theoretical method exists that can reproduce a 1:1 ratio in barrier heights, we study the following three relationships, namely (i) energy differences between top/bridge and top/hollow sites, (ii) diffusion barrier in [100] direction and top/bridge energy difference, and (iii) diffusion barrier in [110] direction and top/hollow energy difference. We find that all three parameter groups follow linear relationships with R^2 values larger than 0.96 (see appendix C Fig. C.2). Using these relationships, it is now possible to plot forward and backwards barriers for diffusion in [100] and [110] direction with respect to the top/bridge energy difference. We find that no point exists, where a 1:1 ratio in activation energies in both diffusion directions can be found, when CO preferentially adsorbs in the top position (see appendix C Fig. C.3). Additionally, it is important to notice that the TBT barriers are always lower than the THT barriers, which disagrees with experimental findings.

The reasons for the discrepancy between experimental data and results from our study are not entirely clear. One potential reason for the mismatch is a difference in coverage. While our computational work focuses on a 2×2 unit cell with a coverage of θ=1/4 monolayers (ML), experimental results were measured for a coverage of θ=0.1 ML. Matching the experimental coverage would require modeling a 3×3 unit cell, which is beyond our current computational capability at RPA level. To estimate the impact of coverage effects, we extrapolated them based on the impact of PBE calculations by using

$$E^{RPA}(\theta = \frac{1}{x}ML) = E^{RPA}(\theta = \frac{1}{4}ML) + E^{PBE}(\theta = \frac{1}{x}ML) - E^{PBE}(\theta = \frac{1}{4}ML) \qquad (4.6)$$

The low coverage calculations are performed on 3×3 surface, $\theta = \frac{1}{9}$, and 4×4 surface, $\theta = \frac{1}{16}$. The results are shown in appendix C Fig. C.5. For the diffusion along the [100] direction, no significant changes are observed: the energetic differences are always smaller than 10 meV. For the diffusion along the [110] direction, coverage effects slightly decrease the barrier from 250 meV at $\theta = \frac{1}{4}$ to 232 meV at $\theta = \frac{1}{9}$ and 219 meV at $\theta = \frac{1}{16}$. Even though this change in energetics when extrapolating results to lower coverages is not sufficient to reach agreement between our calculations and experiments, coverage effects seem to lower barriers along the top-hollow-top pathway more than along the top-bridge top pathway. Additionally, the significant change of the TS position ($d_{CCu,\ xy}$ values from 1.62 Å to 1.37 Å) and the overall profile shape for diffusion along the [110] direction indicate that non-trivial coverage effects might exist. It is possible that these coverage effects cannot be fully captured at PBE level. In future work it will be interesting to see how the coverage effects are present at RPA level, which are not accessible for us at the moment due to the excessive computational cost. That being said, diffusion barriers still follow the linear trends discussed, which indicates that coverage effects cannot recover the behavior described by Alexandrowicz et al.[136]

Results presented in this work reveal a significant mismatch between all theoretical methods and experimental data. At this moment in time the source of this mismatch is not entirely clear. One possibility is that a non-trivial diffusion pathway in either direction has been missed in our study. Another possibility is that experimental measurements will need to be revisited and reinterpreted based on the findings in this work.

4.4 Conclusion

In this work we describe our efforts to model the diffusion of CO on the Cu(001) surface using RPA and compare the results with calculations using different GGA, metaGGA, and hybrid functionals. In a first step we present a k-space embedding strategy for RPA calculations, which significantly reduces the computational cost. We consider the adsorption enthalpies and surface energies using the aforementioned methods. Subsequently we apply this methodology to CO diffusion along two high-symmetry directions of the surface, namely (i) top-bridge-top diffusion along the [100] direction and (ii) top-hollow-top diffusion along the [110] direction. We find that RPA appears to be the only method giving the correct site preference and adsorption enthalpy for CO, and surface energy for Cu(001). DFT methods that give correct site preference (RPBE, BEEF-vdW, and HSE06) may suffer from underestimated surface energies. Our results furthermore reveal qualitative differences in the description of diffusion barriers compared to experiments. While RPA and BEEF-vdW are able to quantatively correctly predict one of the diffusion barriers, no functional reproduces the experimentally observed ratio for diffusion barriers. Since this is a phenomenon shared by all methods, we conclude that it might be necessary to revisit the interpretation of the experimental data.

The results presented in this work show that the incorrectly predicted adsorption site preference for CO on transition metal surfaces using different functionals can qualitatively and quantitatively alter predictions for diffusion pathways of CO on transition metal surfaces. It is well conceivable that similar differences exist for other reactions that involve CO on transition metal surfaces. The shortcomings of the functionals considered, especially the underestimated surface energies indicate that it is necessary to move to more accurate methods, such as RPA, when modeling adsorption across different species. We expect that the methods and results presented here will encourage further investigations on fundamental interactions between CO related species on transition metal surfaces, which are necessary to understand thermocatalytic and electrocatalytic reactions involving CO related species on Cu and other transition metal surfaces.

CHAPTER 5

Towards More Accurate Modelling of CO_2 Electroreduction Mechanism with Many-Body Perturbation Theory

5.1 Introduction

The electrochemical carbon dioxide reduction reaction (CO_2RR) has attracted tremendous interest[5, 168, 169] since its discovery by Hori et al[170]. After years, Cu remains the most important metal catalyst towards C_2 products[171, 172], including ethylene and ethanol, while other metal catalysts mainly produce formate (Pb, In, and Sn) or CO (Au, Ag, Zn, and Pd)[170]. Specifically, the Cu(100) facet has been reported to selectively produce C_2 products at low overpotentials[171]. Although tremendous efforts have been devoted to elucidating the reaction mechanism, the detailed reaction pathways, and especially the nature of the potential-determining step (PDS) are controversial from the experimental side due to limited *in situ* spectroscopy. Computational studies based on density functional theory (DFT) energetics have also been conducted to clarify the reaction mechanism but the conclusion is under debate as well. Regarding the critical C-C coupling step, Calle-Vallejo et al.[173] used the Perdew-Burke-Ernzerhof (PBE) functional[31] and concluded that the PDS is the hydrogenation of *OCCO, preceded by an OC-CO coupling. Montoya et al.[174] used the revised Perdew-Burke-Ernzerhof (RPBE) functional[142] with a charged explicit solvating water layer and concluded the OC-CO coupling to give *OCCO with a different structure compared to the one proposed by Calle-Vallejo et al.[173]. Peng et al.[175] used the Bayesian error estimation functionals[143] (BEEF) and found the step from *OCCO to *OCCOH to be

potential limiting at low overpotential and C-CO coupling to be favored at high overpotential. Regarding other facets, Liu et al.[176] used the BEEF and also found the OC-CO coupling followed by hydrogenation to *OCCOH to be favored on Cu(211). Hussain et al.[177] used the RPBE functional and found ethylene is formed by coupling two $*CH_2$ fragments on Cu(111).

Nevertheless, the aforementioned theoretical studies utilized exchange correlation (XC) functionals at the generalized-gradient approximation (GGA) level while it is difficult for such semi-local density functionals to give simultaneously correct CO adsorption energies and surface energies for Cu(111)[53] and (100) facets[178]. Functionals which describe CO adsorption strength accurately such as RPBE give surface energies[178] underestimated by over 0.5 J/m^2 (ca. 30% of experimental value as 1.8 J/m^2). In addition, all the semi-local functionals fail to predict the correct site for CO adsorption on both Cu(100) and Cu(111) facets, which is often referred to as the CO-adsorption puzzle[34]. These fundamental deficiencies of semi-local density functionals to describe CO adsorption and surface stability naturally raise the question regarding the accuracy of GGA functionals for the intermediate species involved in CO_2RR. This is especially crucial since conclusions on catalytic activity are often derived from the computed results that initial hydrogenation[179] and/or C-C coupling steps[174, 173, 180], involving formation steps of species as *COH, *CHO, *OCCO, *OCCOH, and *OCCHO, are the PDSs. Despite the chemical importance of the mechanistic conclusions taken using DFT-GGA calculations, there is no assessment, to our knowledge, of the accuracy of these exchange-correlation functionals for the CO_2 electrocatalytic reduction on the Cu(100) facet.

Therefore, to correctly describe the CO_2RR process, a method addressing all of the aforementioned issues is necessary. *Ad hoc* corrections[181, 182] do not serve the purpose as the values needed for the intermediates other than CO are generally unknown. Here we propose to consider the adiabatic connection fluctuation dissipation theorem[49, 50] (ACFDT) within the random phase approximation[47, 48] (RPA), which has been shown to simultaneously correctly describe the Cu(100) surface energy and the CO adsorption on Cu(100)[178]. It is

worth noting that the density functional embedding theorem (DFET) developed by Carter et al.[159] has achieved considerable success in describing both the CO adsorption[161] and recently the hydrogenation steps in CO_2RR[8]. The RPA method avoids the symmetry mismatch between the embedded cluster and the metallic surface faced in DFET, benefitting from the fact that an implementation for plane waves in periodic boundary conditions exists. Moreover, the implementation in periodic boundary conditions also gives great convenience to incorporate the existing implicit solvation models, while a explicit solvation description using high level methods requires excessive amount of resources and is hence not affordable. Here we show that it is natural and convenient to incorporate the implicit solvation effects, more specifically, by combining the linearized Poisson-Boltzmann (lPB) equation[80, 81] into the RPA frame. We apply this method to the CO_2RR on the Cu(100) facet, focusing on the CO hydrogenation and C-C coupling steps.

5.2 Methods

5.2.1 Random Phase Approximation

Here we briefly summarize the main formulas of the adiabatic connection fluctuation-dissipation theorem (ACFDT), and more details can be found in the following Refs[54, 49, 50, 55, 56]. Within the ACFDT formalism, the energy of an interacting system with electron density $n(\boldsymbol{r})$ is given by:

$$E[n] = T_{KS}[\{\psi_i\}] + E_H[n] + E_x[\{\psi_i\}] + E_{ion-el}[n] + E_c \tag{5.1}$$

with the kinetic energy term T_{KS} evaluated for the one- electron KS wave functions $\{\psi_i\}$, the Hartree energy $E_H[n]$, the exchange energy $E_x[\{\psi_i\}]$, the interaction between nuclei and electrons $E_{ion-el}[n]$, and the correlation energy E_c.

The ACFDT expression for the correlation energy E_c is:

$$E_c = \int_0^1 d\lambda \int_0^\infty \frac{d\omega}{2\pi} Tr\{\nu[\chi^\lambda(i\omega) - \chi^0(i\omega)]\} \tag{5.2}$$

with the coupling constant λ integrated over the difference between the frequency response

function of the λ-interacting system $\chi^{\lambda}(i\omega)$ and that of the non-interacting system, i.e., KS system, $\chi^{0}(i\omega)$, $i\omega$ the imaginary frequency, ν the Coulomb kernel.

The response function of the non-interacting system, $\chi^{0}(i\omega)$, is expressed as:

$$\chi^{0}_{\boldsymbol{GG'}}(\boldsymbol{q}, i\omega) = \frac{1}{V} \sum_{n,n',\boldsymbol{k}} 2g_{\boldsymbol{k}}(f_{n'\boldsymbol{k}+\boldsymbol{q}} - f_{n\boldsymbol{k}}) \times \frac{\langle \psi_{n'\boldsymbol{k}+\boldsymbol{q}} | \, e^{i(\boldsymbol{q}+\boldsymbol{G})r} \, | \psi_{n\boldsymbol{k}} \rangle \langle \psi_{n\boldsymbol{k}} | \, e^{-i(\boldsymbol{q}+\boldsymbol{G'})r} \, | \psi_{n'\boldsymbol{k}+\boldsymbol{q}} \rangle}{\epsilon_{n'\boldsymbol{k}+\boldsymbol{q}} - \epsilon_{n\boldsymbol{k}} - i\omega} \tag{5.3}$$

with reciprocal lattice vectors $\boldsymbol{G}$ and $\boldsymbol{G'}$, crystal momentum vector $\boldsymbol{k}$ which lies within the Brillouin zone of the primitive cell with volume V, reciprocal vector $\boldsymbol{q}$, k-point weights $g_{\boldsymbol{k}}$, the KS one-electron wave functions and energies of band n and crystal momentum vector $\boldsymbol{k}$ being $\psi_{n\boldsymbol{k}}$ and $\epsilon_{n\boldsymbol{k}}$, and the occupation number function $f_{n\boldsymbol{k}}$.

The response function of the λ-interacting system, $\chi^{\lambda}(i\omega)$ is calculated using the Dyson equation:

$$\chi^{\lambda}(\boldsymbol{q}) = \chi^{0}(\boldsymbol{q}) + \chi^{0}(\boldsymbol{q})[\lambda\nu(\boldsymbol{q}) + f^{\lambda}_{xc}(\boldsymbol{q}, i\omega)]\chi^{\lambda}(\boldsymbol{q}) \tag{5.4}$$

where the f_{xc} is the exchange-correlation kernel. The RPA refers to the treatment of choosing $f_{xc} = 0$.

In practice, the first four terms in Eq. 5.1 are calculated within a Hartree-Fock step based on DFT orbitals and can be combined into a E^{EXX} notation, and the RPA energy in vacuum can be expressed as:

$$E^{RPA} = E^{EXX}([\psi_{occ,vacuum}]) + E^{RPA}_{c}([\psi_{occ,vacuum}, \psi_{uocc,vacuum}]) \tag{5.5}$$

where ψ_{occ} and ψ_{uocc} denotes the occupied and unoccupied orbitals, respectively. We add the vacuum notation to distinguish these orbitals from the orbitals with the presence of implicit solvation, which is discussed in the next section.

5.2.2 RPA with Implicit Solvation

It is worth noting that the correlation energy, $E^{RPA}_{c}([\psi_{occ}, \psi_{uocc}])$, is completely determined by the orbitals.

Firstly, the orbitals with the presence of solvation effects at the DFT level can be achieved

using the linearized Poisson-Boltzmann equation, as implemented by Hennig et al.[80, 81]. We list briefly the the main formulas here and further details can be found in Refs.[80, 81] The linearized Poisson-Boltzmann equation refers to:

$$\vec{\nabla} \cdot \epsilon \vec{\nabla} \phi - \kappa^2 \phi = -\rho_{solute} \tag{5.6}$$

ϵ is the relative permittivity of the solvent as a local functional of the electronic charge density. The total solute charge density, ρ_{solute}, is the sum of the solute electronic and nuclear charge densities, $n(\boldsymbol{r})$and $N(\boldsymbol{r})$, respectively:

$$\rho_{solute}(\boldsymbol{r}) = n(\boldsymbol{r}) + N(\boldsymbol{r}) \tag{5.7}$$

κ is determined by the Debye screening length λ_D and the the shape function $\zeta[n(\boldsymbol{r})]$, which is designed to modulate in the interface region:

$$\kappa^2 = \zeta[n(\boldsymbol{r})] \frac{1}{\lambda_D^2} \tag{5.8}$$

The occupied orbitals with presence of implicit solvation effects, $\psi_{occ,solvation}$, are thus obtained. The unoccupied ones, $\psi_{uocc,solvation}$, can be achieved by a diagonalization step, as done in typical RPA calculations. Starting from these orbitals, and also adding in the solvation energy based on the electron density, which is determined by the occupied orbitals, the RPA energetics incorporating implicit solvation effects are achieved. we named it as RPA-sol:

$$E_{sol}^{RPA} = E^{EXX}([\psi_{occ,solvation}]) + E_c^{RPA}([\psi_{occ,solvation}, \psi_{uocc,solvation}]) + E^{solvation}([\psi_{occ,solvation}]) \tag{5.9}$$

where the solvation energy $E^{solvation}([\psi_{occ,solvation}])$ the solvation energy obtained in the non-self consistent HF step, and essentially this term only depends on the charge density. Nevertheless, the RPA-sol energy is not simply the vacuum RPA energy plus this solvation energy: the orbitals with the presence of implicit solvation, $\psi_{occ/uocc,solvation}$, gives nontrivial contribution to the exchange and correlation components in the RPA-sol energy as well:

$$\begin{aligned} &E^{EXX}([\psi_{occ,solvation}]) + E_c^{RPA}([\psi_{occ,solvation}, \psi_{uocc,solvation}]) \neq \\ &E^{EXX}([\psi_{occ,vacuum}]) + E_c^{RPA}([\psi_{occ,vacuum}, \psi_{uocc,vacuum}]) \end{aligned} \tag{5.10}$$

5.2.3 Computational Setup

All calculations in this paper were performed using the Vienna Ab-Initio Simulation Package[76] (VASP). All the DFT calculations were developed on a basis set of plane waves with a cutoff energy as 550 eV. Core electrons were described with the projector augmented wave (PAW) method. Second order Methfessel-Paxton smearing with sigma value of 0.2 eV was used for all DFT slab optimizations and Gaussian smearing with sigma value of 0.05 eV was used for molecular references. For all the steps involved in RPA calculations, Gaussian smearing with sigma value of 0.05 eV was used.

The slab calculations were performed in a 3×2 unit cell of a three layer slab. We use the experimental lattice constant of 3.615 Å[163] for all the functionals. This value is a good compromise between the PBE value, 3.629 Å and the RPA value, 3.581 Å[53]. This choice ensures that the RPA calculations can use the PBE optimized structures. Repeated images of the slabs are separated by 13 Å (16 Å) for RPA (and DFT). For DFT calculations, we have performed tests using a vacuum thickness of 21 Åand found that the energetic difference is smaller than 1 meV. For RPA calculations, Lébegue et al.[164] have shown that the correlation energy uncertainty is ca. 0.2 meV for vacuum separations larger than 13 Å. In DFT calculations, dipole corrections were applied. In the optimization process, the bottom layers of Cu atoms is kept fixed and the top two layers are relaxed and a 6×8×1 k-point mesh was used. Structural convergence was assumed for forces lower than 0.01 eV/Å.

5.3 Results and Discussion

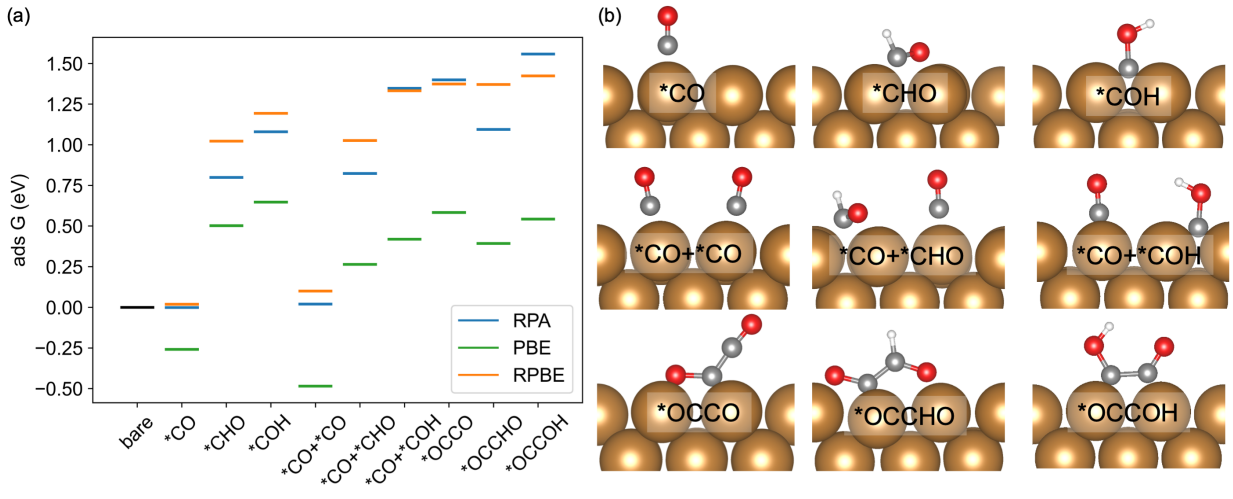

Figure 5.1: (a) Energetics of CO_2RR intermediates considered, *CO, *CHO, *COH, *CO+*CO, *CO+*CHO, *CO+*COH, *OCCO, *OCCHO, and *OCCOH, using RPA and PBE/RPBE functionals at the Cu(100)-vacuum interface. (b) Side view of the atomic structures. For adsorbates with multiple possible sites, energetics are considered for the one with the most stable RPA energy. Cu atoms are shown as brown, O atoms red, C atoms grey, and H atoms white.

Fig. 5.1 shows the RPA energetics of the considered intermediate species, *CO, *CHO, *COH, *CO+*CO, *CO+*CHO, *CO+*COH, *OCCO, *OCCHO, and *OCCOH, in comparison with PBE/RPBE energetics at the Cu(100)-vacuum interface. The energetics are presented following the computational hydrogen electrode (CHE) framework[183], with a potential of at 0 V vs RHE. The PBE energetics show a severe overbinding by 0.25 to 0.5 eV per CO component, in line with the reported overestimation of the CO adsorption strength.[53, 178] In the work of Calle-Vallejo et al.[173], a 0.24 eV correction per CO was applied and this turns to be generally working for *CO, *CO+*CO, and *CHO. However, for all the *COH related adsorbates and coupled adsorbates including *OCCO, *OCCHO, and *OCCOH, this correction appears to be still markedly insufficient. On the other hand, the RPBE energetics show a significant underbinding for most intermediates, consistent with the

underestimated Cu(100) surface energy. It is worth mentioning that for the co-adsorption structures, *CO+*CO and *CO+*CHO, we found the top site CO to be more stable than bridge site CO, in contrast to the PBE prediction due to the known site error (CO puzzle). For the case of *CO+*COH, the top site minimum is not locally stable and was optimized to bridge site CO using DFT methods and we just use this structure. We leave the discussion of detailed energetics to the next paragraph after solvation effects are considered.

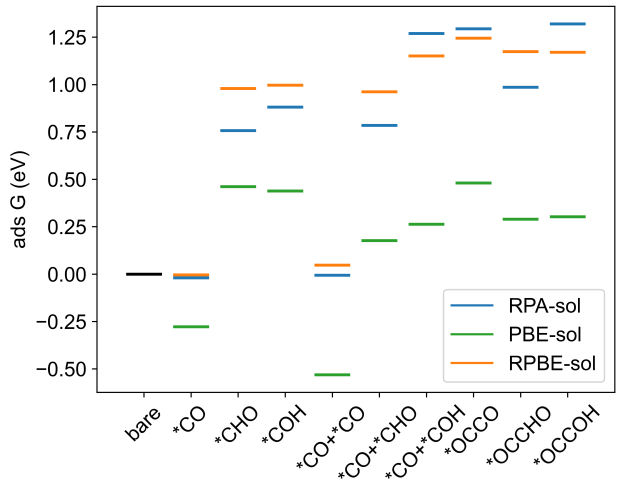

Figure 5.2: Implicitly solvated energetics of CO_2RR intermediates considered, *CO, *CHO, *COH, *CO+*CO, *CO+*CHO, *CO+*COH, *OCCO, *OCCHO, and *OCCOH, using RPA and PBE/RPBE functionals on Cu(100). The methods are termed as -sol to be distinguished from the vacuum energetics.

The solvation effects are critical for the CO_2RR while the explicit solvation is rather computationally expensive and hence beyond our current computational capability at the RPA level. Therefore, we combine the implicit solvation method, more specifically, the implementation of the lPB equation by Hennig et al.[80, 81], into the RPA frame, named as RPA-sol. The RPA-sol energetics are shown in Fig. 5.2, in comparison with implicitly solvated PBE-sol and RPBE-sol energetics. While PBE-sol and RPBE-sol predict similar stability for hydrogenated *CHO and *COH species, RPA-sol predicts *CHO to be 0.12 eV more stable, in line with the results on Cu(111) using DFET[8]. A similar yet more significant phenomenon is observed for the coupling intermediates, *OCCHO and *OCCOH:

RPA-sol energetics show that *OCCHO is stabilized by 0.34 eV compared to *OCCOH, while RPBE-sol and PBE-sol show similar stability for these two intermediates.

The implicit solvation can be further improved as the lPB equation does not account for the hydrogen bonds. Therefore, as shown in the appendix D.3, we compare different existing explicit solvation treatments[176, 175, 184, 185, 186], and some studies[176, 175, 186, 177] found the solvation energies of *OCCOH and *OCCHO are close. Among all the treatments considered, the treatment of Calle-Vallejo et al.[173] relatively stabilizes *OCCOH the most, with a stabilization of 0.38 eV for the COH part in *OCCOH and 0.10 eV for the CHO part in *OCCHO. Using this treatment, corresponding to an extra 0.16 eV stabilization for *OCCOH compared to *OCCHO on implicit solvation energetics, RPBE and PBE both predict *OCCOH to be more stable while RPA still predicts *OCCHO to be more stable by 0.18 eV, leading to the PDS changing from the formation of *OCCOH with RPBE or PBE to the formation of *OCCHO with RPA. It is also worth mentioning that, considering the dynamic water structure with molecular dynamic simulations, Heenen et al.[185] found that the solvation is considerably weaker than that of the static water treatment considered in most publications, which means that the implicit solvation might underestimate the solvation less than found when comparing with the static explicit solvent calculations.

Adsorbate-adsorbate interactions can potentially play a role, and we have performed test calculations to evaluate them (appendix D.4). We found the effect of adsorbate-adsorbate interactions on adsorption energies on the Cu(100) surface to be small when the CO coverage is below 0.5 ML, which is the highest coverage found from experiments[187] or kinetic modeling[176]. Hence, adsorbate-adsorbate interaction can be neglected in the current study. We have also considered the energetics of the further hydrogenation products along the C_1 pathway, *CHOH and *CH_3, as shown in the appendix D Fig. D.3, and no qualitative difference was found between RPA energetics and GGA DFT energetics. Based on this finding and the conclusion of previous studies[188, 173, 174], we do not focus on further hydrogenation products along the C_2 pathway.

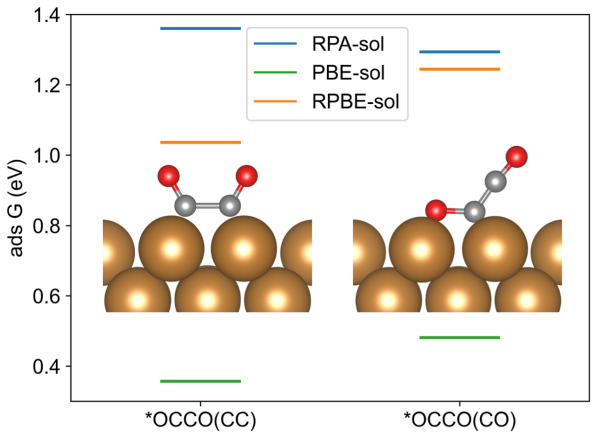

Figure 5.3: Implicitly solvated energetics of the *OCCO intermediate, considered for both the structure proposed by Calle-Vallejo et al.[173], *OCCO(CO) (right) and the structure proposed by Montoya et al.[174], *OCCO(CC) (left), using RPA and PBE/RPBE functionals. Side view of the atomic structures is presented as well, with Cu atoms shown as brown, O atoms red, C atoms grey, and H atoms white.

Among the C-C coupling intermediates, the *OCCO intermediate is involved in different mechanisms proposed using DFT energetics while being specifically controversial: Calle-Vallejo et al.[173] proposed a *OCCO structure binding with the Cu surface using one C atom and one O atom (denoted as *OCCO(CO) hereinafter), whereas Montoya et al.[174] found that an electric field or a charged water layer can stabilize the *OCCO binding with two C atoms (denoted as *OCCO(CC) hereinafter). Later Goodpaster et al.[189] reported that the *OCCO(CC) structure can also be obtained by charging the system, i.e., using a grand-canonical DFT treatment with implicit solvation. Essentially all these treatments apply extra electron density to stabilize the *OCCO(CC) intermediate. Here we investigate the energetics of both structures and results are shown in Fig. 5.3. The *OCCO(CC) structure is obtained by charging the surface using PBE-sol and RPBE-sol, respectively, while the reported energetics correspond to the single point energy calculated at neutral number of electrons. Interestingly, we find that RPBE-sol and PBE-sol show a significant stabilization of the *OCCO(CC) structure, 0.21 eV and 0.12 eV, respectively; RPA-sol, on the other

hand, predicts the *OCCO(CO) structure to be 0.07 eV more stable. More importantly, the over-stabilization of *OCCO(CC) using GGA energetics casts doubt on the proposed mechanism involving formation of *OCCO(CC) by *CO coupling[174].

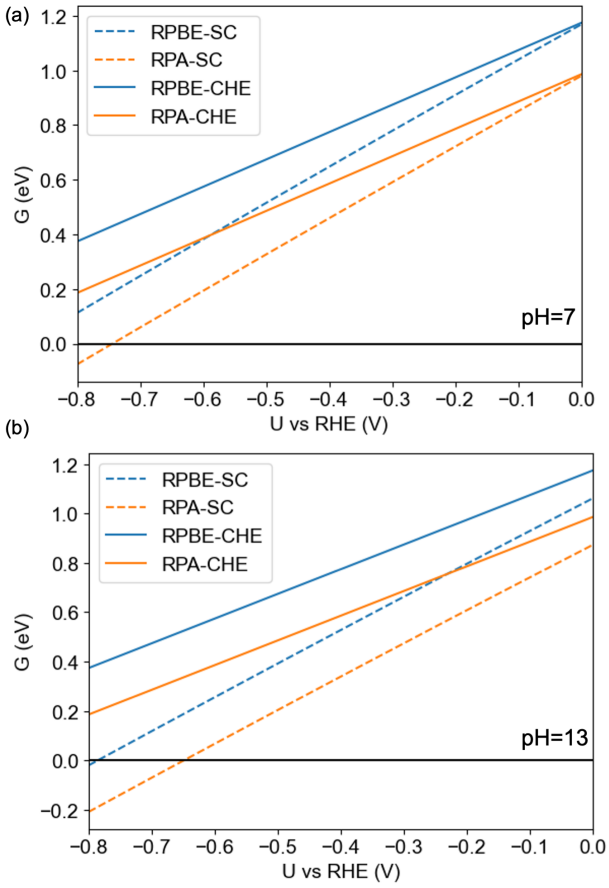

Figure 5.4: Potential dependent adsorption free energy of *OCCHO and predicted onset potential of ethylene production, using RPA and RPBE energetics, at condition of (a) pH=7 and (b) pH=13. The potential effects are treated at both the CHE and the SC level, with RPA-SC energetics being extrapolated as described in Eq. 5.11. The crossing point with the horizontal black line indicates the onset potential.

We then move to the predicted onset potential for ethylene formation considering different coupling species as the PDS. Here, the RPA-sol energetics with CHE treatment, as shown in Fig. 5.2, suggest the formation of *OCCHO by coupling of *CO and *CHO to be the PDS, whereas the predicted onset potential, -0.98 V, appears to be too negative

compared to experimental value[171], -0.4 V. The predicted onset potential for RPBE-sol is even more negative. We found a considerable amount of mismatch originating from the CHE treatment, as it lacks the description of the surface capacitance and the potential of zero charge. Therefore, we turn to the grand-canonical DFT treatment, namely, the surface charging (SC) method[190, 191, 81], which correctly accounts for these effects. The fully grand canonical treatment at the RPA level, namely RPA-SC, is not available yet so we present the extrapolated RPA-SC energetics using RPA-CHE, RPBE-SC, and RPBE-CHE energetics, as the RPBE-sol energetics are more similar to RPA-sol ones than PBE-sol ones:

$$G^{RPA-SC}_{extrapolated}(U) = G^{RPA-CHE}(U) + G^{RPBE-SC}(U) - G^{RPBE-CHE}(U) \tag{5.11}$$

As shown in Fig. 5.4, at the RPBE level, the onset potential changes significantly from $U^{RPBE-CHE}_{onset} = -1.17V$ to $U^{RPBE-SC}_{onset} - 0.88V$. The calculated capacitance and potential of zero charge values using the RPBE functional are provided in the appendix D Table D.12, and match well with the experimental values. After applying this correction to RPA energetics, we get $U^{RPA-SC,extrapolated}_{onset} = -0.74V$, which is significantly lower than $U^{RPA-CHE}_{onset} = -0.98V$ and matches closer with the experimental value, -0.4 V at the condition of pH=7. The difference between $U^{RPA-SC,extrapolated}_{onset}$ and $U^{RPBE-SC}_{onset}$, 0.14 V, is not simply the difference between $U^{RPA-CHE}_{onset}$ and $U^{RPBE-CHE}_{onset}$, 0.19 V: in the SC treatment, the surface capacitance is determined *ab initio*, leading to a non-zero quadratic term in the calculated G-U relationship. This term also naturally predicts correctly the pH dependence of the onset potential: the RPA onset potential changes from $U^{RPA-SC,extrapolated}_{onset} = -0.74V$ to $U^{RPA-SC,extrapolated}_{onset} = -0.65V$ when pH is changed from 7 to 13, matching well with the experimental shift of 0.1 V. Additionally, the solvation treatment can be improved by including a correction for explicit solvation effects: if the solvation corrections of Liu et al.[176] is applied, an onset potential of -0.45 V is obtained, matching very well with the experimental value of -0.4 V. The match of onset potential is hence comparable with the value for the *OCCOH pathway, OC-CO coupling followed by hydrogenation, achieved by Calle-Vallejo et al.[173] with PBE energetics, -0.4 V for Cu(100).

We have further checked the predicted onset potential for ethylene, assuming formation

of *OCCO (CC), *OCCO (CO), and *OCCOH by OC-CO, OC-CO, and OC-COH coupling as the PDS and extrapolated RPA onset potentials are found to be more negative than in the case of *OCCHO (appendix D.6). Therefore, we conclude that the formation of *OCCHO by OC-CHO coupling is the PDS. Considering the more negative predicted onset potentials using *OCCO (CC) and *OCCO (CO) as intermediate, our results suggest that *OCCHO is formed by the coupling of *CO and *CHO, which is often overlooked in DFT studies due to the underbinding of CHO related species. Experimentally, Hori et al.[192] and Koper et al.[171] have shown that the pH dependence is different for C_1 and C_2 pathways. Koper's analysis[193] shows that the pH dependence of the CO_2RR on the RHE scale suggests that the rate determining step does not involve a proton transfer. This is usually interpreted as a coupling between two *CO adsorbates being rate determining but the coupling of *CO and *CHO proposed here as rate determining also satisfies this constraint[189] and hence agrees with experimental results. Moreover, using *in situ* Fourier transform infrared spectroscopy, Koper et al.[194] observed vibrational frequencies of 1191 cm^{-1} and 1584 cm^{-1} and found the vibrational frequencies of *OCCOH to be compatible. We found that *OCCHOH, the further hydrogenation product of *OCCHO, gives frequencies of 1186 cm^{-1} and 1534 cm^{-1}, indicating the *OCCHO pathway can also be compatible with the experimental observations. Moreover, we would like to note that the current treatment assumes that the kinetics are in line with the thermodynamics. A more comprehensive approach requires to calculate the reaction barriers and can be combined with micro-kinetic modeling, allowing better comparison with experimental results[176, 177, 175]. However, the atomic forces at the RPA level for slabs are beyond our current computational power and these aspects may be included in the future.

5.4 Conclusion

To summarize, our results clearly show qualitative and quantitative differences between the more accurate RPA energetics and the PBE/RPBE results, as well as the previous studies using the semi-local density functionals. Formation of *OCCHO by coupling *CO and *CHO is proposed as the PDS, yielding onset potential matching very well with experimental value

and satisfying the observation that the rate determining step does not involve a proton. The shortcomings of the semi-local XC functionals suggest that interpretation based on DFT energetics may need to be more cautious, and it is important to consider the difference between these functionals and more accurate methods like RPA or DFET, when modeling CO_2RR which involves adsorption across various species. The success of combining implicit solvation into the RPA framework is also encouraging for a direct grand canonical treatment at the RPA level.

CHAPTER 6

Modeling Electrochemical Processes with Grand Canonical Treatment of Many-Body Perturbation Theory

6.1 Introduction

Electrocatalysis is at the heart of various sustainable energy conversion and storage technologies[7], such as water splitting[195], fuel-cells[196], and CO_2 conversion[197, 198]. The electrochemical reactions involved in these processes, including carbon dioxide reduction reaction (CO_2RR), hydrogen evolution reaction (HER), oxygen reduction reaction (ORR), etc., happen at solid-liquid interfaces in the presence of an applied electric potential[81]. For the first principles based atomic scale modeling of such electrocatalytic processes, explicitly including the effects of the applied potential have been shown to be essential: the constant electrode potential (CEP) model is found to qualitatively change results and match better with experiments compared to the simpler constant charge model[199, 189, 200]. At the same time, the CEP model requires grand canonical density functional theory[28, 27] (GC-DFT) calculations, i.e., explicitly changing the number of electrons to tune the electrode potential[201, 189, 190, 81].

The aforementioned studies, however, are based on the DFT energies obtained at the generalized gradient approximation (GGA) level. GGA functionals are known to sometimes lead to qualitative and quantitative errors in the description of molecular adsorption. One important example of this shortcoming is the CO adsorption puzzle[33, 34, 35]: GGA functionals incorrectly predict the preference for adsorption in the face center cubic (FCC) site

on the (111) facets and the hollow site on the (100) facets instead of the experimentally determined adsorption in the on top position and overestimate the adsorption energy. The random phase approximation[47, 48] (RPA), a post Hartree-Fock (HF) method based on the many-body perturbation theory[49, 50], has been shown to give a correct description of CO adsorption on various metal surfaces, including copper (Cu)[53, 178]. Additionally, the metal surface energies are described accurately using this method. These two aspects are essential to correctly describe the adsorption energies of adsorbates involved in CO_2RR[192, 171]. Therefore, the combination of the grand canonical treatment with RPA energetics appears as an appealing solution to correctly describe both the molecule-surface interaction[202] and the potential effects. To the best of the authors' knowledge, currently implementations of RPA using periodic boundary conditions are non-self-consistent. Hence the typical approach of grand canonical DFT treatment, which relies on the Fermi level obtained from self-consistent electronic structure calculations, cannot be directly applied.

In this work we develop an alternative approach, which is purely based on the system's energy and can be used to determine the Fermi level via a partial derivative of the energy with respect to the number of electrons. We show that at the DFT level, this approach is equivalent to using the Fermi level value obtained from self-consistent electronic structure calculations. We furthermore demonstrate how this energy based approach can be used to perform grand canonical RPA (GC-RPA) calculations. We then apply this method to the potential dependent adsorption of carbon monoxide (CO) on Cu(100), and show that GC-RPA calculations lead to a qualitatively different description of this process compared to results obtained at the GGA level of theory, performed using the Perdew-Burke-Ernzerhof[31] (PBE) and revised Perdew-Burke-Ernzerhof[142] (RPBE) functionals. These GC-RPA results match better with experimental evidences compared to GC-DFT and illustrate that the grand canonical treatment at the RPA level is a powerful tool to deepen our understanding of interfacial electrochemical phenomena.

6.2 Methods

6.2.1 Theory

We briefly summarize the RPA energy formulas here, and more details can be found in the literature[54, 49, 50, 55, 56]. The total RPA energy consists of the exact exchange (EXX) component, i.e., Hartree-Fock (HF) exchange, calculated for the occupied orbitals and the RPA correlation component based on both the occupied and unoccupied orbitals:

$$E^{RPA} = E^{EXX}([\psi_{occ}]) + E_c^{RPA}([\psi_{occ}, \psi_{uocc}]) \tag{6.1}$$

To apply the grand canonical treatment for electrochemical purposes, we need to account for the implicit solvation in the RPA framework. We account for the presence of solvation effects at the DFT level by computing orbitals combining the linearized Poisson-Boltzmann equation, as implemented by Hennig et al.[80, 81] in VASP.[76] Starting from these orbitals $(\psi_{occ,solvation}, \psi_{uocc,solvation})$, we add the solvation energy based on the electron density, which is determined by the occupied orbitals, to the RPA total energy expression. The RPA energy, which incorporates implicit solvation effects, is then expressed as:

$$E_{sol}^{RPA} = E^{EXX}([\psi_{occ,solvation}]) + E_c^{RPA}([\psi_{occ,solvation}, \psi_{uocc,solvation}]) + E^{solvation}([\psi_{occ,solvation}]) \tag{6.2}$$

where the solvation energy $E^{solvation}([\psi_{occ,solvation}])$ is obtained in the non-self-consistent HF step and only depends on the charge density.

The details of GC-DFT can be found in the literature[190, 191, 81] and we summarize the most important procedures as follows. The net number of electrons, $n_{surface}$, is calculated as:

$$n_{surface} = N_{surface} - N_{surface,neutral} \tag{6.3}$$

where $N_{surface}$ is the number of electrons of the surface system and $N_{surface,neutral}$ is the number of electrons in the neutral, i.e., non-charged, state. The DFT energy for charged states is, in this context, obtained as:

$$E_{surface} = E_{surface,raw} + \epsilon_{Fermi\ shift} n_{surface} \tag{6.4}$$

where $E_{surface,raw}$ is the "raw" energy printed by VASP and $\epsilon_{Fermi\ shift} n_{surface}$ is the necessary[81] correction term accounting for the difference ($\epsilon_{Fermi\ shift}$) in the reference energy of the electron between the "internal" reference level and vacuum. Then the grand canonical electronic energy of a surface model, $G(U_{vac})$, is obtained as:

$$G(U_{vac}) = E_{surface} - n_{surface}\mu_{electron} \tag{6.5}$$

where the chemical potential of an electron, is determined as:

$$\mu_{electron} = qU_{vac} = -eU_{vac} \tag{6.6}$$

where U_{vac} is the potential of the system with reference to the vacuum level and q is the charge of an electron. The potential of the system with reference to the vacuum can be determined using two components in the implementation of Hennig et al.[80, 81]: the Fermi level (ϵ_F) with reference to the "internal" zero energy reference and the Fermi shift which is the difference between the "internal" energy reference and the vacuum level:

$$-eU_{vac} = \epsilon_F + \epsilon_{Fermi\ shift} \tag{6.7}$$

We call this the "SCF approach" herein. In the current implementation of RPA in periodic boundary conditions, the RPA energy is a single shot energy based on underlying DFT orbitals and one-electron energies. Therefore, the self-consistent electronic structure, and hence the self-consistent Fermi level, are not available. As a consequence, the "SCF approach", which uses ϵ_F in Eq. 6.7, cannot be directly applied at the non-self-consistent RPA level. To circumvent this fundamental difficulty, we propose to use an alternative approach, which we call the "energetic" approach and does not require the self-consistent electronic structure. Combining Eq. 6.6 and Eq. 6.7 with the relationship of internal energy E and chemical potential μ in thermodynamics, we have:

$$\epsilon_F = \mu_{electron} - \epsilon_{Fermi\ shift} = \frac{\partial E_{surface}}{\partial n_{electron}} - \epsilon_{Fermi\ shift} = \frac{\partial E_{surface,raw}}{\partial n_{electron}} \tag{6.8}$$

After calculating a series of RPA energies with different number of electrons and performing a quadratic fitting of the $E(n_{surface})$ relationship[81], the Fermi level values can be obtained analytically as a linear function of $n_{surface}$.

It is worth mentioning that for metallic systems the free electronic energy G in GC treatments exhibits a quadratic behavior around the potential of zero charge (PZC), U_0:

$$G(U) = G(U_0) - \frac{1}{2}C(U - U_0)^2 \tag{6.9}$$

where C is the capacitance of the model and the PZC, U_0, is the potential of the neutral, i.e., non-charged system. The PZC can be viewed as the work function of the solvated system as it describes the process of taking one electron from the Fermi level of the neutral system to the vacuum level.

The potential of the system with respect to the standard hydrogen electrode (SHE) can be converted from U_{vac} as:

$$U_{SHE} + \Delta U_{SHE} = U_{vac} \tag{6.10}$$

with the IUPAC recommended value of $\Delta U_{SHE} = 4.44$ V.

6.2.2 Computational Setup

All the calculations in this work were performed with the VASP code[76]. We set the structural convergence criterion for forces to 0.01 eV/Å. Gaussian smearing with a sigma value of 0.05 eV was used for all the geometry optimizations. 5 layer models were used for all the systems as our tests show that the difference between 5 layer model and 6 layer model is smaller than 5 meV.

Gaussian smearing with a sigma value of 0.01 eV was used for the RPA steps, since our tests in a related system (graphene) shows the smaller sigma value (compared to more typically value of 0.05 eV) generally gives better quadratic behavior. We have tested the difference between RPA energetics achieved using sigma values of 0.01 eV and 0.05 eV and found the difference to be smaller than 5 meV. The RPA energetics were based on PBE optimized structure with RPA lattice parameter. The RPA energetics were performed using PBE orbitals and PBE one-electron energies (RPA@PBE), and it has been shown that RPA@RPBE gives essentially the same energetics.[178] The k-point meshes used and excitation cutoff energy benchmark are provided in appendix E.

6.3 Results and Discussion

In a first step, we show that, at the DFT level (exemplified using the PBE functional here), the energetic approach developed here is equivalent to the commonly used SCF approach. Here we consider a 5 layer slab exposing the 1×1 Cu(100) facet with CO adsorbed on the atop site. As shown in Fig. 6.1 (a), the Fermi level values obtained using these two different approaches agree excellently with each other. Consequently, the quadratic relationship between the electronic free energy G and the potential U, and further the adsorption energy, are found to agree very well for these two approaches. Differences in the adsorption energy over the potential range considered here, -1 to 0 V vs SHE, is smaller than 2 meV. The Fermi level and G(U) parabola comparison between the two approaches for the bare Cu(100) facet is provided in appendix E.2

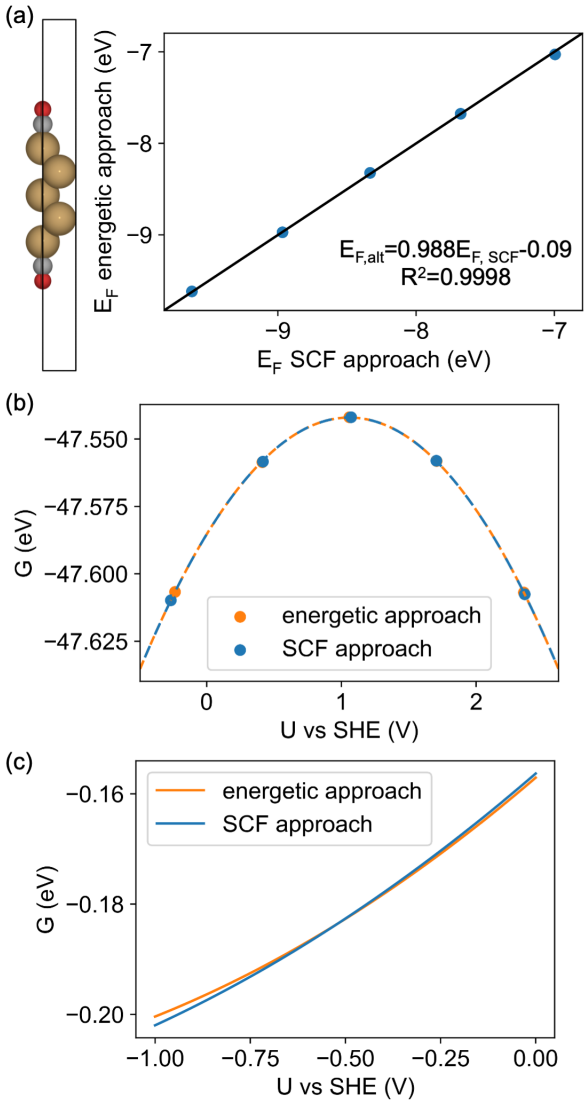

Figure 6.1: (a) Fermi level E_F values at the GGA level obtained using the energetic approach developed in this work compared to the ones taken directly from the SCF electronic structure. The blue dots are the data and the black line indicates a perfect match. The corresponding unit cell structure, a 5 layer slab exposing 1×1 Cu(100) facet with CO adsorbed on the atop site, is shown. Cu atoms are shown as brown, O atoms red, and C atoms grey. (b) The potential dependent free energy of the adsorbed CO system calculated using the energetic approach compared to the results using the SCF approach. Dots are data points and dashed lines are the fitted parabola. (c) The potential dependent adsorption energy of CO in the atop site calculated using the energetic approach compared to the results using the SCF approach.

Having this energetic approach validated at the DFT level, the grand canonical treatment can be further applied to the RPA energetics. We considered a series of different metal facets, the (100), (110), and (111) facets of Cu, Ag, and Au, and test whether the quadratic relationship established in Eq. 6.9 is correctly captured. Indeed, we find that the expected quadratic relationship is achieved for each of these facets. As an example, the quadratic relationship of the Cu(100) facet is shown in Fig. 6.2 (a). The quality of the quadratic relationship is indicated by the good match of PZC estimated from the parabola and the one of the neutral system, i.e., the data point at the apex. It is worth mentioning that using the Fermi level values of the underlying PBE orbitals cannot give the expected behavior around the PZC, as shown in appendix E.3. The quadratic relationship around the PZC indicates that the correct values of the Fermi level are achieved and thus validates our energetic approach. The comparison between the GC-RPA and experimental PZC values is shown in Fig. 6.2 (b).

Using the least square fitting with a fixed slope of 1, we obtained a ΔU_{SHE}^{pred}=5.31 V. Compared to the IUPAC recommended value, 4.44 V, RPA seems to overestimate PZC values. The magnitude of the overestimation is, however, unclear, considering that experiments show a large error bar[203, 204] ($\pm$0.5 V) and that a recent report[205] indicates that the work function of the SHE might be significantly higher. Moreover, a certain extent of overestimation is not entirely surprising, as it has been shown that non-self-consistent RPA (RPA@TPSS) overestimates the ionization potentials for molecules[206]. As we mentioned previously, the PZC, which is directly linked with the work function, serves as an analog to the ionization potential: these energies describe the process of taking one electron from the HOMO or Fermi level to the vacuum level, in the molecular or periodic systems, respectively. It is worth mentioning that the accuracy of molecular properties using RPA methods can be further improved when self-consistent approaches are used[207] and the work function overestimation here may be mitigated as well.

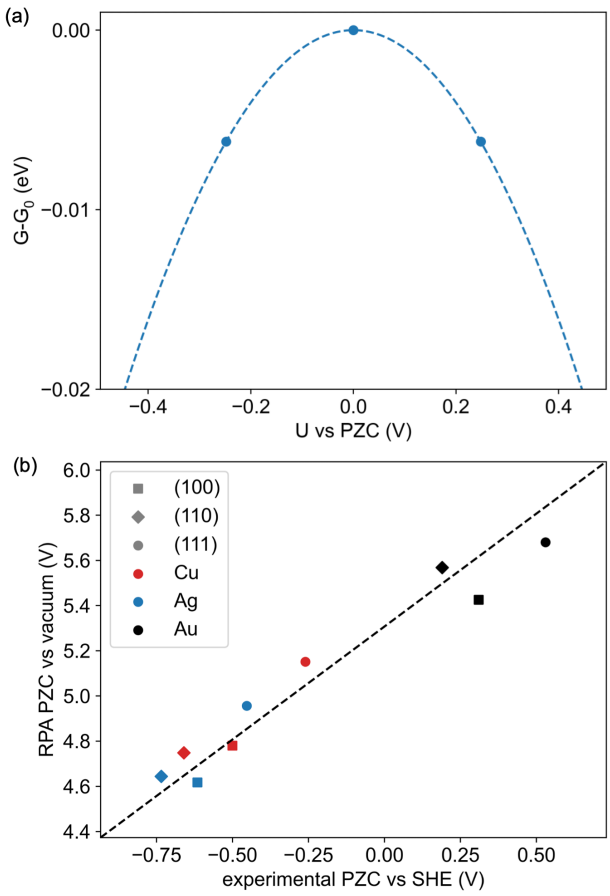

Figure 6.2: (a) The quadratic relationship between the GC-RPA electronic free energy and the potential of the system of a Cu(100) facet model. (b) Comparison between the computed RPA and the experimental potential of zero charge (PZC) values with respect to the standard hydrogen electrode (SHE). The dashed line is a fit of $U_{vac}^{pred} = U_{SHE}^{exp} + \Delta U_{SHE}^{pred}$ to determine the theoretical potential of the SHE versus vacuum, here found to be 5.31 V at the GC-RPA level. The experimental values are taken from literature and the detailed values are listed in appendix E Table table E.4.

We further applied this method to the potential dependent adsorption of a CO molecule on the Cu(100) facet comparing the top and hollow adsorption site, as shown in Fig. 6.3. A 5 layer slab exposing a $\sqrt{2} \times \sqrt{2}$ Cu(100) facet was considered, as this corresponds to the experimentally observed 0.5 monolayer coverage. Experimentally, at -0.9 V vs SHE, CO adsorption in the atop site is still preferred (indicated by the frequencies over 2000

cm^{-1}), forming a $\sqrt{2} \times \sqrt{2}$ pattern. The IUPAC recommended ΔU_{SHE}^{pred}=4.44 V was used here for all the methods and the version with fitted ΔU_{SHE}^{pred}=5.31 V for RPA is provided in appendix E.5. The PBE energetics predict that the hollow site for CO is more stable than the top site for potentials lower than -0.32 V, being consistent with the over-stabilization of the hollow site in the constant charge model. The RPBE and RPA energetics predict the crossover to happen at -1.41 and -1.43 V, respectively, which are both more negative than the experimental probed region and consistent with the experimentally observed atop site adsorption at -0.9 V versus SHE.

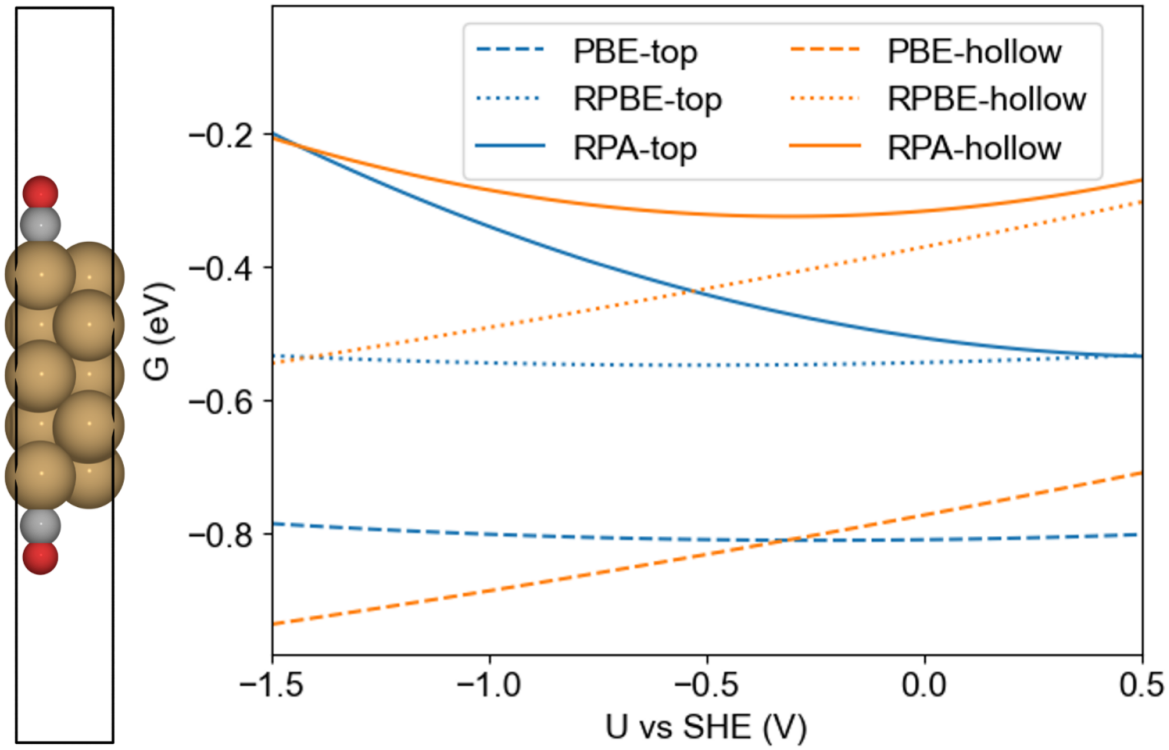

Figure 6.3: Potential dependent energetics of CO adsorbed at top (blue) and hollow (orange) site, using the grand canonical treatment with the PBE (dashed line), RPBE functionals (dotted line), and RPA (solid line). The experimentally inferred $\sqrt{2} \times \sqrt{2}$ structure, where half of atop sites are covered by CO, is shown. Cu atoms are shown as brown, O atoms red, and C atoms grey.

However, a correct description of potential dependent energetics involves more than just the crossing point. Both GGA functionals predict an almost linear dependence of the adsorption energy with respect to the potential for atop and hollow sites. The slopes are close to zero for the CO adsorption at the atop site and positive ($\sim$0.2 eV/V) for the hollow site. The linear relationship indicates that the capacitance, C, in the quadratic relationship (Eq. 6.9) is unchanged before and after the adsorption. Interestingly, at the RPA level, larger curvatures are obtained for both the atop and hollow site adsorption compared to the GGA results, indicating a larger change in double layer capacitance after adsorption, which is consistent with the experimental observation that the double layer capacitance is modified by adsorbates[208, 209, 210]. Moreover, it is worth mentioning that the slope of the adsorption relationships indicates the direction of the charge flow upon adsorption:[190] a positive (negative) slope indicates that charge is injected into (depleted from) the surface after the adsorption, i.e., the system gets reduced (oxidized). The reduction of hollow site adsorption at the GGA level is, however, concerning, as experimentally it has been shown that the addition of a cation, which effectively reduces the adsorbates, will steer the selectivity towards C_2 products[211]. If the reduction predicted by the RPBE functional for the hollow site adsorption happens, the dimerization of CO adsorbed at the metastable hollow site could take place without the presence of cation. In contrast, at the RPA level, the predicted negative slopes, i.e., the depletion of electrons, for both the CO adsorption at the atop and hollow sites are in line with the observed improvement when cations are present. These facts show that at the GGA level, the improvement of the potential dependent stability using the RPBE functional compared to the PBE functional is mostly a vertical shift of the potential dependent adsorption energies. More importantly, the other aspects of the potential dependent energetics, including the curvature reflecting the capacitance and the slope reflecting the charge injection behavior, are still inconsistent with experimental evidences, and can be improved using the GC-RPA energetics.

6.4 Conclusion

In conclusion, we present an approach for electrocatalytic interface simulations combining a grand canonical treatment of electrons and RPA energetics, here called GC-RPA. We applied this method to three facets of Cu, Ag, and Au and found the expected quadratic behavior around the PZC, and a good reproduction of the experimental PZC values.. We further applied this method to the potential dependent CO adsorption on the Cu(100) facet. The grand canonical RPA energetics gives qualitative and quantitative differences compared to the GGA results. Compared to RPBE, which improves upon PBE by shifting energies vertically, GC-RPA predicts larger curvatures, which indicate changes in the capacitance, and different slopes which show a different charge injection mechanism upon CO adsorption. Both observations are more consistent with the experimental evidences compared to the GGA results. We expect this development to pave the way to further electrochemical applications of RPA, and more generally, post-HF methods without a self-consistent electronic structure.

CHAPTER 7

Conclusion

To sum up, we explored the computational modeling of electrochemical systems at two different levels, the DFT level and the MBPT level. At both levels we stressed the importance of correctly describe the electrochemical effects including the solvation effects and the electrochemical potential effects.

At the DFT level, we modeled the complicated SRR process on heteroatom doped holey graphene framework (HGF). We showed that a microsolvation model, which describes the first solvation shell with explicit solvent molecules and the rest by an implicit solvation, is necessary to correctly describe the strong cation nature of Li^+ like species. Moreover, We showed that the defect engineering and the heteroatom doping are two strategies to tune the p-band center of the adsorption sites, which are the edge C atoms, and hence the adsorption energy of the intermediates. Consequently, the optimal intermediate adsorption energy of the heteroatom doped HGF leads to the decrease of the overpotential and the improved battery performance. We further explored the complex reaction network for 16-electron SRR process, revealing two stages separated by the central Li_2S_4 intermediate, in line with experimental CV observations. Moreover, Combining the DFT calculations with *in situ* Raman spectroscopy, we demonstrated that Li_2S_4 and Li_2S_6 represents the dominant intermediates, in which Li_2S_6 is generated by the disproportionation reaction between Li_2S_8 and Li_2S_4 and doesn't directly participate in electrochemical reactions, but contributes to the shuttling problem due to its high solubility and energy favoring its accumulation in the electrolyte. It was found that the optimized N,S-HGF catalytic electrode, benefitting from smaller overpotential, considerably accelerates the conversion of high order LiPSs, leading to faster depletion of soluble LiPSs at higher potential regime, hence mitigating the PS

shuttling effect and boosting the output potential.

To elucidate the structure of this complicated heteroatom doped HGF system, we performed DFT calculations to predict and explain the chemical shifts of N, C, H atoms in N-doped graphene system. Comparisons of predicted chemical shifts with experimental 2D ^{13}C-^{15}N spectra showed good agreement. The major difference between the chemical shifts of graphitic/pyridinic/pyrrolic N-moieties was understood by comparing the electronegativities of the various environments. Furthermore, for each type of environment, the general concept of signal broadening can be decomposed into four different factors, the influences of which are discussed in detail. The first factor is the standalone N/C geometry, where a larger curvature of the graphene edge is found to give a more positive chemical shift. The second factor is the effect of a second N atom nearby: a graphitic N atom close to a pyridinic N decreases the chemical shift, while a pyridinic N close to a graphitic N increases the chemical shift. The third factor is that for each specific structure, the second neighbor C atom experiences a lower chemical shift. The fourth factor is the influence of residual water, which is important to understand the aqueous environment in oxygen reduction reaction or hydrogen evolution reaction. Introduction of this factor matches with the experimental 2D ^{15}N-^{1}H spectrum and provides better agreement with the experimental ^{13}C-^{15}N spectrum. With the free energy taken into account, water adsorption on pyrrolic and pyridinic N sites was found to be more stable and to induce a positive or negative deviation in the chemical shift, respectively. An intuitive correlation between the charge of the probed atom and the chemical shift was confirmed: the smaller the charge, i.e., the higher the electron density, the more shielded the nucleus is, and hence the smaller the chemical shift. The relationship between charge and chemical shifts was discussed, enabling a more detailed understanding of the electronic influence of N doping.

At the MBPT level, we focused on one specific form of the MBPT, the RPA. We firstly exploited a k-space extrapolation scheme to reduce the cost for surface calculations using the RPA and investigated the CO diffusion on Cu(100) facet. We compared the RPA results with results of different GGA, metaGGA, and hybrid functionals. We considered the adsorption

enthalpies and surface energies using the aforementioned methods. Subsequently we applied this methodology to CO diffusion along two high-symmetry directions of the surface, namely (i) top-bridge-top diffusion along the [100] direction and (ii) top-hollow-top diffusion along the [110] direction. We found that RPA appears to be the only method giving the correct site preference and adsorption enthalpy for CO, and surface energy for Cu(001). DFT methods that give correct site preference (RPBE, BEEF-vdW, and HSE06) may suffer from underestimated surface energies. Our results furthermore revealed qualitative differences in the description of diffusion barriers compared to experiments. While RPA and BEEF-vdW are able to quantatively correctly predict one of the diffusion barriers, no functional reproduces the experimentally observed ratio for diffusion barriers. Since this is a phenomenon shared by all methods, we concluded that it might be necessary to revisit the interpretation of the experimental data. The results suggest that the incorrectly predicted adsorption site preference for CO on transition metal surfaces using different functionals can qualitatively and quantitatively alter predictions for diffusion pathways of CO on transition metal surfaces.

Therefore the CO diffusion study suggested that it is necessary to move to more accurate methods, such as RPA, when modeling catalytic processes involving adsorption across different species. We then combined the RPA framework with implicit solvation described using the linearized Poisson-Boltzmann equation to investigate the CO_2 reduction reaction on Cu(100) facet. We showed qualitative and quantitative differences between the more accurate RPA energetics and the PBE/RPBE results, as well as the previous studies using the semi-local density functionals. Formation of *OCCHO was proposed as the potential determinant step, yielding an onset potential matching very well with the experimental value. The shortcomings of the semi-local XC functionals suggest that interpretation based on DFT energetics may need to be more cautious, and that it is important to consider the difference between these functionals and more accurate methods like RPA or DFET, when modeling CO_2RR which involves adsorption across various species.

The success of combining implicit solvation into the RPA framework is encouraging for a direct grand canonical treatment, i.e., adding or removing electrons explicitly to tune the

electrode potential. We further investigated the combination of a grand canonical treatment of electrons and RPA energetics. We proposed an alternative approach, which is purely based on the system's energy and can be used to determine the Fermi level of the non-self-consistent RPA implementation. We applied this method to three facets of Cu, Ag, and Au and found the expected quadratic behavior around the potential of zero charge, and a good reproduction of the experimental potential of zero charge values.. We further applied this method to the potential dependent CO adsorption on the Cu(100) facet. The grand canonical RPA energetics give qualitative and quantitative differences compared to the GGA results. Compared to RPBE, which improves upon PBE by shifting energies vertically, grand canonical RPA predicts larger curvatures, which indicate changes in the capacitance, and different slopes which show a different charge injection mechanism upon CO adsorption. Both observations are more consistent with the experimental evidences compared to the GGA results. We expect all the aforementioned development to pave the way to further electrochemical applications of RPA.

APPENDIX A

Supporting Information for Chapter 2

A.1 Functional Benchmark

We perform the benchmark of (1) the cell potential of Li_2S, (2) cell parameters of Li and Li_2S and volume of S using following functionals: PBE[31], PBE+dDsC[77], vdW-DF-2[212], optPBE[213], optB88[214], opt86b[214], SCAN[79], HSE06[163], HSE06+dDsC, B3LYP[215], B3LYP+dDsC.

The cell potential E is directly linked with the the Gibbs formation energy via:

$$-nFE = \Delta G \tag{A.1}$$

where ΔG is the Gibbs formation energy of Li_2S, with reference to Li and α-sulfur, $\Delta G = G(Li_2S) - G(S) - 2 * G(Li)$, n is the number of electrons evolved in the reaction and takes the value as 2 for this reaction, F is the Faraday's constant. In the unit of eV and V, the E is achieved by simply dividing the Δ value by -2. We follow the same approach with the work of Park et al. [216] to calculate the Gibbs free energy: G is calculated as $G = E_{ele} + ZPE + C_{p,vib} - TS_{vib}$. The free energy components of the SCAN functional are used for the hybrid functionals.

For Li and Li_2S the conventional cells are used. The Li cell contains 2 Li atoms and the Li_2S cell contains 8 Li atoms and 4 S atoms. For S cell we use the unit cell which contains 32 atoms instead of the conventional cell which contains 128 atoms, hence the volume of S cell is 1/4 of the value as noted in the work of Park et al.[216] A 13×13×13 k-point mesh is used for the Li cell. A 3×3×3 k-point mesh is used for the Li_2S cell when using hybrid functionals while for other functionals we use a 7×7×7 k-point mesh. We have performed

tests at the PBE level and find that finer k-point mesh compared to the 3×3×3 one gives an uncertainty of smaller than 3 meV. A 2×2×2 k-point mesh is used for the Li_2S cell when using hybrid functionals while for other functionals we use a 3×3×3 k-point mesh. We have performed tests at the PBE level and find that finer k-point mesh compared to the 2×2×2 one gives an uncertainty of smaller than 1 meV. Structural convergence is assumed for forces lower than 0.01 eV/Å (except the case of S using the B3LYP functional, where 0.02 eV/Å is achieved.) For solid calculations, we raise the cutoff energy of the planewave basis set to 600 eV to avoid the Pulay stress.

Functional	E(V)	Literature Value (V)[216]
PBE	1.96	
PBE+dDsC	2.09	
vdW-DF-2	2.33	2.33
optPBE	2.15	2.15
optB88	2.19	2.20
opt86b	2.09	2.10
SCAN	2.27	
HSE06	2.33	
HSE06+dDsC	2.24	
B3LYP	2.37	
B3LYP+dDsC	2.52	
EXP	2.30	

Table A.1: Calculated cell potential of Li_2S using different functionals.

For the PBE functional, we use the PBE+dDsC energetics of the S cell as the van der Waals interaction is not negligible. If we use the PBE energetics for S the PBE cell potential would be 2.00 V, which is slightly better than 1.95 V but still rather far from the experimental value.

Our calculated values match well with the values of the vdW functionals reported by

Park et al.[216] The target is to find the functionals that provide good match with the experimental cell potential, hence the Gibbs formation energy. The vdW-DF-2, SCAN and HSE06 functionals provide good match with the experimental energetics.

Functional	Li (Å)	Li_2S (Å)	S(Å^3)
PBE	3.42	5.70	1186
PBE+dDsC	3.39	5.62	848
vdW-DF-2	3.39	5.75	900
optPBE	3.42	5.71	868
optB88	3.42	5.69	813
opt86b	3.43	5.69	796
SCAN	3.47	5.68	853
HSE06	3.44	5.60	1128
HSE06+dDsC	3.42	5.63	831
B3LYP	3.42	5.72	1547
B3LYP+dDsC	3.35	5.57	836
EXP	3.48	5.69	824

Table A.2: Calculated cell parameters of Li_2S and Li and cell volume of α-S using different functionals.

Our optB88 values, 3.42 Å for Li lattice parameter, 5.69 Å for the Li_2S lattice parameter, and 813 Å^3 for the S cell volume, match reasonably with the values reported by Park et al.: 3.45 Å for Li lattice parameter, 5.70 Å for the Li_2S lattice parameter, and 805 Å^3 for the S cell volume. From the energetic perspective, the vdW-DF-2, SCAN, and HSE06 functionals are similarly good, while from the geometry perspective, results of the SCAN functional show clearly better match with the experimental data. Hence, we choose the SCAN functional in this work. The structure of Li_2S_2 is also taken from the work of Park et al.

A.2 Free Energy Components of Lithium Polysulfide Species

Temperature is considered to be room temperature, 300K. The gas phase free energy can be calculated:

$$G_{gas} = U + pV - TS$$
$$= E_{ele} + ZPE + \int_0^T C_t\, dT + \int_0^T C_r\, dT + \int_0^T C_{vib}\, dT + pV - TS$$
$$= E_{ele} + ZPE + nk_BT + \int_0^T C_{vib}\, dT - TS$$

where:

G is the Gibbs free energy

U is the internal energy

p is the pressure

V the volume

T is the temperature

S is the entropy, that can be decomposed into its translational, rotational and vibrational components (S_t, S_r, S_{vib})

E_{ele} is the electronic energy.

ZPE stands for the zero point energy.

C_t, C_r, C_{vib} are translational, rotational and vibrational heat capacities.

n takes care for the translational and vibrational heat capacity and pV term, equals to 4 for non-linear molecules, and equals to 3.5 for linear molecules

k_B is the Boltzmann constant

Here we consider the real residual water on surface to be much larger than those in the models, and Gibbs free energy of water to be closer to the case of aqueous environment. However, when water molecule is in aqueous solution, 2 changes need to be made:

1. The pV term vanishes in liquid condition, hence nk_BT term for water will be $3k_BT$.

2. Translational and rotational motions are restricted and the entropy contributions will be reduced. To treat this effect, two approximate schemes are well documented in the literature.

i. The original way follows Wertz.[217]

A parameterized approximation to calculate the loss of entropy is established, and the aqueous entropy is estimated as:

$S_{aq} = 0.54 S_{gas} + 2.86 * 10^{-4}\ eV \cdot K$

ii. Many researchers use half of the gas-phase entropy to estimate the entropy of aqueous phase.[218, 219]

$S_{aq} = 0.5 S_{gas}$

Here we use the method ii to estimate the Gibbs free energy of DOL molecules and the Gibbs free energy of DOL molecule becomes:

$G_{liq} = E_{ele} + 3k_B T + ZPE + \int_0^T C_{vib}\, dT - 0.5 * T * (S_t + S_r + S_{vib})$

All the vibrational components are calculated within the harmonic approximation. Frequencies below 50 cm^{-1} are renormalized to 50 cm^{-1}. First 6 modes are not included to maintain the 3N-6 freedom.

For the DOL molecule, the free energy components are:

	ZPE	$3k_bT$	TS_{gas}	ΔG_{liq}
DOL	2.52	0.078	0.90	2.15

Table A.3: Free energy components of the liquid DOL molecule. All units are in eV.

For each of these close shell Li_2S_x species, we consider two different micro-solvation treatments: each Li is solvated by a first shell of either 2 or 3 DOL molecules, i.e., 4/6DOL-Li_2S_x. We have tried further increase of the number of DOL molecules but geometrically these molecules are not included in the first solvation shell, consistent with the previous finding of Bhatt et al.

Moreover, we consider two different structures for each of these polysulfide species: ring-like structure and chain-like structure.

The Li_2S_x part and the 4/6DOL part are treated separately: the vibrational modes on the Li_2S_x part of each model are calculated and the contribution of the vibrational modes on the DOL molecule part are approximated to be the same as the DOL contribution in 6DOL-Li_2S_4. The averaging process of the 6 DOL molecules are listed as below.

	ZPE	TS_{gas}	ΔG_{liq}
DOL-1	2.56	0.41	2.36
DOL-2	2.55	0.40	2.35
DOL-3	2.56	0.36	2.39
DOL-4	2.56	0.40	2.36
DOL-5	2.56	0.41	2.35
DOL-6	2.55	0.39	2.36
average			2.36

Table A.4: Free energy components of the liquid DOL molecule. All units are in eV.

The values shown here validate the assumption that the micro-solvation DOL molecules have rather similar free energy components.

To compare free energies of models with different number of DOL molecules, we further denote the Gibbs free energy of the Li_2S_x as $G_{liq,net}$ which is defined as:

$$G_{liq,net} = G_{liq,nDOL-Li_2S_x} - nG_{liq,DOL} \tag{A.2}$$

The detailed free energy components of these micro-solvated molecules are listed below.

	ZPE	$3k_bT$	TS_{gas}	$G_{liq,net}$
Li_2S	0.19	0.078	1.26	-17.51
Li_2S_2	0.21	0.078	1.36	-27.72
Li_2S_3	0.23	0.078	1.51	-37.75
Li_2S_4	0.28	0.078	1.61	-47.67
Li_2S_5	0.32	0.078	1.71	-57.37
Li_2S_6	0.36	0.078	1.82	-67.12
Li_2S_7	0.41	0.078	1.90	-76.56
Li_2S_8	0.42	0.078	2.11	-86.42

Table A.5: Free energy components of the Li_2S_x part in ring-like 6DOL-Li_2S_x. All units are in eV.

	ZPE	$3k_bT$	TS_{gas}	$G_{liq,net}$
Li_2S_3	0.24	0.078	1.52	-37.31
Li_2S_4	0.31	0.078	1.63	-46.98
Li_2S_5	0.37	0.078	1.72	-56.59
Li_2S_6	0.41	0.078	1.81	-66.49
Li_2S_7	0.46	0.078	1.91	-76.21
Li_2S_8	0.50	0.078	2.01	-85.99

Table A.6: Free energy components of the Li_2S_x part in chain-like 6DOL-Li_2S_x. All units are in eV.

	ZPE	$3k_bT$	TS_{gas}	$G_{liq,net}$
Li_2S	0.15	0.078	1.34	-16.89
Li_2S_2	0.25	0.078	1.33	-27.41
Li_2S_3	0.26	0.078	1.48	-37.63
Li_2S_4	0.33	0.078	1.56	-47.50
Li_2S_5	0.36	0.078	1.67	-57.24
Li_2S_6	0.40	0.078	1.79	-66.97
Li_2S_7	0.41	0.078	1.93	-76.46
Li_2S_8	0.47	0.078	2.01	-86.00

Table A.7: Free energy components of the Li_2S_x part in ring-like 4DOL-Li_2S_x. All units are in eV.

	ZPE	$3k_bT$	TS_{gas}	$G_{liq,net}$
Li_2S_3	0.22	0.078	1.57	-36.96
Li_2S_4	0.33	0.078	1.57	-46.76
Li_2S_5	0.31	0.078	1.78	-56.57
Li_2S_6	0.39	0.078	1.82	-66.26
Li_2S_7	0.45	0.078	1.93	-75.55
Li_2S_8				

Table A.8: Free energy components of the Li_2S_x part in chain-like 4DOL-Li_2S_x. All units are in eV.

The Li_2S and Li_2S_2 entries do not appear in chain-like tables since we didn't find a local minimum of chain-like structures for these short chain lithium polysulfides: after optimization, the ring-like structure is restored.

The chain-like 4DOL-Li_2S_8 is left empty as electronic convergence problem was met for this structure when implicit solvation was presented. However, the vacuum E_{ele} of chain-like

4DOL-Li_2S_8 is less stable by 0.8 eV compared to the vacuum E_{ele} of ring-like 4DOL-Li_2S_8, and this excludes the possibility of this structure to be the most stable one.

We find that the ring-like 6DOL-Li_2S_x to be always the most stable one and hence use the energetics through this study.

The LiS_3 radical is only considered with 3DOL micro-solvation treatment and ring-like structure. The free energy components are:

	ZPE	$3k_bT$	TS_{gas}	$G_{liq,net}$
LiS_3	0.18	0.078	1.39	-33.46

Table A.9: Free energy components of the LiS_3 part in ring-like 3DOL-LiS_3. All units are in eV.

A.3 Influence of Solubility Limit of Li_2S_4

Experimentally we find that the solubility of Li_2S_4 to be limited in the DOL/DME solvent, ∼0.01 M. After applying this constraint to the potential dependent concentration of the N,S-HGF system, we find the match with experimental data to be better: the peak of Li_2S_4 concentration moves from ∼2.05 V, as shown in chapter 2 Fig. 2.7 right panel, to ∼2.2 V as shown below. The results after applying the solubility constraint matches well with the experimental plateau at 2.25-2.15 V.

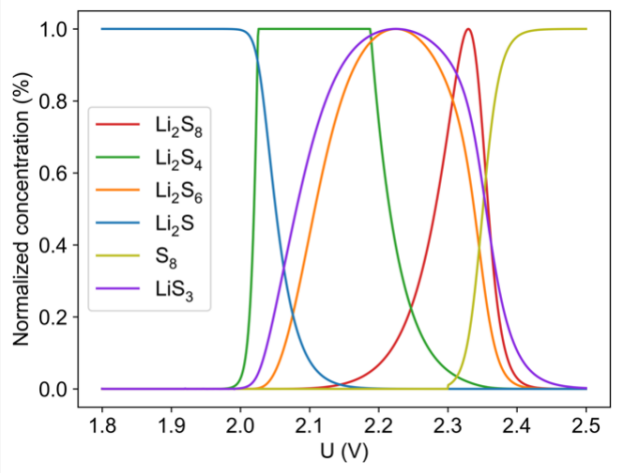

Figure A.1: Simulated concentrations after applying the concentration limit of Li_2S_4 as 0.01 M.

A.4 Construction of the Volcano Plots

As mentioned in chapter 2, we list the 14 different $2e^-$, $4e^-$, and $6e^-$ steps, 12 different probable combinations, and the volcano plots of these combinations.

The 14 different $2e^-$, $4e^-$, and $6e^-$ steps are labelled with [1] through [14].

[1], [2], [3] and [4] are $2e^-$ steps:

[1]

$$Li_2S_4 + Li^+ + e^- \rightarrow LiS_3 + Li_2S$$

$$LiS_3 + Li^+ + e^- \rightarrow Li_2S_3$$

[2]

$$Li_2S_3 + Li^+ + e^- \rightarrow LiS_2 + Li_2S$$

$$LiS_2 + Li^+ + e^- \rightarrow Li_2S_2$$

[3]

$$Li_2S_2 + Li^+ + e^- \rightarrow LiS + Li_2S$$

$$LiS + Li^+ + e^- \rightarrow Li_2S$$

[4]

$Li_2S_4 + Li^+ + e^- \rightarrow LiS_3 + Li_2S$

$LiS_3 + Li^+ + e^- \rightarrow Li_2S_3$

[5], [6], [7], [8], [9], and [10] are 4e$^-$ steps. [5], [6], [7], and [8] start with Li_2S_4 and end with $2Li_2S$+ Li_2S_2. [9] and [10] start with Li_2S_3 and end with $3Li_2S$.

[5]

$Li_2S_4 + Li^+ + e^- \rightarrow LiS_3 + Li_2S$

$LiS_3 + Li^+ + e^- \rightarrow LiS_2 + LiS$

$LiS + Li^+ + e^- \rightarrow Li_2S$

$LiS_2 + Li^+ + e^- \rightarrow Li_2S_2$

[6]

$Li_2S_4 + Li^+ + e^- \rightarrow LiS_3 + Li_2S$

$LiS_3 + Li^+ + e^- \rightarrow S_2 + Li_2S$

$S_2 + Li^+ + e^- \rightarrow LiS_2$

$LiS_2 + Li^+ + e^- \rightarrow Li_2S_2$

[7]

$Li_2S_4 + Li^+ + e^- \rightarrow LiS_2 + Li_2S_2$

$LiS_2 + Li^+ + e^- \rightarrow LiS + LiS$

$LiS + Li^+ + e^- \rightarrow Li_2S$

$LiS + Li^+ + e^- \rightarrow Li_2S$

[8]

$Li_2S_4 + Li^+ + e^- \rightarrow LiS_2 + Li_2S_2$

$LiS_2 + Li^+ + e^- \rightarrow S + Li_2S$

$S + Li^+ + e^- \rightarrow LiS$

$LiS + Li^+ + e^- \rightarrow Li_2S$

[9]

$Li_2S_3 + Li^+ + e^- \rightarrow LiS_2 + Li_2S$

$LiS_2 + Li^+ + e^- \rightarrow LiS + LiS$

$LiS + Li^+ + e^- \rightarrow Li_2S$

$LiS + Li^+ + e^- \rightarrow Li_2S$

[10]

$Li_2S_3 + Li^+ + e^- \rightarrow LiS_2 + Li_2S$

$LiS_2 + Li^+ + e^- \rightarrow S + Li_2S$

$S + Li^+ + e^- \rightarrow LiS$

$LiS + Li^+ + e^- \rightarrow Li_2S$

[11], [12], [13], and [14] are $6e^-$ steps, directly starting with Li_2S_4 and ending with $4Li_2S$.

[11]

$Li_2S_4 + Li^+ + e^- \rightarrow LiS_3 + Li_2S$

$LiS_3 + Li^+ + e^- \rightarrow S_2 + Li_2S$

$S_2 + Li^+ + e^- \rightarrow LiS_2$

$LiS_2 + Li^+ + e^- \rightarrow LiS + LiS$

$LiS + Li^+ + e^- \rightarrow Li_2S$

$LiS + Li^+ + e^- \rightarrow Li_2S$

[12]

$Li_2S_4 + Li^+ + e^- \rightarrow LiS_3 + Li_2S$

$LiS_3 + Li^+ + e^- \rightarrow S_2 + Li_2S$

$S_2 + Li^+ + e^- \rightarrow LiS_2$

$LiS_2 + Li^+ + e^- \rightarrow S + Li_2S$

$S + Li^+ + e^- \rightarrow LiS$

$LiS + Li^+ + e^- \rightarrow Li_2S$

[13]

$Li_2S_4 + Li^+ + e^- \rightarrow LiS_3 + Li_2S$

$LiS_3 + Li^+ + e^- \rightarrow LiS_2 + LiS$

$LiS_2 + Li^+ + e^- \rightarrow LiS + LiS$

$LiS + Li^+ + e^- \rightarrow Li_2S$

$LiS + Li^+ + e^- \rightarrow Li_2S$

$LiS + Li^+ + e^- \rightarrow Li_2S$

[14]

$Li_2S_4 + Li^+ + e^- \rightarrow LiS_3 + Li_2S$

$LiS_3 + Li^+ + e^- \rightarrow LiS_2 + LiS$

$LiS_2 + Li^+ + e^- \rightarrow Li_2S + S$

$S + Li^+ + e^- \rightarrow LiS$

$LiS + Li^+ + e^- \rightarrow Li_2S$

$LiS + Li^+ + e^- \rightarrow Li_2S$

These different $2e^-$, $4e^-$, and $6e^-$ steps are further combined to give the overall reaction pathway and the following combinations are considered: (i) $2e^-+2e^-+2e^-$, (ii) $4e^-+2e^-$, (iii) $2e^-+4e^-$, and (iv) $6e^-$. The volcano plots of different combinations are shown below. The 12 different probable combinations are labelled with (1) through (12). The colors indicate the doping: red for N,S-codoped, blue for N-doped, green for S-doped and black for nondoped models. The shapes indicate the model type: filled circles for inner defect models, triangles for armchair models, and squares for zigzag edge models. The LiS adsorption energy is chosen as the descriptor as it is linked with the adsorption energies of other species.

(i) $2e^-+2e^-+2e^-$

(1) [1]+[2]+[3]

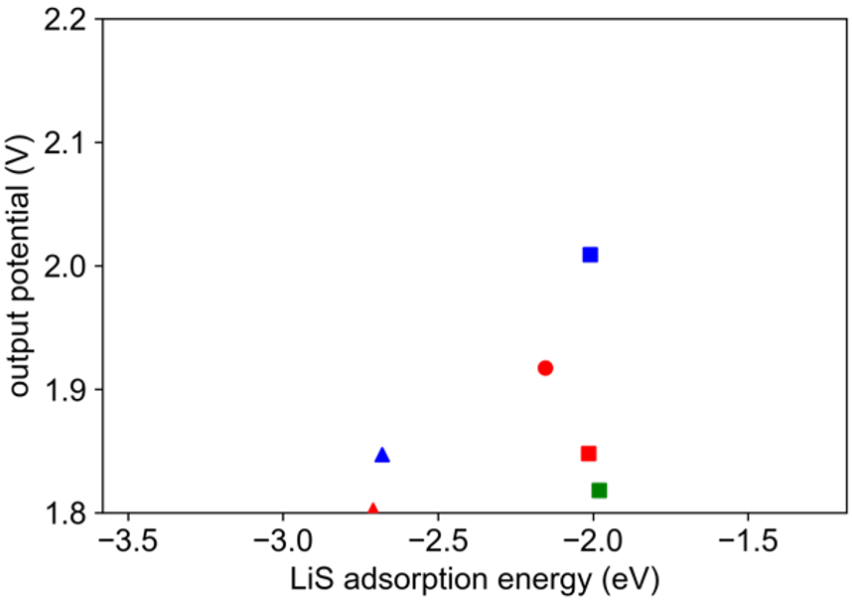

Figure A.2: The output potential of pathway combination (1).

(2) [4]+[3]+[3]

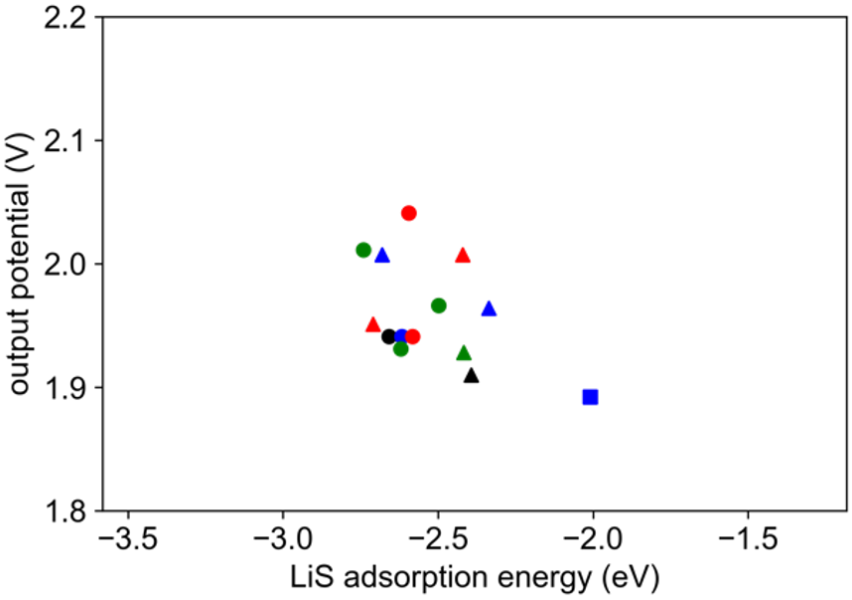

Figure A.3: The output potential of pathway combination (2).

(ii) $4e^-$+$2e^-$

(3) [5]+[3]

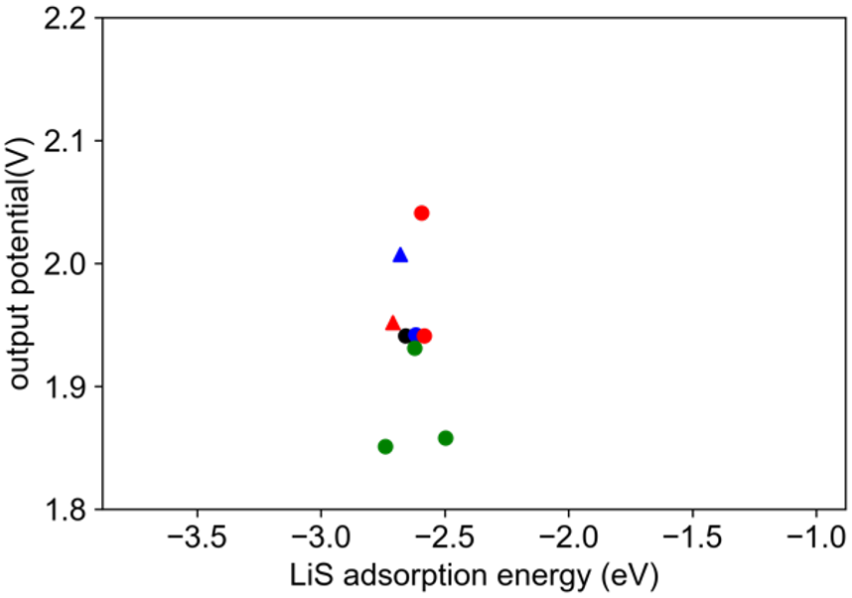

Figure A.4: The output potential of pathway combination (3).

(4) [6]+[3]

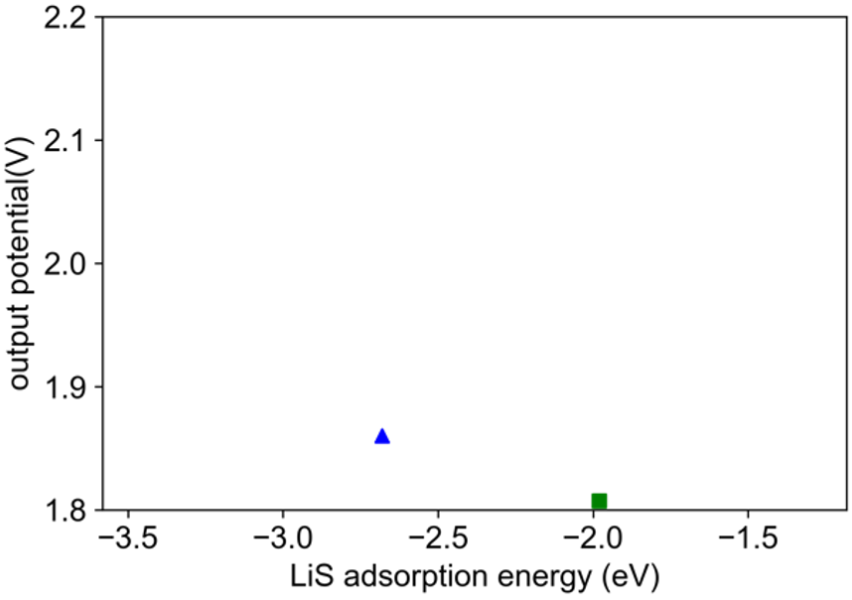

Figure A.5: The output potential of pathway combination (4).

(5) [7]+[3]

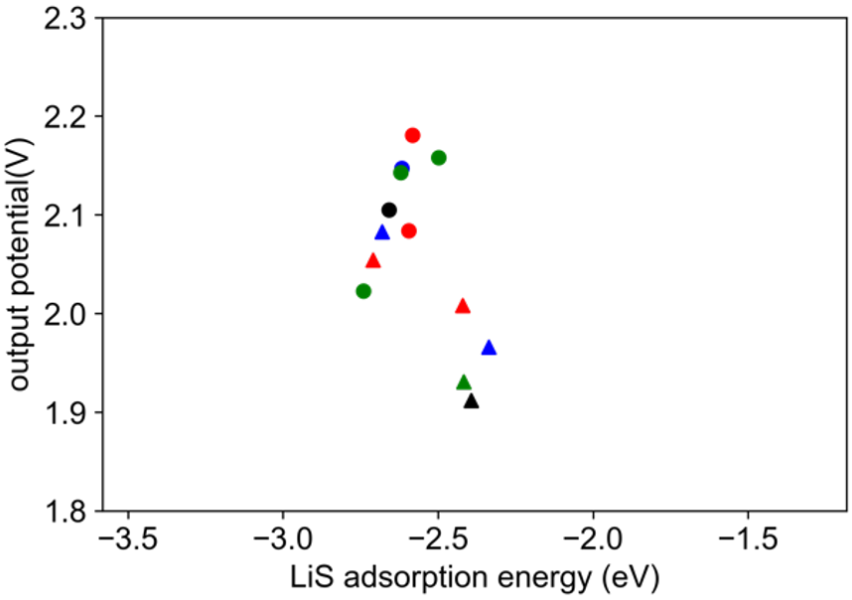

Figure A.6: The output potential of pathway combination (5).

(6) [8]+[3]

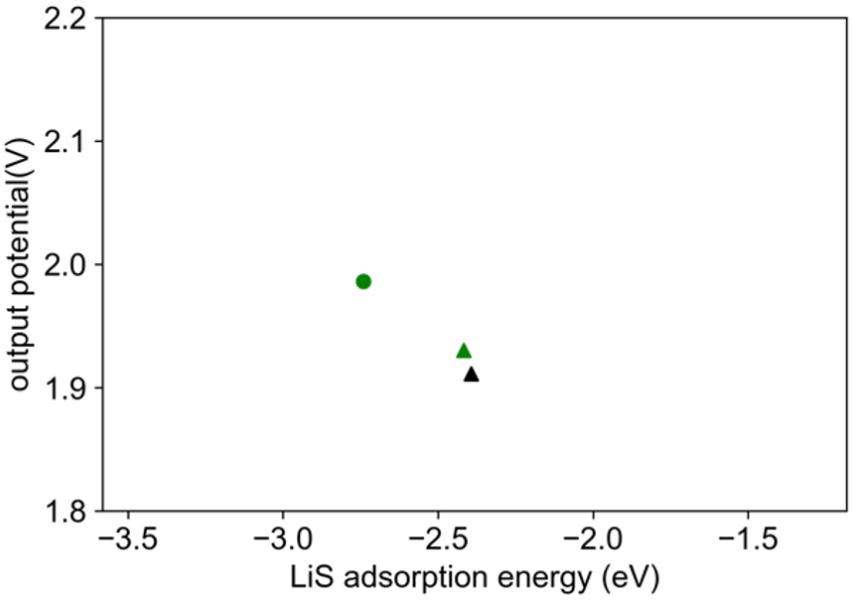

Figure A.7: The output potential of pathway combination (6).

(iii) $2e^-+4e^-$

(7) [1]+[9]

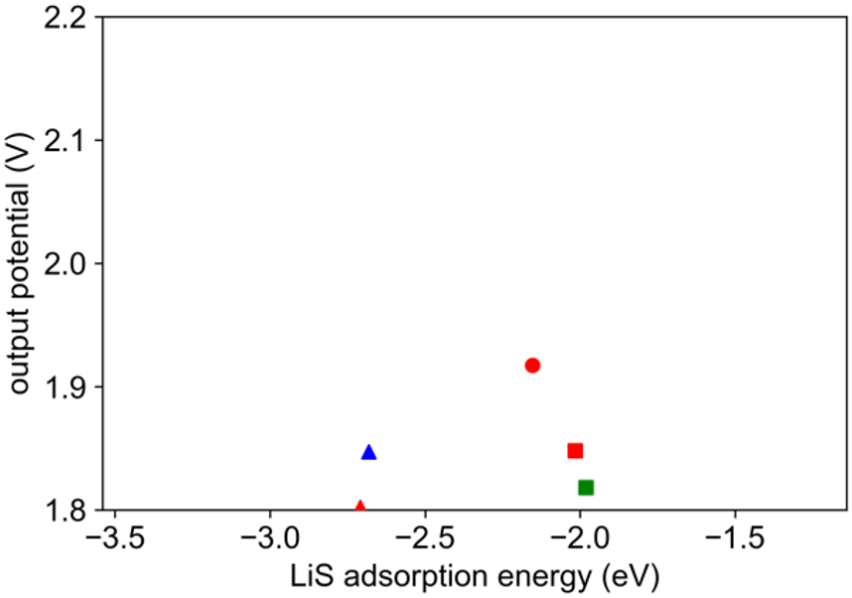

Figure A.8: The output potential of pathway combination (7).

(8) [1]+[10]

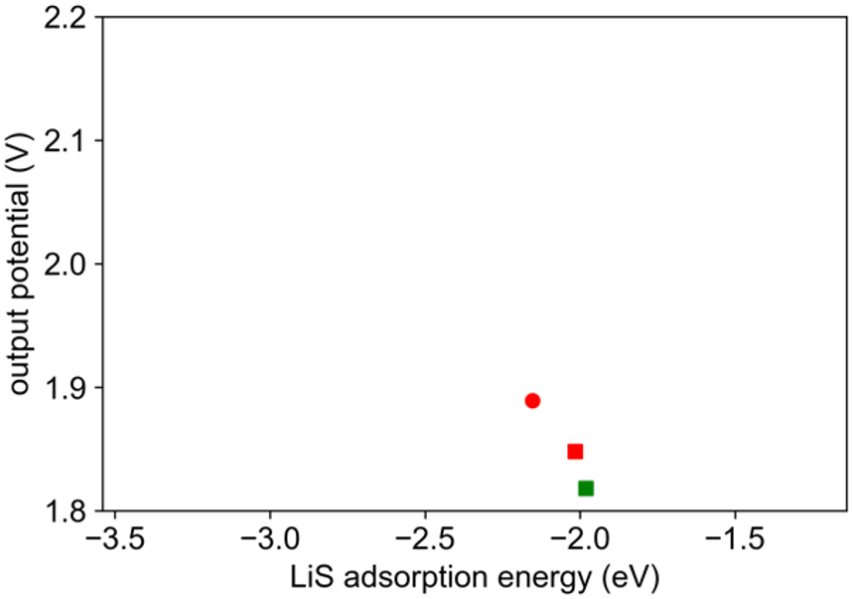

Figure A.9: The output potential of pathway combination (8).

(iv) $6e^-$

(9) [11]

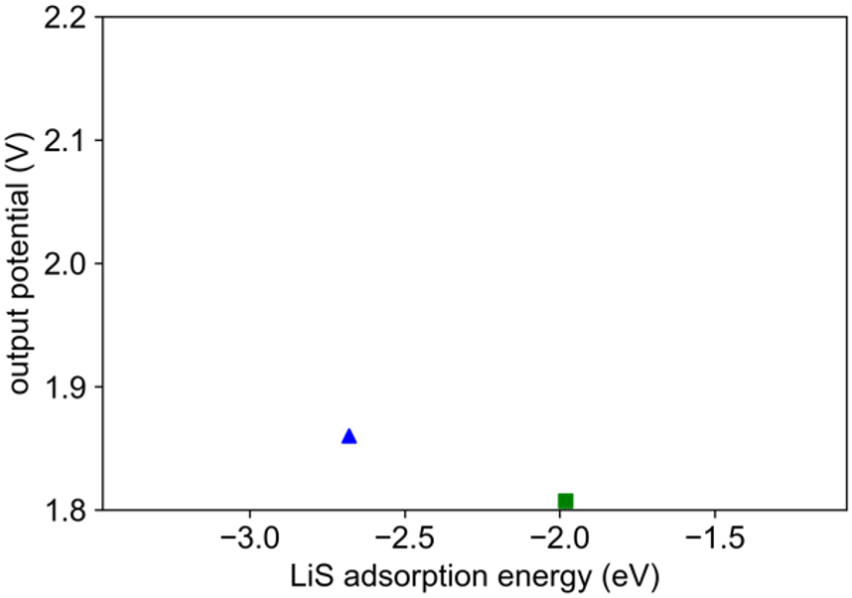

Figure A.10: The output potential of pathway combination (9).

(10) [12]

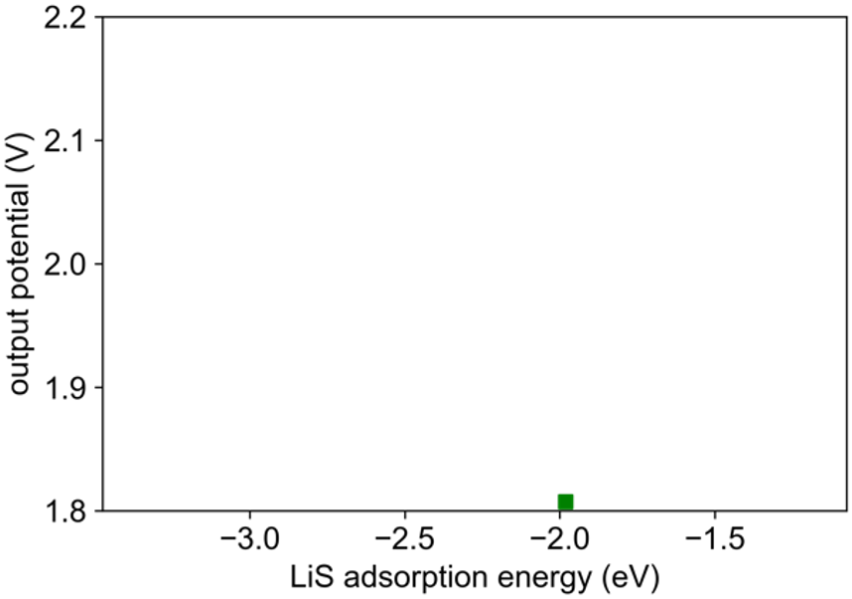

Figure A.11: The output potential of pathway combination (10).

(11) [13]

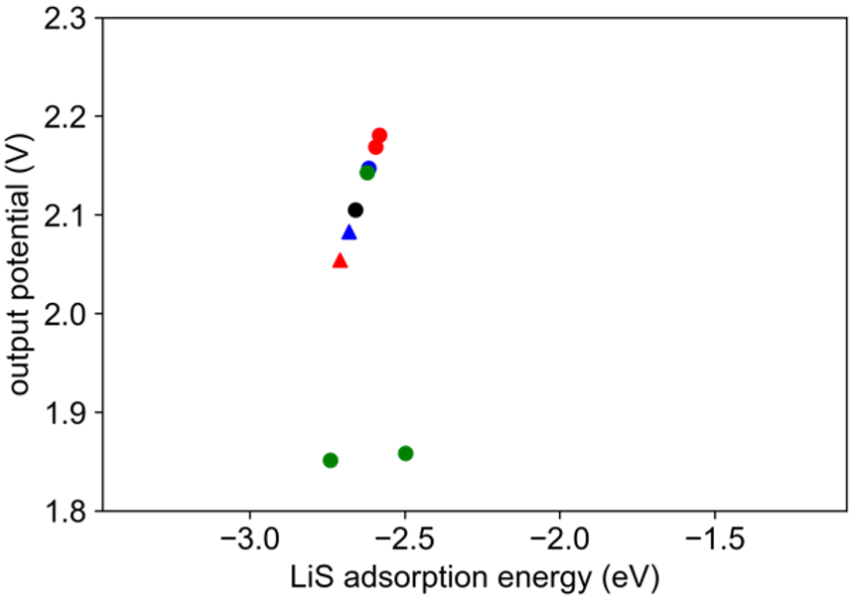

Figure A.12: The output potential of pathway combination (11).

(12) [14]

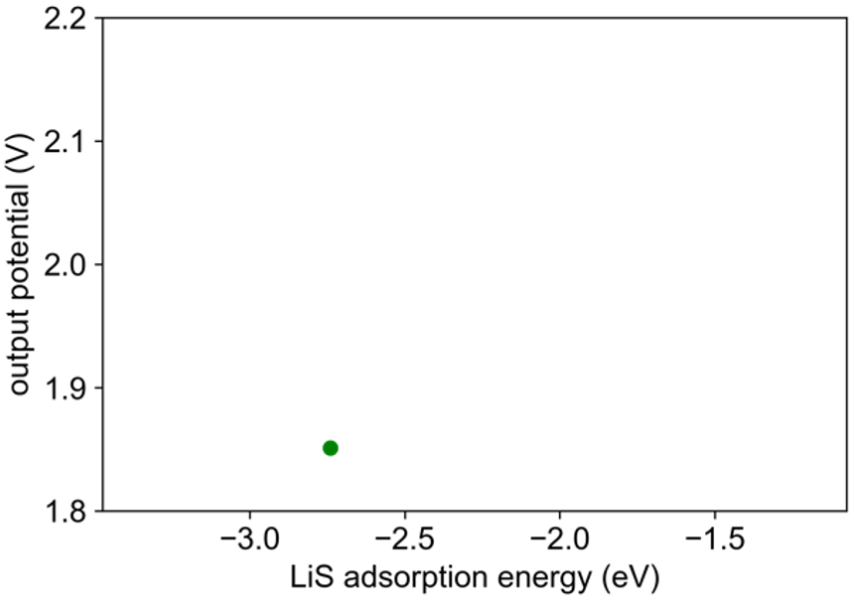

Figure A.13: The output potential of pathway combination (12).

A.5 Raman Spectra Simulation

For S_8 and close shell lithium polysulfides (Li_2S_4, Li_2S_6, and Li_2S_8), we have performed the calculation at both PBE+dDsC and SCAN level, based on structures optimized at respective level. The simulated spectra are shown below, and the major peaks are compared to the experimental results:

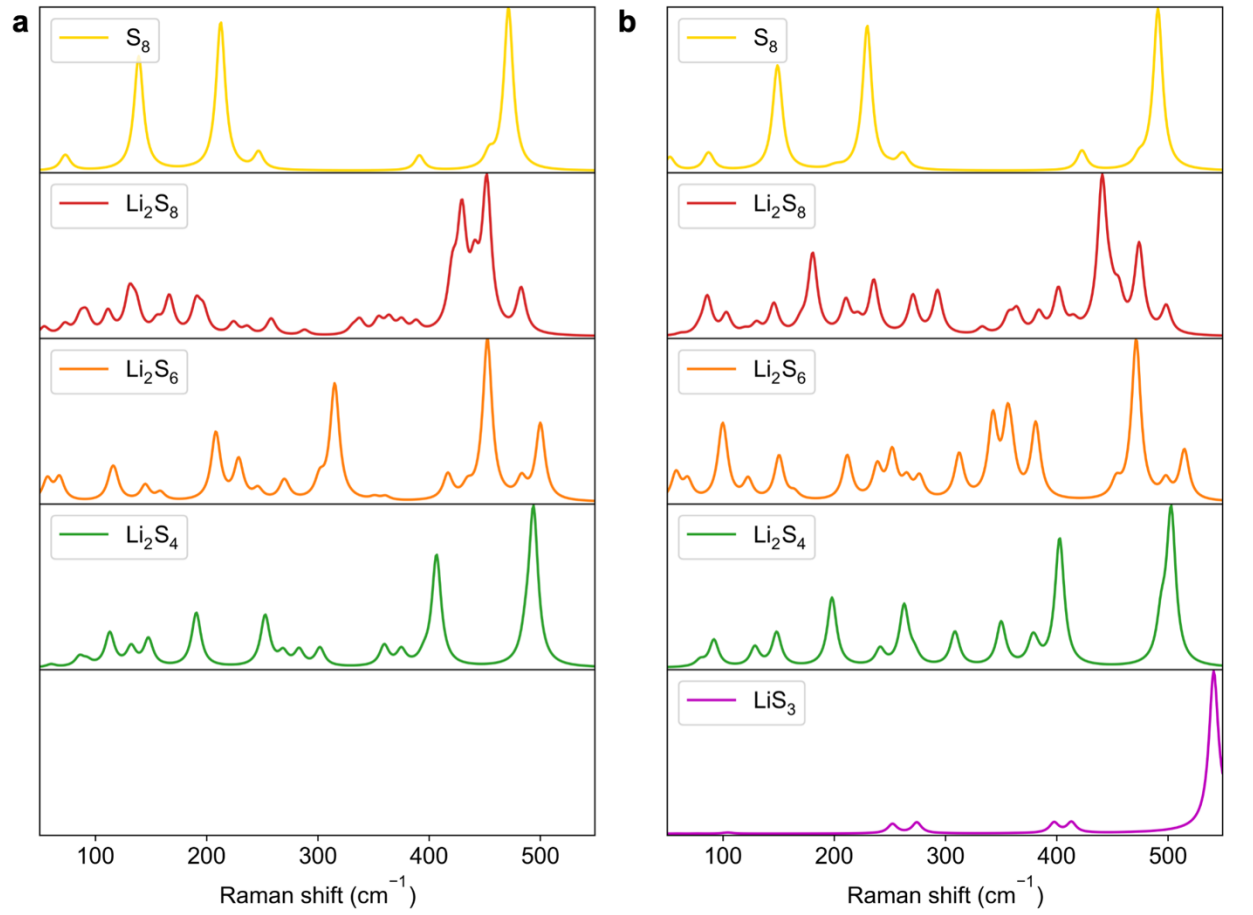

Figure A.14: Simulated Raman spectra using (a) the PBE+dDsC (b) the SCAN functionals. The LiS_3 spectra was only calculated using the SCAN functional.

Peak Position (cm^{-1})	LiS_3	Li_2S_4	Li_2S_6	Li_2S_8	S_8
PBE		190	453	430	139, 213, 471
SCAN	541	198	471	440	150, 230, 491
EXP	533	200	452	441	153, 218, 473

Table A.10: Peak positions and intensities of the simulated Raman spectra compared with experimental results. All peak positions are in the unit of cm^{-1}.

These results show that the match of simulated and experimental peak positions is not a sensitive to functional choice. We choose to present the SCAN peak positions in chapter 2, being consistent with the energetic choice.

APPENDIX B

Supporting Information for Chapter 3

B.1 convergence of chemical shift values with respect to k-point mesh

Model	k-point mesh	^{13}C Chemical Shift (ppm)
Terrace	3*3*1	121.1
Terrace	4*4*1	120.2
Terrace	5*5*1	119.2
Zigzag	5*1*1	108.3
Zigzag	6*1*1	110.2
Zigzag	7*1*1	108.6
Armchair	1*5*1	110.2
Armchair	1*6*1	111.0
Armchair	1*7*1	111.3

Table B.1: convergence of chemical shift values of center C atom with respect to k-point mesh

It can be concluded that our current k-points mesh ensures convergence at 1-2 ppm level.

B.2 convergence of chemical shift values with respect to electronic convergence criteria

The convergence of ^{13}C and ^{15}N chemical shift values with respect to electronic convergence criteria is tested on graphitic N model. Electronic structure convergence criteria (EDIFF values) of 10^{-7}, 10^{-8}, 10^{-9}, and 10^{-10} eV are tested. The first neighbor N-C pair values are shown here. The ^{13}C and ^{15}N chemical shift reference specie used here, alpha-glycine, is always calculated using EDIFF=10^{-10} eV.

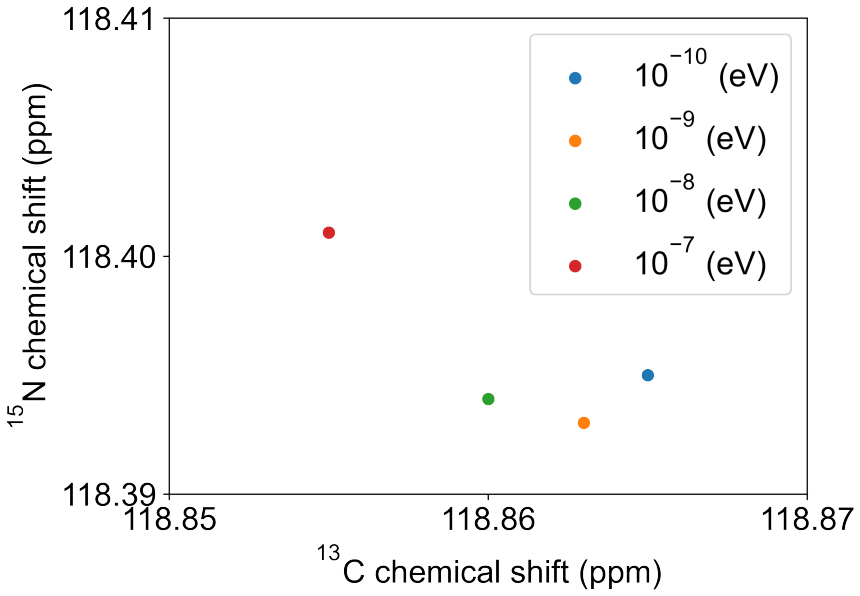

Figure B.1: chemical shift values with respect to electronic convergence criteria of graphitic N model

It can be concluded that the EDIFF=10^{-7} eV setting will have a convergence at 0.02 ppm level. Models calculated with 10^{-8} eV: zigzag edge pyridinic N model, nondoped zigzag edge model, pyrazinic N model-1, pyrazinic N model-2, defected zigzag edge pyridinic N model-1, defected zigzag edge pyridinic N model-2, para graphitic N-graphitic N model, meta graphitic N-graphitic N model Models calculated with 10^{-7} eV: zigzag edge graphitic N model

B.3 convergence of chemical shift values with respect to cutoff energy

Cutoff Energy (eV)	^{15}N Chemical Shift (ppm)	First Neighbor ^{13}C Chemical Shift (ppm)
600	118.4	118.9
700	117.0	118.2

Table B.2: convergence of chemical shift values with respect to cutoff energy

The cutoff energy of the reference specie, alpha-glycine, are also calculated using changing cutoff energy (ENCUT setting in VASP). It can be concluded that our cutoff energy ensures convergence at lower than 1 ppm level.

B.4 influence of including or excluding the the core contribution on chemical shift values

The influence of including or excluding the core contribution on ^{15}N chemical shift values is tested on graphitic N model, pyrrolic N model and pyridinic N model. 4 decimal points are shown in order to show the differences.

Model	^{15}N chemical shift without Core Contribution (ppm)	^{15}N chemical shift with Core Contribution (ppm)
Graphitic N	118.3954	118.3954
Pyrrolic N	242.3043	242.3044
Pyridinic N	115.9484	115.9484

Table B.3: influence of including or excluding the the core contribution on chemical shift values

It can be concluded that including core contribution will lead to a difference at 0.0001

ppm level.

B.5 details of G=0 contribution

This part corresponds to equations 61, 62 and 63 in the work of Pickard *et al*[95]. The bare induced field in reciprocal space is calculated as:

$$\mathbf{B}^{(0)}_{bare}(\mathbf{G}) = \frac{4\pi}{c}\frac{i\mathbf{G}\times\mathbf{j}^{(0)}_{bare}(\mathbf{G})}{G^2} \tag{B.1}$$

However, this equation cannot be applied at **G=0**. Following the convention of Mauri[94], a spherical sample is assumed and then this contribution is calculated as

$$\mathbf{B}^{(1)}_{in}(\mathbf{G}) = \frac{8\pi}{3}\overleftrightarrow{\chi}\mathbf{B} \tag{B.2}$$

B.6 2D solid-state NMR pulse sequences of the (a) dipolar-mediated ^{13}C-^{15}N HQMC NMR experiment and (b) ^{15}N-^{1}H HETCOR-MAS NMR experiment

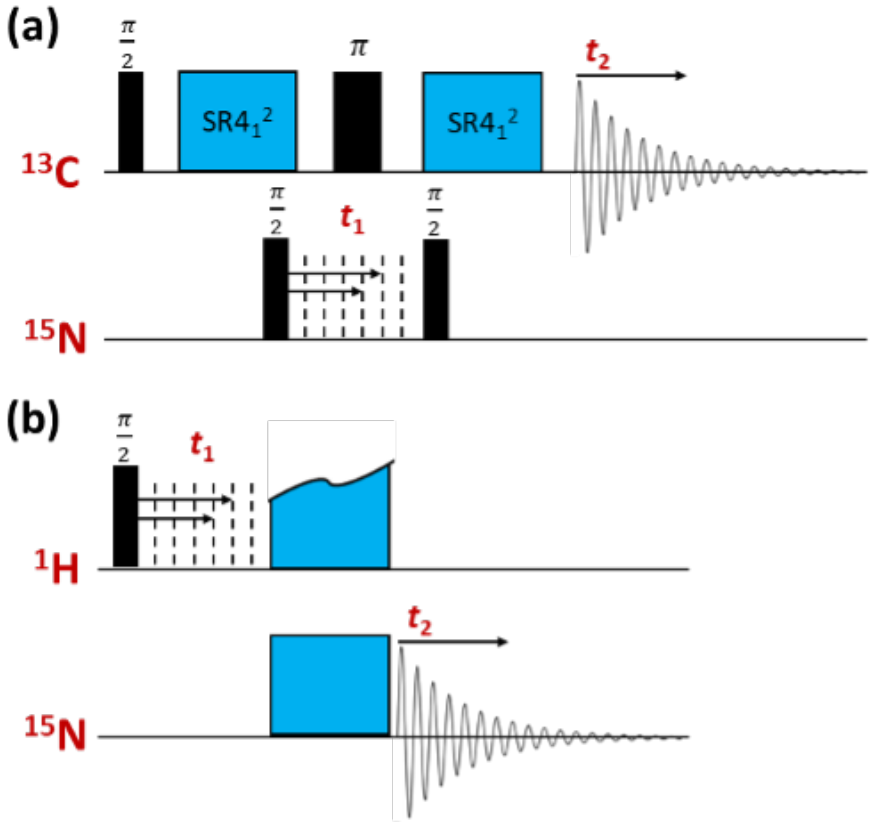

Figure B.2: Schematic diagrams of the 2D solid-state NMR pulse sequences of (a) the dipolar-mediated ^{13}C-^{15}N HQMC NMR experiment used to acquire the spectrum in Figure 2, and (b) the ^{15}N-^{1}H HETCOR-MAS NMR experiment used to acquire the spectrum in Figure 6.

B.7 convergence of ^{13}C chemical shift value of center C atom in armchair and zigzag models with respect to model thickness

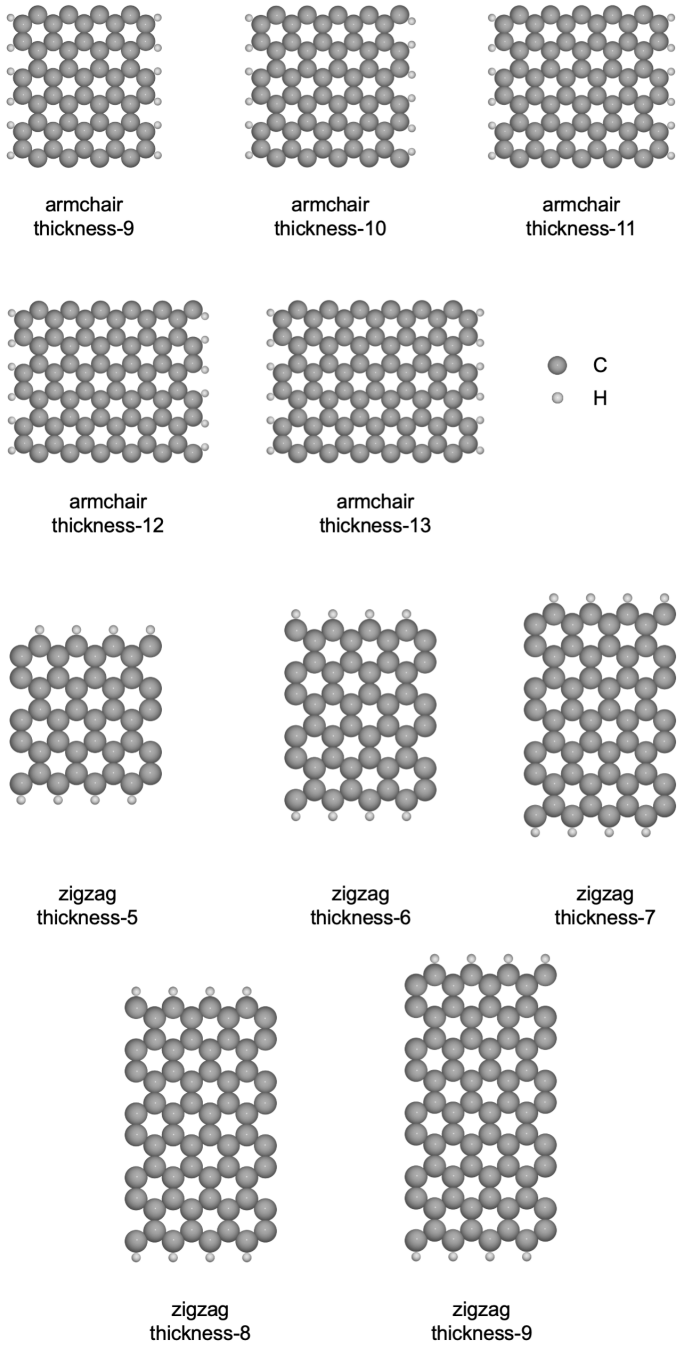

Figure B.3: structures of armchair and zigzag models with different thickness

model	thickness	^{13}C Chemical Shift (ppm)
Armchair	9	111.3
	10	109.3
	11	114.4
	12	109.7
	13	109.5
Zigzag	5	108.6
	6	109.5
	7	112.3
	8	110.7
	9	108.6

Table B.4: convergence of ^{13}C chemical shift values of center C atom in armchair and zigzag models with respect to model thickness

For armchair models, it can be observed that the model with a thickness of 11 has the largest ^{13}C chemical shift value of center C atom, reaching 114.4, whereas other thicker models has a value of 109. We choose to use the model with a thickness as 9, ensuring that the error bar of ^{13}C chemical shift value will be in the range of 2-3 ppm. For zigzag models, it can be observed that the model with a thickness of 8 has the largest ^{13}C chemical shift value of center C atom, reaching 110.7, whereas other thicker models has a value of 109. We choose to use the model with a thickness as 5, ensuring that the error bar of ^{13}C chemical shift value will be in the range of 2-3 ppm.

B.8 structures of models with adsorbed H_2O

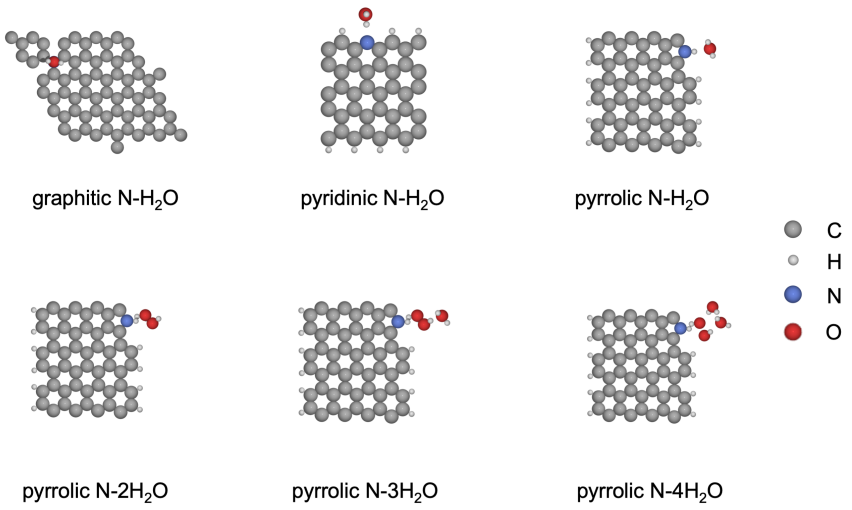

Figure B.4: structures of models with adsorbed H_2O. color scheme: grey: C, white: H, blue: N, red: O.

B.9 influence of water adsorption on ^{15}N chemical shifts

model	^{15}N Chemical Shift (ppm)
graphitic N	118.4
graphitic N-H_2O	124.6
pyridinic N	242.3
pyridinic N-H_2O	217.9
pyrrolic N	115.9
pyrrolic N-H_2O	131.0
pyrrolic N-$2H_2O$	131.2
pyrrolic N-$3H_2O$	136.5
pyrrolic N-$4H_2O$	130.6

Table B.5: influence of water adsorption on ^{15}N chemical shifts

B.10 adsorption free energies of H_2O molecules in graphitic N, pyridinic N, and pyrrolic N models

Energy term (eV)	H_2O	graphitic N-H_2O	pyridinic N-H_2O	pyrrolic N-H_2O	pyrrolic N-2H_2O	pyrrolic N-3H_2O	pyrrolic N-4H_2O
E		-0.189	-0.428	-0.275	-0.732	-1.021	-1.361
ZPE	0.564	0.589	0.638	0.607	1.275	1.909	2.579
C_v	0.078	0.057	0.065	0.043	0.145	0.193	0.267
TS	0.588	0.120	0.130	0.078	0.305	0.387	0.533
G		-0.011	-0.206	-0.051	-0.313	-0.350	-0.440

Table B.6: Adsorption free energies of H_2O molecules in graphitic N, pyridinic N, and pyrrolic N models. All the values are in unit of eV. For water molecule, the C_v term includes $C_{v,trans}$ and $C_{v,rot}$.

We investigated more structures related to pyrrolic N model because the experimental 2D ^{1}H $\{^{15}$N$\}$ NMR spectra give direct information on the pyrrolic species, as it has a N-H bond. Temperature is considered to be room temperature, 300K. The gas phase free energy can be calculated:

$$G_{gas} = U + pV - TS$$
$$= E_{ele} + ZPE + \int_0^T C_t\, dT + \int_0^T C_r\, dT + \int_0^T C_{vib}\, dT + pV - TS$$
$$= E_{ele} + ZPE + nk_BT + \int_0^T C_{vib}\, dT - TS$$

where:

G is the Gibbs free energy

U is the internal energy

p is the pressure

V the volume

T is the temperature

S is the entropy, that can be decomposed into its translational, rotational and vibrational components (S_t, S_r, S_{vib})

E_{ele} is the electronic energy.

ZPE stands for the zero point energy.

C_t, C_r, C_{vib} are translational, rotational and vibrational heat capacities.

n takes care for the translational and vibrational heat capacity and pV term, equals to 4 for non-linear molecules, and equals to 3.5 for linear molecules

k_B is the Boltzmann constant

Here we consider the real residual water on surface to be much larger than those in the models, and Gibbs free energy of water to be closer to the case of aqueous environment. However, when water molecule is in aqueous solution, 2 changes need to be made:

1. The pV term vanishes in liquid condition, hence nk_BT term for water will be $3k_BT$.

2. Translational and rotational motions are restricted and the entropy contributions will be reduced. To treat this effect, two approximate schemes are well documented in the literature.

i. The original way follows Wertz.[217]

A parameterized approximation to calculate the loss of entropy is established, and the aqueous entropy is estimated as:

$S_{aq} = 0.54S_{gas} + 2.86 * 10^{-4}\ eV \cdot K$

ii. Many researchers use half of the gas-phase entropy to estimate the entropy of aqueous phase.[218, 219]

$S_{aq} = 0.5S_{gas}$

Here we use the method ii to estimate the Gibbs free energy of water molecules and the Gibbs free energy of water molecule becomes:

$G_{aq} = E_{ele} + 3k_BT + ZPE + \int_0^T C_{vib}\, dT - 0.5 * T * (S_t + S_r + S_{vib})$

Adsorbed systems are assumed to lose the rotational and translational degrees of freedom, and thus the rotational and translational energies and entropies are neglected.

$G_{water/slab} = E_{ele} + ZPE + \int_0^T C_{vib}\, dT - T * S_{vib}$

Graphene slab is kept fixed when computing the harmonic frequencies.

$G_{slab} = E_{ele}$

The Gibbs free energies confirm the adsorption on different sites, while the adsorption on graphitic N is rather weak.

B.11 relationship between ^{1}H chemical shift values and DDEC6 charge on H atom in side pyrrolic N-H_2O models

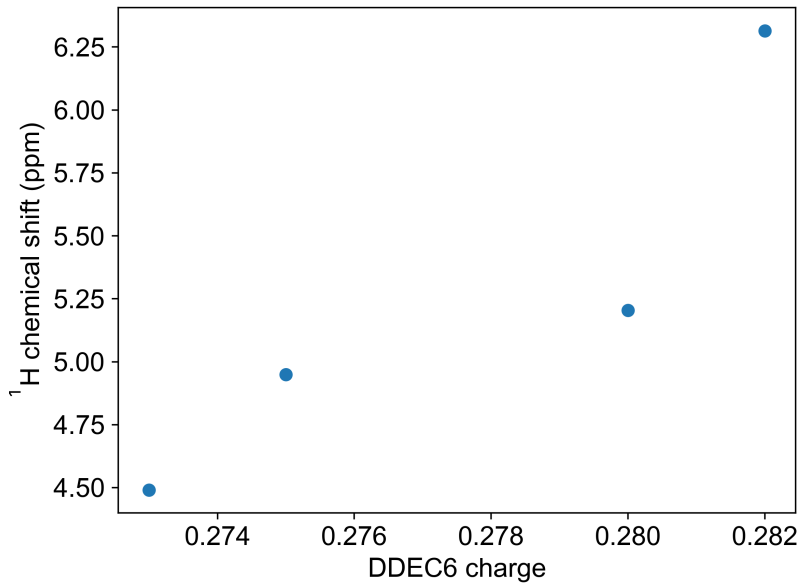

Figure B.5: relationship between ^{1}H chemical shift values and DDEC6 charge on H atom in side pyrrolic N-H_2O models

APPENDIX C

Supporting Information for Chapter 4

C.1 Convergence of RPA Diffusion Energetics with Respect to E_{cut}^{χ}

As indicated in the main text, E_{cut}^{χ} is a parameter that is crucial for numerical accuracy. To confirm that a highest E_{cut}^{χ} of 150 eV is sufficient, we therefore calculated energies for the high symmetry points and transition states for E_{cut}^{χ}=200 eV and results are shown in Table C.1. Our results indicate that increasing E_{cut}^{χ} to 200 eV only leads to differences smaller than 5 meV compared to E_{cut}^{χ}=150 eV.

TBT	Top-Bridge Difference	Barrier
100 eV, 3×3×1	70	103
150 eV, 3×3×1	92	119
200 eV, 3×3×1	92	118
THT	Top-Hollow Difference	Barrier
100 eV, 3×3×1	168	201
150 eV, 3×3×1	228	233
200 eV, 3×3×1	231	235

Table C.1: Convergence of RPA energetics with respect to E_{cut}^{χ}. All values are shown in units of meV. PBE geometries are used.

C.2 Numerical Validation of k-space ONIOM like Scheme

As stated in the main text, we use our embedding scheme to express the RPA energy at E_{cut}^{χ} and a c×c×1 k-point grid as

$$\begin{aligned} E^{RPA}(150eV, c\times c\times 1) \approx \\ E^{RPA}(150eV, a\times a\times 1)+ \\ E^{RPA}(100eV, b\times b\times 1) - E^{RPA}(100eV, a\times a\times 1)+ \\ E^{PBE}(c\times c\times 1) - E^{PBE}(b\times b\times 1) \end{aligned} \tag{C.1}$$

In this equation, a,b, and c are different k-point values, which follow the relationship a<b<c. To show that (1) is valid, we rewrite $E^{RPA}(150eV, c\times c\times 1)$ as

$$\begin{aligned} E^{RPA}(150eV, c\times c\times 1) = \\ E^{RPA}(150eV, a\times a\times 1)+ \\ E^{RPA}(150eV, b\times b\times 1) - E^{RPA}(150eV, a\times a\times 1)+ \\ E^{RPA}(150eV, c\times c\times 1) - E^{RPA}(150eV, b\times b\times 1) \end{aligned} \tag{C.2}$$

It is immediately obvious that C.1 is a good approximation of C.2, and C.1 and C.2 are equivalent if we can show that

$$\begin{aligned} E^{RPA}(150eV, b\times b\times 1) - E^{RPA}(150eV, a\times a\times 1) \approx \\ E^{RPA}(100eV, b\times b\times 1) - E^{RPA}(100eV, a\times a\times 1) \end{aligned} \tag{C.3}$$

and

$$\begin{aligned} E^{RPA}(150eV, c\times c\times 1) - E^{RPA}(150eV, b\times b\times 1) \approx \\ E^{RPA}(100eV, c\times c\times 1) - E^{RPA}(100eV, b\times b\times 1) \approx \\ E^{PBE}(c\times c\times 1) - E^{PBE}(b\times b\times 1) \end{aligned} \tag{C.4}$$

We can now rearrange equations C.3 and C.4 into

$$\begin{aligned} E^{RPA}(150eV, b\times b\times 1) - E^{RPA}(100eV, b\times b\times 1) \approx \\ E^{RPA}(150eV, a\times a\times 1) - E^{RPA}(100eV, a\times a\times 1) \end{aligned} \tag{C.5}$$

and

$$E^{RPA}(100eV, c \times c \times 1) - E^{PBE}(c \times c \times 1) \approx$$
$$E^{RPA}(100eV, b \times b \times 1) - E^{PBE}(b \times b \times 1) \tag{C.6}$$

Equations C.5 and C.6 state that equation C.1 is valid, as long as the energy differences between the two methods of interest are converged with respect to the k-point grid. Additionally, we are not interested in converging the total energy, but in the convergence of the energy differences we study in this work, namely the CO diffusion barriers and the energy differences for CO adsorbed in the top and bridge or top and hollow positions. We therefore display the energy differences in these quantities in Fig. C.1 and the numerical values are shown in Table C.2. We find that $E^{RPA}(100eV, b \times b \times 1) - E^{PBE}(b \times b \times 1)$ varies by less than 10 meV for b$\geqslant$6 and $E^{RPA}(150eV, a \times a \times 1) - E^{RPA}(100eV, a \times a \times 1)$ varies by 1 or 2 meV for a$\geqslant$3. Based on these considerations, we choose b=8 and a=3, which shows that equation 3 is valid. We furthermore want to emphasize that in the THT profile, the PBE profile calculated using a 2×2×1 k-point grid shows an unexpected high energy of the hollow site due to a too low k-point grid. Calculations for this scenario were performed and values are included in the table below as well.

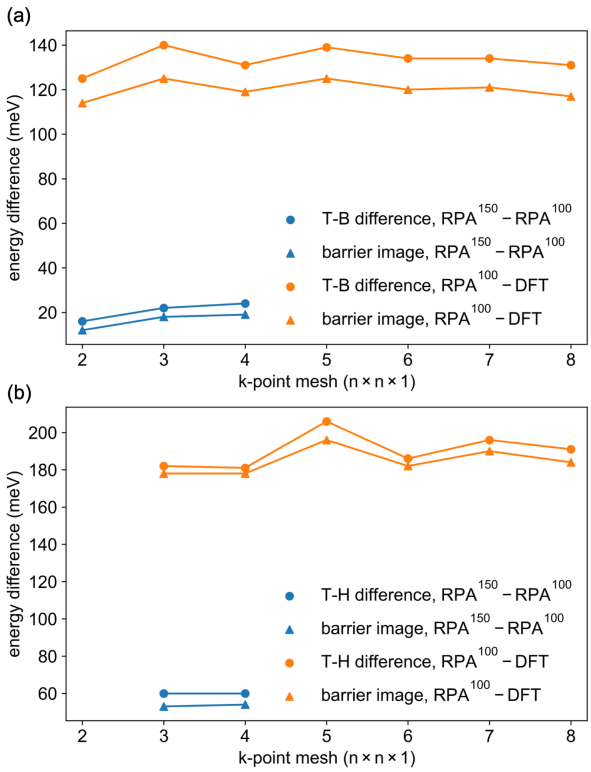

Figure C.1: Convergence of $E^{RPA}(150\ eV, b \times b \times 1) - E^{RPA}(100\ eV, b \times b \times 1)$ and $E^{RPA}(100\ eV, a \times a \times 1) - E^{DFT}(a \times a \times 1)$ in (a) TBT and (b) THT pathway. Note that the barrier denotes the energies correspond to the image that is the barrier image in the extrapolated $E^{RPA}(150\ eV, 15 \times 15 \times 1)$ profile.

TBT	Top-Bridge Difference	Barrier	$E^{RPA}(150\ eV, 15\times15\times1)$ Barrier Image
RPA, 150 eV, 2×2×1	51	77	76
RPA, 150 eV, 3×3×1	92	119	119
RPA, 150 eV, 4×4×1	80	104	104
TBT	Top-Bridge Difference	Barrier	$E^{RPA}(150\ eV, 15\times15\times1)$ Barrier Image
RPA, 100 eV, 2×2×1	35	67	64
RPA, 100 eV, 3×3×1	70	103	101
RPA, 100 eV, 4×4×1	56	85	85
RPA, 100 eV, 5×5×1	136	153	153
RPA, 100 eV, 6×6×1	97	118	118
RPA, 100 eV, 7×7×1	85	106	106
RPA, 100 eV, 8×8×1	93	113	113
TBT	Top-Bridge Difference	Barrier	$E^{RPA}(150\ eV, 15\times15\times1)$ Barrier Image
PBE, 2×2×1	-90	11	-50
PBE, 3×3×1	-70	22	-24
PBE, 4×4×1	-75	14	-34
PBE, 5×5×1	-3	40	28
PBE, 6×6×1	-37	70	-2
PBE, 7×7×1	-49	16	-15
PBE, 8×8×1	-38	20	-4
PBE, 10×10×1	-40	21	-5
PBE, 15×15×1	-38	22	-3

Table C.2: All values are shown in units of meV. PBE geometries are used. For consistency, at PBE level we shown the TS-top difference as barrier.

THT	Top-Hollow Difference	Barrier	$E^{RPA}(150\ eV, 15\times15\times1)$ Barrier Image
RPA, 150 eV, 2×2×1	460	460	403
RPA, 150 eV, 3×3×1	228	234	233
RPA, 150 eV, 4×4×1	121	167	134
THT	Top-Hollow Difference	Barrier	$E^{RPA}(150\ eV, 15\times15\times1)$ Barrier Image
RPA, 100 eV, 2×2×1	408	408	358
RPA, 100 eV, 3×3×1	168	201	179
RPA, 100 eV, 4×4×1	121	167	134
RPA, 100 eV, 5×5×1	226	249	238
RPA, 100 eV, 6×6×1	204	225	214
RPA, 100 eV, 7×7×1	192	111	203
RPA, 100 eV, 8×8×1	173	205	186
THT	Top-Hollow Difference	Barrier	$E^{RPA}(150\ eV, 15\times15\times1)$ Barrier Image
PBE, 2×2×1	275	275	218
PBE, 3×3×1	-14	51	2
PBE, 4×4×1	-60	31	-44
PBE, 5×5×1	20	87	42
PBE, 6×6×1	18	61	32
PBE, 7×7×1	-4	45	13
PBE, 8×8×1	–18	51	1
PBE, 10×10×1	-12	54	8
PBE, 15×15×1	-8	55	11

Similar tests of the convergence of energy differences for CO adsorbed on the Cu(111) surface can be found in Fig. 10.2 of the doctoral thesis of L. Schimka.[162]

C.3 Lattice Parameters and Surface Energies

method	lattice parameter (Å)	surface energy (J/m^2)
PBE	3.629	1.488
PBE+D2	3.567	2.150
PBE+D3	3.562	2.421
RPBE	3.672	1.257
BEEF-vdW	3.651	1.441
SCAN	3.565	1.833
HSE06	3.626	1.347
RPA	3.581	1.914

Table C.3: Lattice parameters used and surface energy calculated. Lattice parameters are shown in the unit of Å and surface energies are shown in the unit of J/m^2. RPA and HSE06 lattice parameters are taken from literature.

C.4 Vacuum Separation Influence

As tested on graphite system, for RPA, the long range correlation uncertainty beyond 13 Å is ca. 0.2 meV. Here we test the influence of vacuum height on RPA energetics: the fluctuations may arise from the fact that we are using PBE geometries.

TBT	Top-Bridge Difference	Barrier
12 Å	72	104
13 Å	70	103
14 Å	68	101
THT	Top-Hollow Difference	Barrier
12 Å	171	200
13 Å	168	201
14 Å	168	198

Table C.4: Influence of vacuum height on RPA energetics. Test is done on $E^{RPA}(100\ eV, 3\times 3\times 1)$ using PBE geometry.

C.5 CO Adsorption Enthalpy Details

The adsorption enthalpy is calculated as

$$H_{ads} = E_{slab+CO} - E_{slab} - E_{CO} + \Delta ZPE + E_{correction} \tag{C.7}$$

where the ΔZPE is the difference of zero point energy of CO in gas phase and on the surface, being calculated within harmonic approximation. We apply a layer correction in line with literature[53] to correct the number to 6 layers results. This term is rather small and PBE value is used for all functional, hence will not affect the conclusions we make in the main text.

$$E_{layer\ correction} = E_{PBE,\ ads,\ 6\ layers} - E_{PBE,\ ads,\ 4\ layers} \tag{C.8}$$

For HSE06 and RPA, we apply a k-point extrapolation. Again, this term in rather small and will not affect the conclusions presented.

$$E_{kpt\ correction} = E_{PBE,\ ads,\ 15\times15\times1} - E_{PBE,\ ads,\ 8\times8\times1} \tag{C.9}$$

method	$E_{slab+CO} - E_{slab} - E_{CO}$	ΔZPE	$E_{layer\ correction}$	$E_{kpt\ correction}$	H_{ads}
PBE	-0.859	0.054	-0.007		-0.812
PBE+D2	-1.071	0.054	-0.007		-1.024
PBE+D3	-1.034	0.054	-0.007		-0.987
RPBE	-0.546	0.054	-0.007		-0.499
BEEF-vdW	-0.604	0.054	-0.007		-0.557
SCAN	-0.997	0.054	-0.007		-0.949
HSE06	-0.586	0.054	-0.007	0.007	-0.532
RPA	-0.554	0.054	-0.007	0.007	-0.500

Table C.5: Detailed energy components of CO adsorption enthalpies presented. All values shown in the unit of eV. For RPA and HSE06, PBE geometries are used.

C.6 Convergence of RPA CO Adsorption Energy with Respect to E_{cut}^{χ}

E_{cut}^{χ}	Adsorption energy
100 eV, 3×3×1	-0.548
150 eV, 3×3×1	-0.560
200 eV, 3×3×1	-0.570
250 eV, 3×3×1	-0.570

Table C.6: Convergence of RPA CO adsorption energy with respect to E_{cut}^{χ}. All values are shown in units of meV. PBE geometries are used.

We found that at $E_{cut}^{\chi} = 200eV$ the convergence of absolute RPA CO adsorption energy is achieved. It is not surprising that the CO adsorption energy requires higher E_{cut}^{χ} compared to diffusion energetics, as it is compares more different systems. To get the $E_{RPA,\ ads,\ 8\times8\times1}$,

the same k-point extrapolation scheme for RPA is performed.

$$E_{RPA,\ 200eV,\ 8\times8\times1} = E_{RPA,\ 200eV,\ 3\times3\times1} + E_{RPA,\ 100eV,\ 8\times8\times1} - E_{RPA,\ 100eV,\ 3\times3\times1} \quad \text{(C.10)}$$

C.7 BEEF-vdW Energy Profile with PBE Geometry

We found it complicated to achieve smooth SCAN energy profile using SCAN geometries. Thus we use PBE geometries. Since we find the SCAN profile to be between PBE and BEEF-vdW, we estimate the possible error by checking the difference of BEEF-vdW using consistent, i.e., BEEF-vdW, or PBE geometries. The influence is found to be within 10 meV.

TBT	Top-Bridge Difference	Barrier
BEEF-vdW, BEEF-vdW geometry	26	51
BEEF-vdW, PBE geometry	25	60
THT	Top-Hollow Difference	Barrier
BEEF-vdW, BEEF-vdW geometry	123	132
BEEF-vdW, PBE geometry	123	133

Table C.7: Influence of using PBE geometry for BEEF-vdW functional as an estimation for uncertainty of using PBE geometries for SCAN functional.

C.8 Energetics of z Shifted Structures at RPA Level

As mentioned in the main text, we optimized the position of the CO molecule in z-direction by shifting the molecule by 0.00 Å, 0.02 Å, 0.04 Å, and 0.06 Å and all results are shown in Table C.8. For all the CO adsorption structures on the Cu(100) surface calculated in this work, we found that a shift of the molecule in z direction by either 0.02 or 0.04 Å leads to the lowest energy. We furthermore performed a parabolic fit for the calculated energies along the z-direction and find that the fitted minima are close to a shift of 0.03 Å, as shown in Table C.9. These shifts are consistent with the results for CO adsorption on the Cu(111)

surface using RPA[53], where the RPA distance of the CO molecule from surface is found to increase by about 0.03 Å. Since energies obtained using parabola fitting are very close to the energies of the most stable discrete z shifts (differences are smaller than 1 meV, as shown in Table C.10), we only report energies for the most stable images with the aforementioned discrete z shifts in this work.

$d_{CCu,\ x}$	0.000	0.085	0.170	0.256	0.341	0.426	0.511	0.596	0.682	0.767	0.852	0.937	1.022	1.108	1.278
TBT-PBE	3.4	3.3	3.3	3.3	3.3	3.4	3.0	3.0	3.1	3.2	3.7	3.4	3.1	3.2	3.7
TBT-0.02	0.0	0.0	0.0	0.0	0.0	0.0	0.0	0.0	0.0	0.0	0.2	0.1	0.0	0.1	0.4
TBT-0.04	0.7	0.6	0.7	0.8	0.8	0.7	0.4	0.6	0.3	0.1	0.0	0.0	0.0	0.0	0.0
TBT-0.06	5.3	5.0	4.9	5.0	5.0	4.7	3.9	4.4	3.7	3.2	2.7	2.7	2.8	2.6	2.4
$d_{CCu,\ xy}$	0.000	0.120	0.240	0.362	0.482	0.602	0.723	0.843	0.964	1.085	1.205	1.325	1.445	1.567	1.807
THT-PBE	3.4	3.3	3.3	3.1	3.3	3.1	3.0	3.1	3.9	3.5	3.2	3.0	2.4	1.8	1.3
THT-0.02	0.0	0.0	0.0	0.0	0.0	0.0	0.0	0.0	0.5	0.4	0.4	0.4	0.1	0.0	0.0
THT-0.04	0.7	0.8	0.7	0.9	0.4	0.6	0.6	0.1	0.0	0.0	0.0	0.0	0.0	0.1	0.7
THT-0.06	5.3	5.1	4.9	5.1	4.2	4.3	4.1	3.3	2.3	2.0	1.9	1.8	1.8	2.1	3.2

Table C.8: Relative energies at RPA level for CO shifted along the z-axis with respect to the PBE geometry. All values are shown in units of meV and are reported with respect to the with most stable shift in z direction.

$d_{CCu,\ x}$	0.000	0.085	0.170	0.256	0.341	0.426	0.511	0.596	0.682	0.767	0.852	0.937	1.022	1.108	1.278
TBT	0.027	0.027	0.027	0.027	0.027	0.028	0.028	0.027	0.029	0.030	0.032	0.031	0.030	0.031	0.033
$d_{CCu,\ xy}$	0.000	0.120	0.240	0.362	0.482	0.602	0.723	0.843	0.964	1.085	1.205	1.325	1.445	1.567	1.807
THT	0.027	0.027	0.027	0.026	0.028	0.028	0.028	0.030	0.034	0.034	0.034	0.034	0.032	0.029	0.023

Table C.9: Optimal z shifts for CO calculated by parabola fitting for each image along the TBT and THT diffusion path on the Cu(001) surface. Values are shown in units of Å.

$d_{CCu,\ x}$	0.000	0.085	0.170	0.256	0.341	0.426	0.511	0.596	0.682	0.767	0.852	0.937	1.022	1.108	1.278
TBT	-0.2	-0.2	-0.2	-0.1	-0.1	-0.1	-0.2	-0.2	-0.3	-0.3	-0.3	-0.3	-0.4	-0.3	-0.2
$d_{CCu,\ xy}$	0.000	0.120	0.240	0.362	0.482	0.602	0.723	0.843	0.964	1.085	1.205	1.325	1.445	1.567	1.807
THT	-0.2	-0.1	-0.2	-0.1	-0.3	-0.2	-0.1	-0.3	-0.2	-0.2	-0.1	-0.1	-0.2	-0.2	0.0

Table C.10: Energy difference between the parabolic fit reported in Table C.9 and the minimum for discrete values reported in Table C.8 for each point along the TBT and THT diffusion path. All values are shown in units of meV. For example, TBT image-1 has a value as -0.2 meV means the minimum of parabola fitting is 0.2 meV more stable than TBT-0.02 image-1, as TBT-0.02 image-1 is calculated to be the discrete minimum, as shown in Table C.8 column image-1.

C.9 Pseudopotential Details

functional	Cu pseudopotential	C pseudopotential	O pseudopotential
PBE	Cu_GW	C_GW	O_GW
RPBE	Cu_GW	C_GW	O_GW
BEEF-vdw	Cu_GW	C_GW	O_GW
SCAN	Cu_GW	C_GW_new	O_GW_new
HSE06	Cu_GW	C_GW	O_GW

Table C.11: Pseudopotentials used for different functionals.

For SCAN calculations, the new version of C and O pseudopotentials were used as metaGGA functionals requires information on the kinetic energy density of the core-electrons. It has been tested that for PBE, the C_GW_new and O_GW_new pseudopotentials leads to a change within 4 meV for the barriers and high symmetry site energy differences.

C.10 RPA Starting Orbitals

Although RPBE and PBE give rather different energetics, RPA@RPBE and RPA@PBE are found to give essentially same energetics.

TBT	Top-Bridge Difference	Barrier
RPA@PBE	70	103
RPA@RPBE	70	104
THT	Top-Hollow Difference	Barrier
RPA@PBE	168	201
RPA@RPBE	168	202

Table C.12: Influence of starting orbitals on RPA energetics. Test is done on $E^{RPA}(100\ eV, 3 \times 3 \times 1)$ using PBE geometry.

C.11 Geometry Parameters of Top, Bridge, and Hollow Site and Transition States

TBT	top site r_{CO}	top site $d_{CCu,\ z}$	TS r_{CO}	TS $d_{CCu,\ z}$	TS $d_{CCu,\ x}$	TS θ_{OCz}	bridge site r_{CO}	bridge site $d_{CCu,\ z}$
PBE	1.15	1.84	1.16	1.71	0.77	164.2	1.17	1.52
PBE+D2	1.15	1.84	1.16	1.73	0.60	163.8	1.17	1.50
PBE+D3	1.15	1.84	1.16	1.72	0.68	163.9	1.17	1.52
RPBE	1.16	1.86	1.17	1.62	0.85	165.8	1.17	1.54
BEEF-vdW	1.15	1.88	1.17	1.70	0.85	163.8	1.16	1.55
RPA	1.15	1.86	1.17	1.60	0.94	172.8	1.28	1.56
THT			TS r_{CO}	TS $d_{CCu,\ z}$	TS $d_{CCu,\ xy}$	TS θ_{OCz}	hollow site r_{CO}	hollow site $d_{CCu,\ z}$
PBE			1.17	1.44	1.08	163.1	1.20	1.17
PBE+D2			1.17	1.51	0.96	159.4	1.20	1.16
PBE+D3			1.17	1.48	1.08	161.1	1.20	1.16
RPBE			1.17	1.48	1.08	163.6	1.20	1.21
BEEF-vdW			1.18	1.30	1.44	169.5	1.19	1.21
RPA			1.19	1.20	1.57	173.7	1.20	1.19

Table C.13: Geometry parameters of all functionals used. Distances are shown in the unit of Å and angle are shown in the unit of °. HSE06 and SCAN are not shown since PBE geometries are used. The following two values are not shown as they remain the same: bridge site $d_{CCu,\ x}$ is always 1.278 Å and hollow site $d_{CCu,\ xy}$ is always 1.807 Å.

C.12 Linear Relationships of Energy Differences and Barriers

We study the following three relationships, namely (i) energy differences between top/bridge and top/hollow sites, (ii) diffusion barrier in [100] direction and top/bridge energy difference, and (iii) diffusion barrier in [110] direction and top/hollow energy difference. The latter two relationships are Bell–Evans–Polanyi (BEP) principle along both the TBT and THT profile. The detailed values are provided in the following figure.

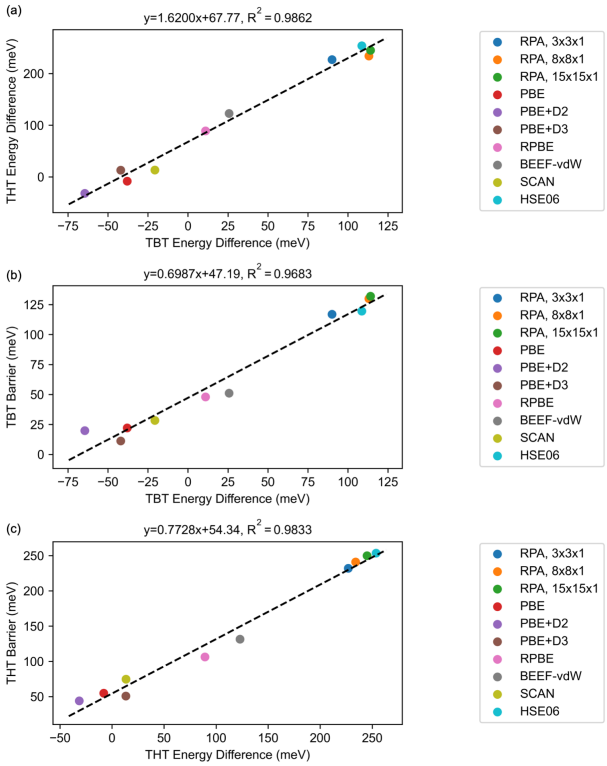

Figure C.2: The linear relationships of energy differences and barriers along (a) energy differences between top/bridge and top/hollow sites, (b) diffusion barrier in [100] direction and top/bridge energy difference, and (c) diffusion barrier in [110] direction and top/hollow energy difference. Values are shown in the unit of meV.

With these linear relationships, the barriers along [100] and [110] directions are determined by energy differences between top/bridge sites. We show that in a wide range of top/bridge site differences, it is impossible to have a THT barrier lower than the TBT barrier. The detailed values are provided in the following figure.

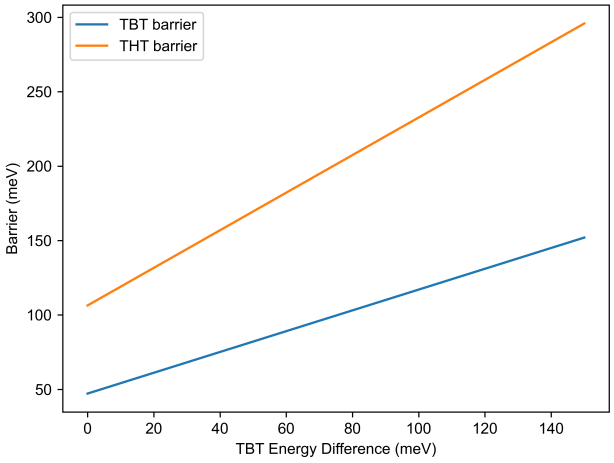

Figure C.3: Fitted barriers along [100] and [110] directions following the aforementioned linear relationships with respect to energy differences between top/bridge sites. We focus on the positive differences as top site is more stable. Top/bridge site differences upto 150 meV are shown.

C.13 Bridge-Hollow-Bridge Diffusion

The bridge-hollow diffusion pathway is investigated using CI-NEB[166] and the energies of bridge site, transition state, and hollow site are shown in Fig. C.4

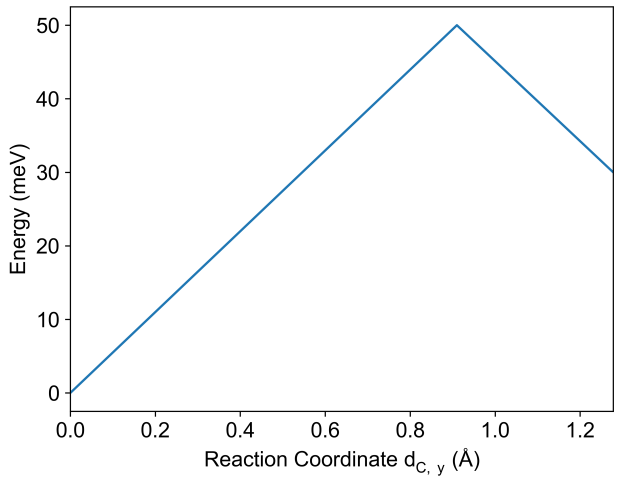

Figure C.4: Energy profiles for the CO diffusion from the bridge site to the hollow site along the [010] direction at PBE level. The y coordinate shift from the bridge site, $d_{C,\ y}$, is utilized as the reaction coordinate.

C.14 Energy Profiles with Coverage Effects

As mentioned in the paper, the 3×3 unit cell is beyond our current computational capability for RPA calculations and PBE coverage effects are utilized:

$$E^{RPA}(\theta = \frac{1}{x}ML) = E^{RPA}(\theta = \frac{1}{4}ML) + E^{PBE}(\theta = \frac{1}{x}ML) - E^{PBE}(\theta = \frac{1}{4}ML) \quad \text{(C.11)}$$

The low coverage calculations are performed on 3×3 surface, $\theta = \frac{1}{9}$, and 4×4 surface, $\theta = \frac{1}{16}$. The results are shown in Fig. C.5. For the diffusion along the [100] direction, no significant changes are observed. For the diffusion along the [110] direction, coverage effects slightly decrease the barrier from 250 meV at $\theta = \frac{1}{4}$ to 232 meV at $\theta = \frac{1}{9}$ and 219 meV at $\theta = \frac{1}{16}$. Even though this change in energetics when extrapolating results to lower coverages is not sufficient to reach agreement between our calculations and experiments, coverage effects seem to lower barriers along the top-hollow-top pathway more than along the top-bridge top pathway. It is worth mentioning that coverage effects lower the energy of CO adsorbed in the hollow site significantly: from 245 meV at $\theta = \frac{1}{4}$ to 202 meV at $\theta = \frac{1}{9}$ and 177 meV at $\theta = \frac{1}{16}$. As the results, the energy of the 1.62 Å image, which is the TS without coverage

effects, decreases significantly as well: from 250 meV at $\theta = \frac{1}{4}$ to 214 meV at $\theta = \frac{1}{9}$ and 192 meV at $\theta = \frac{1}{16}$. However, images close to PBE TS are only slightly lowered, resulting in the TS shifting to earlier position in extrapolated profiles, similar to the different TS positions of PBE and RPA profiles. We want to emphasize that coverage effects were calculated at PBE level, but significant differences in adsorption site preference and overall energies between PBE and RPA might lead to coverage effects of a different magnitude at RPA level. The lateral interaction at PBE level is calculated to be rather small: top site at $\frac{1}{4}$ coverage has a lateral interaction of 13 meV compared to the $\frac{1}{16}$ coverage case.

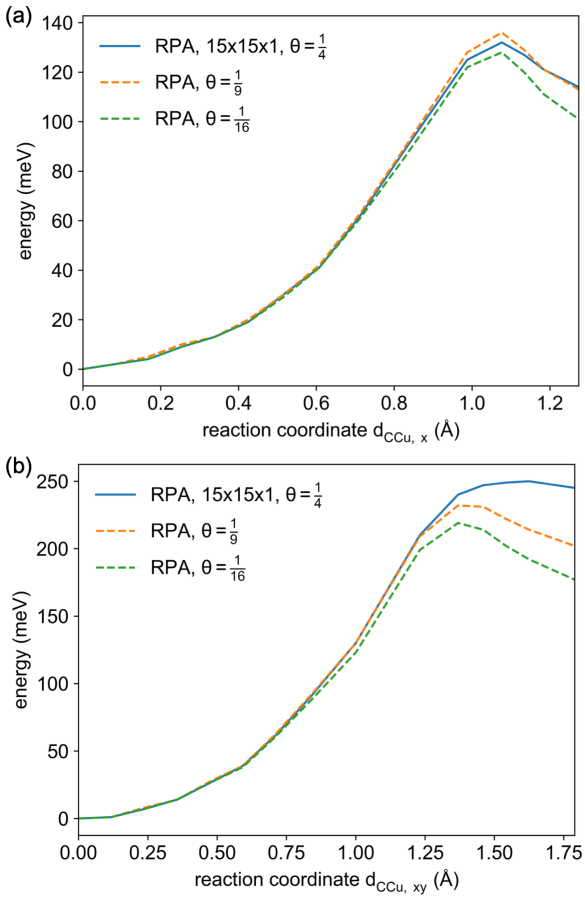

Figure C.5: RPA energy profiles for the CO diffusion along the [100] (a) and [110] (b) direction extrapolated with PBE coverage effects. Extrapolated low coverage profiles shown as dashed lines.

APPENDIX D

Supporting Information for Chapter 5

D.1 Computational Setup

The convergence of adsorption energies with respect to k-point meshes are tested on the CO case using the PBE functional:

k-point mesh	Ads E (eV)
2×3	-0.905
3×4	-0.762
4×6	-0.823
6×8	-0.815
8×12	-0.819

Table D.1: The convergence of CO adsorption energies with respect to k-point meshes using the PBE functional. Raw energies without any correction are presented.

We found that convergence of ca. 5 meV (10 meV) level is achieved with a 6×8 (4×6) k-point mesh. We choose to use a 6×8 k-point mesh at the DFT level.

A correction regarding the number of layers is applied to all the reported energetics:

$$\Delta E_{layers} = E^{PBE}_{6\ layers} - E^{PBE}_{3\ layers} \tag{D.1}$$

The correction values are as follows:

Adsorbate	Correction
*CO	-0.007
*CHO	0.031
*COH	0.016
*CHOH	-0.001
*CH_3	0.006
*CO+*CO	0.044
*CO+*CHO	0.061
*CO+*COH	0.022
*OCCO(CO)	0.034
*OCCO(CC)	-0.058
*OCCHO	-0.018
*OCCOH	-0.002

Table D.2: Layer corrections for different adsorbates. All values are shown in units of eV.

The implicit solvation effects were described using the VASPsol add-on package[80, 81], which implements linearized Poisson Boltzmann model. The dielectric constant of water, 78.4, and the Debye screening length corresponding to 1 M concentration of electrolytes, 3.0 Å, were used.

For all DFT methods, the energy of molecular reference energies (CO and H_2) were calculated using a 15×16×17 $Å^3$ supercell to suppress the spurious interactions between periodic images. RPA calculations relied on optimized PBE structures, and the values were extrapolated to the isolated molecule limit based on a series of calculations with different box sizes (7×8×9 $Å^3$, 8×9×10 $Å^3$, 9×10×11 $Å^3$, and 10×11×12 $Å^3$ for E_{cut}^{χ} =200 eV and 250 eV, and additional 11×12×13 $Å^3$ for E_{cut}^{χ} =100 eV and 150 eV). Molecular calculations were performed with a $\mathbf{\Gamma}$ point only k-point mesh.

The vibrational frequencies were calculated within the harmonic approximation using the PBE functional and frequencies below 50 cm^{-1} were reset to 50 cm^{-1}. We have performed

tests and found that the differences between PBE and RPBE free energy components are below 10 meV. The calculated electronic energies were converted into free energies in the following way: for surface species, only vibrational entropies were included; for gas phase molecules, translational and rotational entropies were included as well. The fugacity values of gas molecules are take from Ref. [43].

$$\Delta G = \Delta E + ZPE - TS \tag{D.2}$$

Adsorbate	ZPE	TS
CO(gas)	0.132	0.690
H_2(gas)	0.266	0.406
H_2O(gas)	0.562	0.675
*CO	0.187	0.182
*CHO	0.437	0.176
*COH	0.450	0.169
*CHOH	0.750	0.193
*CH_3	0.892	0.174
*CO+*CO	0.373	0.363
*CO+*CHO	0.617	0.348
*CO+*COH	0.647	0.273
*OCCO(CO)	0.418	0.237
*OCCO(CC)	0.356	0.251
*OCCHO	0.667	0.256
*OCCOH	0.698	0.247

Table D.3: Free energy components of different adsorbates and gas phase molecules. All values are shown in units of eV.

We choose not to add the van der Waals (vdW) correction as it further overestimates the adsorption strength of intermediates when combined with PBE, while for RPBE it deviates

from the initial purpose of having a correct CO adsorption energy.

D.2 RPA Energetics details

All the RPA energetics were based on PBE geometries. For RPA-sol energetics we also used the vacuum PBE geometries as we have tested both for *CO, *COH and *CHO, starting from PBE and PBE-sol structures while PBE structures give lower energy. The focus of RPA energetics on occupied and unoccupied orbitals leads to two challenges: First, the true orbitals are unknown, and they are typically approximated by orbitals obtained from semi-local DFT functionals[147, 148, 149, 150, 51]. For CO adsorption, it has been shown[178] that the RPA energetics based on PBE, RPA@PBE, and RPBE orbitals, RPA@RPBE, give essentially the same results. In this work, we rely on RPA calculations using the PBE orbitals and PBE one-electron energies (RPA@PBE). Second, in principle an infinite number of unoccupied orbitals exists, and all orbitals need to be considered to arrive at an accurate E_c^{RPA}. However, evaluating expressions for an infinite number of orbitals is not possible in a realistic computational setting. In practical implementations, E_c^{RPA} is evaluated at different orbital cutoff energies E_{cut}^{χ}, and is extrapolated to an infinite orbital cut-off energy using

$$E_c^{RPA}(E_{cut}^{\chi}) = E_c^{RPA}(\infty) + \frac{A}{{E_{cut}^{\chi}}^{\frac{3}{2}}} \tag{D.3}$$

Even though E_c^{RPA} is extrapolated to infinite orbital cut-off energy, extrapolations based on higher E_{cut}^{χ} values improve the accuracy. At the same time, a higher E_{cut}^{χ} significantly increases the cost of calculations and in many cases makes the modeling of extended, periodic systems unfeasible. We test the influence of the E_{cut}^{χ} on the CO adsorption on a 2×2 Cu(100) model with a 3×3×1 k-point mesh and found that at $E_{cut}^{\chi} = 200eV$ the convergence of absolute RPA CO adsorption energy is achieved.

E^{χ}_{cut}	Adsorption energy
100 eV, 3×3×1	-0.548
150 eV, 3×3×1	-0.560
200 eV, 3×3×1	-0.570
250 eV, 3×3×1	-0.570

Table D.4: Convergence of RPA CO adsorption energy with respect to E^{χ}_{cut}. All values are shown in units of eV. PBE geometries are used.

In order to model the extended system, a k-point mesh is needed while the number of k-points included in the computational modeling is directly correlated to the computational cost. In particular, for high cutoff energy RPA calculations, using a dense k-point mesh is often not feasible. Therefore, we use the k-space ONIOM like scheme[53, 178] to describe the energetics.

For the 3×2 surface models, the energy is described using:

$$E^{RPA}(200\ eV, 4\times6\times1, ex) = E^{RPA}(200\ eV, 3\times4\times1) + E^{RPA}(100\ eV, 4\times6\times1) - E^{RPA}(100\ eV, 3\times4\times1) \tag{D.4}$$

In this expression, the first number in brackets refers to the maximum E^{χ}_{cut} value, while the second set of numbers refers to the k-point mesh used, while the second set of numbers refers to the k-point mesh used. The ex notation indicates the extrapolated energetics. Since we are studying a metallic slab extended in x and y direction, only one k-point is used in z direction.

Due to the computational cost, a direct validation with $E^{RPA}(200\ eV, 4\times6\times1, ex)$, which requires direct calculation of $E^{RPA}(200\ eV, 4\times6\times1)$, is beyond our current capability at the RPA level. Therefore, we show the validation at a lower E^{χ}_{cut}, $E^{RPA}(150\ eV, 4\times6\times1, ex)$ for the CO adsorption energetics, as we have shown that the convergence with respect to E^{χ}_{cut} is rather acceptable at $E^{\chi}_{cut} = 150\ eV$. We tested two different choices, to start from either less expensive $E^{RPA}(150\ eV, 2\times3\times1)$ or more costly $E^{RPA}(150\ eV, 3\times4\times1)$.

For the $E^{RPA}(150\ eV, 2\times3\times1)$ case:

$$E^{RPA}(150\ eV, 4\times6\times1, ex) = E^{RPA}(150\ eV, 2\times3\times1)+ \\ E^{RPA}(100\ eV, 4\times6\times1) - E^{RPA}(100\ eV, 2\times3\times1) \tag{D.5}$$

E^{χ}_{cut}	Adsorption Energy
100 eV, 2×3×1	-0.647
100 eV, 4×6×1	-0.536
150 eV, 2×3×1	-0.641
150 eV, 4×6×1	-0.551
150 eV, 4×6×1, ex	-0.531

Table D.5: Convergence of the k-space ONIOM like scheme. All values are shown in units of eV. PBE geometries are used.

For the $E^{RPA}(150\ eV, 3\times4\times1)$ case:

$$E^{RPA}(150\ eV, 4\times6\times1, ex) = E^{RPA}(150\ eV, 3\times4\times1)+ \\ E^{RPA}(100\ eV, 4\times6\times1) - E^{RPA}(100\ eV, 3\times4\times1) \tag{D.6}$$

E^{χ}_{cut}	Adsorption Energy
100 eV, 3×4×1	-0.500
100 eV, 4×6×1	-0.536
150 eV, 3×4×1	-0.516
150 eV, 4×6×1	-0.551
150 eV, 4×6×1, ex	-0.551

Table D.6: Convergence of the k-space ONIOM like scheme. All values are shown in units of eV. PBE geometries are used.

We found that the starting from $E^{RPA}(150\ eV, 2\times3\times1)$ gives a convergence of 20 meV while starting from the more costly $E^{RPA}(150\ eV, 3\times4\times1)$ gives well converged energetics,

with the error below 1 meV. Therefore, for the final energetics presented, energetics were extrapolated from $E^{RPA}(200\ eV, 3\times4\times1)$ to ensure smaller errors from this extrapolation scheme. It can be noted that the k-point mesh is not as dense as the DFT ones. We have performed test with $E^{\chi}_{cut} = 100\ eV$ and various k-point meshes to check the influences:

k-point mesh	Ads E (eV)
2×3	-0.647
3×4	-0.500
4×6	-0.536
6×8	-0.539

Table D.7: The convergence of CO adsorption energies with respect to k-point meshes using at the RPA level with $E^{\chi}_{cut} = 100\ eV$. Layer corrections are not applied here.

We found that using a 4×6 k-point mesh the convergence of ca. 5 meV is achieved. Therefore we report the energetics of $E^{RPA}(200\ eV, 4\times6\times1, ex)$ in this work.

The final vacuum energetics used in this work are:

G_{vac} (eV)	RPA	PBE	RPBE
*CO	-0.002	-0.258	0.019
*CHO	0.799	0.502	1.022
*COH	1.081	0.648	1.194
*CHOH	1.510	1.067	1.617
*CH_3	-0.158	-1.210	-0.001
*CO+*CO	0.021	-0.485	0.100
*CO+*CHO	0.824	0.264	1.026
*CO+*COH	1.348	0.420	1.333
*OCCO(CO)	1.399	0.584	1.374
*OCCO(CC)	1.594	0.640	1.231
*OCCHO	1.094	0.393	1.371
*OCCOH	1.559	0.543	1.423

Table D.8: Vacuum adsorption free energies used in the main text. All values are shown in units of eV.

The final implicitly solvated energetics used in this work are:

G_{sol} (eV)	RPA	PBE	RPBE
*CO	-0.019	-0.278	-0.004
*CHO	0.758	0.462	0.980
*COH	0.881	0.439	0.997
*CHOH	1.257	0.848	1.410
*CH_3	-0.172	-1.220	-0.015
*CO+*CO	-0.006	-0.530	0.047
*CO+*CHO	0.785	0.177	0.962
*CO+*COH	1.269	0.263	1.151
*OCCO(CO)	1.294	0.481	1.245
*OCCO(CC)	1.360	0.357	1.036
*OCCHO	0.986	0.290	1.174
*OCCOH	1.320	0.303	1.170

Table D.9: Implicitly solvated adsorption free energies used in the main text. All values are shown in units of eV.

We have also performed tests on the strain effects, i.e., the difference in adsorption energy compared to the case where PBE, RPBE, and RPA lattice parameters for each method are used. Values shown below are raw adsorption energies without any correction.

Method	lattice parameter	Ads E (eV)
PBE	EXP	-0.815
PBE	PBE	-0.823
RPBE	EXP	-0.537
RPBE	RPBE	-0.567
RPA	EXP	-0.558
RPA	RPA	-0.581
PBE-sol	EXP	-0.834
PBE-sol	PBE	-0.842
RPBE-sol	EXP	-0.560
RPBE-sol	RPBE	-0.589
RPA-sol	EXP	-0.576
RPA-sol	RPA	-0.600

Table D.10: Strain effects of using the experimental lattice parameter. Raw energies without any correction are presented.

We found that the strain effects on adsorption energies are at most 30 meV and hence do not affect the conclusions. Therefore, we use the experimental lattice parameter through this work.

D.3 Comparison of Different Solvation Treatments

We list the explicit solvation corrections of the *OCCOH and *OCCHO used in different works where the numerical values are available.

solvation correction (eV)	*OCCHO	*OCCOH
this work (implicit)	-0.11	-0.23
Liu et al.[176]	-0.5	-0.45
Peng et al.[175]	-0.3	-0.3
Calle-Vallejo et al.[173]	-0.1	-0.38
Heenen et al.[a][177]	0.09	0.12
Ludwig et al.[b][186]	-0.3	-0.3

a: using the value of *CHO and *COH

b: no numerical values provided but cited by Peng et al.

Table D.11: Explicit solvation corrections used by other studies compared with the implicit solvation value used by this work.

D.4 Adsorbate-Adsorbate Interactions

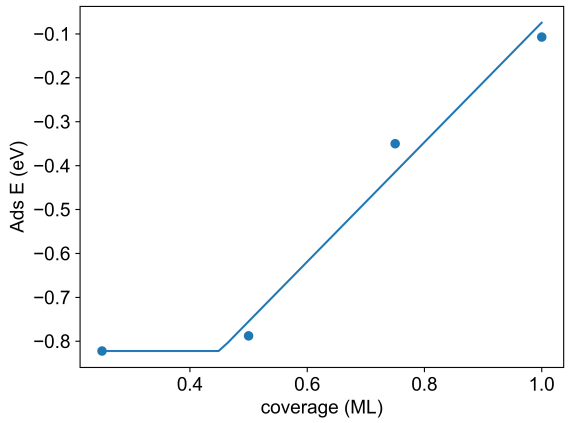

Figure D.1: Coverage dependent CO adsorption on Cu(100) facet using the PBE functional. Solid lines are fitted using the 0.5, 0.75 and 1 coverage data points to estimate the threshold coverage, which is found to be larger than 0.4.

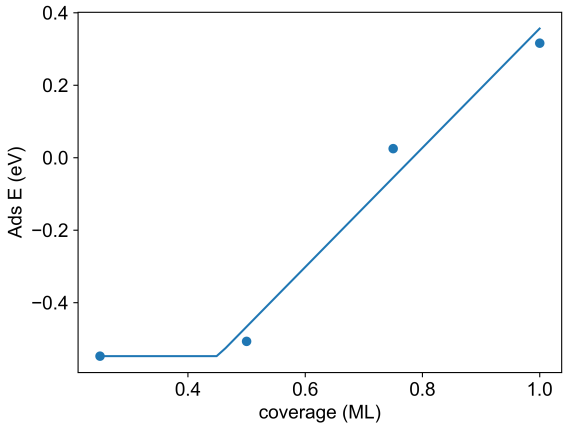

Figure D.2: Coverage dependent CO adsorption on Cu(100) facet using the RPBE functional. Solid lines are fitted using the 0.5, 0.75 and 1 coverage data points to estimate the threshold coverage, which is found to be larger than 0.4.

The adsorbate-adsorbate interactions are critical and we consider these using the approach of Liu et al.[176]. As shown in the figures, we found that on the Cu(100) facet, the coverage effect is not significant until over half coverage: 35 and 41 meV using PBE and RPBE, respectively. We have also fitted a linear relationship using the latter three data points to estimate the threshold coverage, which in both cases are found to be larger than 0.4. As Liu et al. [176] have shown that the highest CO coverage in the CORR or CO_2RR condition is ca. 0.4, we estimate the effects of adsorbate-adsorbate interaction to be weak for Cu(100). For C_2 species, the approach of Liu et al. [176] assumes the the interaction parameters between CO and the C_2 species are the same as the one between CO and CO, which suggests the influence of adsorbate-adsorbate interactions on C_2 species to be also small. Therefore, we do not explicitly add these estimated values into the values presented in the main text.

D.5 Energetics of Further Hydrogenation Products Along the C_1 Pathway

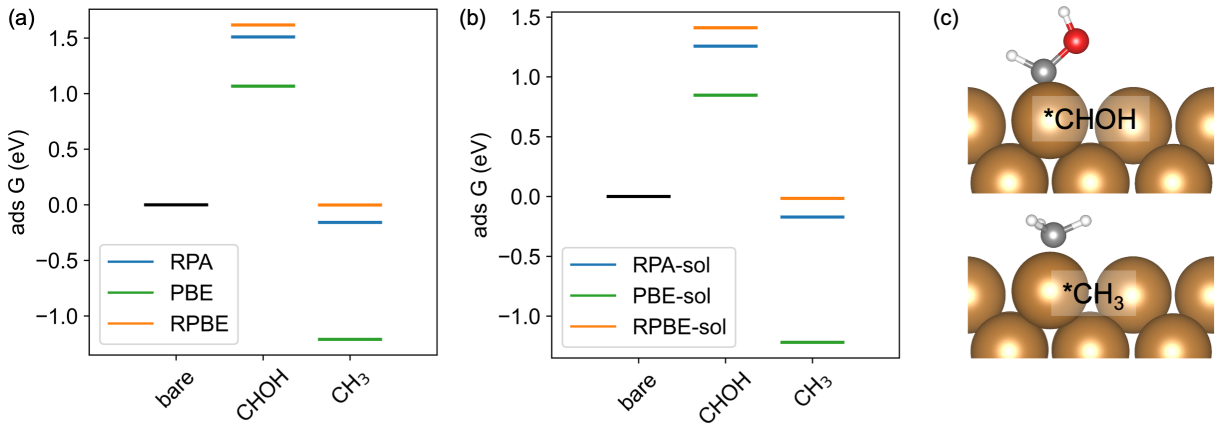

Figure D.3: (a) Energetics of *CHOH and *CH_3 using RPA and PBE/RPBE functionals at the Cu(100)-vacuum interface. (b) Implicitly solvated energetics of *CHOH and *CH_3 using RPA and PBE/RPBE functionals on the Cu(100) facet. (c) Side view of the atomic structures. Cu atoms are shown as brown, O atoms red, C atoms grey, and H atoms white.

We found no qualitative difference between the RPA energetics and the GGA DFT energetics. The RPA energetics were found to be slightly more negative compared to the RPBE values, and this is the case for most of the adsorbates considered.

D.6 Surface Charging and Extrapolated RPA-SC Energetics

In the computational hydrogen electrode (CHE) approach[183], the total chemical potential of the proton-electron pair as a function of applied potential, at all temperature and pH values, can be calculated as:

$$\mu(H^+) + \mu(e^-) = \frac{1}{2}\mu(H_{2(gas)}) - eU^{RHE} \tag{D.7}$$

and when calculating the only the potential response of the proton electron pair in the adsorption energy is considered:

$$G_{adsorption,C_xO_xH_y}(U^{RHE}) = G_{*C_xO_xH_y} - G_{slab} - xG_{CO} - y(\frac{1}{2}\mu(H_{2(gas)}) - eU^{RHE}) \quad \text{(D.8)}$$

where * indicates the adsorbate.

In the surface charging (SC) approach, the potential response of the bare slab and the slab with adsorbates are both considered ab initio, we briefly summarize the main formulas here, and more details can be found in the following Refs[190, 191, 81]. As mentioned by Mathew et al.[81], an correction needs to be applied to the electronic energy:

$$E_{surface} = E^{raw}_{surface} + n_{surface}\Delta U_{ref} \quad \text{(D.9)}$$

where $E^{raw}_{surface}$ is the raw electronic energy of the surface; the $n_{surface}$ is the net charge of the surface, being positive if electrons are removed and negative if electrons are added; ΔU_{ref} is the change in reference potential, i.e., the shift to align the potential in the electrolyte region to zero. Then the grand-canonical electronic energy of a surface model, $F(n)$, as a function of net charge of the surface, $n_{surface}$, corresponding to a certain potential of the system, U^{vac}, is calculated as:

$$F(n) = F(U^{vac}) = E_{surface} - n_{surface}U^{vac} \quad \text{(D.10)}$$

where U^{vac} is the potential of the system with reference to the vacuum, determined ab initio after a grand canonical calculation is finished:

$$W = eU^{vac} \quad \text{(D.11)}$$

where W is the work function of the system after the charge is injected or removed. This potential with reference to the vacuum, U^{vac}, can be converted to potential with reference to the standard hydrogen electrode (SHE), U^{SHE}, using the IUPAC recommended value, $U^{vac} = U^{SHE} + 4.44V$. A further conversion can be done to achieve the potential with reference to the relative hydrogen electrode (RHE), $U^{RHE} = U^{SHE} + k_bTln10pH$.

To validate the grand canonical calculations setups, we compare the calculated potential of zero charge (PZC) and capacitance values of the Cu(100) facet with the experimental values. The extrapolation presented in the main text only utilizes the RPBE and 1M electrolyte concentration. The trend of larger concentration leading to larger capacitance is also observed in the experiments[220].

Method	electrolyte concentration (M)	PZC (V) vs SHE	capacitance (μF/cm^2)
RPBE	1	-0.43	17.2
RPBE	0.1	-0.43	14.7
PBE	0.1	-0.24	14.3
exp[221]		-0.54	
exp[222]		-0.54	
exp[222]		-0.46	
exp[221]			20-25

Table D.12: PZC and capacitance values Cu(100) facet using PBE and RPBE functionals.

The PZC and capacitance values of Cu(100) facet using the RPBE functional matches reasonably well with the experimental values.

At certain potential with reference to the RHE, U^{RHE}, the SC adsorption energy is calculated as:

$$G_{adsorption,C_xO_xH_y}(U^{RHE}) = F_{*C_xO_xH_y}(U^{RHE}) - F_{slab}(U^{RHE}) - xG_{CO} - y(\frac{1}{2}\mu(H_{2(gas)}) - eU^{RHE}) \tag{D.12}$$

where both the potential dependent grand-canonical electronic energies of the slab with adsorbates $F_{*C_xO_xH_y}(U^{RHE})$, and the bare slab, $F_{slab}(U^{RHE})$, need to be calculated.

For all the SC calculations, symmetric slabs of five layers were used, being constructed by the symmetrization of the 3×2 cell, three layer slab models. A slab separation of at least 50 Å ($> 15\lambda_D$ where λ_D is the Debye screening length) was used to ensure the convergence of the electrolyte density[191]. The symmetric model ensures a well defined vacuum energy

level. The side view of the symmetric *OCCHO model is shown is shown for example:

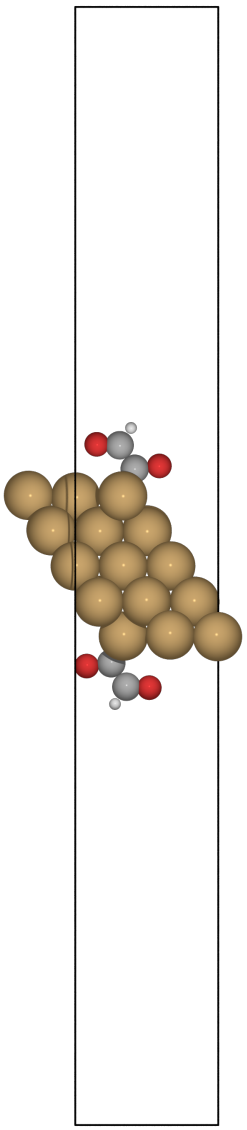

Figure D.4: Side view of the *OCCHO model used in the SC calculation, shown for the neutral charge one. Cu atoms are shown as brown, O atoms red, C atoms grey, and H atoms white. The 3×2 unit cell has a size of 7.668×5.112×60 $Å^3$.

Geometry optimizations were performed with seven different net charges for each system to fit the quadratic relationship between the the grand-canonical electronic energy, $F(U^{SHE})$, and the potential with reference to the SHE. Structural convergence was assumed for forces

lower than 0.02 eV/Å. The $F-U$ relationship of the *OCCHO system is shown for example:

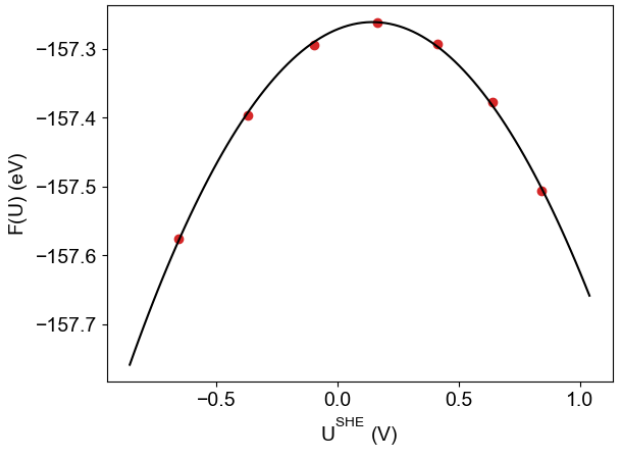

Figure D.5: The grand-canonical electronic energy, $F(U)$, of the *OCCHO system as a function of the potential with reference to SHE, U^{SHE}. Red dots show the calculated energies of systems with different net charges and black curve shows the fitter quadratic relationship.

The same values of layer corrections and free energy components are applied to the symmetric system, with a coefficient of 2, to convert the energies to the final free energies presented. The potential dependent adsorption free energies, $G^{RPA-SC}_{extrapolated}$, $G^{RPA-CHE}$, $G^{RPBE-SC}$, and $G^{RPBE-CHE}$, for *OCCO (CC), *OCCO (CO), and *OCCOH adsorbates, at condition of pH=7, are shown in the following figures. For *OCCO(CC) and *OCCO(CV), only the treatment at the SC level is shown: at the CHE level the adsorption energy does not change with the potential, as no H is presented in these two adsorbates.

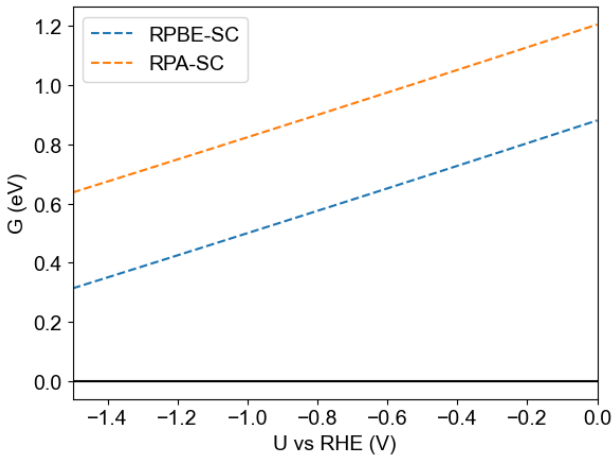

Figure D.6: Potential dependent adsorption free energy of *OCCO(CC) and predicted onset potential of ethylene production, using RPA and RPBE energetics, at condition of pH=7. The potential effects are treated at the SC level, with RPA-SC energetics being extrapolated as described in Eq. 1 in the main text. The predicted onset potential is more negative than -1.5 V versus RHE, suggesting that the formation of *OCCO(CC) is not the PDS.

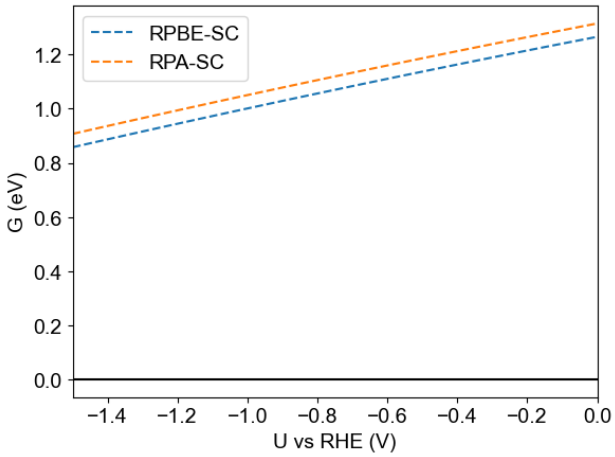

Figure D.7: Potential dependent adsorption free energy of *OCCO(CO) and predicted onset potential of ethylene production, using RPA and RPBE energetics, at condition of pH=7. The potential effects are treated at the SC level, with RPA-SC energetics being extrapolated as described in Eq. 1 in the main text. The predicted onset potential is more negative than -1.5 V versus RHE, suggesting that the formation of *OCCO(CO) is not the PDS.

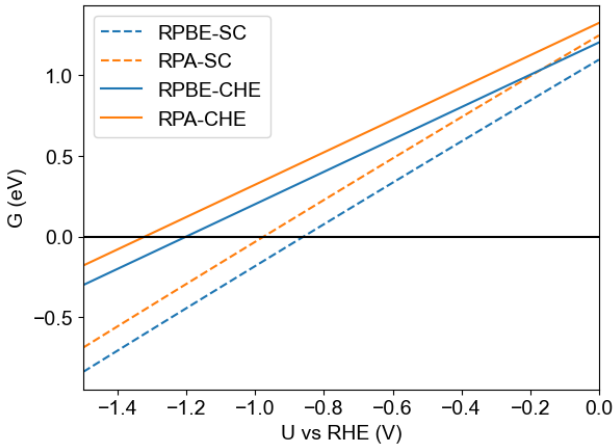

Figure D.8: Potential dependent adsorption free energy of *OCCOH and predicted onset potential of ethylene production, using RPA and RPBE energetics, at condition of pH=7. The potential effects are treated at the CHE and the SC level, with RPA-SC energetics being extrapolated as described in Eq. 1 in the main text. The crossing point with the horizontal black line indicates the onset potential. $U_{onset}^{RPBE-CHE} = -1.17V$, $U_{onset}^{RPA-CHE} = -1.32V$, $U_{onset}^{RPBE-SC} = -0.86V$, $U_{onset}^{RPA-SC} = -0.98V$

APPENDIX E

Supporting Information for Chapter 6

E.1 Computational Details

All the calculations in this work were performed with the VASP code[76] with a plane wave cutoff energy of 550 eV. The lattice parameters for different systems are listed in Table E.1.

System	Method	Lattice Parameter (Å)
Cu	PBE	3.629[178]
Cu	RPBE	3.672[178]
Cu	RPA	3.581[52]
Ag	RPA	4.082[52]
Au	RPA	4.104[52]

Table E.1: The lattice parameters used in this work.

The k-point meshes for different systems are listed in Table E.2.

System	K-point mesh
Cu(100) 1×1	18×18×1
Cu(100) $\sqrt{2} \times \sqrt{2}$ PBE/RPBE	14×14×1
Cu(100) $\sqrt{2} \times \sqrt{2}$ RPA	10×10×1
Cu(110) 1×1	12×16×1
Cu(111) 1×1	20×20×1
Ag(100) 1×1	16×16×1
Ag(110) 1×1	12×16×1
Ag(111) 1×1	20×20×1
Au(100) 1×1	14×14×1
Au(110) 1×1	12×16×1
Au(111) 1×1	20×20×1

Table E.2: The k-point meshes used in this work.

For all DFT methods, the energy of the CO molecule reference energy was calculated using a 15×16×17 Å^3 supercell to suppress the spurious interactions between periodic images. RPA calculations relied on PBE optimized structures, and the values were extrapolated to the isolated molecule limit based on a series of calculations with different box sizes (7×8×9 Å^3, 8×9×10 Å^3, 9×10×11 Å^3, and 10×11×12 Å^3 for E^{χ}_{cut} =200 eV, and additional 11×12×13 Å^3 for E^{χ}_{cut} =100 eV and 150 eV). Molecular calculations were performed with a $\mathbf{\Gamma}$ point only k-point mesh.

The influence of the inter-slab separation on the CO adsorption energy was checked at the PBE level, on a 5 layer 1×1 Cu(100) slab. The adsorption energy is found to be well converged with a separation of 20 Å, as shown in Fig. E.1. Therefore, we use a 20 Å inter-slab separation for the calculations in this work.

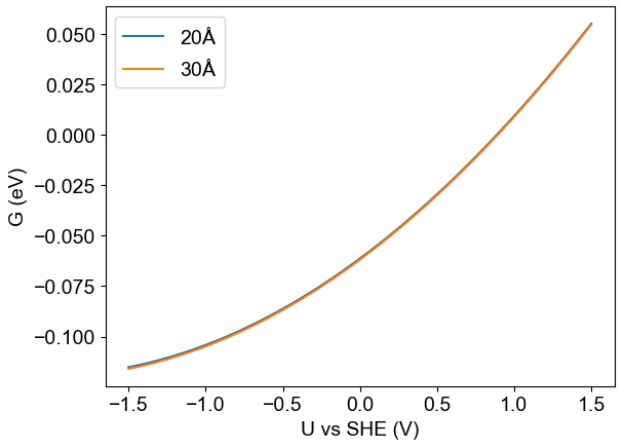

Figure E.1: The influence of the inter-slab separation on the potential dependent CO adsorption energy on the atop site of a 1×1 Cu(100) facet with different separations using the PBE functional.

The influence of the excitation energy cutoff E^{χ}_{cut} on the PZC values was checked at the RPA level, on a 5 layer 1×1 Cu(100) slab. The PZC values was found to be converged to 10 mV level with an excitation energy cutoff E^{χ}_{cut} of 100 eV, as shown in Table. E.3. Therefore, we report the PZC values of different facets with an excitation energy cutoff $E^{\chi}_{cut} = 100\ eV$.

E^{χ}_{cut}	PZC vs SHE (V)
100 eV	0.371
150 eV	0.361
200 eV	0.364

Table E.3: The influence of the excitation energy cutoff E^{χ}_{cut} on the PZC values of a 1×1 Cu(100) slab using the RPA energetics. IUPAC recommended ΔU^{pred}_{SHE}=4.44 V was used.

The influence of the excitation energy cutoff E^{χ}_{cut} on the CO adsorption energy was checked at the RPA level, on a 5 layer 1×1 Cu(100) slab. The adsorption energy is found to be converged to 10 meV level with an excitation energy cutoff E^{χ}_{cut} of 150 eV, as shown in Fig. E.2. Therefore, we report the CO adsorption energies at the RPA level with an excitation energy cutoff $E^{\chi}_{cut} = 150\ eV$.

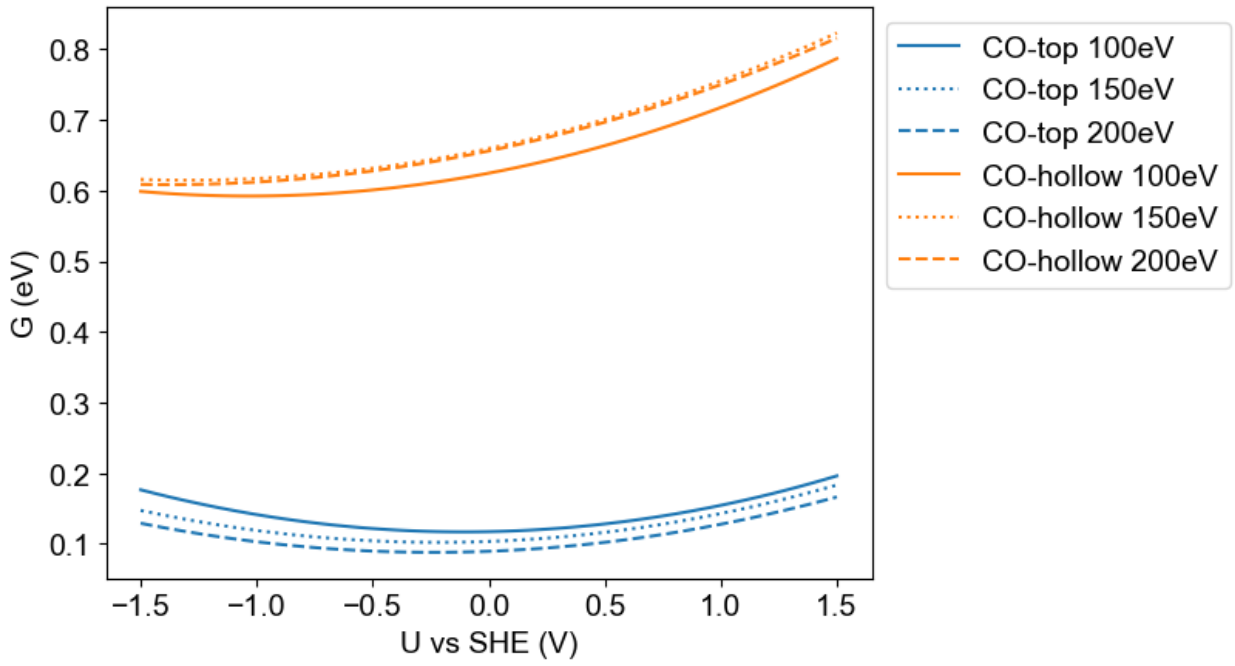

Figure E.2: The influence of the excitation energy cutoff E_{cut}^{χ} on the potential dependent CO adsorption energy on the atop and hollow site of a 1×1 Cu(100) facet.

E.2 Comparison between the SCF and the Energetic Approaches of the Cu(100) Facet at the PBE Level

As indicated in the main text, the comparison between the SCF and the energetic approaches of the bare Cu(100) slab is provided: similar to the case where CO is adsorbed, these two approaches provide very close results for the bare slab.

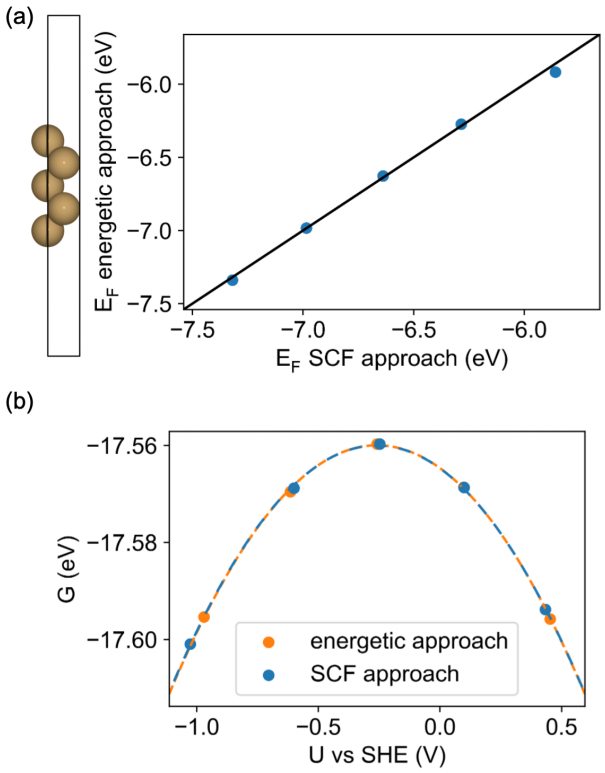

Figure E.3: (a) E_F values achieved using the energetic approach compared to the ones taken directly from the SCF electronic structure. The blue dots are the data and the black line indicates a perfect match. The corresponding structure, a 5 layer slab exposing 1×1 Cu(100) facet, is shown. Cu atoms are shown as brown, O atoms red, and C atoms grey. (b) The potential dependent free energy of the adsorbed CO system calculated using the energetic approach compared to the results using the SCF approach. Dots are data points and dashed lines are the fitted parabola.

E.3 The Grand Canonical Relationship Achieved Using the Fermi Level of the Underlying Orbitals

As indicated in the main text, if an incorrect Fermi level is used, the quadratic behavior around the PZC cannot be achieved. One example is given for the 1×1 Cu(100) slab RPA energetics, using the Fermi level of the underlying PBE orbitals.

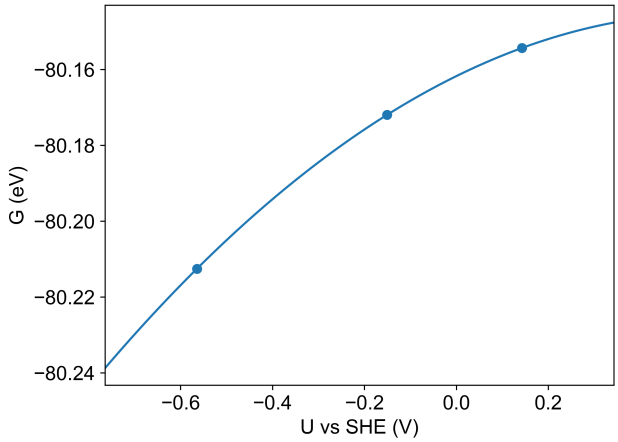

Figure E.4: Grand canonical RPA energetics achieved using the Fermi level of the underlying PBE orbitals.

The incorrect grand canonical energetics here stress the necessity of the alternative approach to get the correct Fermi level.

E.4 Experimental PZC Values

Facet	PZC (V) vs SHE		
Cu(100)	-0.54	Au(100)	0.33
Cu(100)	-0.46	Au(100)	0.29
Cu(110)	-0.63	Au(100)	0.32
Cu(110)	-0.69	Au(100)	0.30
Cu(111)	-0.33	Au(110)	0.19
Cu(111)	-0.20	Au(110)	0.19
Ag(100)	-0.609	Au(111)	0.56
Ag(100)	-0.621	Au(111)	0.56
Ag(100)	-0.616	Au(111)	0.55
Ag(110)	-0.734	Au(111)	0.58
Ag(110)	-0.734	Au(111)	0.47
Ag(110)	-0.735	Au(111)	0.47
Ag(111)	-0.45		
Ag(111)	-0.454		
Ag(111)	-0.454		
Ag(111)	-0.45		
Ag(111)	-0.46		

Table E.4: Experimental PZC values used in this work. All the values are taken from Ref.[222]. Each entry is treated as one separate value and the final values used are simple averaged values of each facet.

E.5 Potential Dependent Energetics of CO Adsorption Using Fitted ΔU_{SHE}^{pred}=5.31 V for RPA

As indicated in the main text, the potential dependent CO adsorption energy can be also calculated using the fitted ΔU_{SHE}^{pred}=5.31 V. As shown in Fig. E.5, this only shifts the RPA crossing to more negative potential and does not affect any conclusion made in the main text.

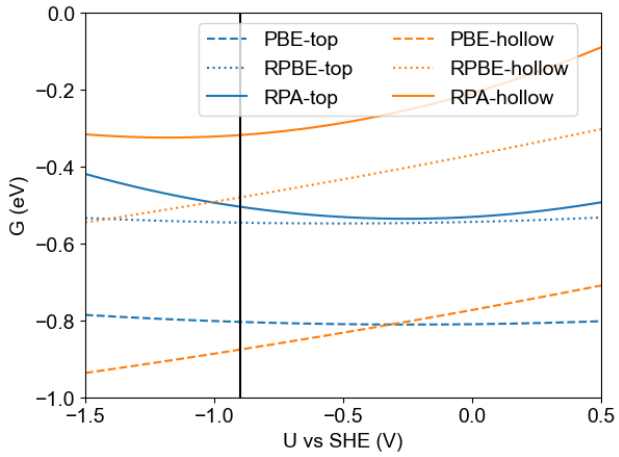

Figure E.5: Potential dependent energetics of CO adsorbed at top (blue) and hollow (orange) site, using the grand canonical treatment with the PBE (dashed line), RPBE functionals (dotted line), and RPA (solid line). The experimentally inferred structure, where half of atop sites are covered by CO was used. The fitted ΔU_{SHE}^{pred}=5.31 V was used to convert the vacuum scale to the SHE scale for the RPA energetics.

Bibliography

[1] Peter U. Clark, Jeremy D. Shakun, Shaun A. Marcott, Alan C. Mix, Michael Eby, Scott Kulp, Anders Levermann, Glenn A. Milne, Patrik L. Pfister, Benjamin D. Santer, Daniel P. Schrag, Susan Solomon, Thomas F. Stocker, Benjamin H. Strauss, Andrew J. Weaver, Ricarda Winkelmann, David Archer, Edouard Bard, Aaron Goldner, Kurt Lambeck, Raymond T. Pierrehumbert, and Gian-Kasper Plattner. Consequences of twenty-first-century policy for multi-millennial climate and sea-level change. *Nat. Clim. Change.*, 6(4):360–369, February 2016.

[2] Stephane Hallegatte, Joeri Rogelj, Myles Allen, Leon Clarke, Ottmar Edenhofer, Christopher B. Field, Pierre Friedlingstein, Line van Kesteren, Reto Knutti, Katharine J. Mach, Michael Mastrandrea, Adrien Michel, Jan Minx, Michael Oppenheimer, Gian-Kasper Plattner, Keywan Riahi, Michiel Schaeffer, Thomas F. Stocker, and Detlef P. van Vuuren. Mapping the climate change challenge. *Nat. Clim. Change*, 6(7):663–668, June 2016.

[3] Carl-Friedrich Schleussner, Joeri Rogelj, Michiel Schaeffer, Tabea Lissner, Rachel Licker, Erich M. Fischer, Reto Knutti, Anders Levermann, Katja Frieler, and William Hare. Science and policy characteristics of the Paris agreement temperature goal. *Nat. Clim. Change*, 6(9):827–835, July 2016.

[4] Peter Alstone, Dimitry Gershenson, and Daniel M. Kammen. Decentralized energy systems for clean electricity access. *Nat. Clim. Change*, 5(4):305–314, March 2015.

[5] Stephanie Nitopi, Erlend Bertheussen, Soren B. Scott, Xinyan Liu, Albert K. Engstfeld, Sebastian Horch, Brian Seger, Ifan E.L. Stephens, Karen Chan, Christopher Hahn, Jens K. Nørskov, Thomas F. Jaramillo, and Ib Chorkendorff. Progress and perspectives of electrochemical CO2 reduction on copper in aqueous electrolyte. *Chem. Rev.*, 119(12):7610–7672, May 2019.

[6] Peter G. Bruce, Stefan A. Freunberger, Laurence J. Hardwick, and Jean-Marie Tarascon. Li–o2 and li–s batteries with high energy storage. *Nat. Mater.*, 11(1):19–29, dec 2011.

[7] Zhi Wei Seh, Jakob Kibsgaard, Colin F. Dickens, Ib Chorkendorff, Jens K. Nørskov, and Thomas F. Jaramillo. Combining theory and experiment in electrocatalysis: Insights into materials design. *Science*, 355(6321):eaad4998, January 2017.

[8] Qing Zhao, John Mark P. Martirez, and Emily A. Carter. Revisiting understanding of electrochemical CO2 reduction on cu(111): Competing proton-coupled electron transfer reaction mechanisms revealed by embedded correlated wavefunction theory. *J. Am. Chem. Soc.*, 143(16):6152–6164, April 2021.

[9] J.K. Nørskov, T. Bligaard, J. Rossmeisl, and C.H. Christensen. Towards the computational design of solid catalysts. *Nat. Chem.*, 1(1):37–46, April 2009.

[10] Albert Bruix, Johannes T. Margraf, Mie Andersen, and Karsten Reuter. First-principles-based multiscale modelling of heterogeneous catalysis. *Nat. Catal.*, 2(8):659–670, June 2019.

[11] Jonathan E. Sutton and Dionisios G. Vlachos. Building large microkinetic models with first-principles' accuracy at reduced computational cost. *Chem. Eng. Sci.*, 121:190–199, January 2015.

[12] Karsten Reuter. Ab initio thermodynamics and first-principles microkinetics for surface catalysis. *Catal. Lett.*, 146(3):541–563, January 2016.

[13] Mie Andersen, Chiara Panosetti, and Karsten Reuter. A practical guide to surface kinetic Monte Carlo simulations. *Front. Chem.*, 7:202, April 2019.

[14] Stephan N. Steinmann and Zhi Wei Seh. Understanding electrified interfaces. *Nat. Rev. Mater.*, 6(4):289–291, March 2021.

[15] Lele Peng, Ziyang Wei, Chengzhang Wan, Jing Li, Zhuo Chen, Dan Zhu, Daniel Baumann, Haotian Liu, Christopher S. Allen, Xiang Xu, Angus I. Kirkland, Imran Shakir, Zeyad Almutairi, Sarah Tolbert, Bruce Dunn, Yu Huang, Philippe Sautet, and Xiangfeng Duan. A fundamental look at electrocatalytic sulfur reduction reaction. *Nat. Catal.*, 3(9):762–770, August 2020.

[16] J.-M. Tarascon and M. Armand. Issues and challenges facing rechargeable lithium batteries. *Nature*, 414(6861):359–367, November 2001.

[17] John B. Goodenough and Kyu-Sung Park. The Li-ion rechargeable battery: A perspective. *J. Am. Chem. Soc.*, 135(4):1167–1176, January 2013.

[18] Peter G. Bruce, Bruno Scrosati, and Jean-Marie Tarascon. Nanomaterials for rechargeable lithium batteries. *Angew. Chem. Int. Ed.*, 47(16):2930–2946, April 2008.

[19] Peter G. Bruce, Laurence J. Hardwick, and K.M. Abraham. Lithium-air and lithium-sulfur batteries. *MRS Bull.*, 36(7):506–512, July 2011.

[20] Arumugam Manthiram, Yongzhu Fu, Sheng-Heng Chung, Chenxi Zu, and Yu-Sheng Su. Rechargeable Lithium–Sulfur batteries. *Chem. Rev.*, 114(23):11751–11787, July 2014.

[21] Quan Pang, Xiao Liang, Chun Yuen Kwok, and Linda F. Nazar. Advances in lithium–sulfur batteries based on multifunctional cathodes and electrolytes. *Nat. Energy*, 1(9):1–11, September 2016.

[22] Yuriy V. Mikhaylik and James R. Akridge. Polysulfide shuttle study in the Li/S battery system. *J. Electrochem. Soc.*, 151(11):A1969, 2004.

[23] Zhenzhen Du, Xingjia Chen, Wei Hu, Chenghao Chuang, Shuai Xie, Ajuan Hu, Wensheng Yan, Xianghua Kong, Xiaojun Wu, Hengxing Ji, and Li-Jun Wan. Cobalt in nitrogen-doped graphene as single-atom catalyst for high-sulfur content Lithium–Sulfur batteries. *J. Am. Chem. Soc.*, 141(9):3977–3985, February 2019.

[24] Zheng-Long Xu, Shenghuang Lin, Nicolas Onofrio, Limin Zhou, Fangyi Shi, Wei Lu, Kisuk Kang, Qiang Zhang, and Shu Ping Lau. Exceptional catalytic effects of black phosphorus quantum dots in shuttling-free lithium sulfur batteries. *Nat Commun*, 9(1):1–11, October 2018.

[25] Jungjin Park, Byeong-Chul Yu, Joong Sun Park, Jang Wook Choi, Chunjoong Kim, Yung-Eun Sung, and John B. Goodenough. Tungsten disulfide catalysts supported on a carbon cloth interlayer for high performance Li-s battery. *Adv. Energy Mater.*, 7(11):1602567, January 2017.

[26] Jingjing Duan, Sheng Chen, Mietek Jaroniec, and Shi Zhang Qiao. Heteroatom-doped graphene-based materials for energy-relevant electrocatalytic processes. *ACS Catal.*, 5(9):5207–5234, August 2015.

[27] P. Hohenberg and W. Kohn. Inhomogeneous electron gas. *Phys. Rev.*, 136(3B):B864–B871, November 1964.

[28] W. Kohn and L.J. Sham. Self-consistent equations including exchange and correlation effects. *Phys. Rev.*, 140(4A):A1133–A1138, November 1965.

[29] David C. Langreth and M.J. Mehl. Beyond the local-density approximation in calculations of ground-state electronic properties. *Phys. Rev. B*, 28(4):1809–1834, August 1983.

[30] John P. Perdew and Yue Wang. Accurate and simple analytic representation of the electron-gas correlation energy. *Phys. Rev. B*, 45(23):13244–13249, June 1992.

[31] John P. Perdew, Kieron Burke, and Matthias Ernzerhof. Generalized gradient approximation made simple. *Phys. Rev. Lett.*, 77(18):3865–3868, October 1996.

[32] A Gil. Site preference of CO chemisorbed on pt(111) from density functional calculations. *Surf. Sci.*, 530(1-2):71–87, April 2003.

[33] Marek Gajdoš, Andreas Eichler, and Jürgen Hafner. CO adsorption on close-packed transition and noble metal surfaces: Trends from ab initio calculations. *J. Phys. Condens. Matter*, 16(8):1141, 2004.

[34] Peter J. Feibelman, B. Hammer, J.K. Nørskov, F. Wagner, M. Scheffler, R. Stumpf, R. Watwe, and J. Dumesic. The CO/Pt(111) puzzle. *J. Phys. Chem. B*, 105(18):4018–4025, November 2000.

[35] G. Kresse, A. Gil, and P. Sautet. Significance of single-electron energies for the description of CO on pt(111). *Phys. Rev. B*, 68(7):073401, August 2003.

[36] Andrew J. Medford, Adam C. Lausche, Frank Abild-Pedersen, Burcin Temel, Niels C. Schjødt, Jens K. Nørskov, and Felix Studt. Activity and selectivity trends in synthesis gas conversion to higher alcohols. *Top. Catal.*, 57(1-4):135–142, October 2013.

[37] Julia Schumann, Andrew J. Medford, Jong Suk Yoo, Zhi-Jian Zhao, Pallavi Bothra, Ang Cao, Felix Studt, Frank Abild-Pedersen, and Jens K. Nørskov. Selectivity of synthesis gas conversion to c2+ oxygenates on fcc(111) transition-metal surfaces. *ACS Catal.*, 8(4):3447–3453, March 2018.

[38] Shyam Kattel, Pedro J Ramírez, Jingguang G Chen, José A Rodriguez, and Ping Liu. Active sites for CO2 hydrogenation to methanol on Cu/ZnO catalysts. *Science*, 355(6331):1296–1299, 2017.

[39] M. Behrens, F. Studt, I. Kasatkin, S. Kuhl, M. Havecker, F. Abild-Pedersen, S. Zander, F. Girgsdies, P. Kurr, B.-L. Kniep, M. Tovar, R.W. Fischer, J.K. Norskov, and R. Schlogl. The active site of methanol synthesis over Cu/ZnO/Al2O3 industrial catalysts. *Science*, 336(6083):893–897, April 2012.

[40] Charles T Campbell and KA Daube. A surface science investigation of the water-gas shift reaction on cu (111). *J. Catal.*, 104(1):109–119, 1987.

[41] Amit A. Gokhale, James A. Dumesic, and Manos Mavrikakis. On the mechanism of low-temperature water gas shift reaction on copper. *J. Am. Chem. Soc.*, 130(4):1402–1414, January 2008.

[42] Tao Cheng, Hai Xiao, and William A. Goddard. Free-energy barriers and reaction mechanisms for the electrochemical reduction of CO on the cu(100) surface, including multiple layers of explicit solvent at pH 0. *J. Phys. Chem. Lett.*, 6(23):4767–4773, November 2015.

[43] Andrew A. Peterson, Frank Abild-Pedersen, Felix Studt, Jan Rossmeisl, and Jens K. Nørskov. How copper catalyzes the electroreduction of carbon dioxide into hydrocarbon fuels. *Energy Environ. Sci.*, 3(9):1311, 2010.

[44] Ruud Kortlever, Jing Shen, Klaas Jan P. Schouten, Federico Calle-Vallejo, and Marc T.M. Koper. Catalysts and reaction pathways for the electrochemical reduction of carbon dioxide. *J. Phys. Chem. Lett.*, 6(20):4073–4082, September 2015.

[45] Kendra P. Kuhl, Etosha R. Cave, David N. Abram, and Thomas F. Jaramillo. New insights into the electrochemical reduction of carbon dioxide on metallic copper surfaces. *Energy Environ. Sci.*, 5(5):7050, 2012.

[46] Andreas Grüneis, Martijn Marsman, Judith Harl, Laurids Schimka, and Georg Kresse. Making the random phase approximation to electronic correlation accurate. *J. Chem. Phys.*, 131(15):154115, October 2009.

[47] P. Nozières and D. Pines. Correlation energy of a free electron gas. *Phys. Rev.*, 111(2):442–454, July 1958.

[48] Judith Harl and Georg Kresse. Cohesive energy curves for noble gas solids calculated by adiabatic connection fluctuation-dissipation theory. *Phys. Rev. B*, 77(4):045136, January 2008.

[49] O. Gunnarsson and B.I. Lundqvist. Exchange and correlation in atoms, molecules, and solids by the spin-density-functional formalism. *Phys. Rev. B*, 13(10):4274–4298, May 1976.

[50] David C. Langreth and John P. Perdew. Exchange-correlation energy of a metallic surface: Wave-vector analysis. *Phys. Rev. B*, 15(6):2884–2901, March 1977.

[51] Judith Harl and Georg Kresse. Accurate bulk properties from approximate many-body techniques. *Phys. Rev. Lett.*, 103(5):056401, July 2009.

[52] Laurids Schimka, René Gaudoin, Jiří Klimeš, Martijn Marsman, and Georg Kresse. Lattice constants and cohesive energies of alkali, alkaline-earth, and transition metals: Random phase approximation and density functional theory results. *Phys. Rev. B*, 87(21):214102, June 2013.

[53] L. Schimka, J. Harl, A. Stroppa, A. Grüneis, M. Marsman, F. Mittendorfer, and G. Kresse. Accurate surface and adsorption energies from many-body perturbation theory. *Nat. Mater.*, 9(9):741–744, July 2010.

[54] D.C. Langreth and J.P. Perdew. The exchange-correlation energy of a metallic surface. *Solid State Commun.*, 17(11):1425–1429, December 1975.

[55] Y.M. Niquet, M. Fuchs, and X. Gonze. Exchange-correlation potentials in the adiabatic connection fluctuation-dissipation framework. *Phys. Rev. A*, 68(3):032507, September 2003.

[56] Nils Erik Dahlen, Robert van Leeuwen, and Ulf von Barth. Variational energy functionals of the green function and of the density tested on molecules. *Phys. Rev. A*, 73(1):012511, January 2006.

[57] Lin Ma, Kenville E. Hendrickson, Shuya Wei, and Lynden A. Archer. Nanomaterials: Science and applications in the lithium–sulfur battery. *Nano Today*, 10(3):315–338, June 2015.

[58] Zhi Wei Seh, Yongming Sun, Qianfan Zhang, and Yi Cui. Designing high-energy lithium–sulfur batteries. *Chem. Soc. Rev.*, 45(20):5605–5634, 2016.

[59] Francesco Bonaccorso, Luigi Colombo, Guihua Yu, Meryl Stoller, Valentina Tozzini, Andrea C. Ferrari, Rodney S. Ruoff, and Vittorio Pellegrini. Graphene, related two-dimensional crystals, and hybrid systems for energy conversion and storage. *Science*, 347(6217):1246501, January 2015.

[60] Bingkun Guo, Teng Ben, Zhonghe Bi, Gabriel M. Veith, Xiao-Guang Sun, Shilun Qiu, and Sheng Dai. Highly dispersed sulfur in a porous aromatic framework as a cathode for lithium–sulfur batteries. *Chem. Commun.*, 49(43):4905, 2013.

[61] Lu Li, Guangmin Zhou, Lichang Yin, Nikhil Koratkar, Feng Li, and Hui-Ming Cheng. Stabilizing sulfur cathodes using nitrogen-doped graphene as a chemical immobilizer for Li s batteries. *Carbon*, 108:120–126, November 2016.

[62] Jiarui He, Gregory Hartmann, Myungsuk Lee, Gyeong S. Hwang, Yuanfu Chen, and Arumugam Manthiram. Freestanding 1T MoS¡sub¿2¡/sub¿/graphene heterostructures as a highly efficient electrocatalyst for lithium polysulfides in Li–S batteries. *Energy Environ. Sci.*, 12(1):344–350, 2019.

[63] Lele Peng, Yue Zhu, Dahong Chen, Rodney S. Ruoff, and Guihua Yu. Two-dimensional materials for beyond-lithium-ion batteries. *Adv. Energy Mater.*, 6(11):1600025, March 2016.

[64] Zhiming Cui, Chenxi Zu, Weidong Zhou, Arumugam Manthiram, and John B. Goodenough. Mesoporous titanium nitride-enabled highly stable lithium-sulfur batteries. *Adv. Mater.*, 28(32):6926–6931, May 2016.

[65] Dashuai Wang, Fei Li, Ruqian Lian, Jing Xu, Dongxiao Kan, Yanhui Liu, Gang Chen, Yury Gogotsi, and Yingjin Wei. A general atomic surface modification strategy for improving anchoring and electrocatalysis behavior of Ti¡sub¿3¡/sub¿C¡sub¿2¡/sub¿T¡sub¿2¡/sub¿ MXene in Lithium–Sulfur batteries. *ACS Nano*, 13(10):11078–11086, August 2019.

[66] Jianming Zheng, Jian Tian, Dangxin Wu, Meng Gu, Wu Xu, Chongmin Wang, Fei Gao, Mark H. Engelhard, Ji-Guang Zhang, Jun Liu, and Jie Xiao. Lewis Acid–Base interactions between polysulfides and metal organic framework in lithium sulfur batteries. *Nano Lett.*, 14(5):2345–2352, April 2014.

[67] Xiulei Ji and Linda F. Nazar. Advances in Li–S batteries. *J. Mater. Chem.*, 20(44):9821, 2010.

[68] M. Wild, L. O'Neill, T. Zhang, R. Purkayastha, G. Minton, M. Marinescu, and G.J. Offer. Lithium sulfur batteries, a mechanistic review. *Energy Environ. Sci.*, 8(12):3477–3494, 2015.

[69] Dong Zheng, Dan Liu, Joshua B. Harris, Tianyao Ding, Jingyu Si, Sergei Andrew, Deyu Qu, Xiao-Qing Yang, and Deyang Qu. Investigation of the Li–S battery mechanism by real-time monitoring of the changes of sulfur and polysulfide species during the discharge and charge. *ACS Appl. Mater. Interfaces*, 9(5):4326–4332, September 2016.

[70] Céline Barchasz, Florian Molton, Carole Duboc, Jean-Claude Leprêtre, Sébastien Patoux, and Fannie Alloin. Lithium/Sulfur cell discharge mechanism: An original approach for intermediate species identification. *Anal. Chem.*, 84(9):3973–3980, April 2012.

[71] Marine Cuisinier, Pierre-Etienne Cabelguen, Scott Evers, Guang He, Mason Kolbeck, Arnd Garsuch, Trudy Bolin, Mahalingam Balasubramanian, and Linda F. Nazar. Sulfur speciation in Li–S batteries determined by operando x-ray absorption spectroscopy. *J. Phys. Chem. Lett.*, 4(19):3227–3232, September 2013.

[72] Qi He, Anna T.S. Freiberg, Manu U.M. Patel, Simon Qian, and Hubert A. Gasteiger. Operando identification of liquid intermediates in Lithium–Sulfur batteries via transmission UV–vis spectroscopy. *J. Electrochem. Soc.*, 167(8):080508, January 2020.

[73] Lijiang Wang, Tianran Zhang, Siqi Yang, Fangyi Cheng, Jing Liang, and Jun Chen. A quantum-chemical study on the discharge reaction mechanism of lithium-sulfur batteries. *Journal of Energy Chemistry*, 22(1):72–77, January 2013.

[74] Qingli Zou and Yi-Chun Lu. Solvent-dictated lithium sulfur redox reactions: An operando UV–vis spectroscopic study. *J. Phys. Chem. Lett.*, 7(8):1518–1525, April 2016.

[75] Guangmin Zhou, Eunsu Paek, Gyeong S. Hwang, and Arumugam Manthiram. Long-life li/polysulphide batteries with high sulphur loading enabled by lightweight three-dimensional nitrogen/sulphur-codoped graphene sponge. *Nat Commun*, 6(1):1–11, July 2015.

[76] Georg Kresse and Jürgen Hafner. Ab initio molecular dynamics for liquid metals. *Phys. Rev. B*, 47(1):558, 1993.

[77] Stephan N. Steinmann and Clemence Corminboeuf. A generalized-gradient approximation exchange hole model for dispersion coefficients. *J. Chem. Phys.*, 134(4):044117, January 2011.

[78] Stephan N. Steinmann and Clemence Corminboeuf. Comprehensive benchmarking of a density-dependent dispersion correction. *J. Chem. Theory Comput.*, 7(11):3567–3577, October 2011.

[79] Jianwei Sun, Adrienn Ruzsinszky, and John P. Perdew. Strongly constrained and appropriately normed semilocal density functional. *Phys. Rev. Lett.*, 115(3):036402, July 2015.

[80] Kiran Mathew, Ravishankar Sundararaman, Kendra Letchworth-Weaver, T.A. Arias, and Richard G. Hennig. Implicit solvation model for density-functional study of nanocrystal surfaces and reaction pathways. *J. Chem. Phys.*, 140(8):084106, February 2014.

[81] Kiran Mathew, V.S. Chaitanya Kolluru, Srinidhi Mula, Stephan N. Steinmann, and Richard G. Hennig. Implicit self-consistent electrolyte model in plane-wave density-functional theory. *J. Chem. Phys.*, 151(23):234101, December 2019.

[82] Arava Leela Mohana Reddy, Anchal Srivastava, Sanketh R. Gowda, Hemtej Gullapalli, Madan Dubey, and Pulickel M. Ajayan. Synthesis of nitrogen-doped graphene films for lithium battery application. *ACS Nano*, 4(11):6337–6342, October 2010.

[83] Yuxi Xu, Zhaoyang Lin, Xing Zhong, Xiaoqing Huang, Nathan O. Weiss, Yu Huang, and Xiangfeng Duan. Holey graphene frameworks for highly efficient capacitive energy storage. *Nat. Commun.*, 5(1):1–8, August 2014.

[84] K. Gong, F. Du, Z. Xia, M. Durstock, and L. Dai. Nitrogen-doped carbon nanotube arrays with high electrocatalytic activity for oxygen reduction. *Science*, 323(5915):760–764, February 2009.

[85] Yong Zhao, Ryuhei Nakamura, Kazuhide Kamiya, Shuji Nakanishi, and Kazuhito Hashimoto. Nitrogen-doped carbon nanomaterials as non-metal electrocatalysts for water oxidation. *Nat. Commun.*, 4(1):1–7, August 2013.

[86] Michel Lefèvre, Eric Proietti, Frédéric Jaouen, and Jean-Pol Dodelet. Iron-based catalysts with improved oxygen reduction activity in polymer electrolyte fuel cells. *Science*, 324(5923):71–74, April 2009.

[87] Haibo Wang, Thandavarayan Maiyalagan, and Xin Wang. Review on recent progress in nitrogen-doped graphene: Synthesis, characterization, and its potential applications. *ACS Catal.*, 2(5):781–794, April 2012.

[88] Dehui Deng, Xiulian Pan, Liang Yu, Yi Cui, Yeping Jiang, Jing Qi, Wei-Xue Li, Qiang Fu, Xucun Ma, Qikun Xue, Gongquan Sun, and et al. Toward n-doped graphene via solvothermal synthesis. *Chem. Mater.*, 23(5):1188–1193, March 2011.

[89] Xiaolin Li, Hailiang Wang, Joshua T. Robinson, Hernan Sanchez, Georgi Diankov, and Hongjie Dai. Simultaneous nitrogen doping and reduction of graphene oxide. *J. Am. Chem. Soc.*, 131(43):15939–15944, November 2009.

[90] L. Zhao, R. He, K.T. Rim, T. Schiros, K.S. Kim, H. Zhou, C. Gutierrez, S.P. Chockalingam, C.J. Arguello, L. Palova, D. Nordlund, M.S. Hybertsen, D.R. Reichman, T.F. Heinz, P. Kim, A. Pinczuk, G.W. Flynn, and A.N. Pasupathy. Visualizing individual nitrogen dopants in monolayer graphene. *Science*, 333(6045):999–1003, August 2011.

[91] Niki Baccile, Guillaume Laurent, Cristina Coelho, Florence Babonneau, Li Zhao, and Maria-Magdalena Titirici. Structural insights on nitrogen-containing hydrothermal carbon using solid-state magic angle spinning ^{13}C and ^{15}N nuclear magnetic resonance. *J. Phys. Chem. C*, 115(18):8976–8982, April 2011.

[92] Bradley F. Chmelka. Materializing opportunities for NMR of solids. *J. Magn. Reson.*, 306:91–97, September 2019.

[93] Helen R. Thomas, Stephen P. Day, William E. Woodruff, Cristina Vallés, Robert J. Young, Ian A. Kinloch, Gavin W. Morley, John V. Hanna, Neil R. Wilson, and Jonathan P. Rourke. Deoxygenation of graphene oxide: Reduction or cleaning? *Chem. Mater.*, 25(18):3580–3588, September 2013.

[94] Francesco Mauri and Steven G. Louie. Magnetic susceptibility of insulators from first principles. *Phys. Rev. Lett.*, 76(22):4246–4249, May 1996.

[95] Chris J. Pickard and Francesco Mauri. All-electron magnetic response with pseudopotentials: Nmr chemical shifts. *Phys. Rev. B*, 63(24):245101, May 2001.

[96] Jonathan R. Yates, Chris J. Pickard, and Francesco Mauri. Calculation of NMR chemical shifts for extended systems using ultrasoft pseudopotentials. *Phys. Rev. B*, 76(2):024401, July 2007.

[97] Mickael Profeta, Francesco Mauri, and Chris J. Pickard. Accurate first principles prediction of ^{17}o nmr parameters in sio$_2$: Assignment of the zeolite ferrierite spectrum. *J. Am. Chem. Soc.*, 125(2):541–548, January 2003.

[98] V. D'Anna, S. Norsic, D. Gajan, K. Sanders, A.J. Pell, A. Lesage, V. Monteil, C. Copéret, G. Pintacuda, and P. Sautet. Structural characterization of the etoh–$TiCl_4$–mgcl$_2$ ziegler–natta precatalyst. *J. Phys. Chem. C*, 120(32):18075–18087, August 2016.

[99] Rachel Nathaniel Kerber, Torsten Kerber, Xavier Rozanska, Françoise Delbecq, and Philippe Sautet. Grafting trimethylaluminum and its halogen derivatives on silica: General trends for ^{27}Al SS-NMR response from first principles calculations. *Phys. Chem. Chem. Phys.*, 17(40):26937–26945, 2015.

[100] Lorenzo Stievano, Frederik Tielens, Iréne Lopes, Nicolas Folliet, Christel Gervais, Dominique Costa, and Jean-François Lambert. Density functional theory modeling and calculation of NMR parameters: An ab initio study of the polymorphs of bulk glycine. *Cryst. Growth Des.*, 10(8):3657–3667, August 2010.

[101] T. Thonhauser, Davide Ceresoli, and Nicola Marzari. NMR shifts for polycyclic aromatic hydrocarbons from first-principles. *Int. J. Quantum Chem.*, 109(14):3336–3342, November 2009.

[102] Nergiz Özcan, Jarkko Vähäkangas, Perttu Lantto, and Juha Vaara. Characteristic spectral patterns in the carbon-13 nuclear magnetic resonance spectra of hexagonal and crenellated graphene fragments. *ChemPhysChem*, 15(9):1799–1808, May 2014.

[103] Jarkko Vähäkangas, Suvi Ikäläinen, Perttu Lantto, and Juha Vaara. Nuclear magnetic resonance predictions for graphenes: Concentric finite models and extrapolation to large systems. *Phys. Chem. Chem. Phys.*, 15(13):4634, 2013.

[104] Dmitry Skachkov, Mykhaylo Krykunov, Eugene Kadantsev, and Tom Ziegler. The calculation of NMR chemical shifts in periodic systems based on gauge including atomic orbitals and density functional theory. *J. Chem. Theory Comput.*, 6(5):1650–1659, April 2010.

[105] Fábio A.L. de Souza, Alan R. Ambrozio, Everson S. Souza, Daniel F. Cipriano, Wanderlã L. Scopel, and Jair C.C. Freitas. NMR spectral parameters in graphene, graphite, and related materials: Ab initio calculations and experimental results. *J. Phys. Chem. C*, 120(48):27707–27716, November 2016.

[106] Leah B. Casabianca. Effect of curvature on carbon chemical shielding in extended carbon systems. *J. Phys. Chem. A*, 120(35):7011–7019, August 2016.

[107] Yuyan Zhang, Juanyuan Hao, Jianwei Li, and Ce Hao. Theoretical study of triiodide reduction reaction on nitrogen-doped graphene for dye-sensitized solar cells. *Theor. Chem. Acc.*, 135(1):23, January 2016.

[108] J. Mason. Conventions for the reporting of nuclear magnetic shielding (or shift) tensors suggested by participants in the NATO ARW on NMR shielding constants at the university of maryland, college park, July 1992. *Solid State Nucl. Mag.*, 2(5):285–288, October 1993.

[109] Philippe Bertani, Jésus Raya, and Burkhard Bechinger. ^{15}n chemical shift referencing in solid state nmr. *Solid State Nucl. Mag.*, 61-62:15–18, July 2014.

[110] Thomas A. Manz and Nidia Gabaldon Limas. Introducing DDEC6 atomic population analysis: Part 1. charge partitioning theory and methodology. *RSC Adv.*, 6(53):47771–47801, 2016.

[111] Nidia Gabaldon Limas and Thomas A. Manz. Introducing DDEC6 atomic population analysis: Part 2. computed results for a wide range of periodic and nonperiodic materials. *RSC Adv.*, 6(51):45727–45747, 2016.

[112] Frances Separovic and Akira Naito. *Advances in Biological Solid-State NMR: Proteins and Membrane-Active Peptides*. Royal Society of Chemistry, 2014.

[113] Malcolm H Levitt. *Spin dynamics: basics of nuclear magnetic resonance*. John Wiley & Sons, 2013.

[114] Nina Fechler, Niels P. Zussblatt, Regina Rothe, Robert Schlögl, Marc-Georg Willinger, Bradley F. Chmelka, and Markus Antonietti. Eutectic syntheses of graphitic carbon with high pyrazinic nitrogen content. *Adv. Mater.*, 28(6):1287–1294, July 2015.

[115] Kent R. Thurber and Robert Tycko. Measurement of sample temperatures under magic-angle spinning from the chemical shift and spin-lattice relaxation rate of ^{79}br in kbr powder. *J. Magn. Reson.*, 196(1):84–87, January 2009.

[116] James P. Yesinowski, Harold D. Ladouceur, Andrew P. Purdy, and Joel B. Miller. Electrical and ionic conductivity effects on magic-angle spinning nuclear magnetic resonance parameters of CuI. *J. Chem. Phys.*, 133(23):234509, December 2010.

[117] Bingwen Hu, Julien Trébosc, and Jean-Paul Amoureux. Comparison of several heteronuclear dipolar recoupling NMR methods to be used in MAS HMQC/HSQC. *J. Magn. Reson.*, 192(1):112–122, 2008.

[118] Takeshi Kobayashi, Dilini Singappuli-Arachchige, Zhuoran Wang, Igor I Slowing, and Marek Pruski. Spatial distribution of organic functional groups supported on mesoporous silica nanoparticles: A study by conventional and dnp-enhanced ^{29}si solid-state nmr. *Phys. Chem. Chem. Phys.*, 19(3):1781–1789, 2017.

[119] Anne Lesage, Dimitris Sakellariou, Stefan Steuernagel, and Lyndon Emsley. Carbon−Proton chemical shift correlation in solid-state NMR by through-bond multiple-quantum spectroscopy. *J. Am. Chem. Soc.*, 120(50):13194–13201, December 1998.

[120] Yongchao Si and Edward T. Samulski. Synthesis of water soluble graphene. *Nano Lett.*, 8(6):1679–1682, June 2008.

[121] Wei Gao, Lawrence B. Alemany, Lijie Ci, and Pulickel M. Ajayan. New insights into the structure and reduction of graphite oxide. *Nat. Chem.*, 1(5):403–408, July 2009.

[122] Daniela C. Marcano, Dmitry V. Kosynkin, Jacob M. Berlin, Alexander Sinitskii, Zhengzong Sun, Alexander Slesarev, Lawrence B. Alemany, Wei Lu, and James M. Tour. Improved synthesis of graphene oxide. *ACS Nano*, 4(8):4806–4814, July 2010.

[123] Sasha Stankovich, Dmitriy A. Dikin, Richard D. Piner, Kevin A. Kohlhaas, Alfred Kleinhammes, Yuanyuan Jia, Yue Wu, SonBinh T. Nguyen, and Rodney S. Ruoff. Synthesis of graphene-based nanosheets via chemical reduction of exfoliated graphite oxide. *Carbon*, 45(7):1558–1565, June 2007.

[124] HA Resing, DC Weber, M Anderson, GR Miller, M Moran, CF Poranski Jr, and L Mattix. NMR shift tensors for polyacetylene and graphite. *Polym. Prepr.*, 23:101, 1982.

[125] Hans Darmstadt, Christian Roy, Serge Kaliaguine, Guoying Xu, Michèle Auger, Alain Tuel, and Veda Ramaswamy. Solid state ^{13}c-nmr spectroscopy and xrd studies of commercial and pyrolytic carbon blacks. *Carbon*, 38(9):1279–1287, 2000.

[126] Shigeki Kuroki, Yuta Nabae, Masayuki Chokai, Masa-aki Kakimoto, and Seizo Miyata. Oxygen reduction activity of pyrolyzed polypyrroles studied by ^{15}n solid-state nmr and xps with principal component analysis. *Carbon*, 50(1):153–162, January 2012.

[127] WJ Gammon, GL Hoatson, BC Holloway, RL Vold, and AC Reilly. Bonding in hard and elastic amorphous carbon nitride films investigated using ^{15}n, ^{13}c, and ^{1}h nmr spectroscopy. *Phys. Rev. B*, 68(19):195401, 2003.

[128] Jiajie Huo, Pu Duan, Hien N. Pham, Yee Jher Chan, Abhaya K. Datye, Klaus Schmidt-Rohr, and Brent H. Shanks. Improved hydrothermal stability of pd nanoparticles on nitrogen-doped carbon supports. *Catal. Sci. Technol.*, 8(14):3548–3561, 2018.

[129] Yichen Hu, Yeonjun Shim, Junghoon Oh, Sunghee Park, Sungjin Park, and Yoshitaka Ishii. Synthesis of ^{13}c-,^{15}n-labeled graphitic carbon nitrides and NMR-based evidence of hydrogen-bonding assisted two-dimensional assembly. *Chem. Mater.*, 29(12):5080–5089, June 2017.

[130] Xianlong Wang, Zhufeng Hou, Takashi Ikeda, and Kiyoyuki Terakura. NMR chemical shifts of ^{15}n-bearing graphene. *J. Phys. Chem. C*, 118(25):13929–13935, June 2014.

[131] J.C. Leger. Menger curvature and rectifiability. *Ann. Math.*, 149(3):831, May 1999.

[132] D.G. Farnum. Charge density-NMR chemical shift correlations in organic ions. In *Advances in Physical Organic Chemistry Volume 11*, volume 11, pages 123–175. Elsevier, 1975.

[133] John P. Perdew, J.A. Chevary, S.H. Vosko, Koblar A. Jackson, Mark R. Pederson, D.J. Singh, and Carlos Fiolhais. Atoms, molecules, solids, and surfaces: Applications of the generalized gradient approximation for exchange and correlation. *Phys. Rev. B*, 46(11):6671–6687, September 1992.

[134] Yanwei Lum, Tao Cheng, William A. Goddard, and Joel W. Ager. Electrochemical CO reduction builds solvent water into oxygenate products. *J. Am. Chem. Soc.*, 140(30):9337–9340, July 2018.

[135] Andrew P. Graham, Frank Hofmann, J. Peter Toennies, Gwyn P. Williams, Carol J. Hirschmugl, and John Ellis. A high resolution helium atom scattering and far infrared study of the dynamics and the lateral potential energy surface of CO molecules chemisorbed on cu(001). *J. Chem. Phys.*, 108(18):7825–7834, May 1998.

[136] G. Alexandrowicz, A.P. Jardine, P. Fouquet, S. Dworski, W. Allison, and J. Ellis. Observation of microscopic CO dynamics on cu(001) UsingH3eSpin-echo spectroscopy. *Phys. Rev. Lett.*, 93(15):156103, October 2004.

[137] Q. Ge and D.A. King. Response to "Comment on 'Surface diffusion potential energy surfaces from first principles"' [J. chem. phys. 114, 1051 (2001)]. *J. Chem. Phys.*, 114(2):1053, 2001.

[138] Peter Fouquet, Roar A. Olsen, and Evert Jan Baerends. Diffusion and vibration of CO molecules adsorbed on a cu(100) surface: A periodic density functional theory study. *J. Chem. Phys.*, 119(1):509–514, July 2003.

[139] David Zanuttini, Fabien Gatti, and Roberto Marquardt. CO quantum dynamics diffusion on cu(1 0 0). *Chem. Phys.*, 509:3–12, June 2018.

[140] Stefan Grimme. Semiempirical GGA-type density functional constructed with a long-range dispersion correction. *J. Comput. Chem.*, 27(15):1787–1799, 2006.

[141] Stefan Grimme, Jens Antony, Stephan Ehrlich, and Helge Krieg. A consistent and accurate ab initio parametrization of density functional dispersion correction DFT-d for the 94 elements h-Pu. *J. Chem. Phys.*, 132(15):154104, April 2010.

[142] B. Hammer, L.B. Hansen, and J.K. Nørskov. Improved adsorption energetics within density-functional theory using revised perdew-Burke-ernzerhof functionals. *Phys. Rev. B*, 59(11):7413–7421, March 1999.

[143] Jess Wellendorff, Keld T. Lundgaard, Andreas Møgelhøj, Vivien Petzold, David D. Landis, Jens K. Nørskov, Thomas Bligaard, and Karsten W. Jacobsen. Density functionals for surface science: Exchange-correlation model development with Bayesian error estimation. *Phys. Rev. B*, 85(23):235149, June 2012.

[144] Aliaksandr V. Krukau, Oleg A. Vydrov, Artur F. Izmaylov, and Gustavo E. Scuseria. Influence of the exchange screening parameter on the performance of screened hybrid functionals. *J. Chem. Phys.*, 125(22):224106, December 2006.

[145] Stephen L. Adler. Quantum theory of the dielectric constant in real solids. *Phys. Rev.*, 126(2):413–420, April 1962.

[146] Nathan Wiser. Dielectric constant with local field effects included. *Phys. Rev.*, 129(1):62–69, January 1963.

[147] Filipp Furche. Developing the random phase approximation into a practical post-Kohn–Sham correlation model. *J. Chem. Phys.*, 129(11):114105, September 2008.

[148] Martin Fuchs and Xavier Gonze. Accurate density functionals: Approaches using the adiabatic-connection fluctuation-dissipation theorem. *Phys. Rev. B*, 65(23):235109, June 2002.

[149] Xinguo Ren, Patrick Rinke, and Matthias Scheffler. Exploring the random phase approximation: Application to CO adsorbed on cu(111). *Phys. Rev. B*, 80(4):045402, July 2009.

[150] Guo-Xu Zhang, Alexandre Tkatchenko, Joachim Paier, Heiko Appel, and Matthias Scheffler. van der waals interactions in ionic and semiconductor solids. *Phys. Rev. Lett.*, 107(24):245501, December 2011.

[151] Thom Vreven, K. Suzie Byun, István Komáromi, Stefan Dapprich, John A. Montgomery, Keiji Morokuma, and Michael J. Frisch. Combining quantum mechanics methods with molecular mechanics methods in ONIOM. *J. Chem. Theory Comput.*, 2(3):815–826, May 2006.

[152] Lung Wa Chung, W.M.C. Sameera, Romain Ramozzi, Alister J. Page, Miho Hatanaka, Galina P. Petrova, Travis V. Harris, Xin Li, Zhuofeng Ke, Fengyi Liu, Hai-Bei Li, Lina Ding, and Keiji Morokuma. The ONIOM method and its applications. *Chem. Rev.*, 115(12):5678–5796, April 2015.

[153] Florian Göltl, Céline Houriez, Marie Guitou, Gilberte Chambaud, and Philippe Sautet. Importance of a nonlocal description of Electron–Electron interactions in modeling the dissociative adsorption of h2 on cu(100). *J. Phys. Chem. C*, 118(10):5374–5382, February 2014.

[154] Qing-Miao Hu, Karsten Reuter, and Matthias Scheffler. Towards an exact treatment of exchange and correlation in materials: Application to the "CO adsorption puzzle" and other systems. *Phys. Rev. Lett.*, 98(17):176103, April 2007.

[155] Joachim Sauer. Ab initio calculations for Molecule–Surface interactions with chemical accuracy. *Acc. Chem. Res.*, 52(12):3502–3510, November 2019.

[156] Florian Libisch, Chen Huang, and Emily A. Carter. Embedded correlated wavefunction schemes: Theory and applications. *Acc. Chem. Res.*, 47(9):2768–2775, May 2014.

[157] Xing Zhang and Emily A. Carter. Subspace density matrix functional embedding theory: Theory, implementation, and applications to molecular systems. *J. Chem. Theory Comput.*, 15(2):949–960, December 2018.

[158] Kuang Yu and Emily A. Carter. Extending density functional embedding theory for covalently bonded systems. *Proc. Natl. Acad. Sci. U.S.A.*, 114(51):E10861–E10870, December 2017.

[159] Chen Huang, Michele Pavone, and Emily A. Carter. Quantum mechanical embedding theory based on a unique embedding potential. *J. Chem. Phys.*, 134(15):154110, April 2011.

[160] Florian Libisch, Chen Huang, Peilin Liao, Michele Pavone, and Emily A. Carter. Origin of the energy barrier to chemical reactions ofO2on al(111): Evidence for charge transfer, not spin selection. *Phys. Rev. Lett.*, 109(19):198303, November 2012.

[161] Sahar Sharifzadeh, Patrick Huang, and Emily Carter. Embedded configuration interaction description of CO on cu(111): Resolution of the site preference conundrum. *J. Phys. Chem. C*, 112(12):4649–4657, March 2008.

[162] Laurids Schimka. *Application of the random phase approximation to complex problems in materials science*. PhD thesis, University of Vienna, retrieved from othes.univie.ac.at, 2012.

[163] Patanachai Janthon, Sijie Luo, Sergey M Kozlov, Francesc Vines, Jumras Limtrakul, Donald G Truhlar, and Francesc Illas. Bulk properties of transition metals: A challenge for the design of universal density functionals. *J. Chem. Theory Comput.*, 10(9):3832–3839, 2014.

[164] S. Lebègue, J. Harl, Tim Gould, J.G. Ángyán, G. Kresse, and J.F. Dobson. Cohesive properties and asymptotics of the dispersion interaction in graphite by the random phase approximation. *Phys. Rev. Lett.*, 105(19):196401, November 2010.

[165] P.E. Blōchl. Projector augmented-wave method. *Phys. Rev. B*, 50(24):17953–17979, December 1994.

[166] Graeme Henkelman, Blas P. Uberuaga, and Hannes Jónsson. A climbing image nudged elastic band method for finding saddle points and minimum energy paths. *J. Chem. Phys.*, 113(22):9901–9904, December 2000.

[167] Charles M. Truong, JoséA. Rodriguez, and D.W. Goodman. CO adsorption isotherms on cu(100) at elevated pressures and temperatures using infrared reflection absorption spectroscopy. *Surf. Sci.*, 271(3):L385–L391, January 1992.

[168] Y. Hori. Electrochemical CO2 reduction on metal electrodes. In *Modern Aspects of Electrochemistry*, pages 89–189. Springer New York, 2008.

[169] Md Golam Kibria, Jonathan P. Edwards, Christine M. Gabardo, Cao-Thang Dinh, Ali Seifitokaldani, David Sinton, and Edward H. Sargent. Electrochemical CO 2 reduction into chemical feedstocks: From mechanistic electrocatalysis models to system design. *Adv. Mater.*, 31(31):1807166, May 2019.

[170] Yoshio Hori, Katsuhei Kikuchi, and Shin Suzuki. Production of co and Ch4In electrochemical reduction of Co2At metal electrodes in aqueous hydrogencarbonate solution. *Chem. Lett.*, 14(11):1695–1698, November 1985.

[171] Klaas Jan P. Schouten, Zisheng Qin, Elena Pérez Gallent, and Marc T.M. Koper. Two pathways for the formation of ethylene in CO reduction on single-crystal copper electrodes. *J. Am. Chem. Soc.*, 134(24):9864–9867, June 2012.

[172] Yoshio Hori, Ichiro Takahashi, Osamu Koga, and Nagahiro Hoshi. Selective formation of c2 compounds from electrochemical reduction of CO2 at a series of copper single crystal electrodes. *J. Phys. Chem. B*, 106(1):15–17, December 2001.

[173] Federico Calle-Vallejo and Marc T.M. Koper. Theoretical considerations on the electroreduction of CO to C2Species on cu(100) electrodes. *Angew. Chem. Int. Ed.*, 52(28):7282–7285, June 2013.

[174] Joseph H. Montoya, Chuan Shi, Karen Chan, and Jens K. Nørskov. Theoretical insights into a CO dimerization mechanism in CO2 electroreduction. *J. Phys. Chem. Lett.*, 6(11):2032–2037, May 2015.

[175] Hongjie Peng, Michael T. Tang, Xinyan Liu, Philomena Schlexer Lamoureux, Michal Bajdich, and Frank Abild-Pedersen. The role of atomic carbon in directing electrochemical CO(2) reduction to multicarbon products. *Energy Environ. Sci.*, 14(1):473–482, 2021.

[176] Xinyan Liu, Philomena Schlexer, Jianping Xiao, Yongfei Ji, Lei Wang, Robert B. Sandberg, Michael Tang, Kristopher S. Brown, Hongjie Peng, Stefan Ringe, Christopher Hahn, Thomas F. Jaramillo, Jens K. Nørskov, and Karen Chan. pH effects on the electrochemical reduction of CO(2) towards c2 products on stepped copper. *Nat. Commun.*, 10(1):1–10, January 2019.

[177] Javed Hussain, Hannes Jónsson, and Egill Skúlason. Calculations of product selectivity in electrochemical CO2 reduction. *ACS Catal.*, 8(6):5240–5249, April 2018.

[178] Ziyang Wei, Florian Göltl, and Philippe Sautet. Diffusion barriers for carbon monoxide on the cu(001) surface using many-body perturbation theory and various density functionals. *J. Chem. Theory Comput.*, 17(12):7862–7872, November 2021.

[179] Alejandro J. Garza, Alexis T. Bell, and Martin Head-Gordon. Mechanism of CO2 reduction at copper surfaces: Pathways to c2 products. *ACS Catal.*, 8(2):1490–1499, January 2018.

[180] Tao Cheng, Hai Xiao, and William A. Goddard. Full atomistic reaction mechanism with kinetics for CO reduction on cu(100) from ab initio molecular dynamics free-energy calculations at 298 k. *Proc. Natl. Acad. Sci. U.S.A.*, 114(8):1795–1800, February 2017.

[181] Sara E. Mason, Ilya Grinberg, and Andrew M. Rappe. First-principles extrapolation method for accurate CO adsorption energies on metal surfaces. *Phys. Rev. B*, 69(16):161401, April 2004.

[182] Marek Gajdoš and Jürgen Hafner. CO adsorption on cu(111) and cu(001) surfaces: Improving site preference in DFT calculations. *Surf. Sci.*, 590(2-3):117–126, October 2005.

[183] J.K. Nørskov, J. Rossmeisl, A. Logadottir, L. Lindqvist, J.R. Kitchin, T. Bligaard, and H. Jónsson. Origin of the overpotential for oxygen reduction at a fuel-cell cathode. *J. Phys. Chem. B*, 108(46):17886–17892, October 2004.

[184] Thomas Ludwig, Joseph A. Gauthier, Colin F. Dickens, Kristopher S. Brown, Stefan Ringe, Karen Chan, and Jens K. Nørskov. Atomistic insight into cation effects on binding energies in cu-catalyzed carbon dioxide reduction. *J. Phys. Chem. C*, 124(45):24765–24775, November 2020.

[185] Hendrik H. Heenen, Joseph A. Gauthier, Henrik H. Kristoffersen, Thomas Ludwig, and Karen Chan. Solvation at metal/water interfaces: An ab initio molecular dynamics benchmark of common computational approaches. *J. Chem. Phys.*, 152(14):144703, April 2020.

[186] Thomas Ludwig, Joseph A. Gauthier, Kristopher S. Brown, Stefan Ringe, Jens K. Nørskov, and Karen Chan. Solvent–Adsorbate interactions and adsorbate-specific solvent structure in carbon dioxide reduction on a stepped cu surface. *J. Phys. Chem. C*, 123(10):5999–6009, February 2019.

[187] Jack H. Baricuatro, Youn-Geun Kim, Carol L. Korzeniewski, and Manuel P. Soriaga. Seriatim ECSTM-ECPMIRS of the adsorption of carbon monoxide on cu(100) in alkaline solution at CO2-reduction potentials. *Electrochem. Commun.*, 91:1–4, June 2018.

[188] Joseph H. Montoya, Andrew A. Peterson, and Jens K. Nørskov. Insights into c-c coupling in CO2electroreduction on copper electrodes. *ChemCatChem*, 5(3):737–742, January 2013.

[189] Jason D. Goodpaster, Alexis T. Bell, and Martin Head-Gordon. Identification of possible pathways for C–C bond formation during electrochemical reduction of CO2: New theoretical insights from an improved electrochemical model. *J. Phys. Chem. Lett.*, 7(8):1471–1477, April 2016.

[190] Stephan N. Steinmann, Carine Michel, Renate Schwiedernoch, and Philippe Sautet. Impacts of electrode potentials and solvents on the electroreduction of CO2: A comparison of theoretical approaches. *Phys. Chem. Chem. Phys.*, 17(21):13949–13963, 2015.

[191] Stephan N. Steinmann and Philippe Sautet. Assessing a first-principles model of an electrochemical interface by comparison with experiment. *J. Phys. Chem. C*, 120(10):5619–5623, March 2016.

[192] Yoshio Hori, Ryutaro Takahashi, Yuzuru Yoshinami, and Akira Murata. Electrochemical reduction of CO at a copper electrode. *J. Phys. Chem. B*, 101(36):7075–7081, September 1997.

[193] Marc T.M. Koper. Theory of multiple proton–electron transfer reactions and its implications for electrocatalysis. *Chem. Sci.*, 4(7):2710, 2013.

[194] Elena Pérez-Gallent, Marta C. Figueiredo, Federico Calle-Vallejo, and Marc T.M. Koper. Spectroscopic observation of a hydrogenated CO dimer intermediate during CO reduction on cu(100) electrodes. *Angew. Chem. Int. Ed.*, 56(13):3621–3624, February 2017.

[195] Yan Jiao, Yao Zheng, Mietek Jaroniec, and Shi Zhang Qiao. Design of electrocatalysts for oxygen-and hydrogen-involving energy conversion reactions. *Chem. Soc. Rev.*, 44(8):2060–2086, 2015.

[196] Hubert A. Gasteiger and Nenad M Marković. Just a dream—or future reality? *Science*, 324(5923):48–49, April 2009.

[197] Cyrille Costentin, Marc Robert, and Jean-Michel Savéant. Catalysis of the electrochemical reduction of carbon dioxide. *Chem. Soc. Rev.*, 42(6):2423–2436, 2013.

[198] Mette Mikkelsen, Mikkel Jørgensen, and Frederik C. Krebs. The teraton challenge. a review of fixation and transformation of carbon dioxide. *Energy Environ. Sci.*, 3(1):43–81, 2010.

[199] Hai Xiao, Tao Cheng, William A. Goddard, and Ravishankar Sundararaman. Mechanistic explanation of the pH dependence and onset potentials for hydrocarbon products from electrochemical reduction of CO on cu (111). *J. Am. Chem. Soc.*, 138(2):483–486, January 2016.

[200] Rui Shang, Stephan N. Steinmann, Bo-Qing Xu, and Philippe Sautet. Mononuclear Fe in n-doped carbon: Computational elucidation of active sites for electrochemical oxygen reduction and oxygen evolution reactions. *Catal. Sci. Technol.*, 10(4):1006–1014, 2020.

[201] Ravishankar Sundararaman and William A. Goddard. The charge-asymmetric nonlocally determined local-electric (CANDLE) solvation model. *J. Chem. Phys.*, 142(6):064107, February 2015.

[202] Per S. Schmidt and Kristian S. Thygesen. Benchmark database of transition metal surface and adsorption energies from many-body perturbation theory. *J. Phys. Chem. C*, 122(8):4381–4390, February 2018.

[203] Sergio Trasatti. Interfacial behaviour of non-aqueous solvents. *Electrochim. Acta*, 32(6):843–850, June 1987.

[204] W. Ronald Fawcett. The ionic work function and its role in estimating absolute electrode potentials. *Langmuir*, 24(17):9868–9875, August 2008.

[205] Jun Haruyama, Tamio Ikeshoji, and Minoru Otani. Electrode potential from density functional theory calculations combined with implicit solvation theory. *Phys. Rev. Materials*, 2(9):095801, September 2018.

[206] Henk Eshuis, Jefferson E. Bates, and Filipp Furche. Electron correlation methods based on the random phase approximation. *Theor Chem Acc*, 131(1):1–18, January 2012.

[207] Jason M. Yu, Brian D. Nguyen, Jeffrey Tsai, Devin J. Hernandez, and Filipp Furche. Selfconsistent random phase approximation methods. *J. Chem. Phys.*, 155(4):040902, July 2021.

[208] T. Pajkossy and D.M. Kolb. Double layer capacitance of pt(111) single crystal electrodes. *Electrochim. Acta*, 46(20-21):3063–3071, July 2001.

[209] Robert S. Hansen, Robert E. Minturn, and Donald A. Hickson. The inference of adsorption from differential double-layer capacitance measurements. *J. Phys. Chem.*, 60(9):1185–1189, September 1956.

[210] Robert S. Hansen, Dennis J. Kelsh, and D.H. Grantham. The inference of adsorption from differential double layer capacitance measurements. ii. dependence of surface charge density on organic nonelectrolyte surface excess. *J. Phys. Chem.*, 67(11):2316–2326, November 1963.

[211] Elena Pérez-Gallent, Giulia Marcandalli, Marta Costa Figueiredo, Federico Calle-Vallejo, and Marc T.M. Koper. Structure- and potential-dependent cation effects on CO reduction at copper single-crystal electrodes. *J. Am. Chem. Soc.*, 139(45):16412–16419, November 2017.

[212] M. Dion, H. Rydberg, E. Schröder, D.C. Langreth, and B.I. Lundqvist. Van der waals density functional for general geometries. *Phys. Rev. Lett.*, 92(24):246401, June 2004.

[213] Jiří Klimeš, David R. Bowler, and Angelos Michaelides. Van der waals density functionals applied to solids. *Phys. Rev. B*, 83(19):195131, May 2011.

[214] Jiří Klimeš, David R Bowler, and Angelos Michaelides. Chemical accuracy for the van der waals density functional. *J. Phys.: Condens. Matter*, 22(2):022201, December 2009.

[215] P.J. Stephens, F.J. Devlin, C.F. Chabalowski, and M.J. Frisch. Ab initio calculation of vibrational absorption and circular dichroism spectra using density functional force fields. *J. Phys. Chem.*, 98(45):11623–11627, November 1994.

[216] Haesun Park, Hyun Seung Koh, and Donald J. Siegel. First-principles study of redox end members in Lithium–Sulfur batteries. *J. Phys. Chem. C*, 119(9):4675–4683, February 2015.

[217] David H. Wertz. Relationship between the gas-phase entropies of molecules and their entropies of solvation in water and 1-octanol. *J. Am. Chem. Soc.*, 102(16):5316–5322, July 1980.

[218] Yong Liang, Song Liu, Yuanzhi Xia, Yahong Li, and Zhi-Xiang Yu. Mechanism, regioselectivity, and the kinetics of phosphine-catalyzed [3+2] cycloaddition reactions of allenoates and electron-deficient alkenes. *Chem. Eur. J.*, 14(14):4361–4373, May 2008.

[219] Pei Wang, Stephan N. Steinmann, Gang Fu, Carine Michel, and Philippe Sautet. Key role of anionic doping for h2 production from formic acid on pd(111). *ACS Catal.*, 7(3):1955–1959, February 2017.

[220] Aneta Łukomska and Jerzy Sobkowski. Potential of zero charge of monocrystalline copper electrodes in perchlorate solutions. *J. Electroanal. Chem.*, 567(1):95–102, June 2004.

[221] Stefan Ringe, Ezra L Clark, Joaquin Resasco, Amber Walton, Brian Seger, Alexis T Bell, and Karen Chan. Understanding cation effects in electrochemical CO 2 reduction. *Energy Environ. Sci.*, 12(10):3001–3014, 2019.

[222] John O'M Bockris, Brian E Conway, and Ralph E White. *Modern aspects of electrochemistry*, volume 22. Springer Science & Business Media, 1992.